Precision Measurement of Strange Quark Asymmetry and Monolithic Pixel Sensors for Vertexing at the FCC-ee

---

Dissertation

zur

Erlangung der naturwissenschaftlichen Doktorwürde (Dr. sc. nat.)

vorgelegt der

Mathematisch-naturwissenschaftlichen Fakultät

der

Universität Zürich

von

Kunal Gautam

aus

Indien

Promotionskommission

Prof. Dr. Florencia Canelli (Vorsitz)

Prof. Dr. Michael Tytgat

Prof. Dr. Freya Blekman

Prof. Dr. Gino Isidori

Dr. Anna Macchiolo

Zürich, 2025

VRIJE
UNIVERSITEIT
BRUSSEL

Thesis submitted in fulfilment of the requirements for the award of the degree of Doctor of Science

PRECISION MEASUREMENT OF STRANGE QUARK ASYMMETRY AND MONOLITHIC PIXEL SENSORS FOR VERTEXING AT THE FCC-EE

Kunal Gautam

September 15, 2025

Promotor:	Prof. Dr. Michael Tytgat (VUB)
Co-promotor:	Prof. Dr. Florencia Canelli (University of Zurich)
Supervisor:	Prof.Dr. Freya Blekman (DESY, University of Hamburg)
Jury:	Prof. Dr. Alberto Mariotti (VUB), chairman
	Prof. Dr. Lea Caminada (University of Zurich)
	Dr. Michele Selvaggi (CERN)
	Dr. Francesca Carnesecchi (CERN)

Faculty of Sciences & Bio-Engineering Sciences
Department of Physics and Astrophysics

The work presented in this thesis has in part or wholly been supervised by:

Prof. Dr. Freya Blekman (DESY, Universität Hamburg)
Prof. Dr. Florencia Canelli (Universität Zürich)
Prof. Dr. Michael Tytgat (IIHE, Vrije Universiteit Brussel)
Dr. Anna Macchiolo (Universität Zürich)
Dr. Armin Ilg (Universität Zürich)

Abstract

Future e^+e^- colliders, such as the FCC-ee, aim to test the Standard Model to the ultimate precision. This requires synergistic progress in detector technology and data analysis techniques. This thesis comprehensively presents the interlinked efforts targeting these goals.

Jet flavour identification algorithms play a crucial role in maximally exploiting the physics potential of the FCC-ee, particularly in the Higgs and electroweak sectors. The `DeepJetTransformer` algorithm, exploiting a transformer-based neural network that is substantially faster to train than state-of-the-art graph neural networks, combines particle-flow reconstruction with advanced vertex reconstruction and hadron particle identification. Beyond an excellent b- and c-jet discrimination, an s-jet tagging efficiency of 40% can be achieved with a 10% ud-jet background efficiency. The impact of $K^\pm/\pi^\pm$ discrimination with varying efficiencies and inclusion of reconstructed V^0s for strange tagging performance is shown. Similarly, the importance of charged jet constituents and reconstructed secondary vertices for bottom and charm tagging is presented. The bottom and charm tagging efficiencies were largely uniform over the entire momentum and polar angle range of interest. However, the strange tagging efficiency showed a dependence on the $K^\pm$ and V^0 multiplicities in different momentum regimes.

A 5σ discovery significance can be achieved while isolating $Z \to s\bar{s}$ events from the exclusive decays of the Z boson with an integrated luminosity of $60\,\mathrm{nb}^{-1}$ of e^+e^- collisions at $\sqrt{s} = 91.2\,\mathrm{GeV}$, corresponding to less than a second of the FCC-ee run plan at the Z boson resonance. The improved strange tagging performance opens new avenues for extracting quark-specific asymmetries, such as the forward-backward asymmetry (A_{FB}). Using advanced neural network-based strange tagging and quark-antiquark jet separation with jet charge, the A_{FB} measurement in the strange decay channel of the Z boson is possible with an absolute statistical precision of $2.6 \cdot 10^{-6}$ at the FCC-ee, considering a luminosity of $125\,\mathrm{ab}^{-1}$ at the Z resonance. The corresponding $\sin^2\theta_W$ value can be measured with an absolute statistical precision of $4.6 \cdot 10^{-6}$.

To support these improvements, ultra-thin, high-resolution, and robust vertex detectors are essential. Recent advancements in the use of ultra-light monolithic active pixel sensors (MAPS), developed in the 65 nm imaging process, for the ALICE ITS3 project by an international consortium of the ALICE collaboration and the CERN EP R&D project envision drastic improvements in vertexing performance. Process modification is introduced by adding a deep low-dose n-type layer, which aids in the depletion of full sensor volume by extending the depletion region laterally while keeping a low sensor capacitance. It leads to faster charge collection and reduction in charge shared with neighbouring pixels, thus improving the detection efficiency.

Pixel response calibration and energy resolution measurements performed with the ^{55}Fe radioactive source in the controlled laboratory environment are presented. Four variants of pixel geometry were tested with a small-scale analogue prototype, APTS, all showing over 99% charge collection efficiency for a small reverse bias voltage of 1.2 V. The impact of geometry variation on detection efficiency, spatial resolution, and radiation tolerance is highlighted. In-pixel efficiency studies show that the loss of efficiency at high thresholds is primarily concentrated at the edges and corners of the pixels. APTS shows sub-3 µm spatial resolution and $> 99\%$ detection efficiency, even under moderate irradiation, satisfying the stringent requirements of ALICE and future collider environments.

Together, these developments highlight the integrated advancements in detector design, reconstruction algorithms, and physics potential, strengthening the next generation of precision measurements at the FCC-ee and beyond.

Acknowledgements

Science is, at its heart, a collective endeavour, an echo of the social bonds that define humanity. Every idea takes shape through dialogue, and every result gains strength through shared effort. This thesis, though written in a single voice, carries the imprint of many others, to whom I owe my deepest gratitude.

First and foremost, I want to express my deepest appreciation to Prof. Freya Blekman for her constant guidance and support. I am continually amazed by how you cultivated my enthusiasm while remaining honest about the realities of life in research. You have been an incredible mentor and have always patiently guided me back to my path. Every interaction with you has been a cheerful learning experience, and I am forever grateful to you.

I would also like to acknowledge my gratitude to Prof. Florencia Canelli, who fostered a collaborative environment that greatly enriched my doctoral journey and has been a constant source of encouragement.

I doubt that many people have had the privilege of working with as many promoters and co-promoters as I have. Therefore, I would like to sincerely thank Prof. Jorgen D'Hondt and Prof. Michael Tytgat for keeping the ship steady through the long voyage of my doctoral studies. I also want to show my appreciation to Dr. Anna Macchiolo for her regular guidance and encouragement.

I have been fortunate to have spent these years of my research with an academic family of sorts. And through these four years, three countries, and several projects, my academic elder brother Armin has been one of the few constants. You brought order to the chaos with your ninja management skills and have left your mark on almost everything I was involved in over these past years.

Speaking of management, I would be remiss if I were to forget to mention the administrative support from Nina, Sophie, Regina, Monika, Birgit, and Anna. I would be filling paperwork instead of writing my thesis if not for you all.

I am very thankful to my ITS3 collaborators; your cheerful attitudes, the promise of ping-pong, and Paolo's Sunday doughnut brought a little sunshine into the windowless SPS facility.

I am very grateful to have met such amazing people at the IIHE and to be able to call them some of my closest friends. Thanks to Santiago, Soumya, Indrani, AR, Rijeesh, Jaydeep, Paramita, Hugues, Marta, Godwin, Nikos, Denice, Felix H, Felix S, Nordin, Max, Saranya, Alexandre, Pavlo, Martin, Katarina, Brussels will always be home. This feeling for Brussels has been further elevated by my HJ housemates.

I would like to thank Eslam, Rebekka, Sascha, Fabian, Pascal, Weijie, Valeriia, and Filip for sharing a wonderful time in Zurich and for being so kind to my comical criticisms. I am also grateful to have had Seco and Henri as two of the most unique and amazing roommates. Try as I might, I cannot keep myself from acknowledging the Alps. During the final stint of my PhD, I had the pleasure of sharing my time in Hamburg and DESY with Divyanshu, Lucia, Keila, Suman, and Gabriele.

To go back to the analogy of family, my academic twin, Edi, has been my constant companion.

Even a quick recap of our journey together has the potential to turn into an epic. I'm glad to have shared this experience with you. These four years have taken us many places, given us many labels (colleague, roommate, friend), and with you, every incident turned into an anecdote worthy to be shared around a fire.

I am deeply grateful to have circles of friends from Guwahati and Copenhagen, who have gifted me with immeasurable love and support. Years later, (the extended) KARISHMA remains my first family outside my home; they are my biggest cheerleaders and my emergency therapists. And my friends in Amsterdam have made my life more beautiful than I could imagine. I apologise for not naming all of my friends individually, but believe that you are very close to my heart and I hope to make you proud.

Going back to $t = 0$, all of this originated with my family. I cannot find words to express the depth of my gratitude for the immense love, support, and sacrifices which have guided me to this stage. I am forever indebted to my parents and my brother, whose unwavering presence and countless quiet acts have carried me through every stage of this journey. Lastly, I would like to thank Trina, and whoever else I can that you are in my life, for more things than I can count. Your faith, kindness, and courage guide me every day.

I would like to dedicate this thesis to the memory of my grandfather, who taught me the value of education and scientific curiosity, and to always smile in the face of adversity.

Kunal Gautam

Author's Contribution

This thesis is the result of original research conducted by the author within the context of doctoral studies in experimental high-energy physics. While benefiting from the collaborative environment of international projects, the results, developments, and interpretations presented here reflect the author's own contributions. The specific contributions are outlined in detail below.

Vertex Reconstruction and Jet Flavour Tagging

The vertex reconstruction algorithm employed in this thesis was originally developed as the vertex reconstruction module of the LCFIPlus algorithm [1]. The author implemented this algorithm in the FCC software framework, with adaptations enabling the reconstruction and identification of V^0s, novel physics observables used for strange jet tagging. The author evaluated the performance of the jet flavour tagging algorithm by analysing efficiency trends across the available ranges of momentum and polar angle, and by isolating $Z \to s\bar{s}$ events from exclusive Z boson decays. These studies were published in an EPJ C article [2], to which the author contributed substantially, including the preparation of the manuscript. The author also summarised the results for the ECFA Higgs, Electroweak, and Top Factory Study Report [3].

Forward-Backward Asymmetry Measurement

The author implemented a momentum-weighted jet charge tagging algorithm to discriminate between quark and antiquark jets. Using this method, the author performed one of the first measurements of the strange-quark forward–backward asymmetry to evaluate the statistical precision achievable at the FCC-ee, complemented by analogous studies for bottom and charm quarks. This work has been presented in the ECFA Higgs, Electroweak, and Top Factory Study Report [3].

Analogue MAPS Characterisation

The author contributed substantially to the characterisation of the analogue properties of MAPS fabricated in the 65 nm CMOS imaging process, using test structures designed by the ALICE ITS3 collaboration. The author was primarily responsible for studying the impact of pixel geometry variations on pixel detector performance. This work resulted in two NIM-A publications [4, 5].

Laboratory Measurements

All measurements with the ^{55}Fe radioactive source reported in this thesis were performed by the author, along with minor adaptations to the data acquisition and analysis framework. The author also performed the analysis of all laboratory measurement data, including the calibration of all APTS-MUX chips.

Testbeam Measurements

The author contributed extensively to several APTS testbeam campaigns at the PS and SPS facilities at CERN, eventually leading one of them. At the SPS facility, the author was primarily responsible for testbeam data acquisition for all APTS-MUX chips, including telescope installation and alignment. The author also carried out the testbeam data analysis for all APTS-MUX chips and produced all results presented in this thesis, with the exception of the in-pixel efficiency measurement.

Contents

Introduction

"The important thing is not to stop questioning. Curiosity has its own reason for existence. One cannot help but be in awe when he contemplates the mysteries of eternity, of life, of the marvelous structure of reality. It is enough if one tries merely to comprehend a little of this mystery each day."

Albert Einstein, 1955

Human curiosity and the quest to comprehend the natural world have formed the foundation of scientific inquiry, and our understanding of the Universe has been drastically transformed over the last century. A structure of the fundamental constituents of the Universe and their interactions has emerged. The scientific theory that describes them is known as the Standard Model of particle physics (SM) and has been one of the most successful achievements of collective human thought. The two foundational pillars of the scientific method are theoretical formulation, i.e. hypothesising or explaining natural phenomena, and empirical validation through experiments and observations. It is the latter that will be the focus of this thesis.

High-energy experiments performed by colliding particles probe nature at the smallest distance scales and recreate the conditions of the early Universe. By colliding particles at ever-increasing energies and intensities, these experiments have not only validated and refined numerous predictions of the SM, but have also uncovered new phenomena that deepen our understanding of the fundamental structure of the Universe.

The next generation of high-energy particle colliders aims to test the SM to its ultimate limits, as well as explore potential deviations signalling New Physics. The first stage of the Future Circular Collider, the FCC-ee, provides one of the most promising and ambitious physics programs by targeting unprecedented luminosity and energy coverage in e^+e^- collisions. The FCC-ee will provide an extraordinary opportunity to study the electroweak bosons and the Higgs boson with remarkable statistical precision. It simultaneously presents novel experimental challenges, requiring coordinated advancement in detector technology and data analysis techniques, both of which are major themes of this thesis.

One of the cornerstones of the FCC-ee physics program is the ability to identify the flavour of quarks that initiate jets in the final state. Jet flavour tagging enables precise studies of heavy-flavour physics, Higgs couplings, and electroweak observables. The discrimination between b-, c-, and s-jets and those originating from lighter quarks is therefore of critical importance. Recent developments in machine learning, in particular neural network architectures capable of exploiting complex particle-flow information and vertex reconstruction, promise major improvements in flavour tagging capabilities at future colliders.

This thesis presents an algorithm for jet flavour identification that employs a transformer-based neural network, called `DeepJetTransformer`. Despite being a general algorithm, the development of this jet flavour tagger focussed on collision events at the Z resonance at the FCC-ee and aimed to improve the strange jet tagging performance by introducing kaon/pion

discrimination and novel reconstruction of neutral strange bosons.

Such improvements in jet flavour tagging will greatly benefit the measurements of quark-specific electroweak observables, such as the forward-backward asymmetry (A_{FB}). The measurement of A_{FB} in the process $e^+e^- \to Z \to q\bar{q}$ at the FCC-ee, exploiting the high-statistics run at the Z resonance, will provide one of the most sensitive tests of the electroweak parameters, including $\sin^2\theta_{\mathrm{W}}$. Studies exploiting neural network-based jet flavour taggers to isolate the $Z \to s\bar{s}$ final state and to assess the achievable statistical precision on the A^s_{FB} measurement are presented in this thesis.

Delivering these physics goals puts stringent constraints on detector design and performance. The tracking detectors are required to be light while providing exceptional spatial resolution, especially the layers close to the interaction point, often referred to as the vertex detector. Monolithic Active Pixel Sensors (MAPS), merging the sensitive volume and the readout circuitry in a single device, have emerged as the leading candidate for the vertex detector technology at the future colliders, including the FCC-ee.

The developments made by the ALICE collaboration at the Large Hadron Collider to upgrade its Inner Tracking System (ITS) to a MAPS-based detector have been instrumental in driving the MAPS technology in large-area detector applications. The next upgrade of the ITS, referred to as the ITS3, relies on the use of ultra-thin MAPS with high granularity and has synonymous requirements to the FCC-ee vertex detectors.

Test structures, with small and large pixel matrices, have been developed in the 65 nm CMOS imaging technology to study the analogue and digital properties of MAPS. Moving to the lower technology node reduces the power consumption of the detectors and enables more complex in-pixel circuits. Process modifications implemented in MAPS allow for the depletion region to extend to the full area of the sensor, improving charge collection and radiation tolerance. This thesis presents the characterisation of MAPS with the Analogue Pixel Test Structure (APTS), studying the impact on pixel geometry, pitch size, and substrate voltage on the charge collection, detection efficiency, energy resolution, spatial resolution, and radiation tolerance.

This thesis presents a coherent set of studies addressing the interrelated challenges in data analysis techniques and detector technology. It begins by presenting the theoretical foundation and the experimental setup of particle colliders and detectors, while introducing the FCC-ee and the IDEA detector concept. It then details the jet flavour tagging algorithm developed for the FCC-ee environment and investigates the achievable precision in the measurement of electroweak observables, specifically the forward-backward asymmetry, by exploiting jet flavour tagging. It further examines the development and characterisation of ultra-thin MAPS with an analogue test structure, and presents the characterisation of MAPS developed in the 65 nm CMOS imaging technology with an ^{55}Fe radioactive source in the laboratory setup and with a hadron beam at the CERN-SPS facility.

Together, these efforts illustrate the synergy between detector design and analysis techniques required to fully exploit the physics potential of future e^+e^- colliders.

Part I

Setting the Stage

1 The Standard Model of Particle Physics

The Standard Model (SM) is one of the most successful accomplishments in the quest to understand the fundamental constituents of the Universe and their interactions. Over the last century, the SM has explained a wide range of phenomena with extraordinary precision, as well as has made several successful predictions, such as the existence of various particles that complete the fundamental make-up of the SM.

In the SM, the wave-particle duality of quantum mechanics is generalised through quantised fields, with particles arising as the excitations of these fields, while the forces are manifested as the interaction of different fields.

1.1 The Gauge Fields

The Quantum Field Theory (QFT) is the foundational framework of the SM, unifying the classical field theory with quantum mechanics and the special theory of relativity. It describes the fundamental particles and their interactions as quantised excitations of matter and gauge fields. A field is represented by the form $\phi_a(x^\mu)$, with a being the index of a field in a group and x^μ being the spacetime 4-vector. The operations on the field are represented by operators $\mathcal{O}$ acting on the field. The mathematical function that encodes the dynamics of the fields is referred to as the Lagrangian, defined as,

$$L(t) = \int d^3x \ \mathcal{L}(\phi_a, \partial_\mu \phi_a, x^\mu), \tag{1.1}$$

where, $\mathcal{L}$ is the Lagrangian density.

QFT is governed by symmetries, which are transformations under which the Lagrangian density remains invariant. These symmetries can non-exclusively be categorised as local, global, or internal, of which the local and the internal symmetries are of particular importance. The fields in the SM are invariant under Lorentz transformation, as required by the special theory of relativity. They are also invariant under the so-called gauge transformation and are said to be gauge invariant. The gauge invariance is a local internal symmetry, in which the Lagrangian density remains invariant under the transformation,

$$\phi_a(x) \rightarrow \phi_a^{'}(x) = U(x)\phi_a(x), \tag{1.2}$$

where $U(x)$ is a unitary transformation operator. The gauge invariance of the fields in the SM results in the corresponding conserved charges.

Particles, defined as the quantised excitation of matter and gauge fields, are categorised into fermions and bosons, based on their intrinsic spin. Fermions are particles with a half-integer spin that follow the Fermi-Dirac statistics and are constrained by Pauli's exclusion principle. Fermions are represented by Dirac spinors, $\psi(x)$ [6]. Bosons are particles with an integer spin that follow the Bose-Einstein statistics. Vector bosons are represented by interacting Yang-Mills fields, A_μ^a [7].

The Lagrangian density of a fermions interacting with a vector field, invariant under local

gauge transformation has the form,

$$\mathcal{L} = \bar{\psi}(x)(\gamma^\mu D_\mu - m_\psi)\psi - \frac{1}{2}\mathrm{Tr}\left(F_{\mu\nu}F^{\mu\nu}\right), \tag{1.3}$$

where γ^μ are complex matrices that follow the Clifford Algebra [6], $D_\mu = \partial_\mu - igA_\mu$ with g being the coupling strength. The field strength, $F_{\mu\nu}$, for the field A_μ is defined as,

$$F_{\mu\nu} = \partial_\mu A_\nu - \partial_\nu A_\mu + ig[A_\mu, A_\nu]. \tag{1.4}$$

1.2 Structure of Matter and Forces

The SM consists of 12 fundamental matter particles, the spin-1/2 fermions, and their anti-particles, 12 fundamental force-carrying particles, the spin-1 gauge bosons, and one spin-0 scalar particle. The gauge bosons manifest in two basic forces: the strong force carried by the gluons and the electroweak interaction carried by γ, $W^\pm$, and Z bosons. The SM interactions follow the Lie algebra group $SU(3) \otimes SU(2)_L \otimes U(1)$ [8]. The fermions are classified into leptons and quarks depending on the forces with which they interact. These particles, including fermions and bosons, and their classification are shown in Figure 1.1.

The electroweak interaction does not conserve parity symmetry and treats left- and right-handed chiral states differently [9]. Due to the chiral nature of the electroweak interaction, the mass terms for fermions, $-m\bar{\psi}\psi$, and gauge bosons, $-M^2A^\mu A_\mu$, cannot be included directly

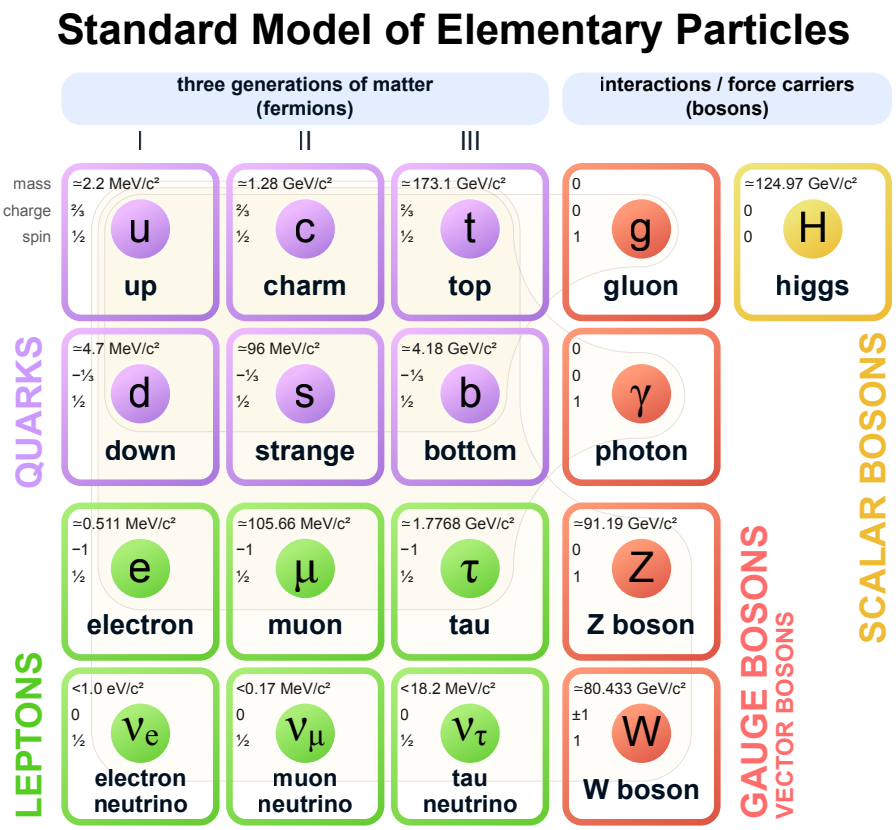

Figure 1.1: The standard model of elementary particles, with particles categorised in different groups. The bosons and the three generations of the fermions, along with their fundamental properties are shown. The lightly-shaded regions assemble the particles depending on the interactions they undergo.

into the SM Lagrangian, as they are not gauge invariant. The massive gauge bosons acquire mass through the electroweak symmetry breaking mechanism, which gives rise to a spin-0 scalar field [10–13]. The fermions gain their mass through the Yukawa interactions with this scalar field [14].

1.2.1 Forces in the SM

In the SM, forces manifest as the interaction between fermionic and bosonic fields. In other words, force is experienced by the interaction and exchange of particles. Of the four fundamental forces in nature, the gravitational force lies outside the scope of the SM, as, currently, there is no experimentally verified theory of quantum gravity, and it is, therefore, not discussed further.

The other three forces, or more accurately, interactions, are the electromagnetic interaction, the weak interaction, and the strong interaction. The electromagnetic interaction is mediated by the photon and is described by the quantised theory of electromagnetism, known as Quantum Electrodynamics (QED) [15, 16]. The weak interaction, which is responsible for particle decays, is mediated by two charged $W^{\pm}$ bosons and one neutral Z boson. The electromagnetic and the weak interactions are related and form the unified electroweak interactions. The strong interaction is mediated by eight gluons and is described by the quantised theory of Quantum Chromodynamics (QCD).

Figure 1.2 shows the scattering of two electrons by the exchange of a photon. The first two diagrams correspond to a time-ordered interaction where time flows from left to right. In the first diagram, a photon is emitted by the upper electron and is later absorbed by the lower electron. In the second diagram, a photon is emitted by the lower electron and is later absorbed by the upper electron. This results in an effective transfer of momentum from one electron to the other, and is consequently experienced as a force. The exchanged photon is a virtual particle and is not observed; thus, only the combined effect of the two diagrams is physically significant. The combined effect is represented by the third diagram, referred to as a Feynman diagram. Such diagrams are very useful to calculate the strength of the interactions, i.e the cross-sections. The Feynman diagrams were first introduced for QED [17] and have since been generalised to include all interactions in the SM.

Quantum Electrodynamics

QED is the fundamental theory of the electromagnetic interactions. It is invariant under the $U(1)$ gauge group, which arises from the mixing of the $SU(2)_L$ and $U(1)_Y$ groups, as detailed later. The electromagnetic interaction is experienced by particles which are electrically charged,

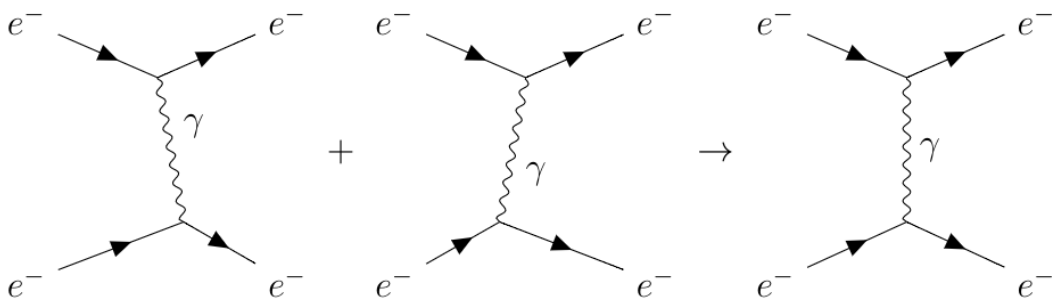

Figure 1.2: The scattering of two electrons through the exchange of a photon in QED. The first two diagrams show the two possibilities for the exchange of the photon. The third diagram shows the combined effect of the two possibilities for the interaction and is known as a Feynman diagram.

and the gauge boson in QED, the photon, is massless.

Quantum Chromodynamics

QCD is the fundamental theory of the strong interactions and is invariant under the $SU(3)$ gauge group, which requires eight generators [18]. These eight generators lead to eight gauge bosons, the gluons. The strong interaction is experienced by particles carrying the colour charge, which can be red, blue, green, or their anti-colours. The massless gluons carry a combination of colour and anti-colour charges, which means that the gluons can self-interact.

The coupling constant for QCD, α_s, decreases with increasing energy scale, leading to its characteristic asymptotic freedom. Equivalently, α_s increases with increasing length scale. However, α_s is very high at low energies, and QCD cannot be treated with the perturbative approach. Owing to the self-interaction of gluons and the high coupling constant, the strong force is constrained to very short length scales. Separating coloured particles to large distances causes the energy of the system to rise, until it's energetically favourable for new coloured particles to be generated, resulting in colour-neutral states. This phenomenon, by which colour-charged particles cannot be isolated but only exist in colour-neutral bound states, is called colour confinement [19].

The colour-neutral states can be iteratively broken in high-energy environments, resulting in a shower of colour-neutral particles, through a process known as hadronisation. Hadronisation falls into the non-perturbative regime of QCD and is still an active field of research.

Electroweak Theory

The unified electroweak interactions are invariant under the $SU(2)_L \otimes U(1)_Y$ gauge group [14]. The $SU(2)_L$ component requires three generators, leading to three gauge fields, $W_\mu^{(k)}$, with $k = 1,\ 2,\ 3$. The conserved charge for these gauge fields is called the weak isospin, T. The $U(1)_Y$ component leads to one gauge field, B_μ and the corresponding conserved charge is called the weak hypercharge, Y.

These four gauge fields combine to form the physical gauge bosons of the electroweak interactions. The mixing results in parity-violating weak interactions and parity-conserving electromagnetic interactions. The chiral structure of the electroweak interactions is designed so that the left-handed fermions form weak isospin doublets, while the right-handed fermions exist in singlets. This structure is reversed for the antiparticles of the fermions.

The mixing of these gauge fields and the electroweak unification is detailed in Section 1.3.

Electroweak Symmetry Breaking and the Brout-Englert-Higgs Mechanism

The chiral structure of the electroweak interactions prevents direct mass terms in the SM Lagrangian. However, the fermions and bosons, with the exception of the photon and the gluons, have been observed to have mass. In the SM, the massive fermions and bosons gain their mass by interacting with a scalar field, called the Brout-Englert-Higgs (BEH) field, through the electroweak symmetry-breaking mechanism, also called the BEH mechanism [11–13].

The BEH field is composed of two scalar fields in a weak isospin doublet,

$$\phi = \begin{pmatrix} \phi^+ \\ \phi^0 \end{pmatrix} = \frac{1}{\sqrt{2}} \begin{pmatrix} \phi_1 + i\phi_2 \\ \phi_3 + i\phi_4 \end{pmatrix}. \tag{1.5}$$

Thus, it has four degrees of freedom.

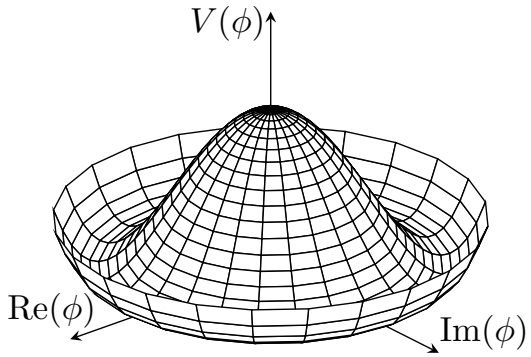

Figure 1.3: The Brout-Englert-Higgs (BEH) potential, $V(\phi)$. The minimum of the potential lies at a non-zero vacuum expectation value of the BEH field, leading to electroweak symmetry breaking.

The Lagrangian for the scalar field, ϕ, is given by,

$$\mathcal{L}_\phi = (D^\mu \phi)^\dagger (D_\mu \phi) - V(\phi), \tag{1.6}$$

where $D_\mu = \partial_\mu + ig_{\mathrm{W}} W_\mu + ig_{\mathrm{Y}} B_\mu$ is the covariant derivative, with g_{W} and g_{Y} being the couplings for the $SU(2)_L$ and $U(1)_Y$ components of the electroweak gauge fields. The potential $V(\phi)$ is,

$$V(\phi) = \mu^2 \phi^\dagger \phi + \frac{1}{2}\lambda(\phi^\dagger \phi)^2. \tag{1.7}$$

Here, the $\phi^\dagger\phi$ term is analogous to a mass-like term for the scalar field, while the $(\phi^\dagger\phi)^2$ term represents the self-interaction of the scalar field. For the potential to have a minimum, λ is required to be positive.

Unlike λ, μ^2 does not have a constraint to be positive or negative for the potential to have a minimum. If $\mu^2 > 0$, the minimum of the potential is at the origin, i.e. $\langle\phi\rangle = 0$, and the above Lagrangian describes a massive scalar doublet in a symmetric electroweak phase. Consequently, the particles in the SM remain massless.

However, if $\mu^2 < 0$, the potential acquires a shape as shown in Figure 1.3 and the minimum of the potential lies at a non-zero value,

$$\langle\phi\rangle = v = \sqrt{-\frac{\mu^2}{\lambda}}, \tag{1.8}$$

which is called the vacuum expectation value (VEV). The choice of the vacuum state breaks the symmetry of the Lagrangian. The non-zero VEV leads to the electroweak gauge fields becoming massive.

The fermions interact with the same BEH scalar field and gain their mass, which can be chosen to agree with the observed masses of the fermions.

1.2.2 Matter Particles in the SM

The observable matter in the universe is formed by particles known as fermions. There are twelve fermions in the SM, which are arranged in three generations. Each generation is composed of a charged lepton, its neutrino, an up-type quark, and a down-type quark. Except for the neutrinos, the mass of which has not been precisely measured, the fermions of successive generations are heavier than the previous ones, but have identical quantum numbers.

All of the fermions experience the weak interactions, while all charged fermions experience the electromagnetic interactions. However, they are categorised based on whether they experience

the strong interactions as leptons and quarks, as shown in Figure 1.1.

Leptons

Fermions with zero colour charge are called leptons; thus, they do not experience strong interaction. Leptons in each generation are composed of a charged lepton, its neutrino, and the corresponding antiparticles. The charged leptons, the electron, the muon, and the tau lepton, have an electromagnetic charge of -1, by convention, and the corresponding antiparticles have an electromagnetic charge of $+1$. The heavier charged leptons can decay into the lighter charged leptons via the weak interaction.

The three neutrinos and their antiparticles are electromagnetically neutral. Neutrinos are also massless in the SM, but have been observed to have mass in experiments measuring the so-called neutrino oscillations [20, 21].

Quarks

Quarks are fermions with colour charge. Each fermionic generation is composed of an up-type quark with an electromagnetic charge of $+2/3$ and a down-type quark with an electromagnetic charge of $-1/3$ and their antiparticles: the up (u) and down (d) quarks in the first generation, the charm (c) and the strange (s) quarks in the second generation, and the top (t) and the bottom (b) quark in the third generation. Each of the six quark flavours appears in three distinct colour-charge states.

Particles in nature cannot exist in a colour-charged state, but must form colour-neutral states due to colour confinement. The bound colour-neutral states formed by quarks are called hadrons. Hadrons formed by a bound quark-antiquark state, such as the pion, are called mesons, while hadrons formed by a bound state of three quarks and antiquarks, such as the proton, are called baryons.

Similar to the lepton, the heavier quarks can decay to lighter quarks via weak interaction. These transitions and the mixing between the different generations of quarks in the SM is described by the Cabibbo–Kobayashi–Maskawa (CKM) matrix [22, 23].

1.3 The *Z* Boson and the Neutral Current Weak Interactions

The bosons for the charged-current weak interaction carry electromagnetic charges, indicating a relation between the electromagnetic and weak forces. In fact, $W^{\pm}$ boson pair can be produced in e^+e^- interactions following the two Feynman diagrams shown in Figure 1.4.

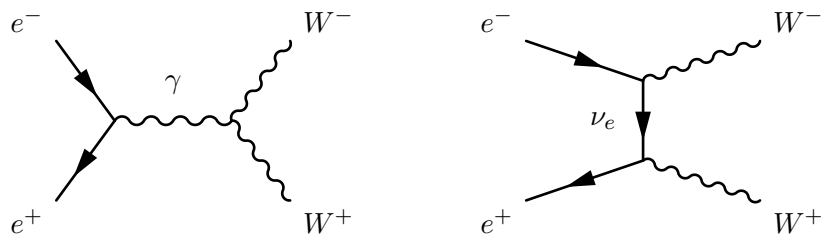

Figure 1.4: The Feynman diagrams for the production of a $W^{\pm}$ boson pair through the process $e^+e^- \to W^+W^-$ in the absence of a neutral electroweak boson.

The W^+W^- production cross-section following from the two given diagrams violates unitarity, as the cross-section continues to increase with the increasing center-of-mass (CoM) energy. The unitarity violation can be avoided by introducing a neutral boson with a coupling that is

related to the couplings for the γ and $W^{\pm}$ bosons. The Feynman diagram presented in Figure 1.5 interferes negatively with the diagrams shown in Figure 1.4, thus avoiding the unitarity violation.

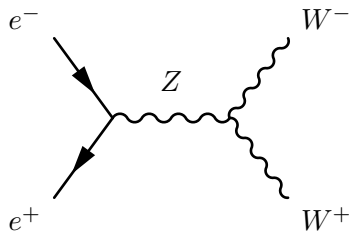

Figure 1.5: The Feynman diagram for the production of a $W^{\pm}$ boson pair through the process $e^+e^- \to W^+W^-$ with an intermediate neutral electroweak boson.

Weak Interaction

The charged-current weak interaction is associated with the $SU(2)$ local gauge symmetry and is invariant under the transformation [24],

$$\varphi(x) \to \varphi'(x) = e^{[ig_{\mathrm{W}}\boldsymbol{\alpha}(x)\cdot\mathbf{T}]},$$

where g_{W} is the weak coupling, $\mathbf{T}$ are the three generators of the $SU(2)$ group, related to the Pauli spin matrices by $\mathbf{T} = \frac{1}{2}\boldsymbol{\sigma}$, and $\boldsymbol{\alpha}(x)$ specifies the local phase. $\varphi(x)$ is referred to as the weak-isospin doublet and takes the form like [24],

$$\varphi(x) = \begin{pmatrix} \nu_e(x) \\ e^-(x) \end{pmatrix}.$$

The local gauge invariance is satisfied by the introduction of three gauge fields, $W_\mu^{(k)}$ with $k = 1,\ 2,\ 3$, each corresponding to a gauge boson. The physical charged-current weak bosons, $W^{\pm}$, are identified as linear combinations of the first two gauge bosons [24],

$$W^{\pm} = \frac{1}{\sqrt{2}}\left(W_\mu^{(1)} \mp iW_\mu^{(2)}\right). \tag{1.9}$$

Electroweak Unification

The Glashow, Salam, and Weinberg (GSW) electroweak unification model replaces the $U(1)$ gauge symmetry of QED with a new $U(1)_Y$ local gauge symmetry, which gives rise to the B_μ gauge field that couples to the so-called weak hypercharge, Y. The interaction term for the B_μ gauge field follows the same form as the QED interaction term, and the photon and the Z boson are identified as linear combinations of the B_μ and the neutral $W_\mu^{(3)}$ gauge fields [24],

$$A_\mu = +B_\mu \cos\theta_{\mathrm{W}} + W_\mu^{(3)} \sin\theta_{\mathrm{W}}, \tag{1.10}$$

$$Z_\mu = -B_\mu \sin\theta_{\mathrm{W}} + W_\mu^{(3)} \cos\theta_{\mathrm{W}}. \tag{1.11}$$

Here, θ_{W} denotes the weak mixing angle.

Family			T^f	T_3^f	Q_f
$\nu_{e\mathrm{L}}$	$\nu_{\mu\mathrm{L}}$	$\nu_{\tau\mathrm{L}}$	1/2	+1/2	0
e_{L}	μ_{L}	τ_{L}	1/2	−1/2	−1
$\nu_{e\mathrm{R}}$	$\nu_{\mu\mathrm{R}}$	$\nu_{\tau\mathrm{R}}$	0	0	0
e_{R}	μ_{R}	τ_{R}	0	0	−1
u_{L}	c_{L}	t_{L}	1/2	+1/2	+2/3
d_{L}	s_{L}	b_{L}	1/2	−1/2	−1/3
u_{R}	c_{R}	t_{R}	0	0	+2/3
d_{R}	s_{R}	b_{R}	0	0	−1/3

Table 1.1: Weak-isospin structure of the SM particles. The subscripts 'L' and 'R' denote left- and right-handed particles. T^f is the weak isospin, T_3^f is the third component of the weak isospin, and Q_f is the electromagnetic charge of a fermion f. [25]

Relationship between Weak and Electromagnetic Couplings

The charged-current weak coupling is related to the electromagnetic coupling through the weak mixing angle [24],

$$e = g_{\mathrm{W}} \sin\theta_{\mathrm{W}}. \tag{1.12}$$

The weak hypercharge, Y, is similarly related to the electromagnetic charge, Q [24],

$$Y = 2\left(Q - T_3\right), \tag{1.13}$$

with T_3 being the third component of the weak-isospin.

The coupling of the physical Z boson is defined as,

$$g_{\mathrm{Z}} = \frac{g_{\mathrm{W}}}{\cos\theta_{\mathrm{W}}} = \frac{e}{\sin\theta_{\mathrm{W}}\cos\theta_{\mathrm{W}}}, \tag{1.14}$$

where the second relation directly follows from Equation 1.12. The Z boson couples differently to left- and right-handed chiral particles, with the two couplings being defined as,

$$g_{\mathrm{L}}^f = T_3^f - Q_f \sin^2\theta_{\mathrm{W}}, \tag{1.15}$$

$$g_{\mathrm{R}}^f = -Q_f \sin^2\theta_{\mathrm{W}}, \tag{1.16}$$

where, Q_f is the charge, and T_3^f is the third component of the weak-isospin of the fermion f. The couplings of the Z boson can also be formulated in terms of the vector and axial-vector couplings,

$$g_{\mathrm{V}}^f = g_{\mathrm{L}}^f + g_{\mathrm{R}}^f, \tag{1.17}$$

$$g_{\mathrm{A}}^f = g_{\mathrm{L}}^f - g_{\mathrm{R}}^f. \tag{1.18}$$

At tree-level, the ratio of the vector and the axial vector couplings, g_{V}^f and g_{A}^f, respectively, is directly related to the mixing angle, $\sin^2\theta_{\mathrm{W}}$ as [25],

$$\frac{g_{\mathrm{V}}^f}{g_{\mathrm{A}}^f} = 1 - \frac{2Q_f}{T_3^f}\sin^2\theta_{\mathrm{W}} = 1 - 4|Q_f|\sin^2\theta_{\mathrm{W}}, \tag{1.19}$$

where, Q_f is the charge, and T_3^f is the weak-isospin of the fermion f. The weak-isospin structure of the fermions is presented in Table 1.1. After the tree-level quantities are modified by radiative corrections, the tree-level parameters in Eq. 1.19 are updated to their 'effective' values, most notably, the mixing angle is updated to $\sin^2\theta_{\mathrm{eff}}^f$.

Decay mode	Branching ratio [%]
$Z \to e^+e^-$	3.3632 ± 0.0042
$Z \to \mu^+\mu^-$	3.3662 ± 0.0066
$Z \to \tau^+\tau^-$	3.3696 ± 0.0083
$Z \to$ invisible	20.000 ± 0.055
$Z \to$ hadrons	69.911 ± 0.056
$Z \to (u\bar{u} + c\bar{c})/2$	11.6 ± 0.6
$Z \to (d\bar{d} + s\bar{s} + b\bar{b})/3$	15.6 ± 0.4
$Z \to c\bar{c}$	12.03 ± 0.21
$Z \to b\bar{b}$	15.12 ± 0.05

Table 1.2: The measured branching ratios of the Z boson for the major decay modes. [20]

Z Boson Decays

Partial decay width of the Z boson at tree level depends on its coupling and mass, and is given by [24],

$$\Gamma(Z \to f\bar{f}) = \frac{g_Z^2 m_Z}{48\pi}(g_V^{f\ 2} + g_A^{f\ 2}). \tag{1.20}$$

The total decay width, which is equal to the inverse of the lifetime of the Z boson in the natural units, is the sum of all partial widths,

$$\Gamma_Z = \sum_f \Gamma(Z \to f\bar{f}). \tag{1.21}$$

Table 1.2 lists the major the branching ratios, defined as $\mathrm{Br}(Z \to f\bar{f}) = \Gamma(Z \to f\bar{f})/\Gamma_Z$ of the Z boson.

Number of Neutrino Generations

As mentioned earlier, only three generations of fermions have ever been observed. If a fourth generation existed, with particles massive enough to avoid detection thus far, the neutrinos of that generation should be light enough to allow for the decay process, $Z \to \nu_4\bar{\nu}_4$. If it is assumed that the invisible decays of the Z boson are only to neutrinos that couple according to the SM expectations, the number of neutrino generations, N_ν, can be determined from the measurement of the total decay width of the Z boson and partial decay widths to hadrons and leptons. Assuming lepton universality, the total decay width of the Z boson can be written as,

$$\Gamma_Z = 3\Gamma_{ll} + \Gamma_{\mathrm{hadrons}} + N_\nu \Gamma_{\nu\nu}^{\mathrm{SM}}, \tag{1.22}$$

where $\Gamma_{\nu\nu}^{\mathrm{SM}}$ is the SM prediction of the Z boson partial decay width to neutrinos. The impact of the number of neutrino generations on the hadronic cross-section of the Z boson is shown in Figure 1.6.

Using the measured values of the total and partial decay widths of the Z boson, the number of neutrino generations has been determined to be three, more accurately [25],

$$N_\nu = 2.9840 \pm 0.0082. \tag{1.23}$$

1.4 Two-Fermion Process in Electron-Positron Interactions

At low CoM energies, the quark pair production in e^+e^- collisions is dominated by a photon exchange. The contribution from the Z boson exchange process starts to become significant

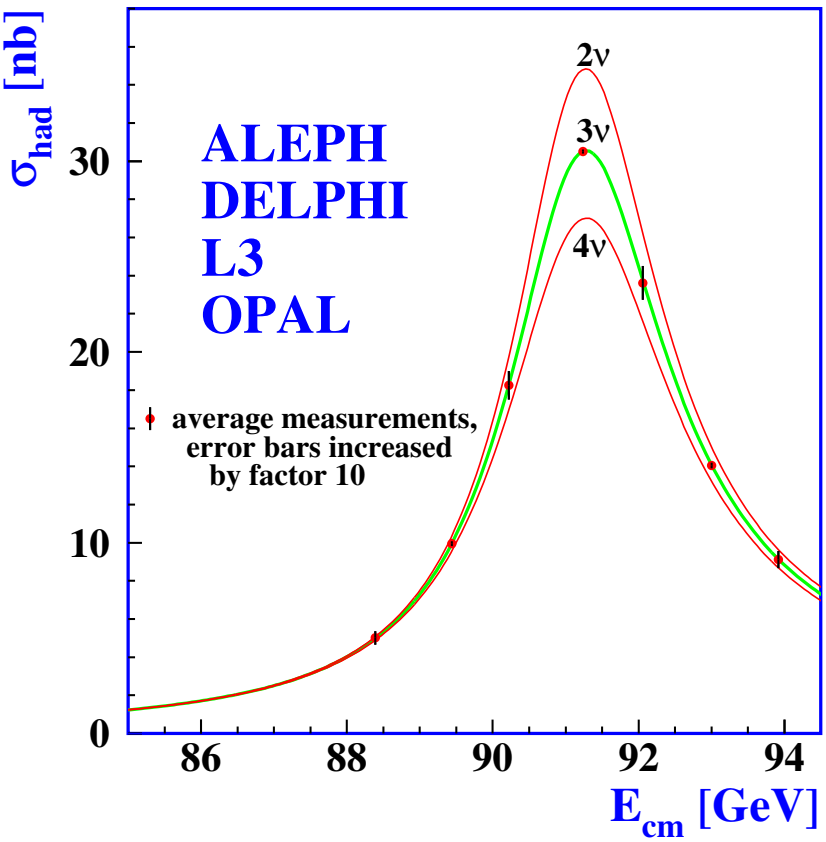

Figure 1.6: The measurements of the hadronic cross-section of the Z boson. The curves present the predictions for the hadronic cross-section for scenarios with two, three, and four generations of SM-like neutrinos. [25]

with increasing collision energies. At energies close to the mass of the Z boson, the process $e^+e^- \to Z \to q\bar{q}$ becomes dominant and the cross-section acquires a Breit-Wigner resonance shape. The two lowest-order Feynman diagrams for the process $e^+e^- \to f\bar{f}$ are shown in Figure 1.7. The SM hadronic cross-section of the e^+e^- interaction, along with its measurements from several experiments, is depicted in Figure 1.8.

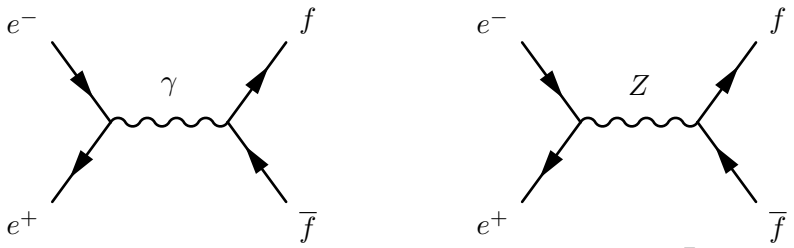

Figure 1.7: The Feynman diagrams for the process $e^+e^- \to f\bar{f}$ via γ/Z exchange.

The higher-order electroweak and QCD corrections, such as the initial and final state photon radiation and final state gluon radiation, are neglected in the following mathematical formalism, but are briefly discussed in Section 1.4.1. The tree-level electroweak cross-section for unpolarised incoming beams contains contributions from three terms: the s-channel photon exchange, the s-channel Z boson exchange, and the interference of the two. It is also referred to as the Born

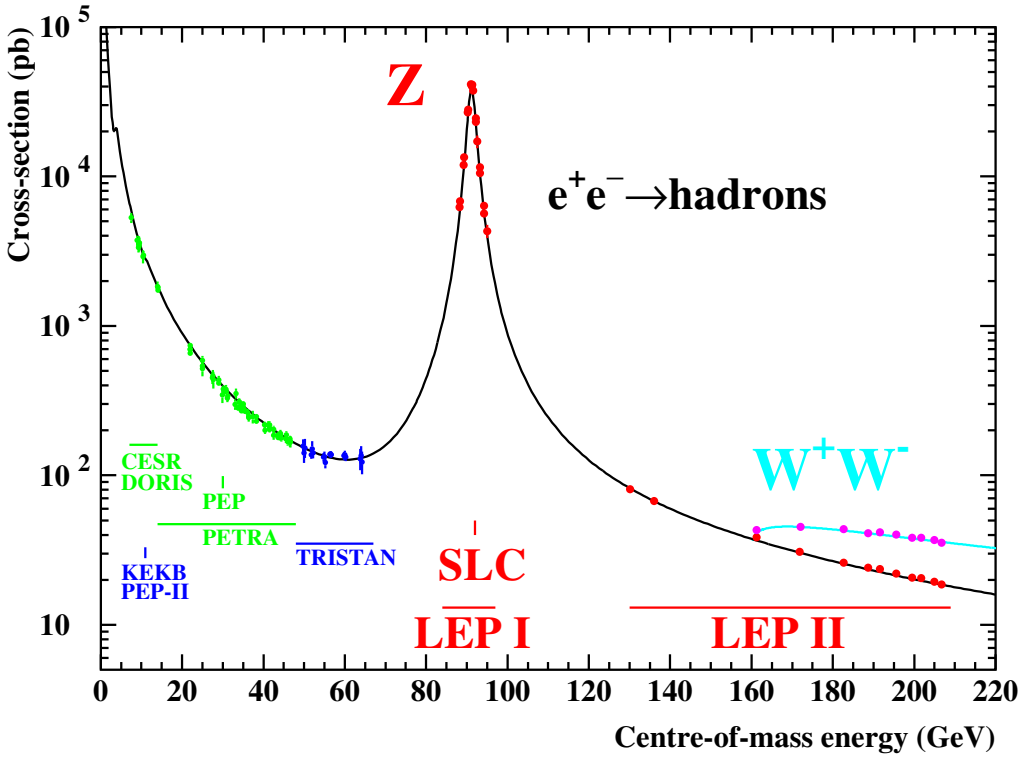

Figure 1.8: The hadronic cross-section for e^+e^- interactions as a function of the center-of-mass energy, with the solid line presenting the SM prediction while the points present the experimental measurements. [25]

approximation and is given by [25, 26],

$$\begin{aligned}\frac{2s}{\pi}\frac{1}{N_c^f}\frac{d\sigma_{\text{ew}}}{d\cos\theta}(e^+e^-\to f\bar{f}) = &\underbrace{|\alpha(s)Q_f|^2(1+\cos^2\theta)}_{\sigma^\gamma}\\ &\underbrace{-\,8\ \text{Re}\left\{\alpha^*(s)Q_f\chi(s)\left[\mathcal{G}_{\text{V}}^e\mathcal{G}_{\text{V}}^f(1+\cos^2\theta)+2\mathcal{G}_{\text{A}}^e\mathcal{G}_{\text{A}}^f\cos\theta\right]\right\}}_{\gamma-Z\ \text{interference}}\\ &\underbrace{\begin{aligned}+\ &16\,|\chi(s)|^2\Big[(|\mathcal{G}_{\text{V}}^e|^2+|\mathcal{G}_{\text{A}}^e|^2)(|\mathcal{G}_{\text{V}}^f|^2+|\mathcal{G}_{\text{A}}^f|^2)(1+\cos^2\theta)\\ &+\ 8\ \text{Re}\{\mathcal{G}_{\text{V}}^e\mathcal{G}_{\text{A}}^{e*}\}\,\text{Re}\{\mathcal{G}_{\text{V}}^f\mathcal{G}_{\text{A}}^{f*}\}\cos\theta\Big]\,.\end{aligned}}_{\sigma^Z}\end{aligned} \tag{1.24}$$

Here, $\chi(s)$ represents the propagator factor for the Z boson exchange and is defined as,

$$\chi(s) = \frac{G_{\text{F}}m_Z^2}{8\pi\sqrt{2}}\frac{s}{s-m_Z^2+is\Gamma_Z m_Z}. \tag{1.25}$$

N_c^f is the colour factor for the outgoing fermion (= 3 for quarks; = 1 for leptons), θ is the angle between the incoming electron and the outgoing fermion, and $\mathcal{G}_{\text{V}}^f$ and $\mathcal{G}_{\text{A}}^f$ are the complex vector and axial-vector couplings of the Z boson to the fermion f.

The $(1+\cos^2\theta)$ terms in Eq. 1.24 contribute to the total cross-section, while the $\cos\theta$ terms manifest in the forward-backward asymmetries. The total cross-section is governed by the exchange of the Z boson at energies near the Z boson resonance. The $\gamma-Z$ interference term dictates the forward-backward asymmetries at the off-peak energies, but its influence diminishes at the Z resonance peak, i.e. $\sqrt{s}=m_Z$.

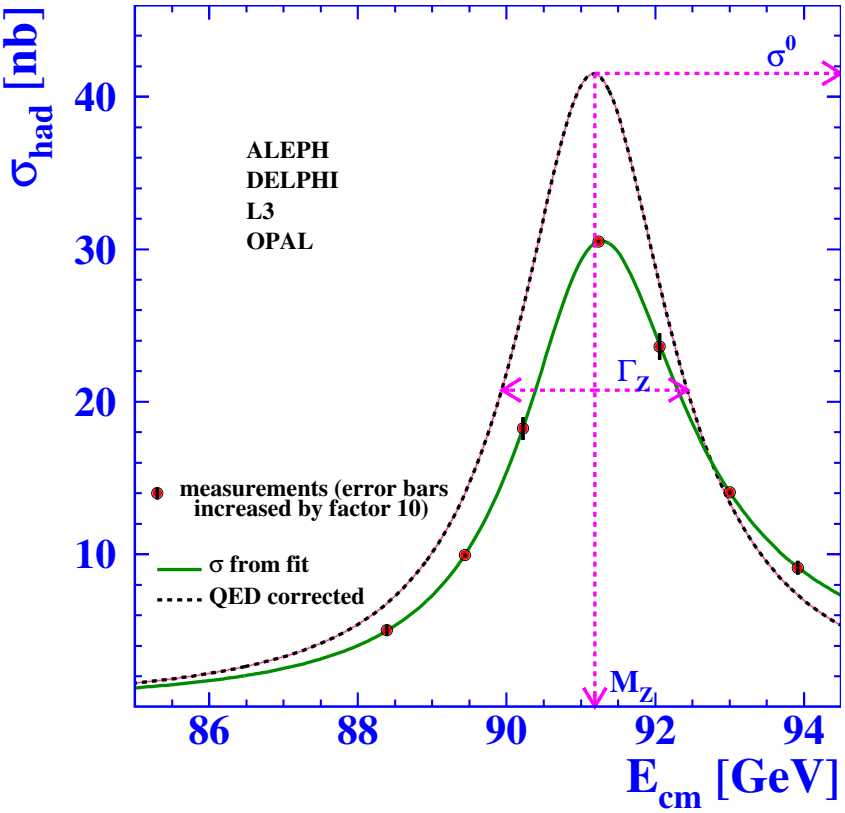

Figure 1.9: The measurements of the hadronic cross-section at the LEP collider. The solid line is the model-independent fit to the measurement. The dashed line incorporates the corrections of the QED photonic effects and is used to obtain the Z boson parameters. [25]

Quark Pair Production

The production of a quark-antiquark pair is a specific case of the two-fermion process described above. The process $e^+e^- \to q\bar{q}$ provides the leading contribution to the hadronic cross-section shown in Figure 1.8 and is pivotal to the studies presented in part of this thesis.

1.4.1 Higher-Order Corrections

The higher-order corrections to the tree-level diagrams shown in Figure 1.7 can be classified into three categories. The hadronic cross-section, before and after introducing these corrections, is shown in Figure 1.9.

QED Corrections

The QED corrections correspond to diagrams with additional real or virtual photon(s). These mainly consist of initial state radiation (ISR) and final state radiation (FSR), virtual photon loops, and interference between ISR and FSR. The ISR reduces the CoM energy and can be corrected for with the so-called radiator functions. The correction effectively shifts the Z resonance cross-section to higher energies. The correction for the FSR is done by updating the cross-section by a factor [27],

$$\sigma_{\text{ew}} \to \sigma_{\text{ew}} \, (1 + \delta_{\text{QED}}). \tag{1.26}$$

Weak Corrections

The weak corrections represent the remaining one-loop diagrams. These include corrections to the propagators, vertex correction excluding the contribution from virtual photons already included in the QED corrections, and box diagrams. These corrections are taken into account by the improved Born approximation, which retains the same form as the Born approximation but uses 'effective' SM parameters.

QCD Corrections

The QCD corrections account for the final state gluon radiation. As gluons do not couple to leptons, these corrections only affect the hadronic final states, e.g. in quark pair production. These corrections are accounted for by introducing a multiplicative factor to the cross-section [27],

$$\sigma_{\text{ew}} \to \sigma_{\text{ew}} \, (1 + \delta_{\text{QCD}}). \tag{1.27}$$

1.5 Electroweak Asymmetries at the *Z* Resonance

The parity-violating nature of neutral-current weak interactions leads to several observable asymmetries in the final-state particles produced in the $e^+e^- \to f\bar{f}$ annihilation process, such as the forward-backward asymmetry and the polarisation asymmetry. At the Z resonance peak, these asymmetries adopt particularly simple expressions with a singular relation to the neutral-current couplings. The energy dependence of the asymmetries, especially in the case of the forward-backward asymmetry, plays a significant role in the precision measurements conducted away from the Z resonance peak. In the following discussion, however, the contributions from photon exchange and its interference with Z boson exchange are not considered, as the studies presented in this thesis are confined to the peak of the Z resonance.

1.5.1 General Formalism

Ignoring the $\mathcal{O}(m_f^2/m_Z^2)$ effects in the limit $E \gg m$, only certain helicity combinations are allowed by the SM for the process $e^-e^+ \to \gamma^*/Z \to f\bar{f}$. The Z boson, or the photon, only couples with a pair of fermions with opposite helicities in such interactions. Thus, the incoming electron-positron pair will either be $e^-_{\text{L}}e^+_{\text{R}}$, with the subscript denoting the helicity of the particle, or $e^-_{\text{R}}e^+_{\text{L}}$. Similarly, the helicity combination of the final state fermion will be either $f_{\text{L}}\bar{f}_{\text{R}}$ or $f_{\text{L}}\bar{f}_{\text{R}}$.

This leads to four possible helicity configuration in the process $e^-e^+ \to \gamma^*/Z \to f\bar{f}$, as shown in Figure 1.10:

- $e^-_{\text{L}}e^+_{\text{R}} \to f_{\text{L}}\bar{f}_{\text{R}}$
- $e^-_{\text{L}}e^+_{\text{R}} \to f_{\text{R}}\bar{f}_{\text{L}}$
- $e^-_{\text{R}}e^+_{\text{L}} \to f_{\text{L}}\bar{f}_{\text{R}}$
- $e^-_{\text{R}}e^+_{\text{L}} \to f_{\text{R}}\bar{f}_{\text{L}}$

Considering only the Z boson exchange diagrams and the real couplings, the differential

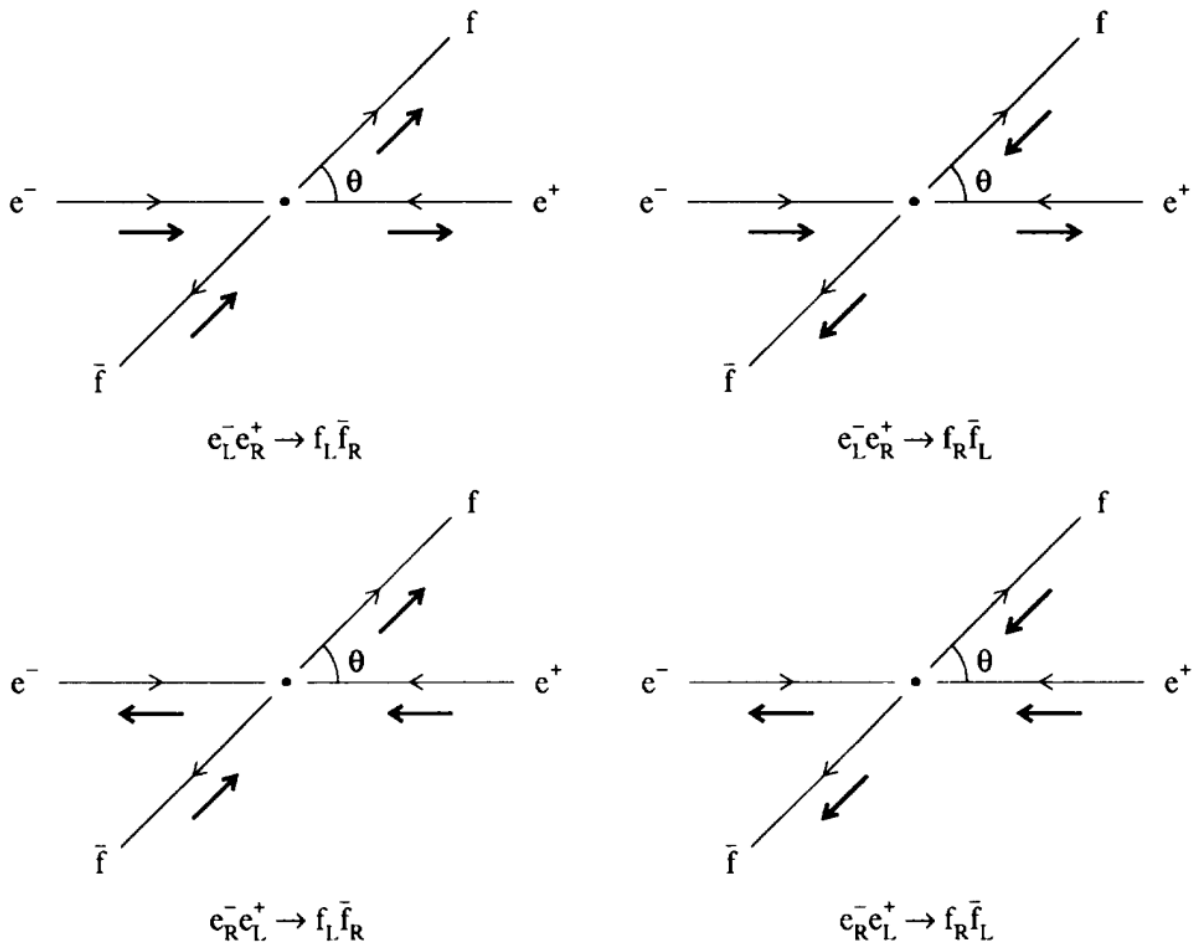

Figure 1.10: The four possible configurations of helicity state combinations in the process $e^+e^- \to f\bar{f}$. [28]

cross-sections for the four helicity configurations are,

$$\begin{aligned}
\frac{d\sigma_{\mathrm{LR}\to\mathrm{LR}}}{d\cos\theta} &\propto {g_{\mathrm{L}}^e}^2 {g_{\mathrm{L}}^f}^2 (1+\cos\theta)^2, \\
\frac{d\sigma_{\mathrm{LR}\to\mathrm{RL}}}{d\cos\theta} &\propto {g_{\mathrm{L}}^e}^2 {g_{\mathrm{R}}^f}^2 (1-\cos\theta)^2, \\
\frac{d\sigma_{\mathrm{RL}\to\mathrm{LR}}}{d\cos\theta} &\propto {g_{\mathrm{R}}^e}^2 {g_{\mathrm{L}}^f}^2 (1-\cos\theta)^2, \\
\frac{d\sigma_{\mathrm{RL}\to\mathrm{RL}}}{d\cos\theta} &\propto {g_{\mathrm{R}}^e}^2 {g_{\mathrm{R}}^f}^2 (1+\cos\theta)^2,
\end{aligned} \tag{1.28}$$

where g_{L} and g_{R} are the left- and right-handed chiral couplings of the neutral-current interaction and θ is the angle between the incoming electron and the outgoing fermion. The chiral couplings are related to the vector and axial-vector couplings as shown in Eq. 1.17 and 1.18. These relations are accurate without requiring corrections when only the tree-level Feynman diagrams are considered.

Combining the four helicity configurations, for unpolarised incoming electrons and positrons, the differential cross-section is given by,

$$\begin{aligned}
\frac{d\sigma_f}{d\cos\theta}(s,\cos\theta,\lambda) = \quad & (1+\cos^2\theta)\, F_0^f(s) + 2\cos\theta\, F_1^f(s) \\
& - \lambda \left[(1+\cos^2\theta)\, F_2^f(s) + 2\cos\theta\, F_3^f(s) \right]
\end{aligned} \tag{1.29}$$

where λ is the helicity of the final state fermion, and F_i^f are the four form factors. The form factors are proportional to the chiral couplings as,

$$\begin{aligned} F_0^f &\propto \left(g_{\mathrm{L}}^{e\ 2} + g_{\mathrm{R}}^{e\ 2}\right)\left(g_{\mathrm{L}}^{f\ 2} + g_{\mathrm{R}}^{f\ 2}\right), \\ F_1^f &\propto \left(g_{\mathrm{L}}^{e\ 2} - g_{\mathrm{R}}^{e\ 2}\right)\left(g_{\mathrm{L}}^{f\ 2} - g_{\mathrm{R}}^{f\ 2}\right), \\ F_2^f &\propto \left(g_{\mathrm{L}}^{e\ 2} + g_{\mathrm{R}}^{e\ 2}\right)\left(g_{\mathrm{L}}^{f\ 2} - g_{\mathrm{R}}^{f\ 2}\right), \\ F_3^f &\propto \left(g_{\mathrm{L}}^{e\ 2} - g_{\mathrm{R}}^{e\ 2}\right)\left(g_{\mathrm{L}}^{f\ 2} + g_{\mathrm{R}}^{f\ 2}\right). \end{aligned} \tag{1.30}$$

The above formalism makes it clear that in the case of pure Z boson exchange, the asymmetries will follow a particular combination of the chiral couplings of the neutral current interaction. This combination is represented by the asymmetry parameter,

$$\mathcal{A}_f \equiv \frac{g_{\mathrm{L}}^{f\ 2} - g_{\mathrm{R}}^{f\ 2}}{g_{\mathrm{L}}^{f\ 2} + g_{\mathrm{R}}^{f\ 2}} = \frac{2 g_{\mathrm{V}}^f g_{\mathrm{A}}^f}{g_{\mathrm{V}}^{f\ 2} + g_{\mathrm{A}}^{f\ 2}} = 2\frac{g_{\mathrm{V}}^f / g_{\mathrm{A}}^f}{1 + (g_{\mathrm{V}}^f / g_{\mathrm{A}}^f)^2}, \tag{1.31}$$

where the equivalence to the vector and axial-vector couplings of the neutral-current interaction follows from Eq. 1.17 and 1.18. The asymmetry parameter, $\mathcal{A}_f$, is also referred to as the chiral coupling asymmetry.

The final equivalence of Eq. 1.31 shows that the asymmetry parameter of a fermion depends only on the ratio of its couplings, thus it carries a one-to-one relation with $\sin^2\theta_{\mathrm{eff}}^f$ in the SM [25].

1.5.2 Forward-Backward Asymmetry

In decay modes where the helicity of the final-state fermions is not accessible, as is the case for the $e^+e^- \to f\bar{f}$ process at colliders, only the form factors F_0 and F_1 can be extracted from the data. Among these, F_0 is related to the total production cross-section as,

$$\sigma_f(s) = \frac{8}{3} F_0^f(s), \tag{1.32}$$

while F_1 is related to the forward-backward asymmetry as,

$$A_{\mathrm{FB}} = \frac{\sigma_{\mathrm{F}} - \sigma_{\mathrm{B}}}{\sigma_{\mathrm{F}} + \sigma_{\mathrm{B}}} = \frac{3}{4}\frac{F_1^f(s)}{F_0^f(s)}, \tag{1.33}$$

where $\sigma_{\mathrm{F}} = \sigma_f(\cos\theta > 0)$ and $\sigma_{\mathrm{B}} = \sigma_f(\cos\theta < 0)$. Thus, the forward-backward asymmetry is defined as the normalised difference in cross-sections for a final-state particle produced in the forward ($\cos\theta > 0$) versus backward ($\cos\theta < 0$) hemisphere in the CoM frame.

The interference term cancels at the peak of the Z resonance, and if the small contribution from the photon exchange diagram is ignored, A_{FB}^f reduces to,

$$A_{\mathrm{FB}}^{0,f} = \frac{3}{4}\mathcal{A}_e\mathcal{A}_f. \tag{1.34}$$

Following Eq. 1.31, $\mathcal{A}_f$ is solely dependent on the ratio of the vector and axial-vector couplings of the Z boson to the fermion f. which in turn has a one-to-one relation with the effective mixing angle $\sin^2\theta^{\mathrm{eff}}$ through Eq. 1.19.

Precision tests of the SM, including measurements of parameters such as the forward-backward asymmetry, and the exploration of the physics beyond it, are the key objectives of experiments at particle colliders, and will be the subject of discussion in the following chapters.

2 Particle Colliders and the Future Circular Collider Project

Particle colliders have been central to experimental high-energy physics, facilitating the exploration of fundamental particle and their interactions at ever-increasing energies. By accelerating particles to near the speed of light and bringing them into collision, the colliders make it possible to probe the nature of matter and the fundamental forces at the smallest scales. Particle colliders enable precision studies of the known fundamental interactions and are ideally suited to produce rare interactions and study unexplored energy regimes.

2.1 Particle Colliders

Particle accelerators are some of the world's largest and most complex machines that propel charged subatomic particles to very high energies with electromagnetic fields. The incoming particles are grouped in bunches, which in turn form particle beams. The particle accelerators collide these particle beams with either a fixed target or another particle beam travelling in the opposite direction at specific interaction points. Higher center-of-mass energies can be achieved by colliding particle beams travelling in opposite directions, as opposed to collisions with a fixed target. Particle accelerators that collide two oppositely travelling beams of particles are referred to as particle colliders.

The individual interactions produced by the colliding particle beams are referred to as events. The particles generated in these collision events traverse the detectors, which are positioned around the interaction points. The physical properties of these particles are measured by detectors employing a multitude of technologies, with the primary aim of reconstructing the primary reaction undergone by the incoming particles at the interaction point, as represented by a Feynman diagram.

2.1.1 Lepton and Hadron Colliders

The most common types of particle colliders are electron-positron colliders, also known as lepton colliders, and proton-(anti)proton colliders, also referred to as hadron colliders. This categorisation, as the name suggests, is based on the types of incoming particles that collide at high energies in such colliders.

The incoming particles in lepton colliders are elementary particles, thus producing very clean collisions. All past and operational lepton colliders have been electron-positron colliders. As these particles have very low mass, their collisions cannot reach energies attainable by using heavier incoming particles with the currently available technology. Proposals for muon colliders have been put forward that can reach higher energies compared to electron-positron colliders while still colliding elementary particles.

Hadron colliders can collide heavy ions, which is a significant part of the physics program of the Large Hadron Collider (LHC) [29], the largest hadron collider ever built. However, they most often collide protons or antiprotons, which are nearly 2000 times more massive than electrons.

Additionally, electron-proton colliders, such as the Hadron–Electron Ring Accelerator (HERA) [30], provide a uniquely precise probe into the structure of the proton and QCD dynamics by colliding a elementary particles with composite particles. Unlike the typically symmetric lepton and hadron colliders, electron-proton colliders are inherently asymmetric.

2.1.2 Linear and Circular Colliders

In addition, particle colliders are also categorised based on their shape: they can be either linear or circular. Neither type of collider is truly linear or circular but is classified by its prominent geometrical shape. Colliders with heavier incoming particles are always circular, but e^+e^- can be either circular or linear.

As mentioned above, the incoming particle beams in high-energy colliders are composed of bunches, which are collided together in what is referred to as bunch crossings. Very few particle collisions actually take place in each bunch crossing. In a circular collider, like the Large Electron Positron (LEP) collider [32], the electron and positron bunches travel in a roughly circular ring in opposite directions. Therefore, they can be collided several times over (about 10^{10} times) before the beams are eventually discarded or dumped. This facilitates a high collision rate, as represented by the instantaneous luminosity (or luminosity), $\mathcal{L}$, which is defined as,

$$\mathcal{L} = \frac{1}{\sigma}\frac{dN}{dt}. \tag{2.1}$$

Here, σ is the cross-section of the process, and dN/dt is the collision event rate. The high luminosity of a circular collider allows for the collection of high-statistics data samples, which

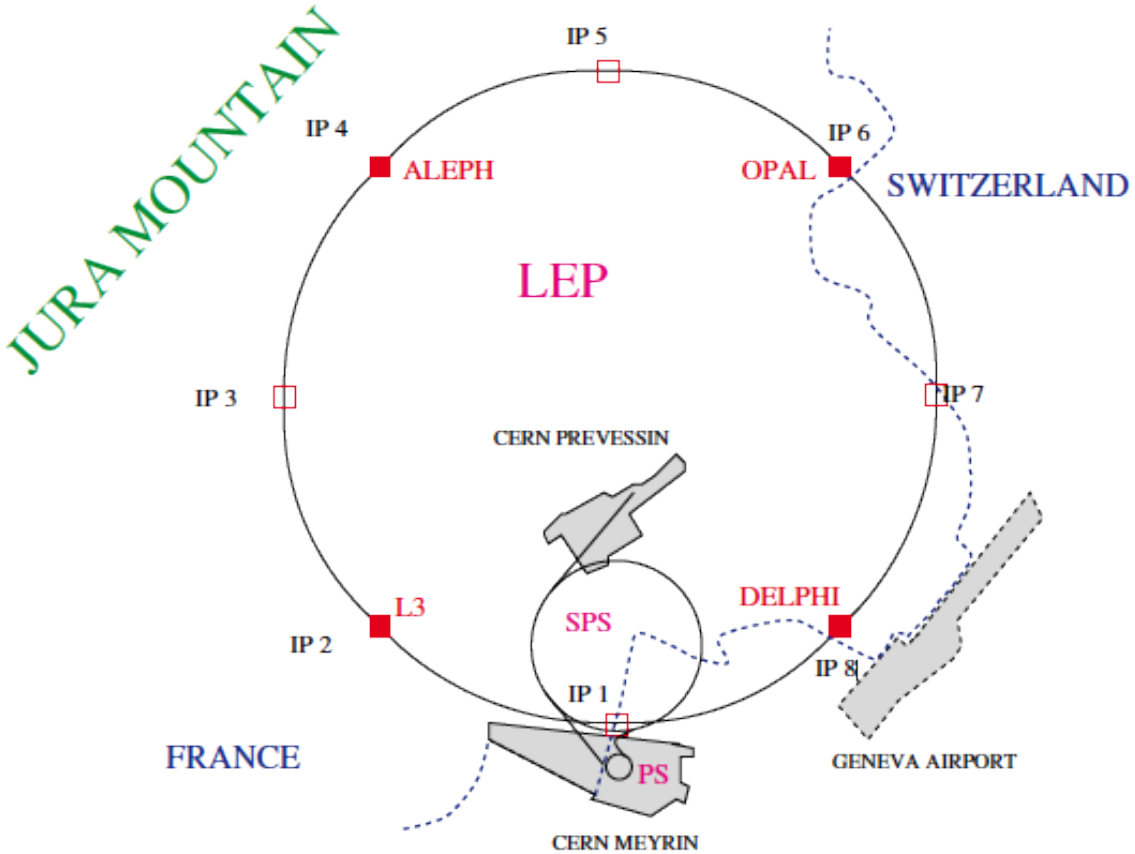

Figure 2.1: The schematic design of the LEP collider, displaying the detectors situated at four of the possible interaction points. [31]

is particularly advantageous for high-precision measurements. Additionally, a circular collider enables more than one interaction point, hence, it can host more than one experiment.

However, particle beams in circular colliders lose energy through synchrotron radiation, which is the electromagnetic radiation emitted by charged particles when they are accelerated radially, i.e. perpendicularly to their direction of travel. The synchrotron energy loss is proportional to the energy, E, and the mass, m, of the charged particle being accelerated and the radius of curvature of the accelerator ring as,

$$U \propto \frac{E^4}{m^4 R}. \tag{2.2}$$

Thus, particles with a lower mass, like the electron, lose significantly more energy through synchrotron radiation. As the energy loss is proportional to the fourth power of the particle energy, this effect can only be mitigated by increasing the radius of the accelerator ring. This effect is not as appreciable for colliders that use heavier particles, such as protons, but it is impractical to build a circular e^+e^- collider that reaches energies higher than 400–500 GeV, as it would require compensation of high energy losses via synchrotron radiation or very large tunnels.

The particles in the incoming beams of a linear collider, like the Stanford Linear Collider (SLC) [33], lose little to no energy through synchrotron radiation as they roughly travel in straight lines. Hence, linear e^+e^- colliders can reach higher center-of-mass (CoM) energies than circular e^+e^- colliders, as well as allow for longitudinal beam polarisation. However, unlike in circular colliders, the bunches cannot be reused after a single bunch crossing, making it challenging to reach higher luminosities.

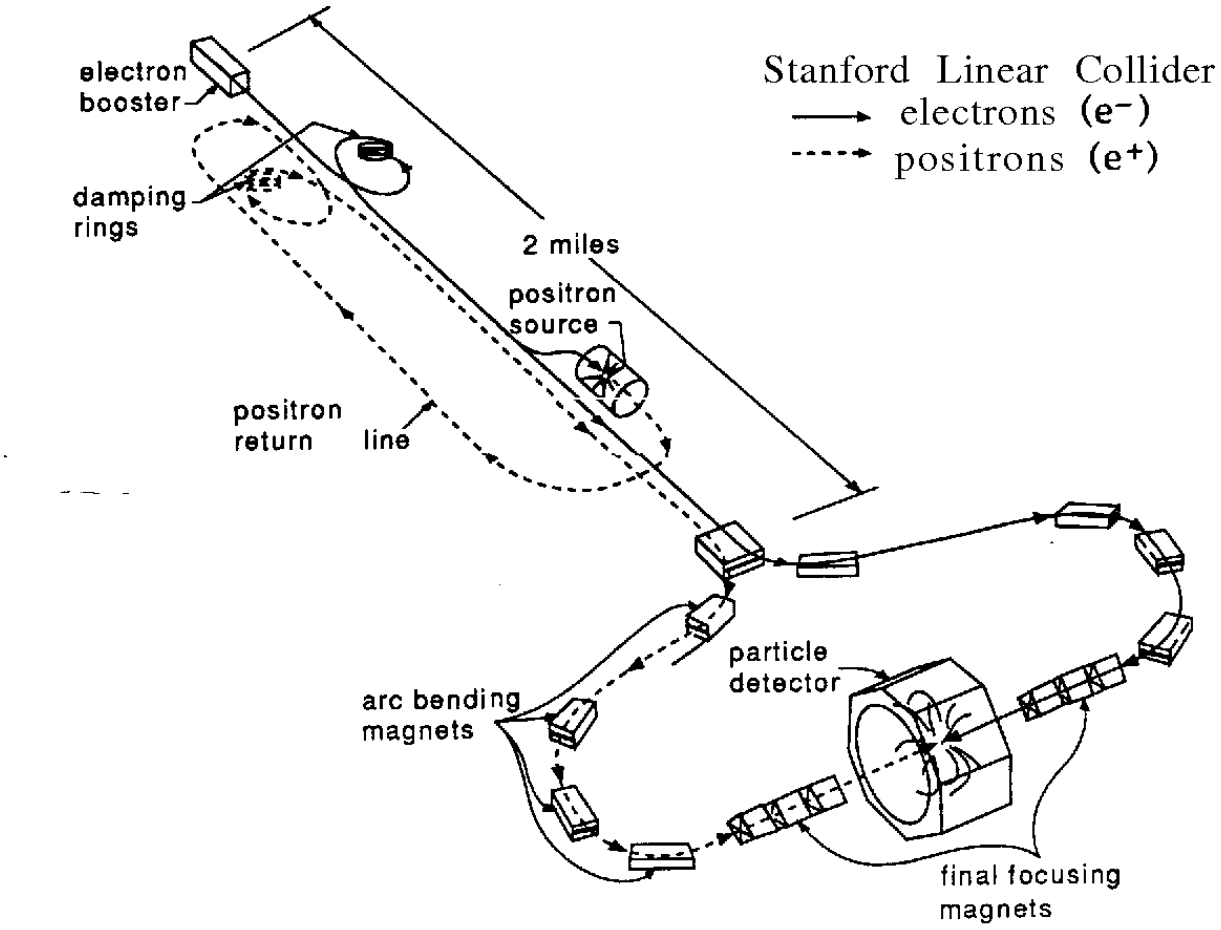

Figure 2.2: The schematic design of the SLC. [34]

The LEP collider, as shown in Figure 2.1, was the largest electron-positron collider ever built with a circumference of approximately 27 km. On the other hand, the SLC, shown in Figure 2.2, is the only linear collider ever built and has a length of 3.2 km.

2.2 The Past and Present Landscape

The Intersecting Storage Rings (ISR) [35] was the first ever hadron collider, reaching much higher energies than the collisions with fixed targets. This led to the shift of the high-energy experiments from fixed-target collisions to beam-beam collisions. The circular e^+e^- collider at DESY, the Positron-Electron Tandem Ring Accelerator (PETRA) [36], led to the discovery of gluons [37, 38]. The SLC was the first and the only linear collider ever built and used polarised electron beams. The Super Proton Synchrotron (SPS) [39] collided proton and antiproton beams and discovered the W and the Z bosons, which are the carriers of the weak interaction. The Tevatron [40] at the Fermilab similarly collided protons and antiprotons, leading to the discovery of the heaviest elementary particle in the SM, the top quark [41, 42]. The LEP collider at CERN performed high-precision electroweak studies and then gave way to the LHC. While the KEKB [43] was an e^+e^- collider dedicated to flavour physics, focussing on the bottom quark, which was eventually upgraded to the SuperKEKB [44].

The LEP-LHC Era

Presently, the LHC, which is hosted in the tunnel that the LEP collider previously occupied, is the largest functioning collider. The LEP collider and the LHC form the perfect example of the complementarity offered by lepton and hadron colliders. After the discovery of the Z boson at the SPS at CERN in 1983 [45, 46], this neutral vector boson was extensively studied at the LEP collider. The measurement of its width constrained the number of neutrino generations to 2.9840 ± 0.0082 [25, 47–50]. The upgrade of the LEP collider, LEP2 [51], also produced the other weak boson, the W boson, while running at the WW threshold, ultimately reaching the collision energy of 209 GeV. Additionally, the LEP collider constrained the mass of the Higgs boson, m_H, from the absence of a signal from the direct searches to be greater than 114 GeV [52]. The upper limit from the Tevatron suggested that m_H was likely not greater than 200 GeV, thus narrowing the window for the discovery of the Higgs boson. The LHC, capable of reaching significantly higher CoM energies than the LEP collider, took the search forward, and the ATLAS and the CMS experiments at the LHC discovered a new particle compatible with the Standard Model Higgs boson [53, 54].

The current landscape of high-energy physics in Europe has been shaped in large parts by the LEP collider and the LHC. The next step in the quest to understand the fundamental particles and forces in the universe requires a machine that can produce the Higgs boson at high luminosities and provide a clean environment to study them with ultra-high precision.

2.3 Proposed Future Colliders

Several proposals have been put forward to build colliders that will improve on the tests of the SM performed by LEP, SLC, and LHC, with an additional target for the potential discovery of 'New Physics'. The major focus of such projects is to design electroweak and Higgs factories, i.e. precision machines that are able to produce the electroweak and the Higgs bosons, and possibly the top quark, at very high luminosities. With the exception of projects, such as the Muon Collider [55] and the upgrade stages of other colliders, most proposed future colliders, at

a matured stage of development, are e^+e^- colliders. As this thesis focuses on a proposed future e^+e^- collider, only this type of colliders will be discussed further.

Linear e^+e^- Colliders

The several proposed linear colliders aim to perform precision measurements at high energies, along with an aim to discover physics beyond the standard model. Using polarised electron and positron beams in linear colliders is more practical than in circular colliders and can compensate the integrated luminosity to almost three orders of magnitude in certain physics cases [56]. A few major proposed linear e^+e^- colliders are discussed below.

The first proposed linear collider is the International Linear Collider (ILC) [57], which is planned to be built in Japan. The ILC was originally designed to operate at the CoM energy of 500 GeV, but it was re-optimised after the discovery of the relatively light Higgs boson to the CoM energy of 250 GeV, with the possibility of two-step upgrade to 500 GeV and 1 TeV. The planned length of the ILC in its various stages is planned to be 30 to 50 km, which is more than 10 times longer than the SLC.

Another proposed linear collider, planned to be built at CERN, is the Compact Linear Collider (CLIC) [58]. It is intended to be operated in three stages, starting from the CoM energy of 380 GeV with a length of 11 km, where it will function as a Higgs factory, reaching up to 3 TeV and a length of 50 km.

The Cool Copper Collider (C^3) [59] is proposed to be an 8 km long linear collider with the planned operation CoM energies of 250 GeV and 500 GeV. It is in the conceptual design phase and early R&D stage.

Lastly, the Linear Collider Facility (LCF) [56], a Higgs factory proposed to be built at CERN, and the Hybrid Asymmetric Linear Higgs Factory (HALHF) [60], a plasma-RF hybrid linear collider, are among the other proposed linear collider projects.

Circular e^+e^- Colliders

The proposed circular e^+e^- colliders are ideal for high-precision measurements as they can achieve higher luminosities compared to the proposed linear colliders. They aim to study the electroweak and Higgs bosons, including flavour physics, as well as the top quark, with unprecedented precision. Two circular e^+e^- colliders have been proposed, which share various similarities in their design.

The Circular Electron-Positron Collider (CEPC) [61, 62] is proposed to be built in China and has a circumference of 100 km. The CEPC is planned to be operated as a Higgs factory for 10 years, with significantly lower run times in the electroweak factory mode. It is planned to be operated at the $t\bar{t}$ threshold for 5 years. The CEPC is designed to potentially be replaced by a hadron collider in the same tunnel.

A post-LHC circular collider project has been proposed at CERN, called the Future Circular Collider (FCC) [63, 64]. The first phase of the FCC is an e^+e^- collider, called the FCC-ee, which is planned to have a circumference of 90.7 km, over 3 times that of the LEP collider. The FCC-ee is designed to operate at four different CoM energy modes, starting from around 91.2 GeV at the Z pole to 365 GeV, over the $t\bar{t}$ threshold. The FCC-ee is planned to be upgraded to a hadron collider, referred to as the FCC-hh, reaching CoM energies of 85 TeV [65].

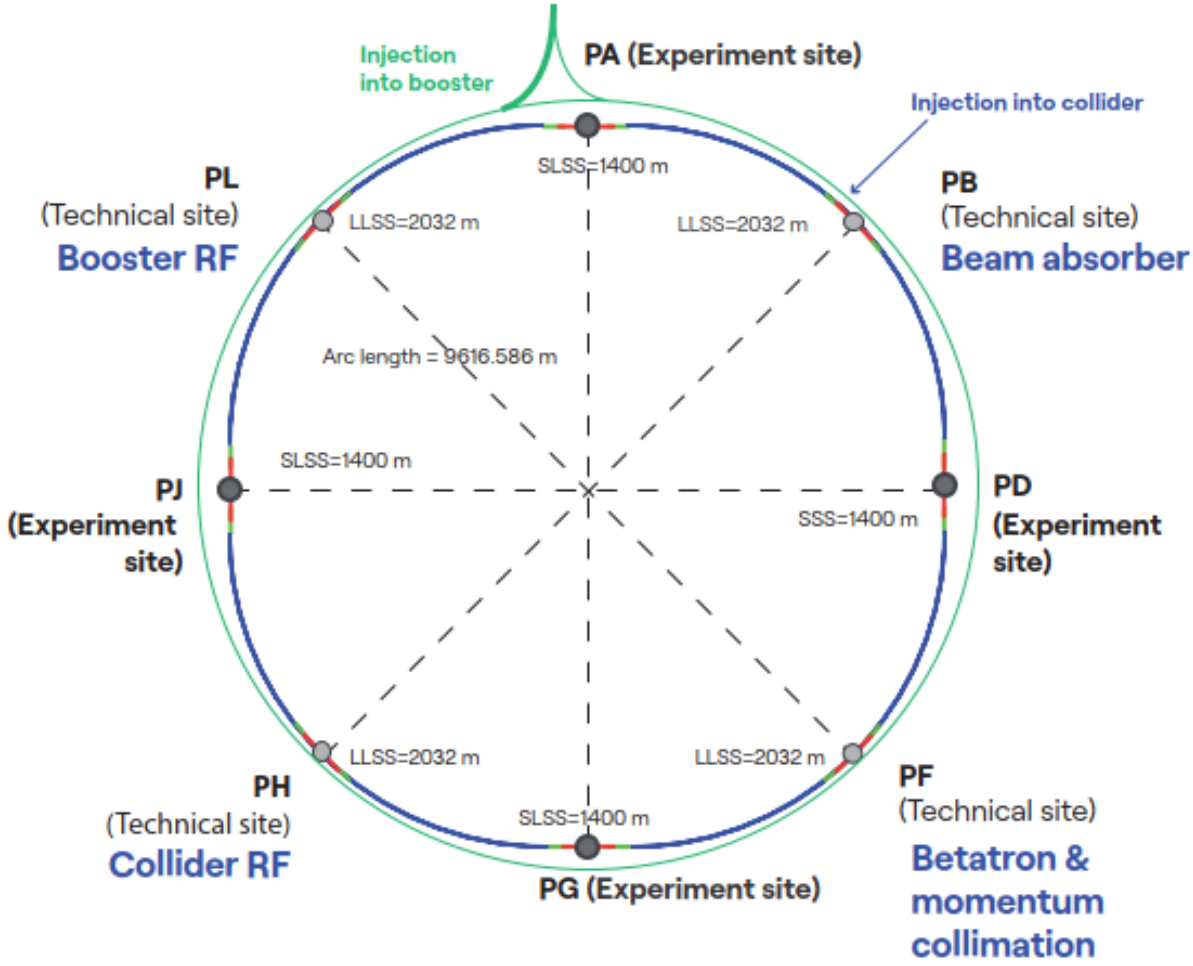

Figure 2.3: FCC-ee schematic with 4-fold symmetry

2.4 The Future Circular Collider Integrated Project

The Future Circular Collider integrated project aims to build e^+e^-, pp, and ep colliders in a 90.7 km circular tunnel in the Geneva region [65]. The FCC project is planned to be operational from the late 2040s, with the tunnel initially hosting an e^+e^- collider, the FCC-ee, for a dedicated run plan of 15 years. The e^+e^- collider will then be replaced by a hadron collider in the same fashion as LHC replaced LEP, reaching unprecedented energies. The integrated project offers the possibility to complementarily study physics at known energy scales with ultra-high precision and explore and test 'New Physics' at very high energy scales. FCC also aims to provide electron-hadron collisions for high precision deep-inelastic scattering studies.

The work presented in this thesis corresponds to the development of the FCC-ee, and it will be discussed in detail below.

2.4.1 FCC-ee

Initially conceptualised as a stand-alone project [71], the FCC-ee [72] is a proposed e^+e^- collider and the first stage of the FCC integrated project. Figure 2.3 shows the layout schematic of the FCC-ee, showing its 4-fold symmetry. It is currently planned to run at four different CoM energy modes: at and around the Z pole for 4 years, at the W^+W^- threshold for 2 years, as a Higgs factory at the CoM energy of 240 GeV, dominantly producing the Higgs boson through the Higgs-strahlung process for 3 years, at the top quark pair production threshold for 1 year,

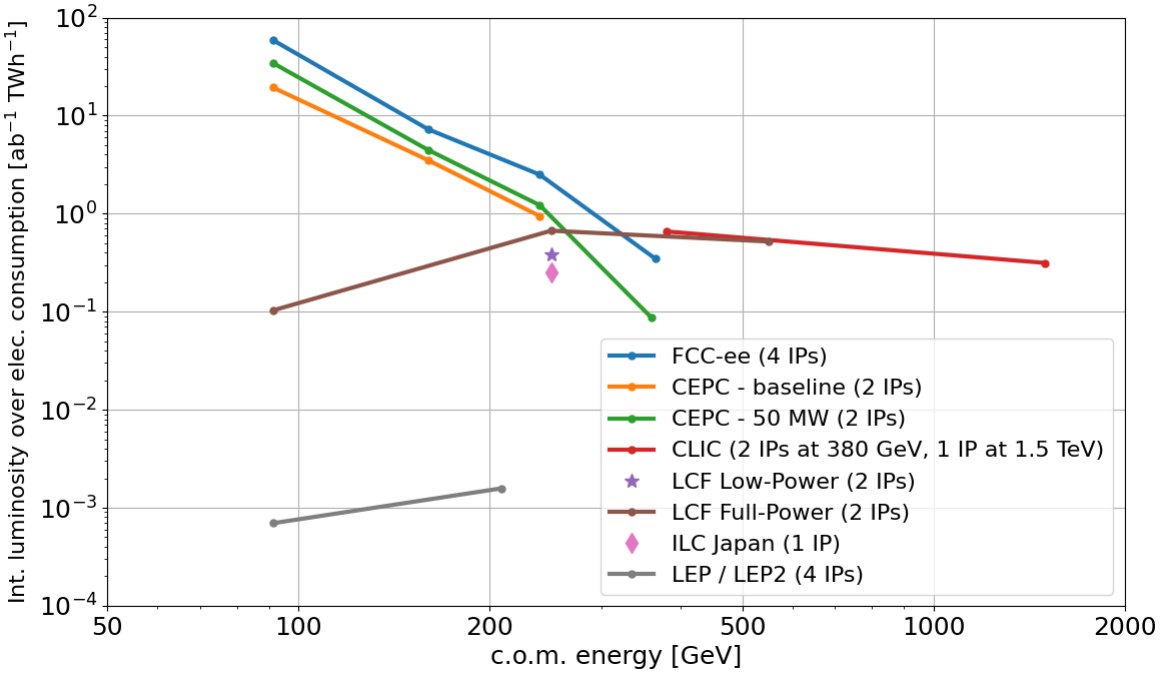

Figure 2.4: The expected integrated luminosities at the proposed e^+e^- colliders, normalised by their electricity consumption, as a function of the center-of-mass energy. [66–70]

and at and above the $t\bar{t}$ threshold for 5 years with the CoM energy of 300–365 GeV. The run parameters of the FCC-ee, including the instantaneous luminosity per interaction point (IP) and the integrated luminosities for the four IPs, as well as the number of events, are presented in Table 2.1.

Figure 2.4 shows the luminosities expected at four CoM energy modes at the FCC-ee as well as the luminosities achievable by the baseline designs of other proposed e^+e^- colliders, normalised by their electricity consumption. It shows that the FCC-ee is the most sustainable collider over the entire range of center-of-mass energies at which it is planned to be operated [66].

The proposed FCC-ee program provides a unique opportunity to push the Z boson measurements to their ultimate limit. The four-year-long FCC-ee run at and around the Z resonance will produce an unprecedented 6×10^{12} total decays. The integrated luminosity expected at the Z resonance at FCC-ee is 125 ab^{-1}, along with integrated luminosities of 40 ab^{-1} at the CoM energies of 88 GeV and 94 GeV each, about 10^6 times that of LEP. The statistical errors on the mass and width of the Z boson can be reduced from 1.2 MeV and 2 MeV to 5 keV and 8 keV [72], respectively. Lower center-of-mass energy spread due to beam energy calibration will benefit

Working point	***Z* pole**	***WW* thresh.**	***ZH***	***tt̄***	
$\sqrt{s}$ [GeV]	88, 91, 94	157, 163	240	340–350	365
Lumi/IP [10^{34} cm^{-2}s^{-1}]	140	20	7.5	1.8	1.4
Lumi/year [ab^{-1}]	68	9.6	3.6	0.83	0.67
Run time [year]	4	2	3	1	4
Integrated lumi. [ab^{-1}]	205	19.2	10.8	0.42	2.70
Number of events	6×10^{12} Z	2.4×10^8 WW	2.2×10^6 ZH + 65k $WW \to H$	2×10^6 $t\bar{t}$ + 370k ZH + 92k $WW \to H$	

Table 2.1: Operating points and projected event yields at FCC-ee for various centre-of-mass energies. [73]

in reducing the systematic uncertainty of these quantities. Measuring the forward-backward and polarisation asymmetries is a powerful method to estimate the effective weak mixing angle, $\sin^2\theta_{\mathrm{W}}^{\mathrm{eff}}$, for which the statistical uncertainty is expected to reduce to about 10^{-6}, corresponding a more than thirty-fold improvement [72].

Studying the hadronic decay channels of the Z boson is a very important aspect of the FCC-ee physics program. The couplings and decay widths of the Z boson have only been measured to the heavier quarks, b and c. The only study of the s quark decay of the Z boson available in the literature is preliminary [74]. For the lighter quarks, s, u, and d, these properties are typically only listed collectively for up-type and down-type quarks [20]. Similarly, the axial and vector couplings have also been collectively measured for up-type and down-type quarks [20].

Future colliders with a dedicated Z boson run, like FCC-ee, will improve the precision of all these measurements and make the s quark, and potentially the u and d quarks, accessible. Individual measurements of the quark vector and axial couplings should be possible via their forward-backward asymmetries, corresponding partial decay widths of the Z boson, and the precise knowledge of A_e, the asymmetry parameter of the e^-e^+ pair. The experimental systematic uncertainties corresponding to these measurements are also expected to drastically improve due to better detector designs [72].

The unprecedented luminosities at the FCC-ee uniquely facilitate tests of the SM but, at the same time, present novel challenges in reducing systematic uncertainties. The circular collider design provides the opportunity for four interaction points, each of which can host a different detector experiment. Such detector concepts, namely Innovative Detector for Electron–positron Accelerators (IDEA) [75, 76], CLIC-Like Detector (CLD) [77], A Lepton Lepton collider Experiment with Granular Read-Out (ALLEGRO) [78], and an adaptation of the International Large Detector (ILD) [79] for the FCC-ee, called ILD@FCC-ee, are currently being studied.

The IDEA detector concept has been used in the work presented in this thesis and will be described in the next chapter.

3 Particle Detectors and the IDEA Detector Concept

Modern particle detectors are large, layered structures comprising detector subsystems, each of which performs a specific task and is dedicated to precisely measuring the particular physical properties of traversing particles produced in the collision event. Particle properties, such as energy and spatial position, while passing through the plane of a detector layer, are measured for different classes of particles. More complex and secondary properties of the particles, like the trajectories of the charged particles used to calculate particle momentum and charge, and the secondary decay vertices, are reconstructed from the primary information measured by the detectors.

3.1 A General-purpose Particle Detector

A typical particle detector at a collider is composed of a cylindrical barrel, centered around the axis of the beam pipe, that is closed on each side by flat end caps. Hence, the detector is positioned to cover an almost complete solid angle, all the way down to near the beam pipe.

Each detector subsystem utilises different forms of particle interactions with matter to measure specific properties of the particles passing through them. Some of the common subdetector elements are detailed below. It must be noted that the positional order of the detector subsystems presented below is not universally true.

All four detectors at the LEP collider, ALEPH [80], DELPHI [81], L3 [82], and OPAL [83], were general-purpose detectors, as are the ATLAS [84] and CMS [85] experiments at the LHC.

3.1.1 Tracking System

The first subdetector system surrounding the beam pipe is dedicated to tracking the trajectories of charged particles and is thus known as a tracking detector. Tracking detectors are typically composed of several sensitive detector layers, with which a passing charged particle interacts. These discrete measurement points are used to reconstruct the trajectory of the charged particle. Charged particles follow curved trajectories in the presence of an axial magnetic field. Measuring the direction and the curvature of a charged particle trajectory determines the charge and the momentum of the particle, respectively.

The tracking detectors must consist of as little material as possible, denoted by their material budget, while providing excellent precision on the spatial measurement. Measuring the differential energy loss per unit length, dE/dx, or the number of ionisation clusters per unit length, dN/dx, aids in particle identification (PID) [86, 87]. It is especially beneficial to discriminate between kaons and pions, as the energy loss per unit distance in a material, as described by the Bethe-Bloch equation presented in Section 9.2, is different for particles with the same momenta but different masses.

Two major categories of tracking detectors are gaseous detectors and solid-state detectors. Gaseous detectors can be lighter than solid-state detectors and are generally significantly larger,

with significantly more measurement points. They have low multiple Coulomb scattering due to lower material density, but solid-state detectors can achieve better precision of individual spatial measurements.

Vertex Detector

The innermost layers of the tracking detector are often referred to as the vertex detector. The vertex detector is dedicated to performing very precise spatial measurements of particles very close to the interaction point. High granularity is crucial for vertex detectors as they experience the highest particle flux of all the subdetector systems. Ultra-precise spatial measurements near the interaction points by the vertex detectors are essential for accurate reconstruction of decay vertices of unstable particles produced in the collision events. Good vertex reconstruction is vitally important for the identification of hadronic flavour of jets, among other physics studies.

Vertex detectors and the development of silicon-based technology are the focus of part of this thesis, which is presented in Chapters 9-12.

3.1.2 Solenoid Magnet

Charged particles experience the Lorentz force in the presence of a magnetic field and follow a curved trajectory. Particle detectors employ a powerful solenoid electromagnet to produce such an axial magnetic field, with a typical strength of 1–4 T. The solenoid magnet is typically positioned between the tracking detector and the calorimeter(s). However, it can also be placed outside the calorimeters to reduce the energy loss of particles before they reach the calorimeter.

Some experiments employ additional magnet systems, such as the toroidal magnets in the ATLAS detector [84], along with the central solenoid magnet.

3.1.3 Calorimeter System

The next active subdetector systems that envelop the tracking detector are the calorimeters. The calorimeters aim to stop the particles, which undergo interactions with the material in the calorimeters, and measure the deposited energy and the location of the energy deposit. The interaction of particles with the material in the calorimeter results in showers of secondary particles, which are then measured.

The calorimeter system is typically composed of two parts, as the electromagnetic interactions initiate and terminate over shorter distances than hadronic interactions. The inner calorimeter is the electromagnetic calorimeter (ECAL). The ECAL is optimised for particles that interact only electromagnetically, i.e. electrons and photons, but also detects other particles which interact electromagnetically. The ECAL is surrounded by the hadronic calorimeter (HCAL), which tends to be significantly larger than the ECAL. The HCAL aims to stop particles that undergo strong interactions, i.e. the hadrons. The HCAL is generally not as precise as the ECAL, in both the energy measurement and the localisation of the energy deposits. This is due to the intrinsically larger fluctuations in the development of hadronic showers, including the energy losses in nuclear excitation and breakup. It must be noted that the particles reaching the calorimeter system have undergone secondary interactions in inner subdetector systems, including the ECAL for hadrons, thus losing a fraction of their energies.

The so-called dual-readout calorimeter utilises both scintillation light signals, produced for non-relativistic and relativistic particles, and Cherenkov light signals, produced only for relativistic particles. The ratio of the two is utilised to discriminate between electromagnetic and hadronic showers and measure the fraction of the electromagnetic component of the hadronic

showers on an event-by-event basis, thus nullifying the effects of fluctuations in traditional HCALs [76, 88].

3.1.4 Muon Chambers

As muons do not interact strongly and lose significantly less energy compared to electrons in electromagnetic interactions in matter due to their high mass, they are the only particles, other than the neutrinos, that can traverse large quantities of matter without losing a significant fraction of their energy. Therefore, they penetrate the HCAL in a particle detector. Dedicated detectors, known as muon chambers, which are typically gaseous tracking detectors, are placed outside all the other subdetector systems, including the calorimeters.

As they are the only detectable particles that pass through the rest of the detector system, any charged particles that leave a signature in the muon chambers are identified as muons.

3.1.5 Detectors for Particle Identification

Techniques, such as energy loss measurements (dE/dx), ionisation cluster counting (dN/dx) [87], and time-of-flight [89], provide PID capabilities to distinguish among charged hadrons. A combination of these PID techniques is generally required as they are effective in complementary momentum ranges. However, some detectors include a dedicated subdetector system for particle identification. Cherenkov detectors, such as the Ring Imaging Cherenkov (RICH) Detector, exploit the Cherenkov radiation emitted by charged particles moving faster than the speed of light in a certain medium to distinguish these charged particles, especially kaons, pions, and protons.

3.1.6 Timing Detectors

Timing detectors are designed to precisely measure the arrival time of charged particles, reaching a time resolution of picoseconds, by detecting the prompt signals generated by charged particles, such as ionisation, or the emission of Cherenkov or scintillation light. A few of the most widely used technologies are fast scintillators coupled to photomultiplier tubes (PMTs) or silicon photomultipliers (SiPMs), ultra-fast silicon sensors like low-gain avalanche detectors (LGADs), and multi-gap resistive plate chambers (MRPCs). They provide crucial information for event reconstruction and aid in particle identification through the time-of-flight measurement.

3.2 Detector Concepts for the FCC-ee

Four conceptual general-purpose detector designs are being developed for the FCC-ee. Firstly, the CLD detector concept [77] has been adapted from the latest CLIC detector model [90] to the FCC-ee. The IDEA detector concept [75, 76] has been specifically developed for the FCC-ee. The ALLEGRO detector concept [78] is the most recent and is comprised of a noble liquid calorimeter. The ILD@FCC-ee detector concept is an adaptation of the detector model developed for the ILC, featuring a Time Projection Chamber (TPC), which is being investigated for its operation at the Z resonance.

The requirements for the detectors of the FCC-ee have been laid out in the ECFA detector R&D roadmap [91], and more recently in the FCC Feasibility Study (FCC-FS) report [73]. The tracking detector must have low material and consume low power, while providing very good precision on the position measurements. The calorimeters need to cover a large area with a fine granularity, while being fast. The ECAL must have an excellent energy resolution. The energy

resolution of the central tracking detector must be excellent to provide a good measurement of the differential energy loss for PID, and the muon detectors must also be highly granular, providing tail catching for calorimetric showers along with muon identification capabilities.

3.2.1 The IDEA Detector Concept

A simulation of the IDEA detector concept [92], implemented in the `Delphes` framework [93], has been used for reconstruction of the event samples used in this thesis.

The innermost part of the IDEA detector is the solid-state vertex detector. It is based on monolithic active pixel sensors (MAPS), described in Chapter 9. It consists of three inner layers with a space point resolution of 3 µm and two outer barrel and three disk layers on each side with a space point resolution of 7 µm, as implemented in detector simulations. The innermost layer is positioned at a radius of 1.7 cm. In a later update of the detector design, the innermost layer has been moved to 1.2 cm. Both designs have been used for different studies presented in this thesis.

The vertex detector is enclosed by the drift chamber, incorporating 112 layers of 100 µm resolution. The drift chamber forms the central tracking system of the detector. The multiple Coulomb scattering of particles is minimal in the drift chamber due to the main gas component being Helium.

Two layers of silicon sensors surround the drift chamber to provide a very precise space point measurement. A single-hit resolution of 7 µm (90 µm) along the ϕ (z) dimension is assumed. These layers also provide a timing measurement to aid in time-of-flight computation, which provides an additional PID variable to the number of ionisation clusters per unit length (dN/dx) measured in the tracking detector.

The tracker sits inside a high-temperature superconducting solenoid magnet with a 2 T magnetic field. The electron and the positron beams cross at an angle of 30 mrad at the interaction points of the FCC-ee; thus, they are both at an angle of 15 mrad with the axial magnetic field produced by the solenoid magnet. To minimise the effect of the magnetic field on the beam spread and the beam trajectory, the magnetic field strength has been limited to a maximum of

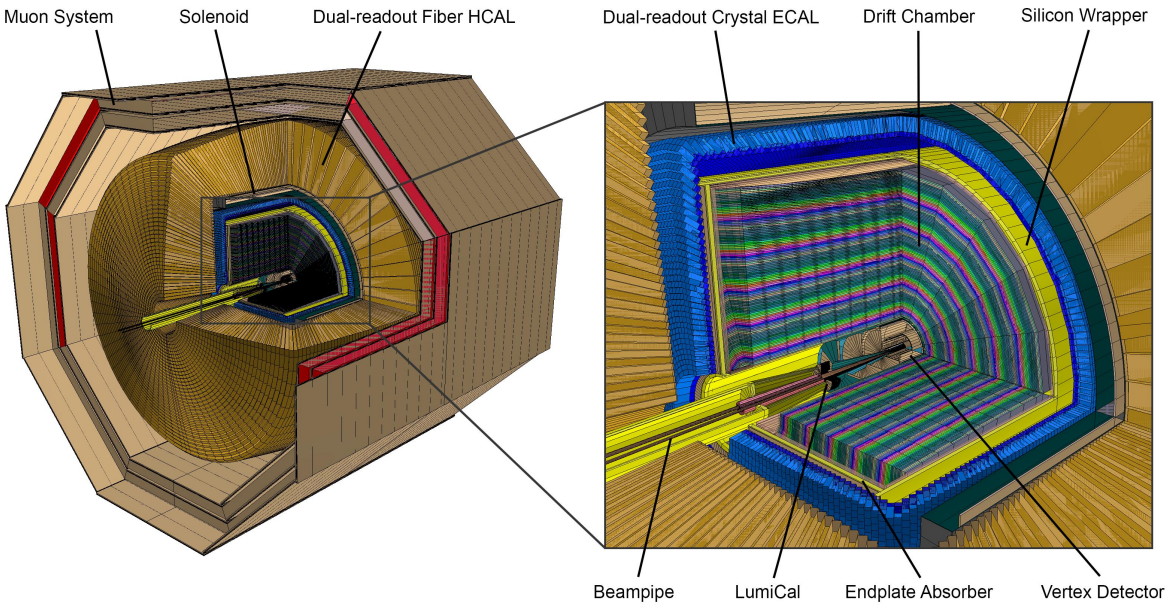

Figure 3.1: Schematic of the IDEA detector concept. [92]

2 T for all FCC-ee detectors [67] [1].

The magnet system is followed by a dual-readout calorimeter that is sensitive to independent signals from the scintillation and the Cherenkov light production. This results in a good energy resolution for both electromagnetic and hadronic showers. An upgrade of the detector concepts includes a crystal ECAL to improve the energy resolution of electromagnetic showers, placed before the dual-readout HCAL.

The calorimeter is enveloped by the muon system, consisting of layers of chambers embedded in the magnet return yoke. The detector geometry has been modified since generating the first set of event samples used in the jet flavour identification study presented in this thesis, and further optimisation is in progress.

Coordinate System

A spherical coordinate system is used for the IDEA detector and in the studies presented in this thesis. The origin of the coordinate system is at the center of the detector system, and the positive z-axis is in the direction of travel of the incoming positrons. The positive x-axis points away from the center of the FCC-ee ring and the y-axis points upwards. The polar angle, θ, is defined as the angle between the radial line and the positive z-axis and the azimuthal angle, ϕ, is defined as the angle of rotation of the radial line around the positive z-axis. [73]

It must be noted that the definition of polar angle, θ, at the FCC-ee is opposite to that defined in the mathematical formulation described in Section 1.5. Experiments at most of the other colliders, including the LEP collider, defined the positive z-axis as the direction of travel

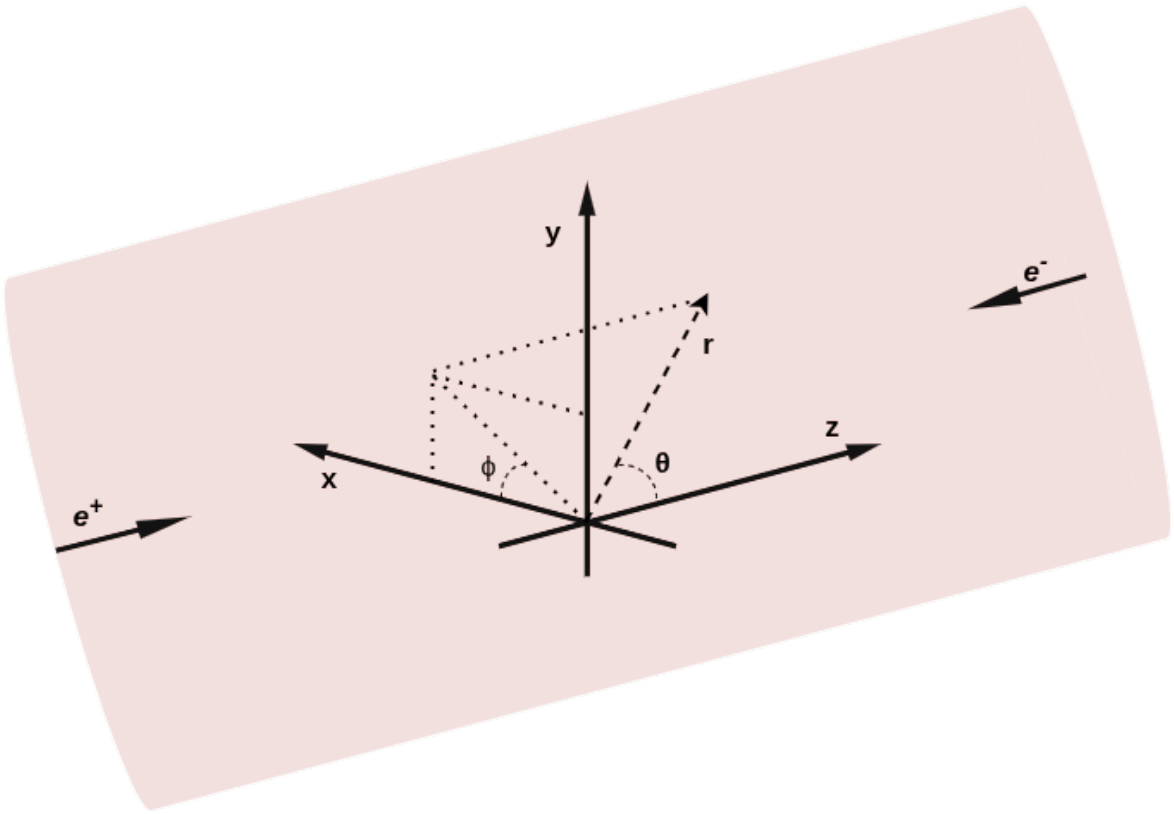

Figure 3.2: The geometrical coordinate system used by the detector concepts at the FCC-ee. The positive z-axis is defined as the direction of travel of the incoming positrons.

[1] The feasibility of magnetic field strengths of up to 3 T is under investigation for FCC-ee runs above the Z resonance [76]

of the incoming electron, and therefore described the polar angle as the angle with respect to the direction of travel of the incoming electrons. This difference is consequential for the forward-backward asymmetry measurement and will be addressed when necessary.

Part II

Jet Flavour Identification at the FCC-ee

4 Event Simulation and Reconstruction

Simulating particle collision events and the corresponding detector response is crucial in devising and optimising physics analysis strategies. It is also essential to assess the physics potential of future experiments. The frameworks used to simulate the particle collisions and interactions are tuned with the help of the data from past and present experiments to simulate the interactions as accurately as possible. Monte-Carlo (MC) methods are used to simulate these interactions and generate event samples with high statistics.

Similarly, simulating the detector response is critical for accurately studying the MC-generated particle interactions in realistic conditions. Detector response simulation is also pivotal in guiding the design and evolution of a new detector concept or a detector upgrade. It aids in the development of a detector design optimised by the requirements of physics studies, which in turn guides the development of the necessary technology.

The simulation of particle interactions as well as the detector response is fundamental to evaluate and demonstrate the potential and the opportunities of the proposed future collider projects, such as the FCC-ee.

4.1 Event Generation

`Pythia8.303` [94] is used for event generation, parton showering, and hadronisation. Event samples have been generated for several different processes to be used in the studies presented in this thesis. The event samples used to train and evaluate the jet flavour tagging classifier, presented in Chapter 6, are henceforth referred to as the 'tagging samples'. The tagging samples are also used in the study presented in Chapter 7. The event samples used in the measurement of the forward-backward asymmetry are hereafter referred to as the 'asymmetry samples'.

4.1.1 The Tagging Samples

The simulated event samples used for training and evaluation consist of the process $e^+e^- \to Z \to q\bar{q}$, where $q \equiv b, c, (u, d, s)$, at the CoM energy ($\sqrt{s}$) of 91.2 GeV. Figure 4.1 shows the Feynman diagram representing this process.

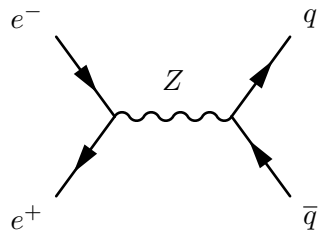

Figure 4.1: The leading order Feynman diagram for the process $e^+e^- \to Z \to q\bar{q}$.

Higgs Boson Samples

A separate set of event samples, used for the comparison of jet flavour tagging performance, was generated with the process $e^+e^- \to Z(\to \nu\nu)H \to q\bar{q}$, where $q \equiv b, c, (u, d, s)$, at $\sqrt{s}$ of 240 GeV. The same reconstruction and jet clustering were applied as for the tagging samples at the Z resonance.

4.1.2 The Asymmetry Samples

The event samples used for the forward-backward asymmetry measurement is composed of the process $e^+e^- \to Z \to q\bar{q}$, where $q \equiv b, c, s, (u, d)$, at the $\sqrt{s}$ of 91.2 GeV. It can be noted that the major difference compared to the tagging samples is that the events for the process $Z \to s\bar{s}$ are separately generated.

The values of $\sin^2\theta_W$ were unmodified.

Background Event Samples

Events generated with the process $e^+e^- \to Z \to l^+l^-$, where $l \equiv e,\ \mu,\ \tau$, at the $\sqrt{s}$ of 91.2 GeV, were used as the background samples in the forward-backward asymmetry study along with the asymmetry samples. The values of $\sin^2\theta_W$ were, similar to the asymmetry samples, kept unmodified.

4.2 Reconstruction

The signals generated in a particle detector must be used to reconstruct the properties of the particles passing through it in order to enable studies of the physical processes undergone in the collision event. Neither the detector measurements nor the reconstruction is perfect and introduces uncertainties to the particle properties. Additionally, the particle detectors, or the algorithms used for reconstruction, do not generally exhibit uniform performance over the entire available phase space. While working with MC-generated event samples, these detector effects must be simulated and applied with the aim of performing a realistic study.

The full simulation frameworks simulate the detailed detector, modelling the detector response, which includes the interaction of particles with the active and passive parts of the detector. On the other hand, the fast simulation frameworks simulate the detector in a simplified manner, where the detector response is parametrised, trading accuracy in the simulation for speed.

Fast simulations are important tools during the evolution of a detector design, especially in the initial stages of its development. In the works presented in this thesis, the `Delphes` framework [93] is used for event reconstruction, assuming the IDEA detector concept [75, 92].

4.2.1 Delphes Fast Simulation

The `Delphes` framework is used to emulate the detector effect on the MC-generated sample. The fast simulation of the IDEA detector concept is implemented in `Delphes` by defining the detailed geometry of the subdetector systems of the detector design. It must be noted that the `Delphes` framework, unlike `Geant4` [95], does not truly simulate the interaction of the particle with the material in different parts of the detector. `Delphes` emulates detector effects by applying efficiencies in different momentum and energy regimes and smearing the kinematic properties of particles as they pass through the simulated detector layers.

Detector Geometry

In the latest geometry of the IDEA detector design implemented in `Delphes`, used for the asymmetry samples, the three inner layers of the vertex detector are radially positioned between 1.2 cm and 3.15 cm, each with an equivalent silicon thickness of 280 µm. The two outer layers of the vertex detector are positioned at 15 cm and 31.5 cm and have an equivalent silicon thickness of 280 µm and 470 µm, respectively. The drift chamber is composed of 112 layers positioned between 36 cm and 2 m, with a thickness of approximately 15 mm. The two layers of the silicon wrapper are positioned at 2.04 m and 2.06 m, and the magnet envelopes this setup at a radial distance of 2.25 m. The pre-shower detector, located before the calorimeter, is positioned at 2.35 m.

Three disks of the vertex detector are positioned on each side of the interaction point at the distances of 25.75 cm, 62 cm, and 93 cm along the beam line for the asymmetry sample. Whereas, for the tagging sample, the vertex detector consists of four disks on each side, positioned between 40 cm and 92 cm.

For the tagging samples, the innermost layer of the vertex detector is positioned at 1.7 cm, and the thickness of both of the outer layers of the vertex detector is 470 µm.

The calorimeters are not defined as geometrical objects.

4.2.2 Tracking

In the tagging samples, a tracking efficiency of 99.7% is assumed in `Delphes` for electrons, muons and charged hadrons with energy $E > 0.5$ GeV that lie within acceptance. This efficiency is reduced to 65% (4%) for $0.5 > E > 0.3$ GeV ($E < 0.3$ GeV). [96]

In the asymmetry samples, a tracking efficiency of 100% is assumed for the charged particles within acceptance with a transverse momentum $p_T > 0.1$ GeV. While a 0% efficiency is assumed for charged particles with $p_T < 0.1$ GeV. [97]

Fake tracks are not considered.

Canonical track parameters, along with their covariance matrix, are calculated for each of the tracks to describe its helical trajectory. These can be determined if the instantaneous position

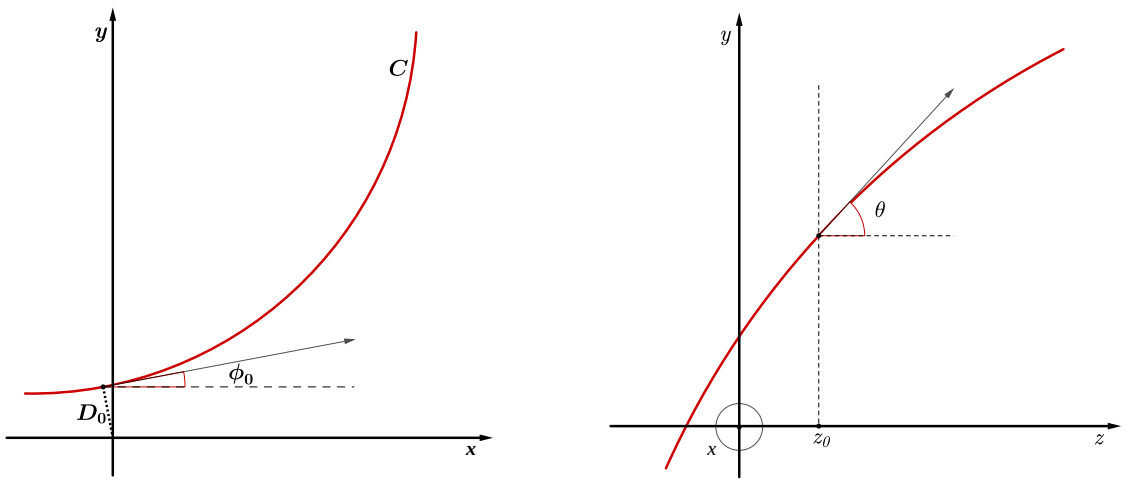

(a) **(b)**

Figure 4.2: Canonical parameters of a particle track. The red curve indicates the trajectory of the particle. $\odot$ sign in the second illustration depicts that the positive x-axis points out of the page. [98]

of the track, its momentum at that point, and its charge are known [99]. The five canonical track parameters, shown in Figure 4.2, are,

1. $\boldsymbol{\lambda}$ signifies the polar angle of the track, $\lambda = \cot(\theta)$, where θ is the polar angle of the track with respect to the $+z$-axis.
2. $\boldsymbol{C}$ represents the signed half-curvature of the track, $C = 1/2R$, where R is the track's radius of curvature. It is positive (negative) for negatively (positively) charged particles.
3. $\boldsymbol{D_0}$ is the signed transverse impact parameter. It is the distance of the track's point of closest approach to the origin in the transverse plane. The sign of D_0 is assigned indirectly by the sign of its product with the half-curvature, D_0C, which is negative (positive) if the origin of the coordinate system lies inside (outside) the track circle in the transverse plane.
4. $\boldsymbol{z_0}$, the longitudinal impact parameter, is the z coordinate of the track position at the point of closest approach to the origin in the transverse plane.
5. $\boldsymbol{\phi_0}$ is the azimuthal angle of the track momentum at the point of closest approach to the origin.

The canonical parameters of tracks are manipulated, within the limits defined by the covariance matrix, to fit them to a common vertex point.

4.2.3 Particle Flow

The particle flow reconstruction algorithm [100] uses the combined information from all detector subsystems. Particles are measured and categorised, following their signals in the different detector subsystems, using the most precise information to achieve the best visible mass resolution. Tracking is used for charged particles, ECAL energy measurement is used for photons, and HCAL energy measurement is used for neutral hadrons. Stable particles are, thus, split into the following categories:

- charged particles
  - charged hadrons
  - electrons
  - muons
- photons
- neutral hadrons

All particles corresponding to one of the above categories are classified as visible particles. As the total energy and the total momentum of the collision event are known, any missing energy (momentum) after summing up the energies (momenta) of all the visible particles, referred to as the missing energy (momentum), signifies the presence of neutrinos. Since the center-of-mass energy of the collision is known, the missing invariant mass can also be calculated.

The parameters for the ECAL and HCAL resolutions were retuned for the asymmetry samples to achieve close to ideal visible mass resolution. The reconstructed invariant mass of the Z boson for the two sets of samples is shown in Figure 4.3.

Electrons

Electrons and positrons are identified by associating an ECAL signature with a track. However, electrons often emit bremsstrahlung radiation, which may leave an unassociated signature in the

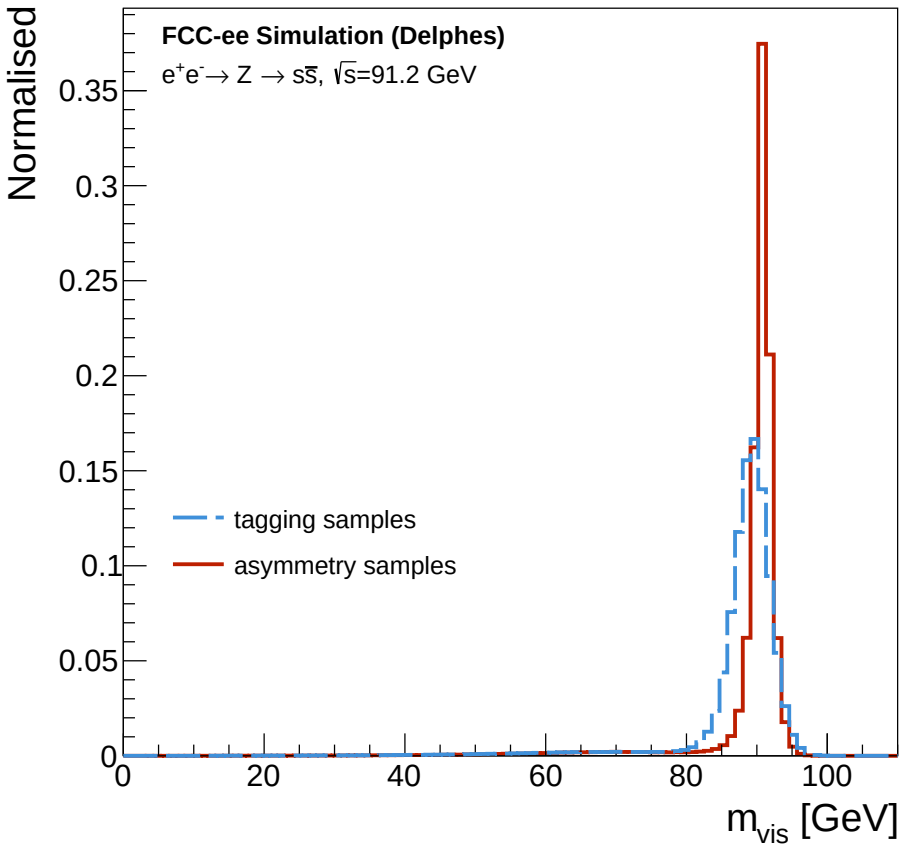

Figure 4.3: The normalised visible invariant mass distributions for the tagging sample and the asymmetry sample.

ECAL. In modern and future experiments, several techniques are used to recover the energy lost via bremsstrahlung radiation, where energy deposits in the ECAL are clustered in an attempt to associate the signature with an extrapolated track. Additionally, due to the very small mass of the electron, energy-momentum matching ($E_{\text{ECAL}}/p_{\text{track}} \approx 1$) is used to recover the bremsstrahlung energy.

Photons

Particles that leave a signature in the ECAL, which cannot be associated with a track, are identified as photons.

Photons can undergo e^+e^- pair production, especially in the presence of dense material, by the process $\gamma X \rightarrow e^+e^-X$. This results in a decay vertex with two close, oppositely charged tracks. Such a decay vertex is a type of V^0 particle, which is discussed later in this chapter. `Delphes` does not simulate pair conversion of photons; therefore, in the samples used in this thesis, photons can be identified simply as ECAL signatures without associated tracks.

Charged Hadrons

Charged hadrons are identified by associating a track with the energy deposits in the ECAL and HCAL, as the charged hadrons deposit a fraction of their energy in the ECAL and are completely stopped in the HCAL.

Neutral Hadrons

Neutral hadrons are identified as particles that leave energy deposits in the ECAL and HCAL, but cannot be associated with a track.

Muons

Particles that deposit insignificant energy in the ECAL and the HCAL, and leave a signature in the muon system, are identified as muons. The track from the tracking detector is extrapolated to associate it with the track reconstructed in the muon system.

In `Delphes`, tracking efficiencies and resolutions, as mentioned above, are applied to the muons from the MC-generated samples, and they are isolated.

4.2.4 Particle Identification

The primary PID strategies at the IDEA detector concept are the ionisation cluster counting [101], supplemented by ToF measurements [72, 102], expected to provide better than 3σ $K^{\pm}/\pi^{\pm}$ separation up to a few tens of GeV.

In the work presented in this thesis, however, the $K^{\pm}/\pi^{\pm}$ classification is generically emulated, instead of relying on any particular PID technique, with several scenarios of different efficiency to correctly identify $K^{\pm}$. The baseline scenario is composed of a 90% efficiency of $K^{\pm}$ identification and a 10% efficiency of misidentifying $\pi^{\pm}$ as $K^{\pm}$. The $K^{\pm}$ identification efficiency and the $\pi^{\pm}$ misidentification efficiency are chosen to be constant over the entire momentum range for all the scenarios. The baseline PID scenario was deliberately conservative with respect to the state-of-the-art $K^{\pm}$ identification at the FCC-ee, and instead follows PID studies at Belle, which found the average efficiency and fake rate for charged particles between 0.5 and 4 GeV/c to be $(87.99 \pm 0.12)\%$ and $(8.53 \pm 0.10)\%$, respectively [103].

4.3 Jets

Partons, i.e. quarks and gluons, are not observed as free individual particles in high-energy physics experiments. They undergo fragmentation, by virtue of processes like gluon radiation or gluon splitting, and form hadrons, which further radiate and decay into other hadrons, leptons, and photons, and form collimated showers of particles within the detector volume. These showers are referred to as jets. It is the jet, and not the initial parton, which is observed in a particle detector. The original parton must be identified from the properties of the jet to reconstruct the primary interaction undergone at the interaction point.

4.3.1 Fragmentation and Hadronisation

The colour field lines of a quark-antiquark ($q\bar{q}$) pair travelling back-to-back in the center-of-mass frame, as those produced from the decay of the Z boson in an e^+e^- collision, are constrained in a tube-like region, unlike the electromagnetic field lines, owing to the self-interaction of gluons. The available energy in this region causes new $q\bar{q}$ pairs to form, and thus the structure is broken into smaller and smaller pieces, leading to the formation of ordinary hadrons.

Partons are particles with colour charge. Due to the principle of colour confinement, however, partons cannot exist in free coloured states, but instead form colourless hadrons. The process through which coloured partons transform into colourless hadrons is called hadronisation.

The initial hard decay process and the further parton showering, i.e. gluon emission or splitting, if any, occur at high enough energies to be modelled with perturbative QCD. However, due to the non-perturbative nature of QCD at lower energies ($< 1\,\text{GeV}$), the hadronisation process falls under the regime of non-perturbative QCD and is currently best described by phenomenological models and MC methods.

Lund String Model

The Lund string model [104] is one of the most widely used non-perturbative QCD models used to simulate the hadronisation of partons produced in a collision event. It is the hadronisation model used to generate the samples described above.

As mentioned above, the colour field lines of a $q\bar{q}$ pair are constrained in a tube-like region. The fundamental approximation of the Lund string model is that the potential energy of a colour singlet, such as a $q\bar{q}$ pair, is linearly proportional to the distance between the two objects,

$$V(r) \approx \kappa r, \tag{4.1}$$

where $\kappa (\sim 1\,\text{GeV}\,\text{fm}^{-1})$ is the string tension. The $q\bar{q}$ system, along with the flux lines, is referred to as a string. The distance, r, between the original $q\bar{q}$ pair increases as they move apart, i.e. the string stretches, and the energy of the system increases linearly, until it is energetically favourable for a new $q\bar{q}$ pair to be formed. The string breaks to produce a new $q\bar{q}$ pair and results in two smaller strings, thus reducing the energy stored in the string, while conserving the momentum and energy of the system. This process is iterated until the energy stored by the remaining string segments falls below the threshold to form a new $q\bar{q}$ pair.

4.3.2 Jet Reconstruction and Clustering Algorithms

Jet reconstruction is performed by clustering the particle flow-style objects reconstructed by `Delphes` with `FastJet-3.3.4` [105]. Clustering the multitude of particles produced in a collision event into a handful of jets simplifies the structure of the event. At the same time, these jets serve as the observable manifestation of the initiating partons. Several clustering algorithms were tested, of which a comparison among three prominent algorithms is presented here.

As particles are merged to reconstruct a jet, the method used to combine the momenta of the particles is called the recombination scheme. The 'E-scheme', as used by the LHC experiments, is employed with all three algorithms described below, in which the momenta of the particles are added in a four-vector sum.

Anti-k_T Algorithm

The anti-k_T clustering algorithm [106] is designed for the cylindrical coordinate system and uses two distance parameters to cluster particles into jets: a distance parameter between particles, d_{ij}, and a distance parameter between particles and the beam, d_{iB},

$$d_{ij} = \min\left(\frac{1}{p_{\text{T}i}^2}, \frac{1}{p_{\text{T}j}^2}\right)\frac{\Delta R_{ij}^2}{R^2}, \tag{4.2}$$

$$d_{iB} = \frac{1}{p_{\text{T}i}^2}\ . \tag{4.3}$$

Here, $\Delta R_{ij}^2 = (y_i - y_j)^2 + (\phi_i - \phi_j)^2$, with $p_{\text{T}i}$, y_i, and ϕ_i are the transverse momentum, rapidity, and the azimuthal angle of the particle i, and R is the jet-radius parameter, which is a user-

defined variable. If a particle is closer to another particle than the beam, i.e. $d_{ij} < d_{iB}$, they are clustered together into a so-called pseudo-jet. Particle objects are thus merged into pseudo-jets until the parameter d_{ij} for all pseudo-jets exceeds the respective d_{iB} parameter.

The anti-k_T algorithm results in cone-shaped jets and is primarily used in hadron collisions.

Generalised e^+e^- k_T Algorithm

The generalised e^+e^- k_T clustering algorithm [105], also referred to as the inclusive e^+e^- k_T algorithm, is designed for the spherical coordinate system, which is suitable for e^+e^- collision events. The e^+e^- k_T algorithm also uses the two distance parameters,

$$d_{ij} = \min\left(E_i^{2p}, E_j^{2p}\right) \frac{(1-\cos\theta_{ij})}{(1-\cos R)}, \tag{4.4}$$

$$d_{iB} = E_i^{2p}. \tag{4.5}$$

Here, E_i is the energy of particle i and θ_{ij} is the angle between particle i and j. Particles are clustered in a similar fashion to that done for the anti-k_T algorithm. If $R \leq \pi$, as in this work, a pseudo-jet object, i, is called an 'inclusive' jet if it is at an angle $\theta_i j > R$ from all other objects. Depending on the choice of the additional configuration parameter, p, the inclusive e^+e^- k_T algorithm can result in either clustered jets in a cone-like shape or irregular shape.

Exclusive e^+e^- k_T Algorithm

The exclusive e^+e^- k_T clustering algorithm [107], also referred to as the 'Durham' algorithm, is also designed for the spherical coordinate system and especially for e^+e^- collision events. It only uses a single distance parameter between the particle objects, d_{ij},

$$d_{ij} = 2\min\left(E_i^2, E_j^2\right)(1-\cos\theta_{ij}) \ . \tag{4.6}$$

The implementation of the Durham algorithm in `FastJet` does not normalise to the total energy of the event [105], unlike the original algorithm.

Particles are merged into a clustered jet until $d_{ij} > d_\mathrm{cut}$, where d_cut is a predefined threshold. The Durham algorithm also allows to force all particles to be clustered into a predefined number of jets, N_jets, which is particularly convenient at e^+e^- colliders, as, in most cases, all particles reconstructed in the detector originate from the decay of the particle produced in the collision event, unlike pp collisions, which can include beam remnants, i.e. parts of the initial protons that did not undergo hard scattering. If N_jet is defined, then d_cut is dynamically calculated to cluster particles until only N_jet jets remain.

The Durham algorithm results in irregularly-shaped jets and is very robust against gluon emissions and gluon splitting.

4.3.2.1 Performance Evaluation

The three algorithms presented above were compared to reconstruct the Z boson invariant mass with $Z \to s\bar{s}$ events. For the anti-k_T algorithm and the inclusive e^+e^- k_T algorithm, the jet-radius parameter was set to 0.5, and two jets with the highest momentum were considered for events with more than two jets to reconstruct the Z boson invariant mass. The inclusive e^+e^- k_T algorithm is run in the k_T configuration with $p = 1$. Exactly two jets were required for the exclusive e^+e^- k_T algorithm.

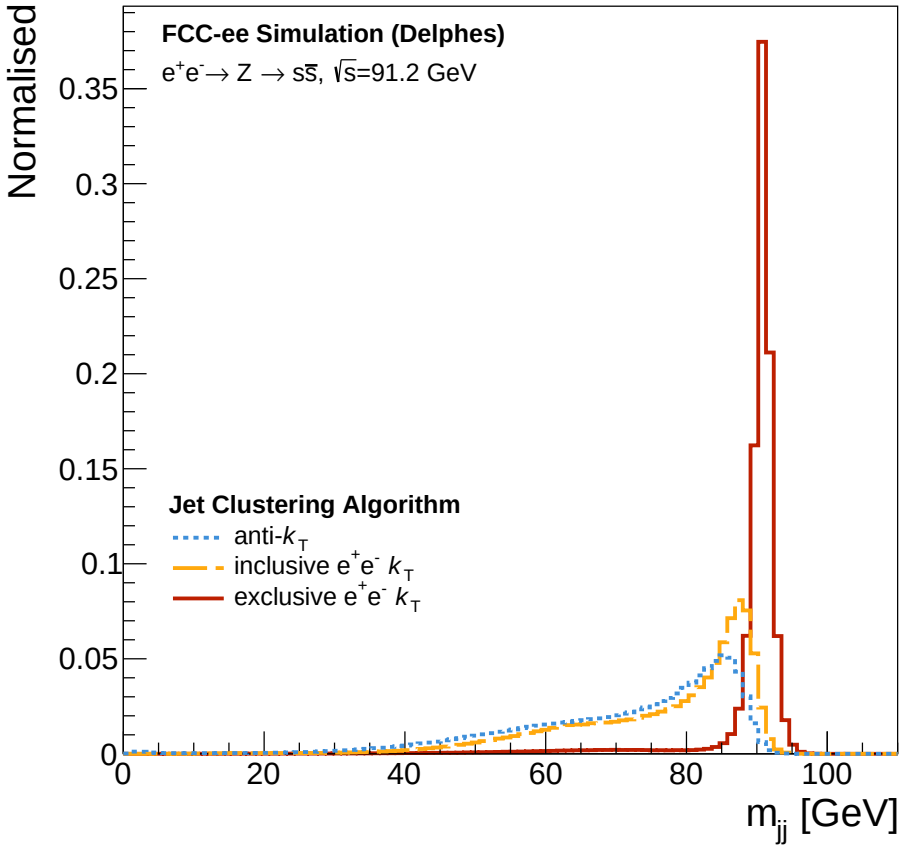

Figure 4.4: The normalised invariant mass distributions of di-jet systems, clustered with three different algorithms, in the process $e^+e^- \to Z \to q\bar{q}$ at the $\sqrt{s}$ of 91.2 GeV.

Figure 4.4 shows the invariant mass distribution of the Z boson for the three clustering algorithms. Since the jets clustered with the exclusive e^+e^- k_T algorithm include all reconstructed final particles, they were observed to satisfy the requirements of this study by most accurately reproducing the Z boson reconstructed invariant mass signature. No additional selections were applied to the samples for training and evaluation of the jet flavour tagging classifier presented in the next chapters.

4.3.3 Truth Flavour Labelling

Assigning a flavour label to an MC-generated jet is not a straightforward task, as different definitions focus on different aspects of the jet's properties to assign these labels. Some definitions prioritise the initiating parton, while others emphasise the presence of particular hadrons or partons in the MC history of the jet. This flavour labelling is crucial in reconstructing the primary interaction undergone in the collision event. Thus, in the absence of a uniquely accurate flavour definition, the one used for any particular study must be noted, as the conclusions of the study will inevitably be correlated to the chosen definition.

In this study, the jets are assigned an MC flavour as the flavour of the quarks to which the Z boson decays. Besides simplicity, this has the added benefit that other studies for future facilities use the same definition.

4.4 Vertex Reconstruction

The massive particles produced in the collision event of the incoming particles at the interaction point, like the Z boson and Higgs boson, have negligible lifetimes and decay almost instantly. This decay vertex, which is essentially within the beam spot around the interaction point, is referred to as the primary vertex. The beam spot is the finite region where the two beams cross each other. Some of the particles produced at the primary vertex can have finite lifetimes. A few hadrons with finite lifetimes, containing b, c, or s quarks, are listed in Table 4.1.

Quark	**Hadron**	**Lifetime** [$\times 10^{-12}$ s]	**Decay Length** [mm]	**Mass** [GeV]
b	B^0	1.5	0.45	5.28
	B^+	1.6	0.48	5.28
	Λ_b^0	1.5	0.45	5.62
c	D^0	0.4	0.12	1.86
	D^+	1.0	0.30	1.87
	Λ_c^+	0.2	0.06	2.29
s	K_S^0	89.5	26.85	0.50
	Λ^0	263.2	78.96	1.12

Table 4.1: Lifetime, decay length, and mass of a few most commonly observed hadrons containing bottom, charm, or strange quarks [20]. The decay length is defined as $c\tau$, where c is the speed of light and τ is the lifetime of the particle in seconds.

Vertex reconstruction is essential to find the primary interaction vertex and the secondary decay vertices of the long-lived b, c, and s hadrons, or the τ leptons. It helps improve the b- and c-tagging performance and aids in s-tagging. Charged tracks can be fitted to reconstruct the primary and the displaced secondary vertices. These displaced vertices can either be the decay vertices of b and c hadrons (SVs) or those of the long-lived hadrons containing s quarks, like K_S^0 or Λ^0, commonly referred to as V^0s, which are neutral particles that decay into a pair of oppositely charged tracks. All displaced vertices except V^0s are referred to as SVs. The properties of SVs and V^0s, such as their masses, displacements, and charged track multiplicities, can be used to identify the decaying hadrons and, in effect, the jet flavour. The SVs can even be used to reconstruct the entire hadronic decay chain.

Similarly, reconstructing and identifying the V^0 vertices can be used to identify s-jets, as K_S^0 and Λ^0 are the particles carrying most of the momentum of some s-jets [108]. Distinguishing V^0s from SVs also helps to reduce the misidentification of some b- and c-jets as s-jets, as V^0 decay vertices may have signatures that resemble those of decay vertices of hadrons containing b or c quarks.

The vertex reconstruction in this study has been performed using an implementation of the vertexing module of the `LCFIPlus` framework [1, 98]. It has been implemented in `FCCAnalyses` [109], the FCC software framework, using a χ^2-based vertex fitter [110]. The constraints and parameters have been kept the same as in the original implementation [1]. Vertex reconstruction is performed after jet clustering; thus, it is performed separately for each jet of the event, with the exception of reconstructing the primary vertex.

4.4.1 Primary Vertex

All tracks from the event are fitted to a common vertex. Then tracks with the highest χ^2 contribution to the fit are sequentially removed until the χ^2 of the vertex fit is below a predefined

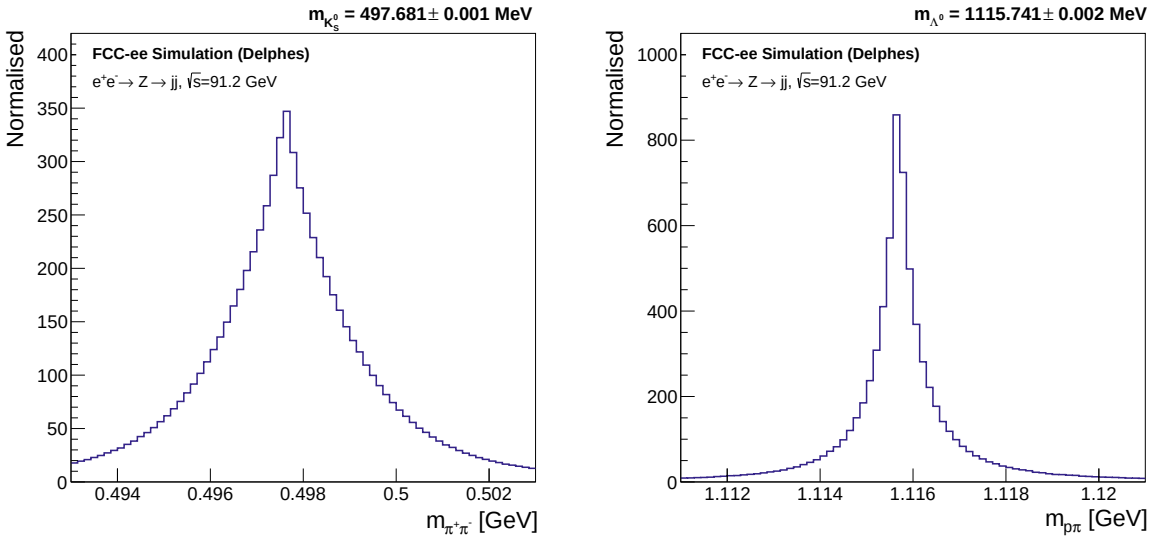

(a) Reconstructed K_S^0 **(b)** V^0 multiplicities

Figure 4.5: Performance of V^0 reconstruction. Invariant mass distribution of (a) reconstructed K_S^0 vertices and (b) reconstructed Λ^0 vertices. The quoted masses are the mean and the error on the mean of the distributions.

threshold. A χ^2 threshold of 25 is used in the vertex reconstruction implementation used in the work presented in this thesis.

Tracks originating from the primary vertex are not used in the reconstruction of the V^0 particles and the SVs.

4.4.2 V^0 Particles

Reconstructing and identifying V^0 particles is important for strange jet tagging. Rejecting tracks originating from the V^0 decays is also crucial for an accurate and efficient reconstruction of secondary vertices. Thus, the V^0 particles are identified before reconstructing the SVs. Two decay processes of V^0 particles are considered:

$$K_S^0 \to \pi^+\pi^-$$
$$\Lambda^0 \to p\pi^- \quad \text{OR} \quad \bar{\Lambda}^0 \to \bar{p}\pi^+.$$

Since V^0 particles decay to a pair of oppositely-charged particles, to search for particle tracks originating from V^0 decay vertices, all possible oppositely-charged pairs of tracks are fitted to form two-track vertices. These vertices are referred to as V^0 candidates. Three variables are calculated for these V^0 candidates: the invariant mass (m), the distance from the interaction point (r), and the collinearity factor ($\hat{\mathrm{p}} \cdot \hat{\mathrm{r}}$), to ensure that the V^0 originates from the primary vertex. These three variables are tested against the sets of constraints summarised in Table 4.2. Unlike in standard vertex reconstruction algorithms, the V^0s are not discarded but stored and assigned a particle ID based on the set of 'tight' constraints that they pass.

The invariant mass of the reconstructed K_S^0s and Λ^0s can be seen in Figure 4.5, demonstrating a good reconstruction of V^0s and their properties. The mass of the tracks used to calculate the invariant mass of the V^0 is decided based on the set of constraints the V^0 passes with a certain permutation of the two tracks. In contrast, all tracks are assumed to be pions in the invariant mass calculation for the SVs.

Figure 4.6 displays the V^0 multiplicity in jets from $Z \to q\bar{q}$ events. No reconstructed V^0s

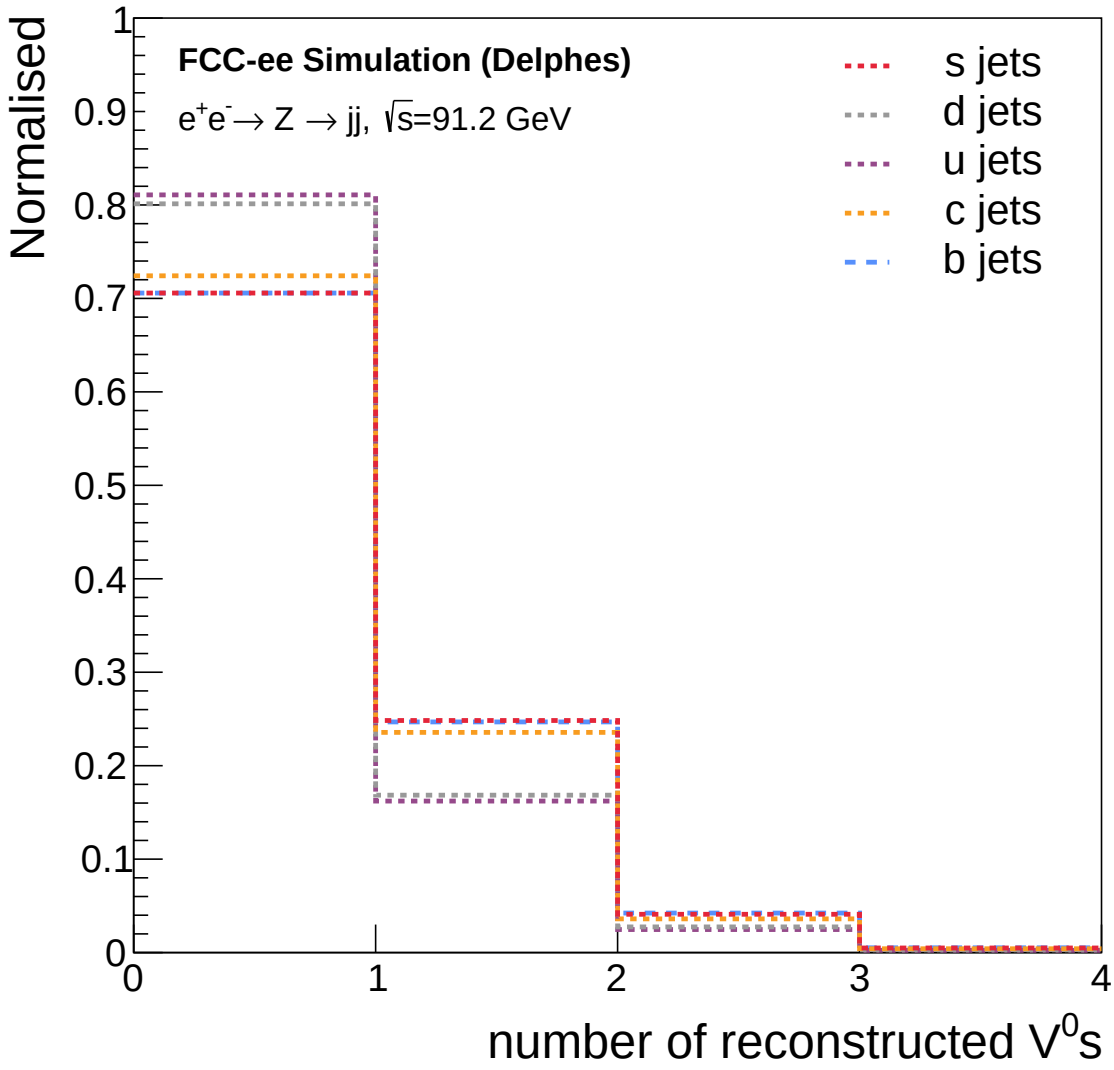

Figure 4.6: The reconstructed V^0 multiplicity in jets from $e^+e^- \to Z \to q\bar{q}$ events at $\sqrt{s} = 91.2$ GeV, where $q \equiv u, d, s, c, b$. The distributions for b- and s-jets overlap almost perfectly.

are found for most of the jets. But, a higher fraction of heavy- and strange-flavoured jets contain reconstructed V^0s than u- and d-jets, which justifies the importance of V^0 rejection before attempting to reconstruct SVs. It is also evident that more s-jets have one or more reconstructed V^0s than u- and d-jets, making V^0s an important discriminator of s-jets against lighter quark jets.

4.4.3 Secondary Vertices

The tracks originating from the primary vertex or V^0 particles are not considered while reconstructing SVs. Secondary vertex reconstruction is initiated by fitting a two-track vertex (seed) with the lowest χ^2 from the vertex fit, while still passing a predefined χ^2 threshold and the criteria mentioned in Ref. [1]. Particularly, if this seed vertex passes the 'loose' set of constraints presented in Table 4.2, it is discarded. A track is attached to this seed if it still results in a vertex with a χ^2 of the vertex fit below the threshold. If more than one track satisfies this condition, the track resulting in the vertex with the lowest χ^2 is selected. This process is repeated until the resulting vertex no longer passes the criteria specified in Ref. [1]. The tracks forming the

	K_S^0		Λ^0	
	tight	loose	tight	loose
m [GeV]	$[0.493, 0.503]$	$[0.488, 0.508]$	$[1.111, 1.121]$	$[1.106, 1.126]$
r [mm]	> 0.5	> 0.3	> 0.5	> 0.3
$\hat{\mathbf{p}} \cdot \hat{\mathbf{r}}$	> 0.999	> 0.999	> 0.99995	> 0.999

Table 4.2: Summary of the default V^0 selection criteria [1]. M is the invariant mass, and p is the momentum of the V^0 candidate. r is the distance of the V^0 candidate from the primary vertex. The collinearity of the V^0 candidate is defined as $\hat{p} \cdot \hat{r}$. The set of 'tight' constraints has been used to identify V^0s in this study, while the set of 'loose' constraints has been used to remove the V^0 background while reconstructing SVs.

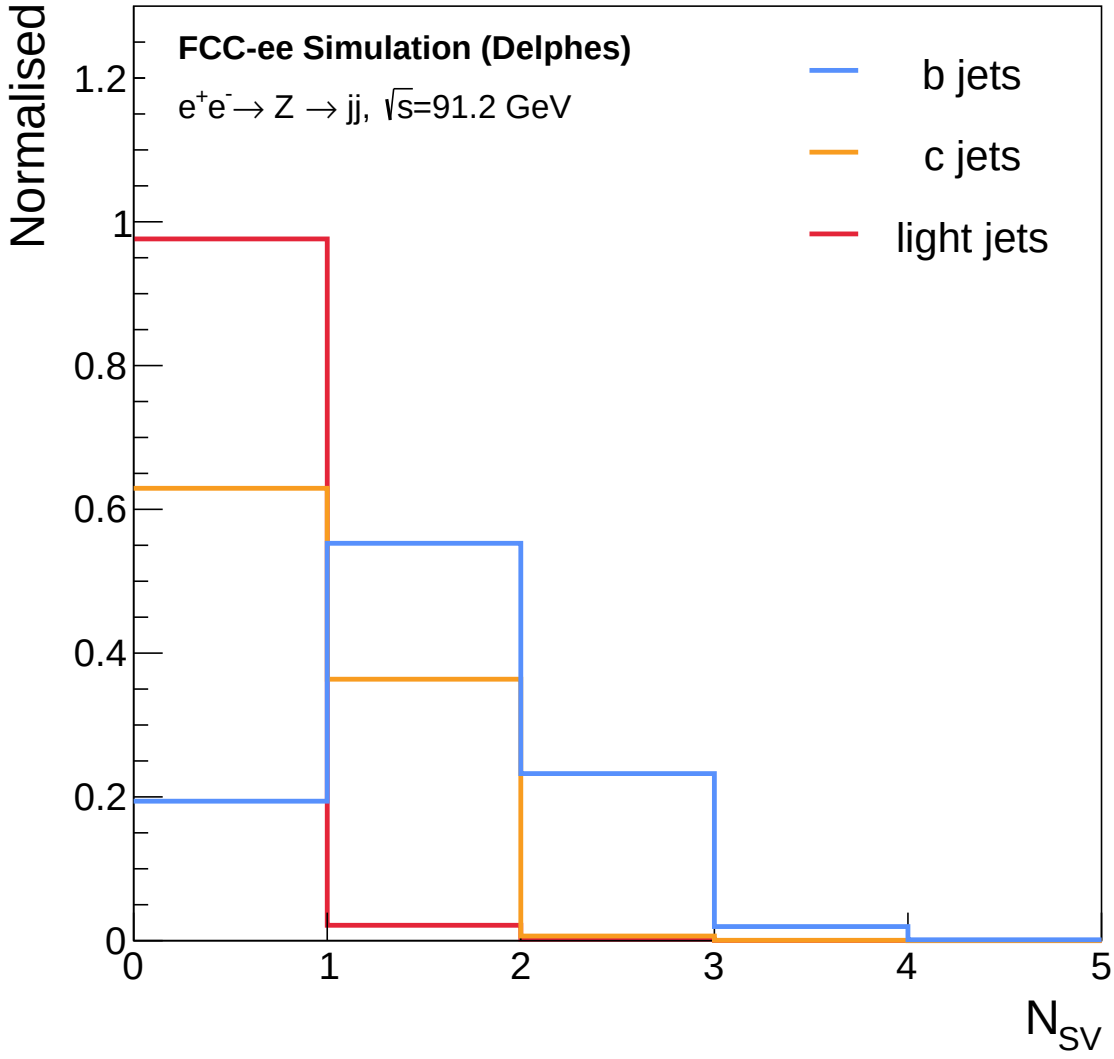

Figure 4.7: SV multiplicity in jets from $e^+e^- \to Z \to q\bar{q}$ events. The term "light jets" here collectively refers to u-, d-, and s-jets.

SV are stored and removed from the original set, and more SVs are reconstructed recursively until no more seeds pass the required constraint thresholds.

Due to the near-diagonal CKM matrix, the cascading decay chain of heavier quarks is expected to be $b \to c \to s \to (u, d)$. Hence, the SV multiplicity tends to be higher in b-jets

compared to c-, s-, u-, and d-jets, as shown in Figure 4.7.

In the following chapters, jet flavour identification at the FCC-ee is investigated using a transformer-based neural network architecture, with a novel implementation of reconstructed V^0s as a distinguishing feature and assessing the impact of different PID assumptions on classifying performance.

5 The DeepJetTransformer Model

Machine learning (ML) is a field of computer science composed of decision-making algorithms that enable systems to extract patterns in data and optimise their performance by automatically learning and improving from experience and feedback. It performs predictive tasks while aiming to minimise the predictive error. ML algorithms can be classified into supervised, unsupervised, or semi-supervised learning based on whether the input data used to train the algorithm, or a fraction of it, is labelled or not. Supervised learning aims to learn the mapping between inputs and outputs, while the objective of unsupervised learning is to extract hidden features within the data.

5.1 Training

In supervised learning, training is performed on a dataset to determine the learnable parameters of the algorithm, such as weights, to reduce the error between the predicted output, $\hat{y}$, and the known output, y. This error is quantified by a loss function. A commonly used loss function for classification tasks is cross-entropy, which is defined as,

$$\mathcal{L}_{\text{CE}} = -(y \log(\hat{y}) + (1 - y) \log(1 - \hat{y})). \tag{5.1}$$

The ML model aims to minimise the loss function during the training process.

The training data is generally split into a training set and a validation set. The training set is used to adjust the learning parameters by minimising the loss function, while the validation set acts as an unbiased intermediate evaluation during training. A new dataset, called the test set, is used for an unbiased evaluation of the generalisation ability of the model.

5.1.1 Performance Metrics

Several metrics can be used to evaluate the classification performance of an algorithm. A ubiquitous way to present the performance is by plotting the Receiver Operating Characteristics (ROC) curves. ROC curves plot the True Positive Rate (TPR) against the False Positive Rate (FPR), where TPR represents the proportion of correctly predicted outcomes by the algorithm, and FPR represents the proportion of incorrectly predicted presence of a class. The area under the ROC curve (AUC) is a single scalar metric that summarises the performance of the algorithm, where an AUC = 1 indicates perfect performance, while AUC = 0.5 represents a random guess.

5.2 Neural Networks

Neural networks (NNs) are computational models in ML inspired by the working of neurons in the human brain. They use a combination of functions to transform a vector of inputs into the desired output.

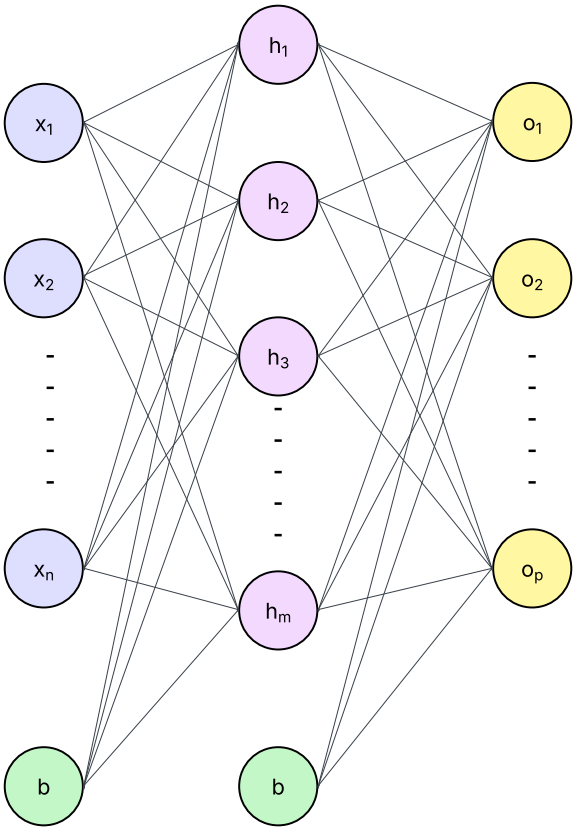

Figure 5.1: The schematic of an MLP with three layers, including an input layer with n features, a hidden layer with m nodes, and an output layer with p nodes. The biases for each layer are represented by the green cells.

Perceptrons

A perceptron can be considered the foundational element of NNs and was originally proposed as a binary classifier. The perceptron, employed as a binary classifier, computes the weighted sum of the inputs x_i with weights W_i and adds a bias b. A step function is applied on the sum to get the final output, which can then be compared to the truth label y. The weights W_i and the bias b are learnable parameters of the perceptron, which can be updated by using a loss function.

Multilayer Perceptrons

Classification tasks typically require a non-linear transformation. Multilayer perceptrons (MLPs) extend the model of a simple perceptron by introducing one or more hidden layers between the input and the output, where each layer performs a linear transformation passed through a non-linear activation function. MLPs employ a fully connected feed-forward architecture, as displayed in Figure 5.1, where a node in a layer is connected to every node in the next layer and the output of one layer is used as the input by the next layer. The number of output nodes can be chosen based on the classification task. The SoftMax function is generally used for multi-class classification to normalise the output discriminants into a probability distribution and is defined as,

$$\text{SoftMax}(x) = \frac{e^{x_i}}{\sum_j e^{x_j}}. \tag{5.2}$$

Activation Functions

Activation functions process the output of a node. In MLPs, the activation functions are used to introduce non-linearity, without which an MLP can only perform a linear transformation. Among the several non-linear activation functions, ReLU [111] is one of the most commonly used and is defined as,

$$\mathrm{ReLU}(x) = \max(0, x). \tag{5.3}$$

Dropout Regularisation

When a network model fits the training data too closely, there's a risk of overfitting, which refers to the situation where the model gets overly optimised to the training dataset and may not be generalised for new datasets. Thus, regularisation includes strategies to avoid overfitting to the training data, of which dropout regularisation [112] is one of the most crucial forms. It includes randomly deactivating some nodes along with all incoming and outgoing connections from the network during training to prevent the network from becoming overly dependent on particular nodes.

5.3 Machine Learning-based Jet Flavour Taggers

The application of ML is ideally advantageous for classifying jet flavours, given the abundant MC-generated training samples. The development of jet flavour identification has continuously evolved at the LHC and, with time, has begun to heavily rely on ML algorithms [113, 114]. This progress has inspired the algorithms designed to identify jet flavours at the FCC-ee [2, 115, 116].

Jet flavour classification with single physics-motivated variables has been significantly outperformed with the introduction of ML approaches, which include Neural Networks (NNs) and Boosted Decision Trees (BDTs) [114, 117–119]. Numerous architectures, as well as jet structure representations, have been implemented with successive improvements in jet flavour classification. These include Dense Neural Networks (DNNs) [120], Recurrent Neural Networks (RNNs) [121], Convolutional Neural Networks (CNNs) [122, 123], and Graph Neural Networks (GNNs) [115, 124, 125].

Architectures using a Graph-based representation of jets with jet constituents acting as the nodes and pairwise features acting as edges, such as `ParticleNet` [115], have shown some of the best classification performance. Additionally, Transformer networks, architectures that employ a self-attention mechanism [126], described in Section 5.4, to extract relative feature importance, have reached state-of-the-art performance in jet flavour classification [119, 127–129]. The `Particle Transformer` (`ParT`) [129] model combines the attention mechanism with a graph representation of jets.

5.4 DeepJetTransformer

Following the successful application of the attention mechanism in Natural Language Processing (NLP) [126, 130] or Computer Vision (CV) [131] tasks, Transformer blocks were chosen as the core architectural components for the `DeepJetTransformer` model [2, 116]. Transformers constitute a class of neural networks that exploit the scaled dot-product attention (SDPA) mechanism [126], which enables the model to concentrate on the most informative parts of the input sequence, as it processes each element. The attention mechanism dynamically evaluates the relevance of every constituent within the jet to assign them weights, thus capturing intricate

correlations throughout the jet structure. Such an adaptive, global weighting approach equips the Transformer to effectively encode contextual information, which is essential for learning and constructing coherent high-level features.

The particle cloud representation of the jet structure, which has been prevalent since the introduction of `ParticleNet` [115], views the jet as an unordered, permutation-invariant set of its constituents. It utilises the fact that there is no hierarchical structure or positional ordering among the jet constituents. The `DeepJetTransformer` model was designed by using the particle cloud representation; hence, it was required to be invariant under the permutation of the jet constituents[1]. The same has been done by other transformer-based taggers employing the particle cloud representation [129].

Transformers also consider the jet as a complete graph, connecting all constituents of the jet through the attention mechanism, allowing the model to reconstruct high-level features by extracting subtle correlations among jet constituents. This is analogous to a fully connected graph network, where the edge features are replaced by the attention scores. It has been shown that Transformer models can achieve improved performance, especially relative to graph models [129, 132]. Thus, a Transformer-based model was selected to develop a jet flavour identification algorithm.

Embedding

A complete and accurate jet representation is achieved by including elements of different natures, such as charged and neutral particles, SVs and V^0s, associated with the jet. MLP layers are used to project the different jet constituent features to input features of the same dimension.

Scaled-Dot Product Attention

Of the various types of attention mechanisms, the scaled-dot product attention (SDPA) is the key component employed by Transformer models. It utilises three input matrices: the query matrix, Q, representing the tokens for which the attention weights are computed, the key matrix, K, and the value matrix, V, representing the keys and the values of all tokens. When used along with the jet representation, these tokens are analogous to the constituents of the jet.

Self-attention [126] is a specific configuration of the attention mechanism and has been employed by `DeepJetTransformer`, where the three matrices are projected from the same input, X, thus, capturing correlations among the elements of the same input sequence. The input X is projected into the three matrices through distinct linear transformations: $Q = XW^Q$, $K = XW^K$, and $V = XW^V$, where W^Q, W^K, and W^V are weight matrices. The SDPA is then obtained by,

$$\text{Attention}(Q, K, V) = \text{SoftMax}\left(\frac{QK^T}{\sqrt{d_k}}\right)V, \tag{5.4}$$

where d_k is the dimension of the query and the key matrices.

Multi-Head Attention

Transformer models allow for parallelisation of the SDPA operation over multiple attention subspaces, known as multi-head attention (MHA). Thus, MHA enables the extraction of complementary high-level features by independently projecting the query, key, and value matrices

[1]Permutation invariance is in opposition to most Transformer models established around the principle of causality [126, 130].

for each attention head, h_i, as: $Q_i = XW_i^Q$, $K_i = XW_i^K$, and $V_i = XW_i^V$. The SDPA operation is performed for each attention head, and their output representations are concatenated and passed through a linear layer. The operation performed by the MHA layer is represented as,

$$\mathrm{MHA}(Q, K, V) = \mathrm{Concat}(h_1, ..., h_n)W^O, \tag{5.5}$$

$$h_i = \mathrm{Attention}(Q_i, K_i, V_i). \tag{5.6}$$

Here, W^O is the weight matrix used to project the concatenated output of the attention heads.

As mentioned above, `DeepJetTransformer` employs the particle cloud representation; therefore, it does not use positional encoding, as done by the original Transformer implementation [126]. Instead, the MHA module only utilises permutation invariant mechanisms, established by the properties of permutation equivariance and invariance of function composition [133]. This ensures that the jet representation produced by the network model observes the properties of the particle cloud representation. The invariance of the flavour classification by the network under the permutation of jet constituents is ensured by incorporating a permutation-invariant attention pooling.

Heavy Flavour Transformer Block

The MHA module constitutes the core element of the fundamental component of the model's architecture, referred to as the Heavy Flavour Transformer (HFT) block. Before being passed through the HFT blocks, the distinct jet constituent inputs are fed into an embedding stage, following which they are concatenated into a single jet constituent feature tensor. The HFT block is implemented as follows:

- The feature inputs are fed into an MLP layer, which is followed by a ReLU activation function.
- The output of the MLP layer is passed to an MHA layer with eight heads. This is followed by residual connection and layer normalisation.
- Finally, the MHA layer feeds into a fully connected feed-forward layer with residual connection and layer normalisation.

Attention Pooling

An attention pooling, which acts similarly to a max or average pooling layer but employs an attention mechanism and uses learned parameters, is used to capture essential features and summarise the jet information into a classification-relevant representation. This stage incorporates an MLP layer to enable local feature extraction, followed by a SoftMax activation function to calculate attention weights, which are then used to perform a weighted sum to condense the information. Batch normalisation is used to improve the performance of the layer. The ReLU activation function and dropout regularisation are employed to introduce non-linearity and prevent overfitting, respectively.

5.4.1 DeepJetTransformer Architecture

The global structure of the model architecture of `DeepJetTransformer`, as illustrated in Figure 5.2, can be described in terms of the components defined above.

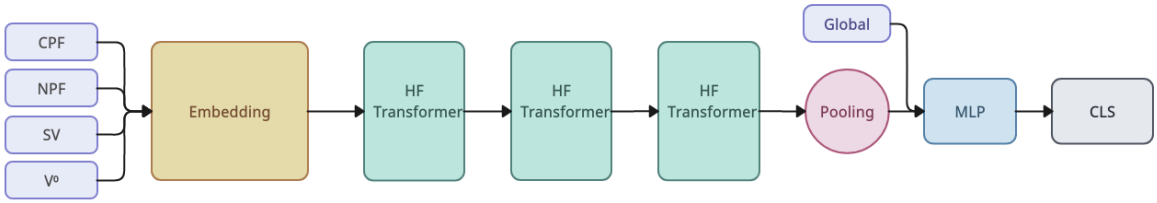

Figure 5.2: Schematic structure of `DeepJetTranformer` model.

The input features of different types of jet constituents are passed through the embedding layer, which consists of an MLP with three layers of output feature dimensions of 64, 128, and 128, respectively. Each layer employs the ReLU activation function, residual connection, and batch normalisation, following which a dropout rate of 0.1 is applied. The outputs of the embedding layer are concatenated to form a single global tensor that includes all constituents and represents the jet. The concatenated tensor is passed through three successive HFT blocks, each with a dimension of 128 and a dropout rate of 0.1. The jet representation output of the HFT blocks is summarised with an attention pooling layer, the output of which is concatenated with the jet-level features, resulting in a vector containing 135 features for jet flavour classification. This vector, containing 128 features emerging from the attention pooling layer and seven representing the jet-level features, is passed through a three-layered MLP, similar to the input embedding layer, with output feature dimensions of 135 each. This is fed into the classification layer comprising an MLP with a single layer, followed by a SoftMax activation function.

5.4.2 Training Methodology

The deep learning framework `PyTorch (v1.10.1)` [134] was used to construct and train the `DeepJetTransformer` neural network model. The Lookahead optimiser [135] with hyperparameters $k = 6$ and $\alpha = 0.5$ was employed, and RAdam [136] was used as the base optimiser, configured with a learning rate of 5e-3 and decay rates $(\beta_1,\ \beta_2) = (0.95,\ 0.999)$. Training proceeded for 70 epochs with a batch size of 4000. A linear learning rate decay was applied per epoch, beginning after 70% of the training period and gradually reducing the rate to 5e-5 by the final epoch. Optimisation was done with a cross-entropy loss function. The training dataset consisted of 1 million jets, 80% used for training and 20% for validation. Model performance was evaluated on an independent test set of 1 million jets. Full documentation of the sample preparation, training strategy, and associated code is available at: DeepJetFCC[2].

[2]https://github.com/Edler1/DeepJetFCC/tree/master/docs

6 Jet Flavour Identification with DeepJetTransformer

The precise measurement of the SM parameters is one of the vital motivations for the proposed future lepton colliders [61, 72, 137, 138]. This includes precision studies of the hadronic decay channels of the Z boson, improved sensitivity for the Higgs boson coupling to the bottom (b) quark as well as the measurement of the SM Yukawa coupling for the charm (c) quark, and potentially for the strange (s) quark [139–141]. Accomplishing these objectives entails an efficient and accurate reconstruction of the hadronic decays of these bosons. It has been established that excellent jet flavour identification is crucial to access the maximal physics potential offered by the future collider projects [108, 142–145], and the assessment of the achievable precision in the measurement of scarcely studied processes is being investigated.

Strange Jet Tagging

Strange jet discrimination, or strange jet tagging, is widely regarded as one of the challenging types of jet flavour classification. Consequently, it has received substantially less attention than bottom and charm jet tagging or quark-gluon discrimination. It essentially stems from the fundamental treatment of the strange and down jets in the SM. Unlike the differing colour factors of quarks and gluons, or the displaced decay vertices and tracks of hadrons containing the bottom or charm quark, both QCD and the electroweak theory treat strange and down jets identically in the massless limit prior to their decay, leaving almost no fundamental discriminating features between the two flavours. However, a larger fraction of the total scalar momentum of the jets, defined as the sum of the scalar momentum of its constituents, is carried by strange hadrons in the case of strange jets, as opposed to in down jets, as exploited in the context of hadron colliders [146]. In practice, this becomes apparent through a higher (lower) kaon (pion) multiplicity in strange jets than in down jets. Thus, differentiating $K^{\pm}$ from $\pi^{\pm}$ and reconstructing K^0_S is critical to strange jet identification [146–148].

SLD [149] tagged $Z \to s\bar{s}$ events by looking for the absence of reconstructed b and c hadrons and the presence of $K^{\pm}$ or K^0_S [150]. Particle identification (PID) was performed at SLD, as at DELPHI [81], with a RICH detector. At most other detectors, energy loss (dE/dx) was used for PID [82, 83], with the addition of timing at ALEPH [80]. The detector concepts at the FCC-ee foresee the use of techniques like energy loss (dE/dx) [86], ionisation cluster counting (dN/dx) [87], time-of-flight [89], and compact-Ring Imaging CHerenkov (RICH) detectors.

In the flavour identification algorithm presented in this chapter, the dominant fraction of momentum carried by strange hadrons is exploited, firstly by including V^0 variables and secondly through $K^{\pm}/\pi^{\pm}$ discrimination. The cleaner environment at lepton colliders and the powerful PID capabilities of the proposed detector concepts facilitate making strange jet tagging feasible.

This work is also presented in an EPJ C publication [2] and has been summarised in the ECFA Higgs, electroweak, and top factory study [3].

The jet-flavour tagging algorithm `DeepJetTransformer`, introduced in Section 5.4, is trained on the simulated event samples presented in Section 4.1. The input features used for training are described below, followed by an evaluation of the performance and its dependence on various detector-reconstructed properties.

6.1 Distinguishing Principles for Jet Flavour Identification

A few differing but well-defined physical principles have traditionally been used for jet flavour identification based on the jet flavour that is to be identified. These principles are also the dominant distinguishing features in the ML-based tagging algorithms. Measurable variables can be defined based on these physical principles to aid in the identification of the jet flavours. Some of these principles and variables are noted below.

Displaced Tracks and Vertices

Jets originating from the heavier b and c quarks contain hadrons with significant lifetimes that travel distances of the order of millimeters from the interaction point before they decay into lighter hadrons. The heavy quark flavour tagging algorithms used at the LEP collider [151, 152] and the Tevatron [153, 154] experiments exploited variables derived from the displaced charged tracks originating from the decay of these hadrons containing b or c quarks to distinguish the heavy quark flavoured jets from strange quark jets (s-jets), up quark jets (u-jets), down quark jets (d-jets), and gluon jets (g-jets). These displaced charged tracks are commonly fitted to reconstruct the original decay vertices of the hadrons containing b or c quarks, also called secondary vertices (SVs). The properties of these SVs, like their mass and displacement, are some of the most important inputs used to identify bottom quark jets (b-jets) and charm quark jets (c-jets).

Particle Identification

Strange quarks are treated identically to down quarks by QCD and Electroweak theory in the massless limit prior to their decay. Discriminating between strange and down jets is particularly challenging due to the same fractional charge of the initiating quarks. In practice, however, strange hadrons carry a larger fraction of the total scalar momentum of strange jets, compared to hadrons consisting of up and down (ud) quarks. The total scalar momentum is obtained by summing over the scalar momentum of all jet constituents. This idea was also explored in the context of hadron colliders [146]. Strange jets tend to have a higher kaon multiplicity and a lower number of pions than u- and d-jets. Therefore distinguishing $K^{\pm}$ and $\pi^{\pm}$ and reconstructing K^0_S is crucial for strange jet identification [146–148].

Jet Charge

The difference in the electric charge of the jet-initiating quark can also be used to distinguish different jet flavours. However, the variables defined to exploit this property, such as the momentum-weighted jet charge, have limited efficiency due to hadronisation and formation of neutral particles in the jets. Due to the differing charges of the up quark ($+\frac{2}{3}$) and the down quark ($-\frac{1}{3}$), the jet charge can be used to distinguish the u- and d-jets. It is also used to separate jets originating from the quarks and antiquarks.

Colour Factor

The discrimination of quarks vs gluons dominantly relies on properties derived from their differing colour factors $C_F = 4/3$ vs $C_A = 3$, like the jet width and shape, and the jet constituent multiplicity.

6.2 Input Features

Three major categories of input features that are utilised for model training are defined with the properties of each jet and its constituents. All input features are built using information reconstructed with `Delphes` detector simulation, described in Section 4.2, unless stated otherwise. These variables, as described in Table 6.1, 6.2, and 6.3, are fed into a neural network, the architecture of which is described in Section 5.4. The distributions of a few variables are shown in Figure 6.1 and the distinguishing power of some of these variables is discussed below.

Jet-level Variables

The jet kinematics are represented by variables defined using the 4-momentum of the jet, as detailed in Table 6.1. The momentum magnitude and the energy define the kinematic makeup of the jet, while θ and ϕ of the jet define its angular position. The multiplicities of charged and neutral particles represent the constituent split of the jet, and the jet angularity [155] represents the shape of the jet through the angular distribution of the jet constituents weighted by the normalised constituent energies. The truth label of the jet flavour is assigned by defining five binary variables, `isB`, `isC`, etc., out of which only one is set to 1.

Figure 6.1a shows that the jet 3-momentum magnitude distribution of b- and c-jets tends to be more spread out than that of s-, u-, and d-jets. This is due to the longer decay chain in c-jets than s-, u-, and d-jets, and even longer decay chains in b-jets, where more momentum can be lost through neutrinos than in s-, u-, and d-jets.

Jet Constituents Variables

All future collider detector concepts are designed to be used with a particle flow algorithm [156, 157]. Therefore, jet constituents are subdivided into five sets according to the typical particle flow candidate categories: charged hadrons, neutral hadrons, electrons and positrons ($e^{\pm}$), photons (γ), and muons ($\mu^{\pm}$). Kinematic variables are defined for each jet constituent using its 4-momentum, as listed in Table 6.2. The number of charged jet constituents and neutral jet constituents is individually limited to 25. This is enforced by truncating the input feature

Input Feature	Description
$\lvert p\rvert,\ E,\ m$	3-momentum magnitude, energy, and invariant mass of the jet
θ, ϕ	polar and azimuthal angle of the jet axis
$\mathrm{N}_{\mathrm{charged}}$	charged particle (track) multiplicity in the jet
$\mathrm{N}_{\mathrm{neutral}}$	neutral particle multiplicity in the jet
$\lambda_\beta^\kappa = \Sigma_{i\in\mathrm{jet}} z_i^\kappa R_i^\beta$	jet angularity as sum of normalized jet constituent energy (z_i) and angular distance to jet axis (R_i) for ($\kappa = 0$, $\beta = 0$), ($\kappa = 1$, $\beta = 0.5$), ($\kappa = 1$, $\beta = 1$), ($\kappa = 1$, $\beta = 2$), ($\kappa = 0$, $\beta = 2$)
`isU/D/S/C/B/G`	MC flavour assigned to the jet

Table 6.1: Description of global features associated with each jet.

array of a given jet if the charged/neutral jet constituent multiplicity exceeds 25, and conversely, the input feature array is zero-padded if the charged/neutral jet constituent multiplicity is below 25.

The five canonical track parameters, representing the helical trajectory, are defined for every charged jet constituent or track. The transverse and longitudinal impact parameters, D_0 and z_0, respectively, and the half-curvature are defined directly, while the two angular parameters, the polar angle θ_{rel} and the azimuthal angle ϕ_{rel} are defined relative to the angular position of the jet axis. The total angular distance of the track to the jet represents the spread of the charged particles within the jet. The charge and the invariant mass of the track are defined as absolute parameters, while the 3-momentum magnitude and the energy of the track are defined relative to the respective properties of the jet. The binary variables, `isKaon`, `isMuon`, and `isElectron`, represent if the particle is identified as a $K^{\pm}$, a $\pi^{\pm}$, or an $e^{\pm}$, respectively.

An important distinguishing variable for b-jet identification is the transverse impact parameter, D_0, which is higher for tracks in the bottom flavour jets as the decaying b hadrons have a significantly longer lifetime than c or the lighter s, u, and d hadrons (except for V^0s). The differentiating effect between flavours caused by this can be seen more clearly in the transverse impact parameter significance, defined as $S(D_0) = D_0/\sigma_{D_0}$, where σ_{D_0} is the uncertainty in the measurement of the transverse impact parameter. It is depicted in Figure 6.1b.

The most challenging background for s tagging is ud-jets. Two powerful distinguishing vari-

Input Feature	Description
$D_0(z_0)$	signed transverse (longitudinal) impact parameter
$D_0/\sigma_{D_0}(z_0/\sigma_{z_0})$	signed transverse (longitudinal) impact parameter significance
$\theta_{\text{rel}}(\phi_{\text{rel}})$	polar (azimuthal) angle of track with respect to the jet axis
R	angular distance of track and jet axis
C	half-curvature of the track
$m_{\text{ch.}}, q$	track invariant mass and charge
$\frac{\lvert p\rvert_{\text{ch.}}}{\lvert p\rvert_{\text{jet}}}, \ln(\lvert p\rvert_{\text{ch.}}), \ln\left(\frac{\lvert p\rvert_{\text{ch.}}}{\lvert p\rvert_{\text{jet}}}\right)$	(normalised) magnitude of track momentum and logarithms
$\frac{E_{\text{ch.}}}{E_{\text{jet}}}, \ln(E_{\text{ch.}}), \ln\left(\frac{E_{\text{ch.}}}{E_{\text{jet}}}\right)$	(normalised) track energy and logarithms
`isKaon`	if the particle is identified as a $K^{\pm}$
`isMuon`	if the particle is identified as a $\mu^{\pm}$
`isElectron`	if the particle is identified as an $e^{\pm}$
$\theta_{\text{rel}}(\phi_{\text{rel}})$	polar (azimuthal) angle of particle with respect to the jet axis
R	angular distance of neutral particle and jet axis
$\frac{\lvert p\rvert_{\text{neut.}}}{\lvert p\rvert_{\text{jet}}}, \ln(\lvert p\rvert_{\text{neut.}}), \ln\left(\frac{\lvert p\rvert_{\text{neut.}}}{\lvert p\rvert_{\text{jet}}}\right)$	(normalised) magnitude of particle momentum and logarithms
$\frac{E_{\text{neut.}}}{E_{\text{jet}}}, \ln(E_{\text{neut.}}), \ln\left(\frac{E_{\text{neut.}}}{E_{\text{jet}}}\right)$	(normalised) neutral particle energy and logarithms
`isPhoton`	if the particle is identified as a Photon

Table 6.2: Description of features associated with each jet constituent. The sets of variables are divided into charged particles (tracks) and neutral particles.

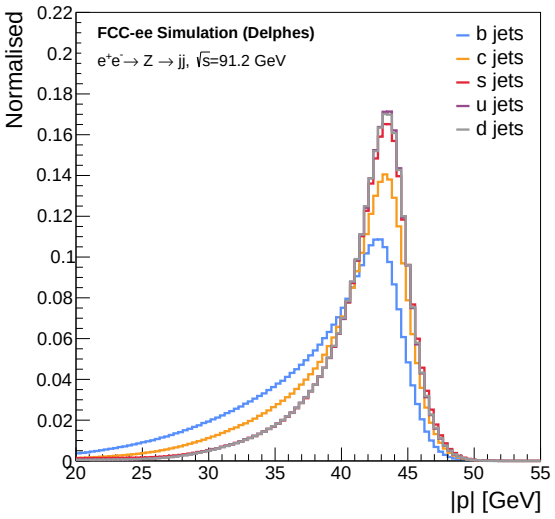

(a) Jet Momentum.

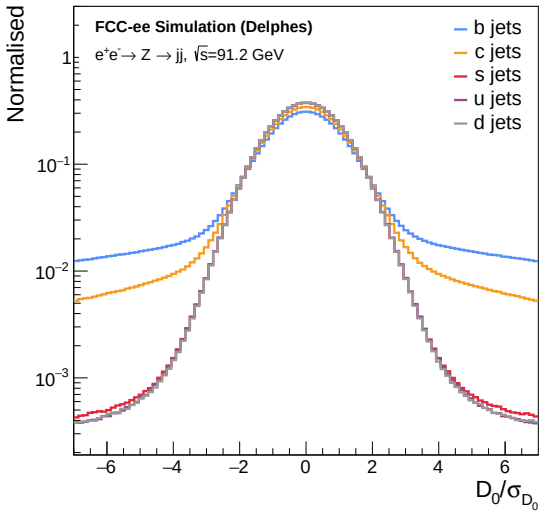

(b) Transverse impact parameter significance.

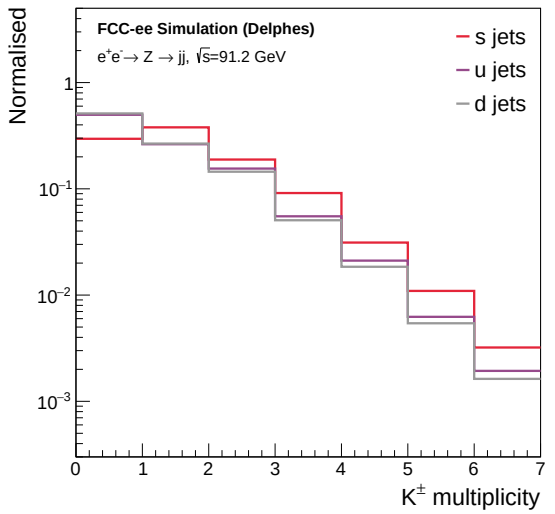

(c) Kaon multiplicities.

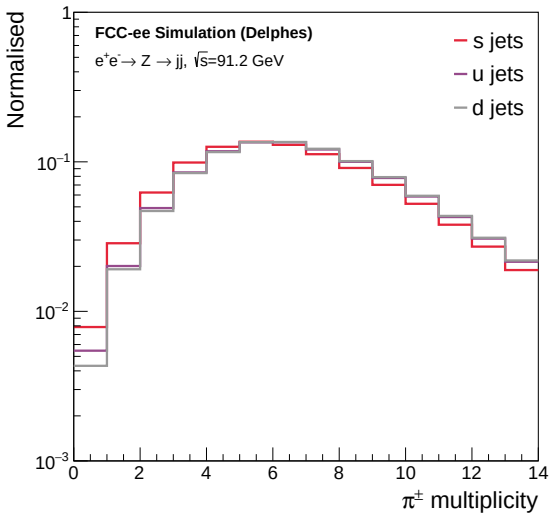

(d) Pion multiplicities.

Figure 6.1: Distinguishing features in the clustered jets of $e^+e^- \to Z \to q\bar{q}$ events at $\sqrt{s} = 91.2$ GeV, separated by flavour. Fig 6.1b shows a property of the jet constituents, while the rest show properties of the clustered jets. The IDEA detector concept was used for reconstruction.

ables tend to be the multiplicities of charged and neutral Kaons and Pions, exploiting the conservation of strangeness during hadronisation in strange jets. These can be seen in Figure 6.1c and 6.1d.

Only the angular variables and the normalised 3-momentum magnitude and energy are defined for neutral jet constituents, as they cannot be detected within the tracker. The binary variable `isPhoton` is set to 1 if the jet constituent is identified as a photon.

Reconstructed Vertex Variables

Charged tracks are first fitted to find the V^0s, and the remaining tracks are used to reconstruct SVs, as described in Section 4.4. Feature variables are defined separately for both classes of reconstructed vertices (V^0s and SVs) and are listed in Table 6.3. Up to 4 V^0s and 4 SVs are

considered per jet. The V^0 and SV input feature arrays are truncated or zero-padded, similar to charged and neutral jet constituent arrays.

The 3-momentum magnitude and the invariant mass of the reconstructed vertices represent their kinematic properties. The invariant mass of SVs is calculated by assuming every track to be a pion, while for V^0s, it is calculated by assuming the track combination that passes the constraints mentioned in Table 4.2. The χ^2 and the N_{DoF} indicate the quality of the vertex fit. The angular position relative to the jet axis are represented by θ_{rel} and ϕ_{rel}, while d_{3D} and d_{xy} represent the distance of the reconstructed vertex from the reconstructed PV. The collinearity parameter represents the deflection of the vertex compared to the PV. As the V^0s are reconstructed for predefined decays, the PDG ID is added only for the V^0s to aid in PID.

Input Feature	Description
$\lvert p\rvert,\ m$	3-momentum magnitude and invariant mass of the SV
N_{tracks}	track multiplicity of the SV
χ^2, N_{DoF}	χ^2 and number of degrees of freedom of the SV
θ_{rel}, ϕ_{rel}	polar and azimuthal angle of the SV with respect to the jet axis
$\hat{p}.\hat{r}$	collinearity of SV with respect to PV
d_{3D}, d_{xy}	3D and transverse distance of the SV from the PV

Table 6.3: Description of features associated with each reconstructed secondary vertex. Similar features, with the addition of PDG ID [20], are also defined for V^0s while comparing the performance of the tagger trained with and without V^0s.

As mentioned in Section 4.4, b-jets tend to have a higher SV multiplicity than c-, s-, u-, and d-jets. It is a dominant property in identifying b-jets and, to some extent, c-jets.

The reconstructed V^0s also help improve PID by identifying the neutral strange hadrons, K_S^0 and Λ^0, therefore, aiding in strange tagging.

6.3 Tagging Performance

The performance of `DeepJetTransformer` was evaluated on clustered jets from $Z \to q\bar{q}$ events at $\sqrt{s} = 91.2$ GeV and $Z(\to \nu\nu)H(\to q\bar{q})$ events at $\sqrt{s} = 240$ GeV. Individual and separate training were performed for each process.

Classifier

The outputs of the classifier, which are normalised by using the SoftMax function, represent the probability with which the tagging algorithm assigns a certain flavour to the jet, and are referred to as 'softmaxed classifier outputs' hereafter. These softmaxed classifier outputs for the five output nodes, S_q with $q \equiv b,\ c,\ s,\ u,\ d$, are shown in Figure 6.2. For each of the five quark flavours, binary classifiers were defined as,

$$S_{ij} = \frac{S_i}{S_i + \sum_j S_j}, \tag{6.1}$$

where i is the flavour of the signal and j are the background flavours with $j \neq i$. ROC curves were computed with the classifier S_{ij} for every combination of i and j. Only one background flavour was considered for each case. These ROC curves are shown in Figure 6.3. The efficiency increases moving towards the right, and the background efficiency, also referred to as the misidentification

efficiency or mistag rate, increases while moving from bottom to top. Hence, a trend towards the bottom-right region of the ROC curves signifies better performance.

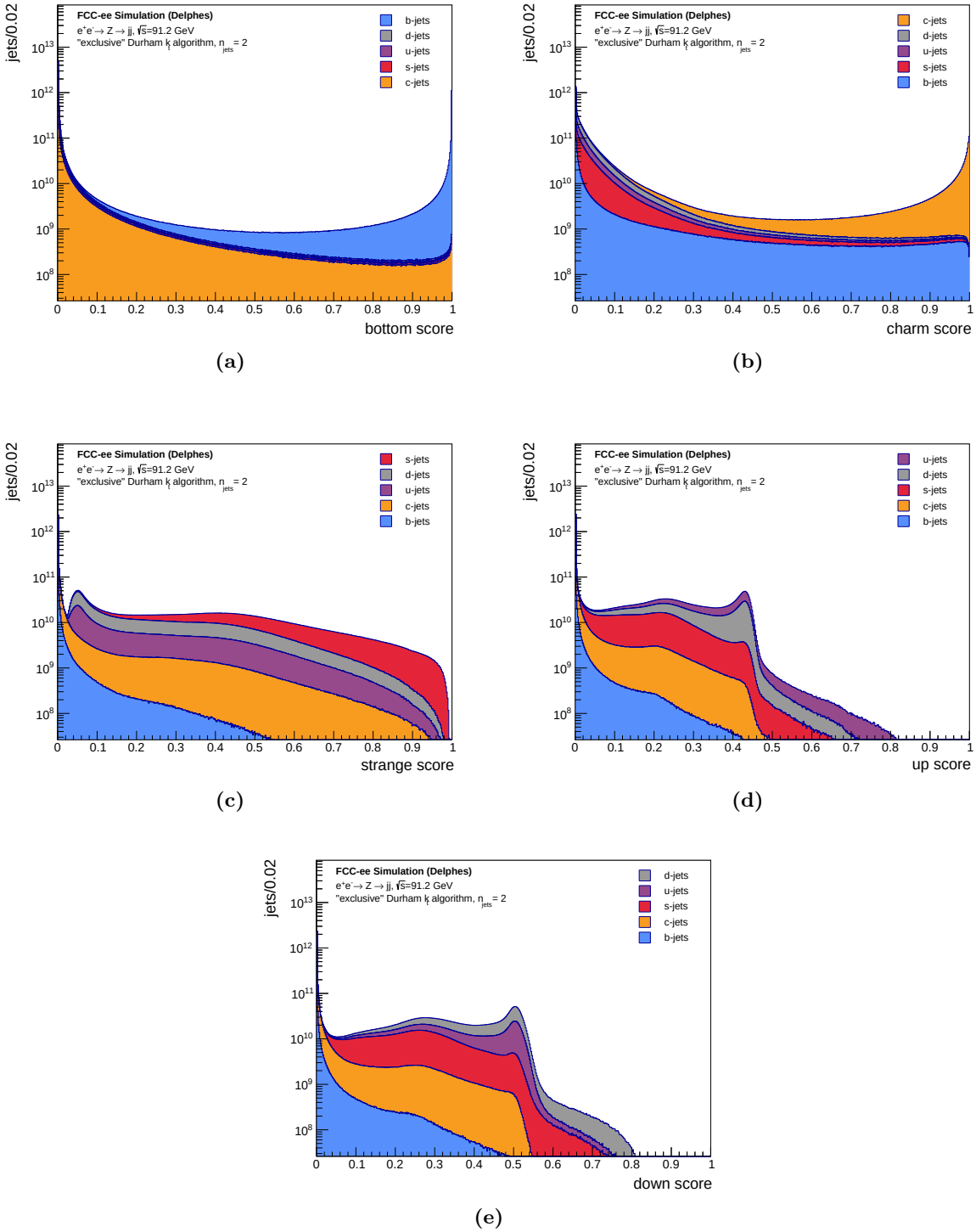

Figure 6.2: The softmaxed classifier outputs (S_i) of the five output nodes of `DeepJetTransformer` trained with clustered jets of $e^+e^- \to Z \to q\bar{q}$ events at $\sqrt{s} = 91.2$ GeV. The contributions of different MC flavours have been displayed.

6.3.1 Performance at the Z Resonance

The emphasis of the performance evaluation in the following will be placed on the Z resonance. The solid lines in Figure 6.3 depict the tagging performance at the Z resonance.

b tagging

Figure 6.3a shows an excellent b-jet tagging performance with the discrimination between b-jets and the lighter s-, u-, and d-jets being the strongest, owing to the presence of reconstructed SVs and displaced tracks in b-jets. The dominant background in b tagging arises from c-jets due to the similarity of b- and c-jets with a single reconstructed SV. It can also be seen in Figure 6.2a that the softmaxed classifier output for the b-jet flavour node, or the bottom score, of the b-jets tend to be high, with c-jets as the dominant background with higher bottom scores. The lighter s-, u-, and d-jets are mainly clustered in the first two bins.

A signal efficiency, ϵ_{sig}, of 85.7% can be achieved at the background efficiency, ϵ_{bkg}, of 1% while discriminating b-jets against c-jets, while against the lighter s-, u-, and d-jets, $\epsilon_{\text{sig}} \approx 99\%$ can be reached at $\epsilon_{\text{bkg}} = 1\%$.

c tagging

The discrimination of c-jets against the lighter s-, u-, and d-jets displays similar performance, as shown in Figure 6.3b, with the discrimination of c and s-jets being slightly worse. The c-jet discrimination against b-jets shows a better performance as compared to against the lighter quark jet flavours in the high efficiency regime over a c tagging efficiency of 80%, at which point discrimination against b-jets shows worse performance. Similar performance turnovers are also seen for other tagging algorithms, such as `ParticleNetIDEA` [158, 159]. The dominant b-jet background and the sub-dominant s-jet background with low to mid charm scores can also be observed in Figure 6.2b. This is primarily due to no SVs being reconstructed in a significant fraction of c-jets, leaving few discriminating variables between the two flavours.

At $\epsilon_{\text{bkg}} = 1\%$ against the background of b-jets, a charm signal efficiency, ϵ_{sig} of 68.4% can be reached and $\epsilon_{\text{sig}} = 76.3\%$ can be achieved in the discrimination against s-jets at $\epsilon_{\text{bkg}} = 1\%$.

s tagging

The discrimination of s-jets shows the best performance against b-jets, as displayed in Figure 6.3c. The c-jets are considerably more difficult to discriminate against, with the c-jet background coming from jets where the charm hadron decays into a strange hadron, but only the strange hadron (V^0) can be reconstructed, or jets where the strange hadron carries excess momentum. As mentioned before, u- and d-jets are the most challenging backgrounds. The high strange scores from the c-, u-, and d-jets can also be seen in Figure 6.2c. Some discrimination against the light u- and d-jets can still be achieved by putting the threshold at high values of the strange score, owing to the $K^{\pm}/\pi^{\pm}$ separation and the V^0 reconstruction.

Against the background of c-jets at $\epsilon_{\text{bkg}} = 1\%$, a strange signal efficiency, $\epsilon_{\text{sig}} = 36.1\%$ can be achieved. However, against the more challenging d-jet background only a moderate discrimination can be observed with $\epsilon_{\text{sig}} = 10\%$ at $\epsilon_{\text{bkg}} = 1\%$.

u and d tagging

Figures 6.3d and 6.3e show that the separation of u- and d-jets is the most challenging. Figures 6.2d and 6.2e show almost overlapping distributions of the softmaxed classifier outputs for u-

and d-jets. With u-jets as the signal, a tagging efficiency $\epsilon^{u}_{\text{sig}} = 15\%$ at the background efficiency $\epsilon^{u}_{\text{bkg}} = 10\%$, which is a better performance than a random classifier, albeit not significantly. The

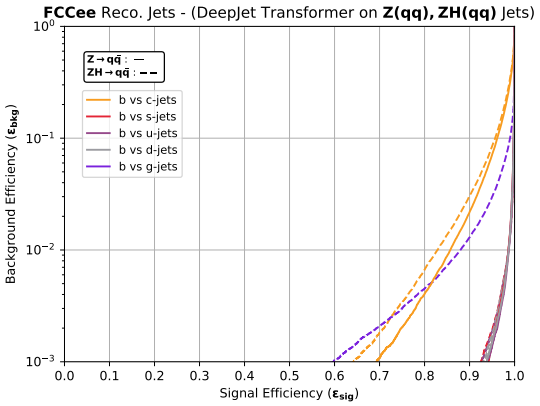

(a) bottom tagging

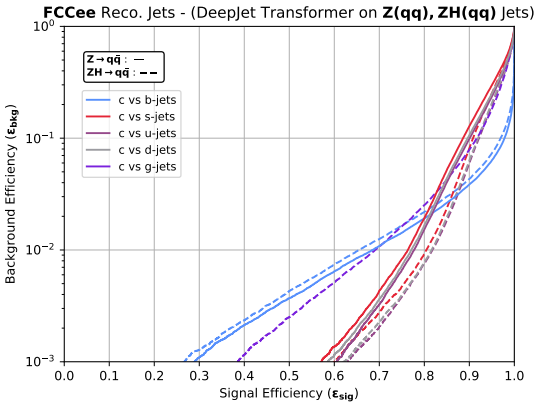

(b) charm tagging

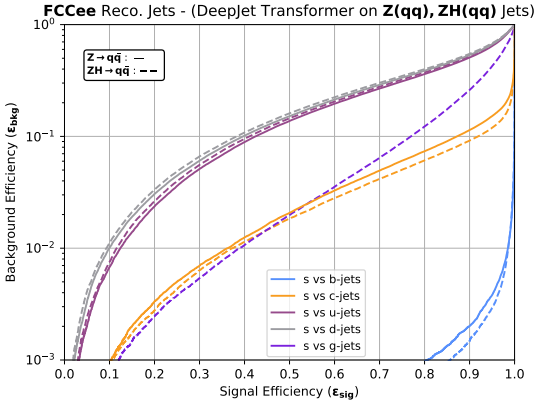

(c) strange tagging

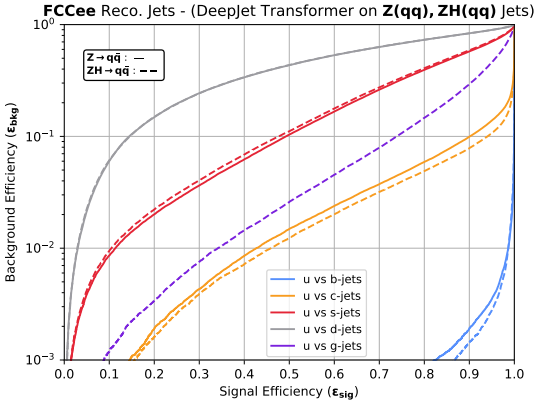

(d) up tagging

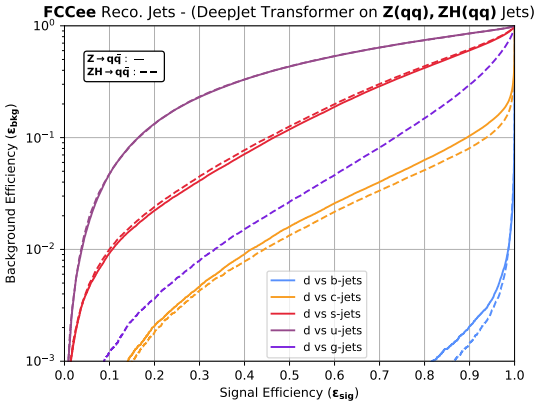

(e) down tagging

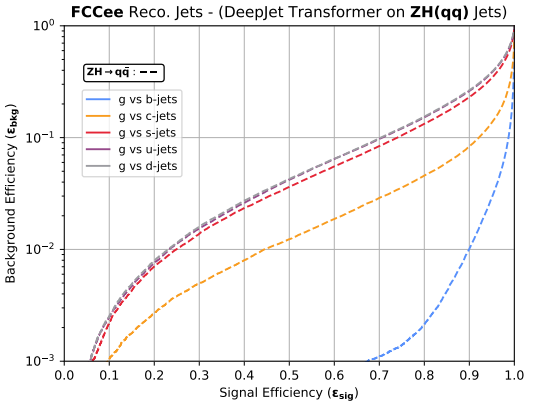

(f) gluon tagging

Figure 6.3: ROC curves for each S_{ij} combination, as defined in Eq. 6.1, where i is the signal parton flavour and j is the background flavour. The solid lines correspond to the classification of jets at the Z resonance at $\sqrt{s} = 91.2$ GeV, while the dashed lines correspond to the classification of jets from $Z(\to \nu\nu)H(\to q\bar{q})$ events at $\sqrt{s} = 240$ GeV. The tagger was trained separately for each process. No quark-gluon discrimination results are presented for jets from $Z \to q\bar{q}$ events as the Z boson does not decay into gluons.

discrimination is likely related to a mapping to the initiating parton's charge, such as the jet charge [160, 161], the effect of which is diluted by the presence of antiquarks.

6.3.2 Performance with the Higgs Process

The classification performance evaluation with $H \to q\bar{q}$ events is primarily done as a comparison to other jet flavour taggers developed for future colliders, like `ParticleNetIDEA` [158, 159]. The dashed lines in Figure 6.3 depict the tagging performance with the Higgs process. Gluon tagging is only presented for the Higgs process, as the Z boson does not decay into gluons.

No clear and obvious trends can be observed while comparing to the performance at the Z resonance. The b tagging performance is slightly worse, notably against the c-jet background. The highest performance improvement compared to the Z resonance, in the ROC area under the curve metric, is seen while discriminating c-jets against the lighter s-, u-, and d-jets. In most other cases, the classification performance is slightly worse.

The best quark-gluon discrimination can be observed against b-jets, as shown in Figure 6.3f. The multiplicity and the momentum distribution of the jet constituents play some role in this discrimination, but the dominating discriminating variable is the presence or absence of reconstructed SVs. The discrimination against c-jets is worse compared to b-jets, as no SVs can be reconstructed for a significant fraction of c-jets. The worst quark-gluon discrimination is seen against the lighter s-, u-, and d-jets because of their similar jet compositions.

6.3.3 Tagging Efficiency

The tagging efficiency of `DeepJetTransformer` was evaluated for three cases: b vs c tagging, c vs s tagging, s vs ud tagging. Figure 6.4 shows the efficiency of `DeepJetTransformer` over the entire jet momentum range and the jet axis polar angle (θ) range for all three cases for two working points. The efficiency for b vs c tagging and c vs s tagging is mostly uniform, showing a good performance for all jet momenta. Similarly, the performance is largely uniform over the θ range for all three cases, degrading at the extremes due to jet constituents being lost by fiducial cuts.

However, the s vs ud tagging efficiency displays a peculiar distribution over the momentum range of interest, as shown in Figure 6.4e. This was found to be dependent on the two most distinguishing features for identifying s-jets: $K^{\pm}/\pi^{\pm}$ discrimination and V^0 reconstruction. The *low-momentum* ($24 < |p| < 35\,\mathrm{GeV}$) strange jets, on average, have lower $K^{\pm}$ multiplicities, which leads to a reduced tagging efficiency. The *very-low-momentum* ($|p| < 24\,\mathrm{GeV}$) strange jets have a significantly low total charged-particle multiplicity, making V^0 reconstruction crucial. The majority of such jets have a single reconstructed V^0, helping identify the s-jets. On the other hand, the *low-momentum* strange jets tend to have multiple V^0s, splitting the already low jet momentum among these V^0s and other hadrons. This is expected to make the strange jet identification more ambiguous. Hence, the s tagging efficiency rises at very low momenta.

A similar but exaggerated trend in the distribution is seen for the looser working point of 10% mistag rate for jets with momentum values below 25 GeV. The efficiency is observed to be stable in momentum above this value. As stated above, some of this increase in s tagging efficiency can be attributed to the presence of a reconstructed V^0 in jets with low particle multiplicities. Another important aspect to note is that only a small fraction of jets ($< 1\%$) with such very low momenta are present in Z boson decays. This means that these low-momentum jets will not have a large contribution to the training of the neural network or the working point determination, which will both be dominated by the bulk of the momentum distribution. It must also be stated

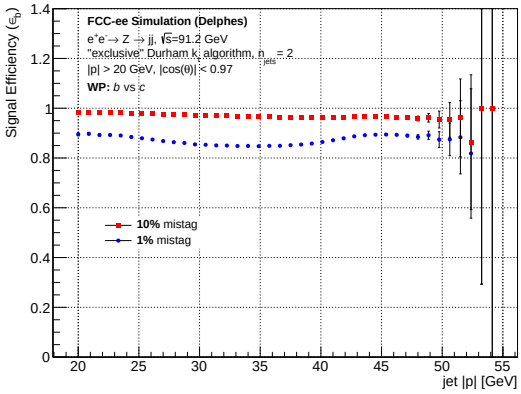

(a) b vs c.

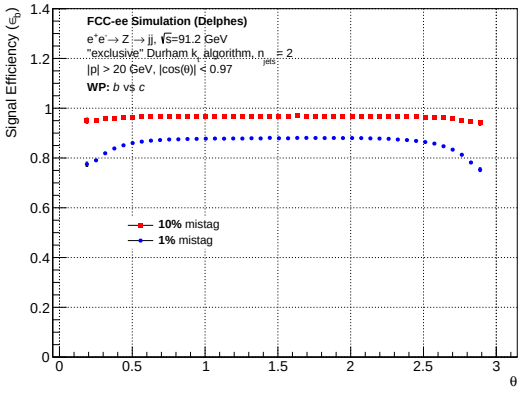

(b) b vs c.

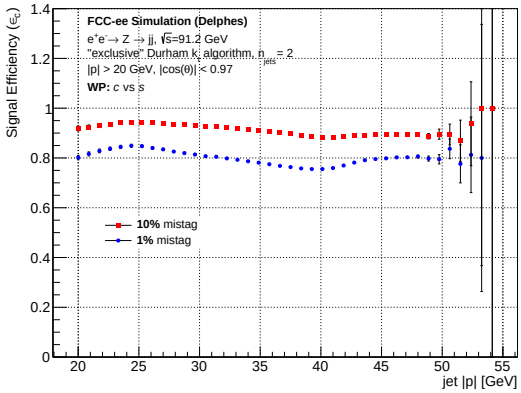

(c) c vs s.

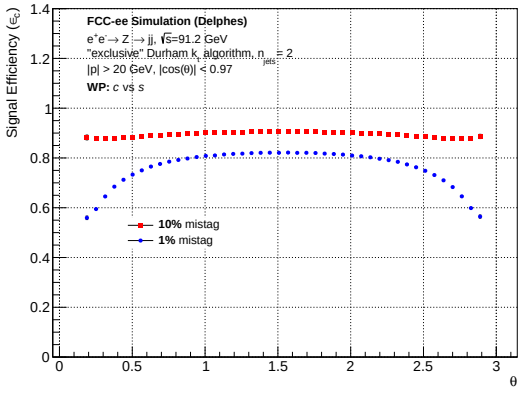

(d) c vs s.

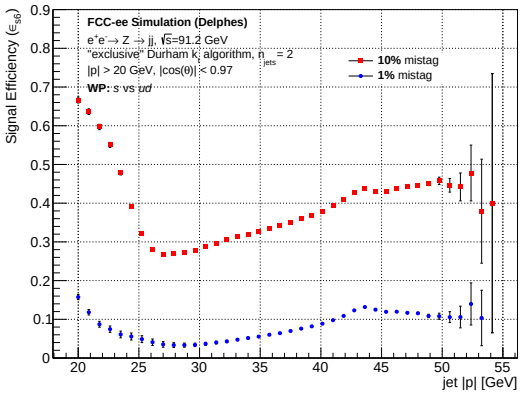

(e) s vs ud.

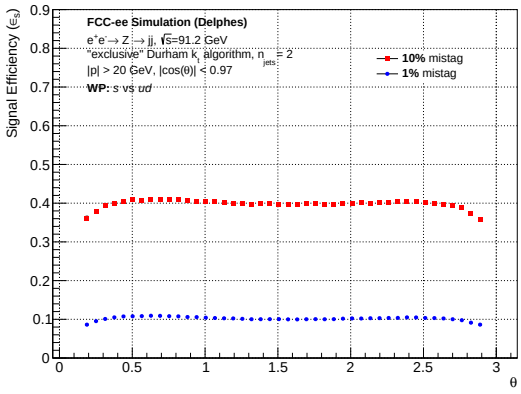

(f) s vs ud.

Figure 6.4: The jet flavour tagging efficiency over the range of jet momentum and the jet axis polar angle for jets of $e^+e^- \to Z \to q\bar{q}$ events at $\sqrt{s} = 91.2$ GeV. Three cases at 1% and 10% background efficiencies are shown: b vs c tagging, c vs s tagging, s vs ud tagging.

that the ud-jet background efficiency for the working point of 10% mistag rate also increases to 40% for momenta less than 25 GeV. This fact implies that this part of the jet momentum phase space is likely not optimally examined by the neural network. A potential method to improve would be to use training weights flattened over the jet momentum and train on much larger samples with this part of the momentum distribution sufficiently populated. But since these

jets contribute to a very small fraction of the total Z boson decays, the improvement in analyses requiring strange tagging would likely not be significant unless the physics case is specific.

6.3.4 Qualitative Comparison with Other Taggers

`DeepJetTransformer` was trained and evaluated with $H \to q\bar{q}$ events for comparison with other jet flavour taggers, especially the ones developed for future colliders, like `ParticleNetIDEA`. A quantitative comparison is not presented as different tagging algorithms utilised different event samples and input features; however, `DeepJetTransformer` displays similar performance trends as `ParticleNetIDEA`.

`ParticleNetIDEA` exhibits a better strange tagging performance against the background of ud-jets compared to `DeepJetTransformer`. The better performance of `ParticleNetIDEA` can be credited to the PID techniques employed, such as ionisation cluster counting and time-of-flight, as opposed to the conservative PID estimates used by `DeepJetTransformer`. The performance of `DeepJetTransformer` in bottom-gluon discrimination surpasses that of `ParticleNetIDEA`, particularly below the signal efficiencies of 90%. `DeepJetTransformer` shows a better rejection of b-jet background for all signal quark jet flavours, owing to the inclusion of SVs.

`DeepJetTransformer` training can be performed within 2 hours, reaching convergence after roughly 50 epochs on an NVIDIA Tesla V100s GPU, due to the efficient transformer blocks being the central components of its architecture. It has approximately 10^6 parameters and its computational complexity is around 19.7 MFLOPs. With its fast training cycles, `DeepJetTransformer` is an ideal choice to study the impact of detector design, which is constantly evolving for future colliders, on jet flavour tagging.

6.3.5 Impact of Quality of Particle Identification

To study the impact of the quality of particle identification on the performance of jet flavour tagging, several $K^{\pm}$ classification scenarios were considered. Each scenario corresponded to a particular $K^{\pm}$ identification efficiency, i.e. the probability with which a kaon is correctly identified, and a $\pi^{\pm}$ misidentification efficiency, i.e. the probability with which a pion is incorrectly identified as a kaon. The limiting cases with $K^{\pm}$ identification efficiencies of 0% and 100%, both with a $\pi^{\pm}$ misidentification efficiency of 0% and henceforth referred to as the 'no $K^{\pm}$ID' and the 'perfect $K^{\pm}$ID' scenarios, are also considered. Table 6.1 shows all the considered scenarios.

$K^{\pm}$ ID efficiency	0%	60%	90%	95%	100%
$\pi^{\pm}$ misID efficiency	0%	10%	10%	10%	0%

Table 6.4: Considered scenarios for $K^{\pm}$ and $\pi^{\pm}$ particle identification performance.

The impact from the addition of the PID variables is assessed in reference to the 'no $K^{\pm}$ID' scenario in this section. It must be noted that the 'no $K^{\pm}$ID' scenario is not the baseline. Major performance improvement was seen in the discrimination of s-jets against the light ud-jets, as shown in Figure 6.5. A strange tagging efficiency, ϵ_{sig}, of 31.6% was achieved in the 'no $K^{\pm}$ID' scenario at the background efficiency, ϵ_{bkg}, of 10%. Improvements in ϵ_{sig} of 11.4% ,25.9%, and 32.9% with respect to the 'no $K^{\pm}$ID' scenario were observed at the same $\epsilon_{\text{bkg}} = 10\%$, as the $K^{\pm}$ID efficiency was increased to 60% 90%, and 95%, respectively. The largest performance improvement with respect to the 'no $K^{\pm}$ID' scenario of 82.9% in the ϵ_{sig} was seen with the 'perfect $K^{\pm}$ID' scenario. The gain in efficiency is significant even compared to the $K^{\pm}$ID efficiency of 95%, where the $\pi^{\pm}$ misidentification efficiency is 10%, indicating that a reduction

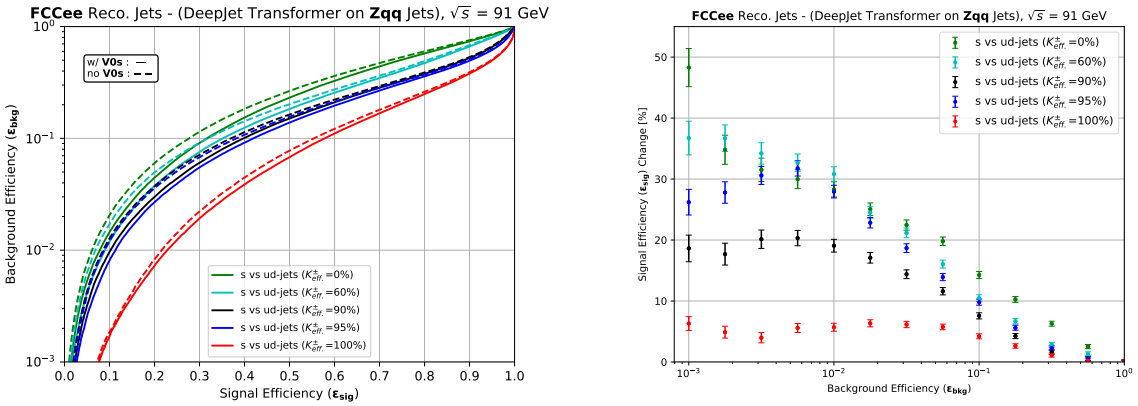

(a) ROC curves **(b)** Percent change in signal efficiency

Figure 6.5: The dependence of strange jet tagging performance on the inclusion of V^0s and charged Kaon identification scenarios. (a) ROC curves for s vs ud tagging at the Z resonance at $\sqrt{s} = 91.2$ GeV. Solid lines represent results with the inclusion of V^0s, while dashed lines show the results without them. (b) Percent change in signal efficiency (ϵ_{sig}) with the inclusion of V^0s for s vs ud tagging for each of the $K^{\pm}$ID scenarios listed in Table 6.4. The axes are swapped with respect to Figure 6.5a to present the percent change in signal efficiency (ϵ_{sig}) as a function of 12 fixed background efficiencies (ϵ_{bkg}).

of this misidentification of pions as kaons is crucial to improve the strange tagging performance. This is due to the high $\pi^{\pm}$ multiplicity in s-jets.

An improvement in the charm tagging efficiency of 1.8% against ud-jets at a $\epsilon_{\text{bkg}} = 10\%$ was observed moving to the 'perfect $K^{\pm}$ID' scenario, as compared to the 'no $K^{\pm}$ID' scenario with a c tagging efficiency of 89.3%. A 12.5% performance improvement in the ϵ_{sig} from 13.6% to 15.3% was noted at a $\epsilon_{\text{bkg}} = 10\%$, while discriminating u-jets against d-jets. The performance improvements in other cases were inappreciable.

6.3.6 Impact of Neutral Kaon reconstruction

An excess of V^0s, reconstructed K^0_S and Λ^0, carrying a large fraction of the jet momenta, is also a distinguishing feature of strange jets. Figure 6.5b shows the percentage improvement in the strange tagging efficiency against ud-jets for the PID scenarios listed in Table 6.4. A signal efficiency improvement of 14.3% was observed for the 'no $K^{\pm}$ID' scenario at a background efficiency of 10%, as opposed to a 4.2% improvement for the 'perfect $K^{\pm}$ID' scenario. This trend proves the importance of reconstructed V^0s in the identification of strange jets, particularly when the $K^{\pm}$ multiplicities are low or the $K^{\pm}/\pi^{\pm}$ discrimination is inferior. Insignificant performance gains were observed for all other classifications.

6.3.7 Importance of Feature Classes and Individual Variables

The Permutation Feature Importance method [162, 163] was employed to estimate the impact of a particular variable class, like charged particles, on the classifier performance. The values of the variables under a class were randomly permuted among all jets in the evaluation dataset, while the variables from other classes were kept unchanged. Thus, the contribution of the permuted variable class to the performance of the classifier is interrupted, and the change in the performance of the classifier, achieved in this manner, gives an estimate of the importance of the given variable class in the overall performance of the classifier.

The performance change from variable class permutation was studied by evaluating `DeepJet-Transformer` in three classification scenarios: b- vs c-jets, c- vs s-jets, and s- vs ud-jets. The absolute change in the efficiency at two background efficiencies, $\epsilon_{bkg} = 10\%$ and $\epsilon_{bkg} = 0.1\%$, for five variable classes is presented in Table 6.5.

Variable Class		Jet-level	Charged	Neutral	SV	V^0
$\epsilon_{bkg} = 10\%$	b vs c	2.4%	62.4%	2.2%	13.9%	0.1%
	c vs s	1.2%	65.7%	2.9%	29.6%	0.2%
	s vs ud	7.6%	59.4%	21.8%	5.0%	16.4%
$\epsilon_{bkg} = 0.1\%$	b vs c	6.6%	97.0%	8.0%	89.9%	0.6%
	c vs s	9.3%	96.1%	11.0%	77.9%	0.2%
	s vs ud	35.9%	91.0%	57.3%	7.4%	43.8%

Table 6.5: Performance decrease in signal efficiency (ϵ_{sig}) after permutation of variable classes defined in Section 6.2 for fixed background efficiencies (ϵ_{bkg}) of 10% and 0.1%.

At the background efficiency of 10%, the variables from the charged jet constituents class, shown in Table 6.2, were found to be the most important. This is due to the fact that the charged particles are the most numerous reconstructed objects in the jets, as well as owing to the inclusion of track parameters. The variables from the reconstructed SV class, shown in Table 6.3, were observed to largely influence the c- vs s-jet discrimination and weakly impact the b- vs c-jet performance. However, this class of variables were almost insensitive in the discrimination of s-jets from ud-jets, as most of these jets have no reconstructed vertices. Instead, the variables from the neutral jet constituent and reconstructed V^0 classes were solely important for s- vs ud-jet discrimination, justifying the inclusion of V^0s for strange jet identification through the conservation of strangeness.

Similar trends were seen at the background efficiency of 0.1%, i.e. in the high-purity regime. The SV variable class becomes crucially important for the discrimination of b- and c-jets, as well as c- and s-jets, showing that the presence and properties of SVs, particularly their multiplicity, are important criteria to identify heavy quark flavour jets. The impact of V^0 variable class in the discrimination of s- and ud-jets also rises in the high purity regime.

The relative importance of the individual variables, rather than entire variable classes, was similarly studied, where a particular variable was randomly permuted among all jets in the evaluation dataset. The performance change at the background efficiencies of 10% and 0.1% is presented for a set of six most impactful variables in Table 6.6.

Variable		$\ln(E_{\text{ch.}})$	$K^{\pm}$ID	m^{SV}	$\lvert p\rvert^{V^0}$	z_0	D_0/σ_{D_0}
$\epsilon_{bkg} = 10\%$	b vs c	3.5%	0.2%	3.0%	0.1%	7.8%	11.6%
	c vs s	23.8%	0.5%	0.3%	0.2%	20.9%	39.1%
	s vs ud	12.8%	38.8%	0.0%	9.2%	23.3%	26.7%
$\epsilon_{bkg} = 0.1\%$	b vs c	13.8%	0.9%	67.2%	0.8%	34.1%	45.0%
	c vs s	57.6%	4.8%	7.0%	0.3%	56.2%	79.5%
	s vs ud	35.0%	59.0%	0.4%	34.7%	60.5%	80.1%

Table 6.6: Performance decrease in signal efficiency (ϵ_{sig}) after permutation of individual variables defined in Section 6.2 for fixed background efficiencies (ϵ_{bkg}) of 10% and 0.1%. A set of seven variables, chosen among the most impactful, is presented here.

6.3.8 Discussion on Flavour Definition

Assigning the flavour label to a reconstructed jet can be a challenging and ambiguous task. A flavour definition can assign a different flavour to an MC-generated jet than the original quark flavour, depending on which properties of the jet are prioritised by the flavour definition. Jet flavour definitions are a continuously evolving discipline, and various definitions have been used at past and current collider experiments. The performance of `DeepJetTransformer` with two such definitions was studied for Z boson decays to estimate the impact of changing flavour definitions.

The Z boson definition, which has been used as the baseline in this thesis and introduced in Section 4.3, assigns the flavour of the quark to which the Z boson decays as the flavour of the jet, thus ignoring the hadronisation and fragmentation of the quark. The Ghost Matching algorithm [164], used at CMS, takes the hadronisation and fragmentation effects into account by clustering hadrons and partons from the MC history of the jet. The Ghost Matching algorithm then assigns the jet flavour by finding these hadrons and partons, which are clustered with the same jet clustering algorithm as the reconstructed jet, after scaling their momenta to a minuscule quantity.

The discrimination of s-jets against the background of ud-jets shows the largest performance difference between the two definitions. The strange tagging efficiency with the Ghost Matching definition was observed to be 11.8% higher than with the Z boson definition at the background efficiency of 10%. Such significant changes in performance make it essential to account for the used flavour definitions while comparing different flavour tagging algorithms.

6.4 Conclusion

Following in the success of deep learning techniques in analysing complex jet structures to extract subtle definitive features, jet flavour identification with `DeepJetTransformer` displays a comparable performance with other state-of-the-art jet flavour taggers developed for future e^+e^- colliders while allowing for short training times, making it an excellent choice to study the influence of detector designs on jet flavour tagging performance. It is essential to study the effects of detector design choices on the potential physics studies, especially for future collider projects, where the detector concepts are constantly evolving. It is worth emphasising that, despite being tailored to FCC-ee and the IDEA detector, the conclusions are broadly applicable, and `DeepJetTransformer` can be employed in other collider projects with suitable modifications for jet clustering algorithms, energy regimes, and different detector configurations, such as the applied PID strategies.

In addition to an excellent performance of bottom and charm jet classification, the notable strange tagging performance of `DeepJetTransformer`, combined with the high-statistics Z resonance event samples at the FCC-ee, enables the isolation of very pure samples of the $Z \to s\bar{s}$ process. Such pure samples enable precise measurements, such as the coupling of the strange quark to the Z boson and the strange quark asymmetry parameters.

These results confirm the importance and necessity of particle identification techniques, especially for strange quark studies, as was also noted by some previous studies [108, 142, 158]. Thus, strange tagging puts stringent requirements on the PID strategies employed at the FCC-ee detectors. Similarly, the significance of reconstructed vertices, SVs and V^0s, on the tagging performance demands an exquisite resolution from the vertex detectors. Particularly in the case of strange tagging, while aiming for high purity, this complements the PID techniques and improves the achievable performance.

In the following chapter, `DeepJetTransformer` is utilised to isolate a very pure sample of the $Z \to s\bar{s}$ process from the exclusive decays of the Z boson at the FCC-ee.

Part III

Exploring the Strange Quark at the Z Resonance

7 Isolating $Z \to s\bar{s}$ Events from Exclusive Hadronic Decays of the Z Boson

Strange jet tagging at future colliders has been investigated as a probe to enable precision measurements in the Higgs sector [108, 165], and the impact of using dN/dx and time-of-flight on strange jet tagging performance for jets originating from Higgs boson decay was explored using a graph neural network [158]. Here, `DeepJetTransformer` is employed to isolate $Z \to s\bar{s}$ events from the exclusive hadronic decays of the Z boson in the FCC-ee environment.

The decay of the Z boson to the five quark flavours is relatively uniform, unlike the decays of the Higgs boson, where none of the decay channels to $q\bar{q}$ pairs are suppressed. Therefore, while tagging a particular jet flavour, every other flavour has to be discriminated against. Isolating $Z \to s\bar{s}$ events from the exclusive hadronic decays of the Z boson forms an especially challenging case in strange jet tagging as it requires the elimination of both the heavy-quark (b and c) jets and the light-quark (u and d) jets. The dominant discriminating variables against the heavy-quark jets are the displaced tracks and the reconstructed SVs, while it is the presence of a high-momentum strange hadron against the light-quark jets. It makes isolating $Z \to s\bar{s}$ events from the exclusive hadronic decays of the Z boson an ideal metric to assess the performance of `DeepJetTransformer` in the FCC-ee environment. It simultaneously allows a unique opportunity to access a hitherto scarcely studied channel.

This work has been presented in an EPJ C publication. [2].

7.1 Event and Jet Selection

The $e^+e^- \to Z \to q\bar{q}$ samples, where $q \equiv b, c, s, u, d$, described and referred to as the 'tagging samples' in Section 4.1, are used for this study. These are the same samples used to evaluate the performance of `DeepJetTransformer` in Section 6.3. Further backgrounds are not considered but are expected to be well under one per cent of the total expected yield around the Z boson resonance, as shown in Section 8.1. An event is selected only if exactly two jets can be reconstructed from its final reconstructed particles. Events with jets outside the fiducial boundaries of the detector are excluded. An event is selected if both of its jets have a 3-momentum magnitude ($|\vec{p}|$) greater than 20 GeV and the polar angle (θ) of their jet axes within 14 and 166 degrees, corresponding to $\cos(\theta) < 0.97$. The two jets of every event are required to have the same MC flavour, as defined in Section 4.3. All jets from $Z \to q\bar{q}$ events are independently evaluated using `DeepJetTransformer`.

Table 7.1 shows that events with jets of all flavours have very similar efficiencies for the thresholds imposed by the fiducial boundaries of the detector. The events of all flavours are mostly unimpacted by the momentum magnitude threshold. However, the events with heavier jets show slightly lower efficiencies compared to the events with light-quark jets due to undetected neutrinos generated in hadronic decays in the heavier jets, leading to lower reconstructed jet momenta.

	Efficiency [%]				
	$Z \to b\bar{b}$	$Z \to c\bar{c}$	$Z \to s\bar{s}$	$Z \to u\bar{u}$	$Z \to d\bar{d}$
jet $\lvert\vec{p}\rvert$	97.31	98.43	97.52	99.03	98.94
jet axis $\cos(\theta)$	95.99	96.08	96.15	96.11	96.13

Table 7.1: The efficiencies to select $Z \to q\bar{q}$ events for the two selection variables imposing fiducial boundary limits on the quark jets.

7.2 Performance

Discriminants are defined using the softmaxed classifier outputs from `DeepJetTransformer` to sequentially remove the heavy-quark flavour background (b- and c-jets) and the light-quark flavour background (u- and d-jets). The Z boson invariant mass is reconstructed from the tagged jets at different working points to test the purity of the sample after strange jet tagging.

7.2.1 Discriminants

The s-jets are first tagged to be discriminated from b- and c-jets by defining the discriminant, as in Eq. 6.1, with s-jets as signal and b- and c-jets as background:

$$S_{s \text{ vs. } bc} = \frac{S_s}{S_s + S_b + S_c}. \tag{7.1}$$

The distribution of this discriminant, marking the contribution of all five flavours, is shown in Figure 7.1a. The ROC curve was computed for this discriminant and is shown in Figure 7.1b. The signal efficiency is nearly 100% at the mistag rate of 10%; however, it goes down to around 55% and 18% for mistag rates of 1% and 0.1%, respectively. Tagging performed by applying a threshold on this discriminant is hereafter referred to as 'anti-b/c' tagging.

For the jets that pass the threshold on this discriminant, another discriminant is defined to

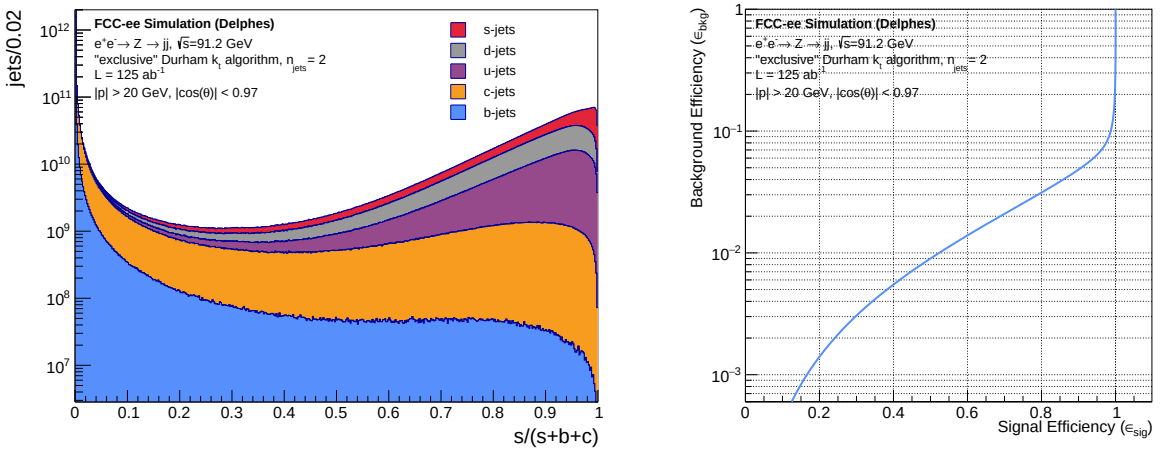

(a) **(b)**

Figure 7.1: The discriminant defined to perform the anti-b/c tag and its performance. a) The distribution of the anti-b/c tag discriminant defined in Equation 7.1 with contributions from jets of all flavours marked. d) The ROC curve showing the performance of the anti-b/c tag with s-jets as signal and the jets of the other four flavours as background.

distinguish s-jets from u- and d-jets through the same method:

$$S_{s \text{ vs. } ud} = \frac{S_s}{S_s + S_u + S_d}. \tag{7.2}$$

$S_{s \text{ vs. } ud}$ is calculated separately for the jets passing the anti-b/c threshold corresponding to three different mistag rates. Tagging performed by applying a threshold on the $S_{s \text{ vs. } ud}$ discriminant is hereafter referred to as 'anti-u/d' tagging. The chosen anti-b/c mistag rates are 10%, 1%, and 0.1%, and the distributions of the anti-u/d discriminants corresponding to these three mistag rates are shown in Figure 7.2. The ROC curves for all three cases were calculated and are shown in Figure 7.2d. Figure 7.2a shows that the scenario with 10% mistag rate on the anti-b/c tag consists of a considerable b- and c-jet background, while this background is significantly reduced for the scenario with 1% mistag rate, as seen in Figure 7.2b. The scenario with 0.1% mistag rate, presented in Figure 7.2c, shows that the few c-jets which pass the anti-b/c tag have high anti-u/d tag scores, as they are seen similar to s-jets by the jet flavour tagger.

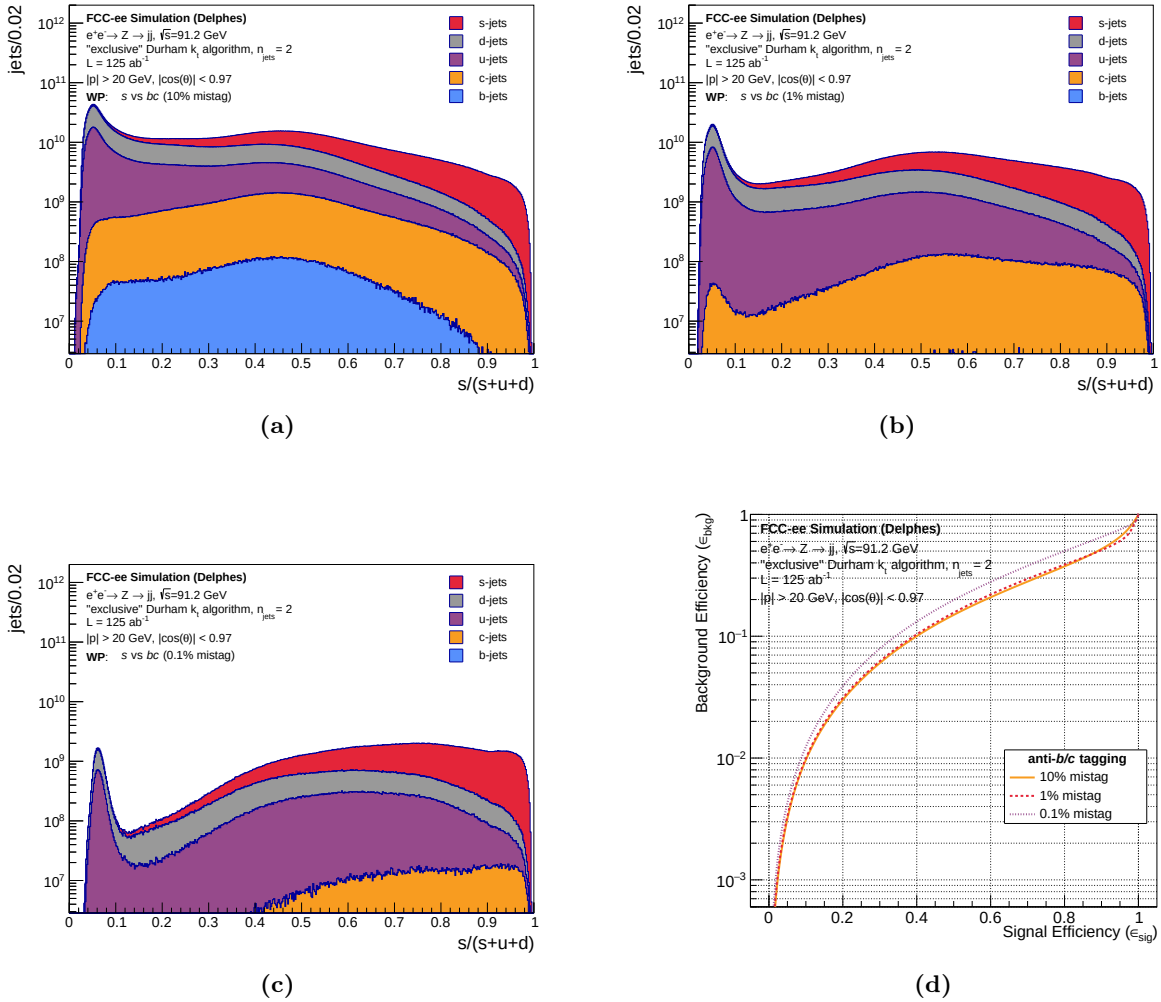

Figure 7.2: The discriminants defined to perform the anti-u/d tag for different anti-b/c mistag rates and their performances. a-c) The distribution of the anti-u/d tag discriminants defined in Equation 7.2 for anti-b/c mistag rates of 10%, 1%, and 0.1%, respectively, with contributions from jets of all flavours marked. b) The ROC curves showing the performance of the three previously defined anti-u/d tagging discriminants with s-jets as signal and the jets of the other four flavours as background.

The ROC curves presented in Figure 7.2d show that the signal efficiency drops from $\sim 40\%$ to $\sim 34\%$ at an anti-u/d mistag rate of 10% as the anti-b/c mistag rate is changed from 10% or 1% to 0.1%. This is due to the fact that the anti-b/c tagged sample at the mistag rate of 0.1% consists mainly of only the signal s-jets and the background u- and d-jets, the discrimination against which is the most difficult.

7.2.2 Working Points

As shown in Table 7.2, the working points are defined for four different sets of mistag rates. Working Point 1 (WP1) corresponds to a mistag rate of 10% while tagging s-jets versus the background of b- and c-jets and a mistag rate of 10% while tagging s-jets versus the background of u- and d-jets. Working Point 2 (WP2) corresponds to a stricter mistag rate of 1% while tagging s-jets versus the background of b- and c-jets, keeping the mistag rate the same as WP1 while tagging s-jets versus the background of u- and d-jets. Both mistag rates are 1% for Working Point 3 (WP3). Working Point 4 (WP4) is the tightest scenario, with both mistag rates being 0.1%.

WP1 is expected to have the lowest signal purity of the four chosen working points, and the signal purity is estimated to improve with the tighter working points. However, the number of signal events is also expected to decrease with higher purity as the tagging efficiency is lower at the tighter working points. It is evident from Figures 7.1b and 7.2d.

		Mistag Rate [%]	**Efficiency** [%]	$N_{\mathbf{sig}}$	$N_{\mathbf{bkg}}$
WP1	s vs bc	10	98.93 ± 0.03	7.35×10^{11}	1.35×10^{12}
	s vs ud	10	40.03 ± 0.04	1.45×10^{11}	3.25×10^{10}
WP2	s vs bc	1	54.18 ± 0.04	2.38×10^{11}	2.06×10^{11}
	s vs ud	10	39.28 ± 0.06	5.10×10^{10}	5.57×10^{9}
WP3	s vs bc	1	54.18 ± 0.04	2.38×10^{11}	2.06×10^{11}
	s vs ud	1	10.05 ± 0.11	1.12×10^{10}	4.77×10^{8}
WP4	s vs bc	0.1	17.96 ± 0.06	3.23×10^{10}	6.98×10^{9}
	s vs ud	0.1	1.98 ± 0.33	3.56×10^{8}	3.38×10^{6}

Table 7.2: The efficiencies to select s quark jets and the mistag rates to select other flavours at four different working points. The expected yields, calculated for an integrated luminosity of $125\,\mathrm{ab}^{-1}$, are also listed. The signal is defined as $Z \to s\bar{s}$ events while the background is composed of $Z \to q\bar{q}$ (all quark flavours but strange) events. The number of observed events is significantly above the canonical discovery significance of five standard deviations for all working points.

Looser working points are suitable for analyses where maximising signal yield is crucial. However, for high-precision studies, such as quark-specific asymmetry measurements, maintaining a pure sample is essential, making tighter working points preferable. It is important to note that extremely tight working points, like WP4, can significantly reduce signal yield and consequently degrade the statistical precision of the measurement.

7.2.3 Reconstructed Z Boson Peak

The Z boson resonance is reconstructed using the 4-momentum of the two jets of each event. The reconstructed invariant dijet mass distribution, separated by the MC flavour of the resulting hadronic jets, is shown in Figure 7.3. The hadrons in b-jets tend to have longer decay chains,

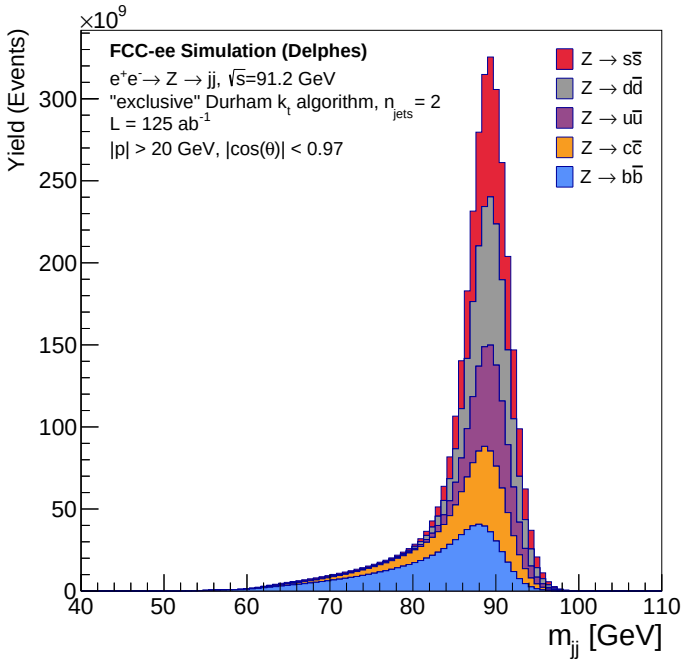

Figure 7.3: The distribution of the reconstructed invariant mass of the dijet system before tagging with contributions from events of all five quark flavours indicated.

causing a fraction of the momentum to be lost via neutrinos, resulting in a pronounced tail of the invariant mass distribution towards lower values for $Z \to b\bar{b}$. Similarly, the $Z \to c\bar{c}$ reconstructed invariant mass distribution also shows a tail, but for the lighter-quark flavour jets, s, u, and d, a clear peak can be seen at the Z resonance.

These jets are first tagged to remove the background of b- and c-jets by defining the discriminant, as described in Section 7.2.1. If both jets from a Z boson decay event pass this tagging

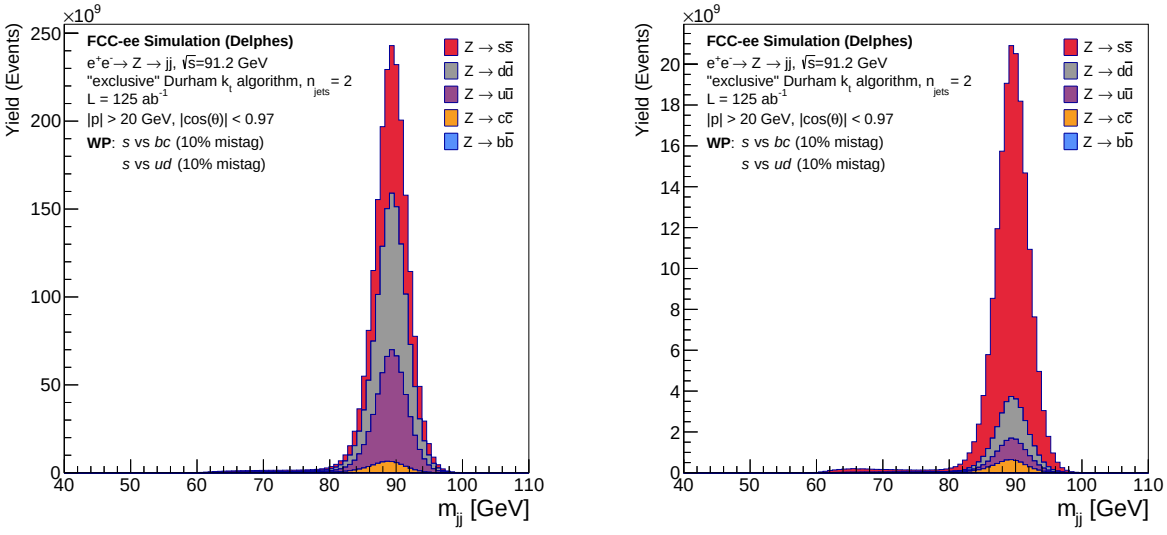

(a) **(b)**

Figure 7.4: The reconstructed invariant mass of the dijet system after tagging both jets with `DeepJetTransformer`, corresponding to WP1 in Table 7.2, for an assumed integrated luminosity of $125\,\mathrm{ab}^{-1}$. Both jets are required to be tagged in each case. Shown are (a) the distribution after the rejection of b- and c-jets vs s-jets at 10% mistag rate, (b) the distribution after rejection of b- and c-jets at 1% and u- and d-jets vs 10% mistag rate.

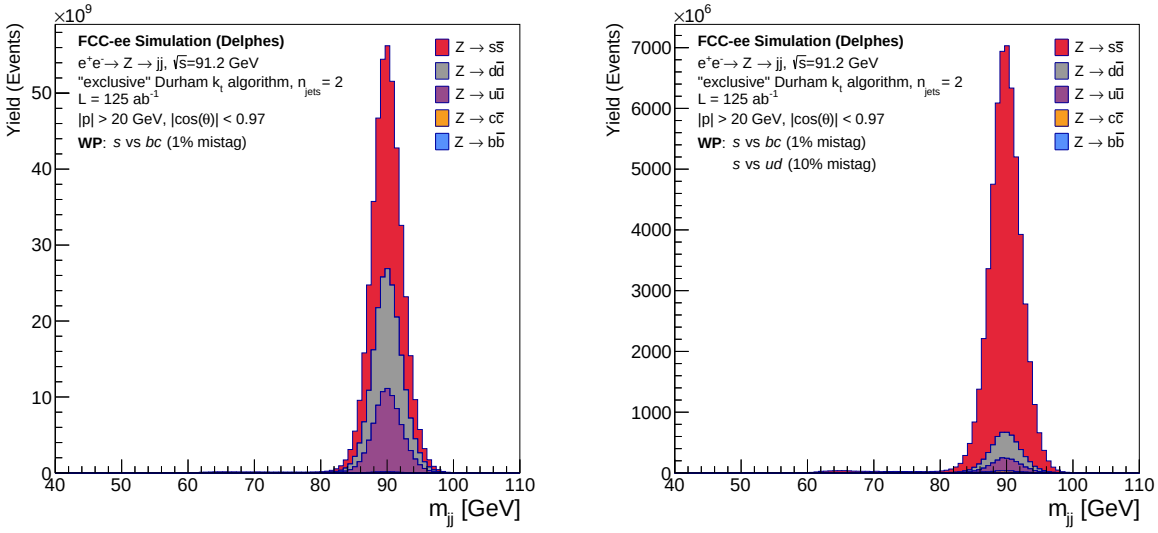

(a) **(b)**

Figure 7.5: The reconstructed invariant mass of the dijet system after tagging both jets with `DeepJetTransformer`, corresponding to WP2 in Table 7.2, for an assumed integrated luminosity of $125\,\mathrm{ab}^{-1}$. Both jets are required to be tagged in each case. Shown are (a) the distribution after the rejection of b- and c-jets vs s-jets at 1% mistag rate, (b) the distribution after rejection of b- and c-jets at 1% and u- and d-jets vs 10% mistag rate.

requirement, they are used to reconstruct the invariant mass. The distribution of this invariant mass is displayed in Figures 7.4a, 7.5a, 7.6a, and 7.7a, corresponding to each of the four working points, with the contributions of the MC flavours of the jets indicated. After the anti-b/c tag at a 10% mistag rate, most of the $Z \to b\bar{b}$ background is removed, but a substantial amount of $Z \to c\bar{c}$ events are left. At a tighter working point of 1% and 0.1% mistag rate, most of the

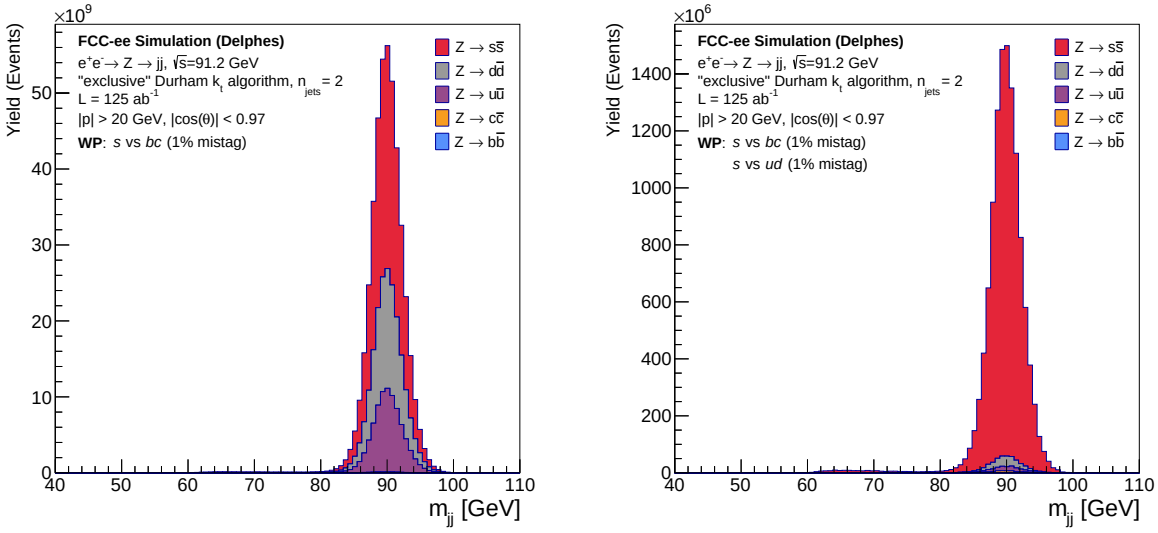

(a) **(b)**

Figure 7.6: The reconstructed invariant mass of the dijet system after tagging both jets with `DeepJetTransformer`, corresponding to WP3 in Table 7.2, for an assumed integrated luminosity of $125\,\mathrm{ab}^{-1}$. Both jets are required to be tagged in each case. Shown are (a) the distribution after the rejection of b- and c-jets vs s-jets at 1% mistag rate, (b) the distribution after rejection of b- and c-jets at 1% and u- and d-jets vs 1% mistag rate.

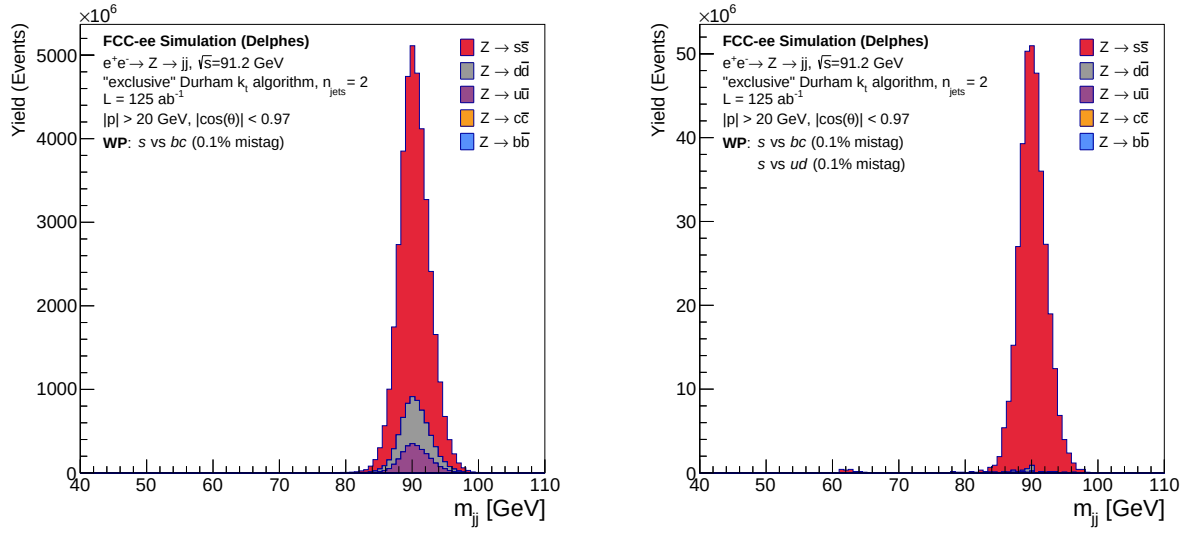

Figure 7.7: The reconstructed invariant mass of the dijet system after tagging both jets with `DeepJetTransformer`, corresponding to WP4 in Table 7.2, for an assumed integrated luminosity of $125\,\text{ab}^{-1}$. Both jets are required to be tagged in each case. Shown are (a) the distribution after the rejection of b- and c-jets vs s-jets at 0.1% mistag rate, (b) the distribution after rejection of b- and c-jets at 1% and u- and d-jets vs 0.1% mistag rate.

heavy-quark flavour background is removed.

The jets from the events passing the anti-b/c tag requirement are subsequently tagged with the s vs ud quark tagger to remove the background of u- and d-jets. Figures 7.4b, 7.5b, 7.6b and 7.7b show the distribution of the reconstructed invariant mass of the Z boson after this additional tag for each of the four working points. After the anti-u/d tag at a 10% mistag rate, a significant amount of $Z \to u\bar{u}$ and $Z \to d\bar{d}$ background is left, but a purer sample is achieved at tighter working points, resulting in an extremely pure sample at the working point of 0.1% mistag rate.

Both jets of every event are required to pass the tagging requirements in each selection stage. The signal efficiencies after each subsequent cut, corresponding to the four working points with increasing purity, are reported in Table 7.2.

7.2.4 Discovery Significance

The reconstructed Z resonance after tagging, especially at WP3 and WP4 in Figures 7.6 and 7.7, shows that the $Z \to s\bar{s}$ sample is extremely pure after requiring the two consecutive tags on each jet from Z boson decay events. The discovery significance, Z, in the unit of standard deviation, σ, is defined [166] as,

$$Z = \sqrt{2\left[(N_{\text{sig}} + N_{\text{bkg}})\log\left(1 + \frac{N_{\text{sig}}}{N_{\text{bkg}}}\right) - N_{\text{sig}}\right]}. \tag{7.3}$$

N_{sig} and N_{bkg} refer to the number of signal and background events, respectively. Signal is defined as $Z \to s\bar{s}$ events while the background is composed of $Z \to q\bar{q}$ (all quark flavours but strange) events. It is apparent from Table 7.2 that all four working points are significantly above the canonical discovery significance of 5σ at the integrated luminosity of $125\,\text{ab}^{-1}$. It is important to realise that machine backgrounds and irreducible backgrounds from other standard

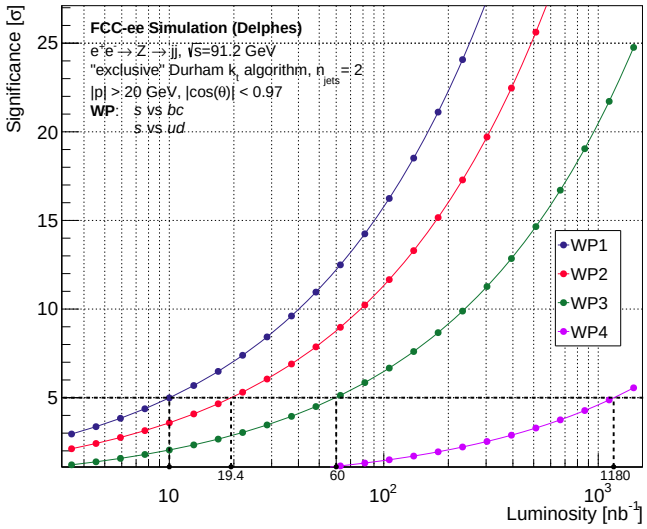

Figure 7.8: Discovery Significance as a function of integrated luminosity for the four working points corresponding to Table 7.2. The points noted by the x-axis intersecting with the dashed vertical lines are the luminosities required at the four respective working points to achieve the canonical discovery significance of 5σ.

model processes are not considered in this study and are at the per cent level. However, the remarkable sensitivity warrants an investigation of how limited the integrated luminosity can be to observe $Z \to s\bar{s}$ in the considered scenario.

Figure 7.8 shows the discovery significance of the process $Z \to s\bar{s}$, under the background-free scenario, as a function of the integrated luminosity. It can be seen that a 5σ significance can be achieved with minuscule luminosities compared to the FCC-ee run plan, even at the tightest working point. For WP3, corresponding to Figure 7.6b, a 5σ significance can be reached with a luminosity of 60 nb^{-1}. This is equivalent to *less than a second* of the nominal FCC-ee run at the Z resonance. Table 7.3 presents the luminosities required to achieve a 5σ significance at each of the four predefined working points.

	WP1	**WP2**	**WP3**	**WP4**
integrated luminosity [nb^{-1}]	10	19.4	60	1180

Table 7.3: Integrated luminosities required to reach the canonical discovery significance of 5σ at the four previously defined working points.

7.3 Conclusion

The excellent strange jet tagging performance of `DeepJetTransformer`, together with the high-statistics event samples available at the Z resonance at the FCC-ee, enables the isolation of very pure, statistically significant $Z \to s\bar{s}$ samples.

7.4 Summary and Discussion

Systematic uncertainties arising from the jet flavour tagging algorithm have not been explored in this study. Data-to-simulation scale factors for b-jets can be measured with a precision of approximately $\pm 2.5\%$ for jets with $30 < p_{\text{T}} < 50$ GeV at the LHC experiments. Tagging

algorithms at the future colliders are expected to achieve significantly smaller uncertainties, even for charm and strange jet tagging.

These developments will pave the way for high-precision measurements at the FCC-ee that require ultra-pure $Z \to q\bar{q}$ samples, particularly for the three heaviest flavours to which the Z boson decays. A few potential applications are the vector and axial coupling measurements of the Z to up- and down-type quarks and possibly even to individual quark flavours, and the quark-specific asymmetry measurements of the Z boson in the hadronic decay channels. The LEP Collider experiments and the SLD performed comprehensive measurements of the forward-backward asymmetry for $e^+e^- \to b\bar{b}$ [20], similar precise measurements for the charm and the strange quark, and possibly the u, d quarks, will become feasible at the FCC-ee.

The next chapter presents an assessment of the achievable precision in the strange quark forward-backward asymmetry measurement using a transformer-based jet flavour tagger.

8 The Forward-Backward Asymmetry at the Z Resonance

The hadronic forward-backward asymmetry (A_{FB}) is an important observable for future colliders, as it provides valuable insight into the underlying interactions of fundamental particles. A_{FB} is sensitive to the dynamics of fermionic and bosonic interactions and is one of the electroweak precision observables that consistently deviates in standard model precision tests when examining it for heavy flavour [167, 168]. Observing these asymmetries with high precision at future facilities can, therefore, help identify discrepancies between experimental data and standard model predictions.

The measurement of the forward-backward asymmetry for quarks requires the identification of the flavour and the charge of the quarks, as well as the direction of the quarks. Since the quarks themselves are inaccessible in the experimental environment, the flavour and the charge of the quarks are estimated by determining the flavour and the charge of the hadronic jet, while the direction of the quark is extracted by measuring the direction of the jet axis. The value of the forward-backward asymmetry, A_{FB}^{q}, can be measured by counting events with quark jets in hemispheres defined with respect to the direction of the travelling electron and positron or by performing a χ^2-fit of the asymmetry distribution constructed by the distribution of the polar angle of the quark and antiquark jet axes with respect to the electron and positron beams.

The sensitivity of A_{FB} at future colliders is an important benchmark. With the previous era accelerator facilities and detectors, typically the identification of bottom and maybe charm quarks was reliable, but with the increased interest in the origin of the mass and generational structure of the standard model, and with modern jet flavour taggers becoming available that can also tag strange and maybe even up and down quarks [2, 129], it becomes possible also to measure the A_{FB} for other quark flavours than A_{FB}^{b} and A_{FB}^{c}, something previously not possible with competitive precision [169, 170]. In this work, we assess the sensitivity to measure A_{FB} for bottom, charm, and strange quarks, with a representative collider and detector scenario (IDEA detector concept [75] at FCC-ee [72]).

This study has been presented in the ECFA Higgs, electroweak, and top factory study [3].

8.1 Event Selection

The simulated samples consist of the process $e^+e^- \to Z \to q\bar{q}$ (and $e^+e^- \to Z \to l^+l^-$ for background) at $\sqrt{s}$ of 91.2 GeV, described and referred to as the 'asymmetry samples' in Section 4.1. The event sample is scaled to correspond to a luminosity of $125\,\mathrm{ab}^{-1}$.

The aim of the first set of selection is to reduce/remove the leptonic background from the sample so that it is mainly populated by $Z \to q\bar{q}$ events. Figure 8.1 shows the distribution of the invariant mass reconstructed from the two jets of the Z boson decay events. Due to the undetected neutrinos from the decays of the tau lepton, the reconstructed tau jet momentum is significantly lower. Therefore, a clear peak is not seen for the reconstructed invariant mass of the Z boson in the τ decay channel. Putting a constraint on the invariant mass of the reconstructed invariant mass of the Z boson is expected to reduce the majority of the background from the

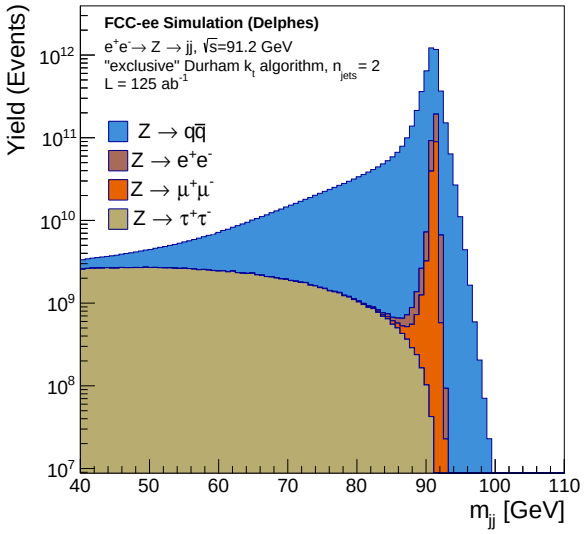

Figure 8.1: The distribution of the reconstructed invariant mass of the dijet system before applying any event or jet selection criteria, with contributions from events of all three lepton flavours and the combined contribution from $Z \to q\bar{q}$ events indicated. The distributions are shown in the log-scale to highlight the contribution from the leptonic background.

$Z \to \tau^+\tau^-$ events. Since the reconstructed invariant mass distribution for the b quark decay channel also shows a tail due to the decay of the hadrons containing the b quark, this constraint cannot be too strict, or it will eliminate a notable fraction of the $Z \to b\bar{b}$ events. The distribution for the $Z \to \mu^+\mu^-$ and $Z \to e^+e^-$ events shows a very narrow peak, which would leave the background from these events to be mostly unaffected. However, a majority of the $Z \to \mu^+\mu^-$ and $Z \to e^+e^-$ events are expected to have exactly two final tracks. In a few cases, the muon or the electron may radiate a photon, which may either convert to an e^+e^- pair, resulting in two additional tracks or may produce tracks by interacting with the material in the detector. But requiring the number of tracks in the event to be more than two should eliminate nearly all of the background from the $Z \to \mu^+\mu^-$ and $Z \to e^+e^-$ events.

Therefore, following the fiducial cuts on the jet momentum and the jet axis, further selection criteria were applied on the sample to reduce/remove the irreducible backgrounds: the invariant mass of the two-jet system was constrained to reduce background contributions from 2-photon production and the tau decay channel of the Z boson; events were required to have more than two reconstructed tracks to reduce the electron and muon channel background; the jet momenta were required to be dominated by hadrons instead of muons to further suppress leptonic Z boson decays. The last two of these variables are labelled as 'jet ID with muons' and 'jet ID with hadrons' and are defined as,

$$\text{jet ID with muons} \equiv \text{jetID}_{\mu^\pm} = \frac{\sum |p^{\mu}|}{|p_{\text{jet}}|}, \tag{8.1}$$

$$\text{jet ID with hadrons} \equiv \text{jetID}_{\text{had}} = \frac{\sum |p^{\text{had}}|}{|p_{\text{jet}}|}. \tag{8.2}$$

Figure 8.2 shows the distribution of these variables. It can be seen in Figure 8.2a that the momentum is carried by muons for the majority of the $Z \to \mu^+\mu^-$ events, while some $Z \to \tau^+\tau^-$ events also have a high fraction of their momentum carried by muons. These are events where the τ lepton goes through a pure leptonic decay to a muon. The majority of the $Z \to e^+e^-$ and $Z \to q'\bar{q}'$ events are clustered in the first bin of this distribution, as the dominant fraction of the

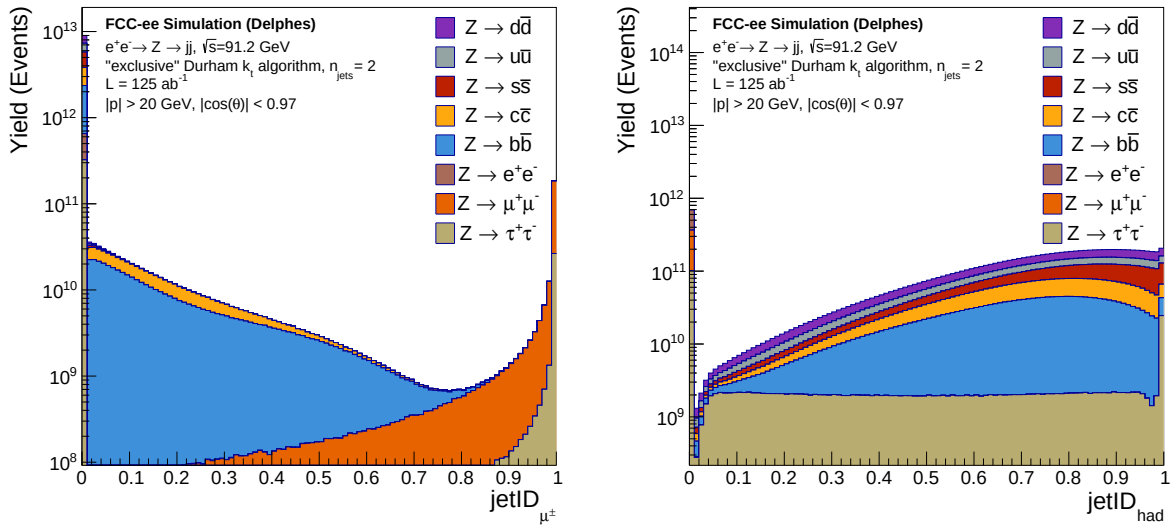

(a) **(b)**

Figure 8.2: The distributions of fractions of jet momenta carried by (a) muons and (b) hadrons, labelled as 'jet ID with muons' and 'jet ID with hadrons'. The contributions from different two-fermion decay channels of the Z boson are indicated.

momentum in the jets from these events is not carried by muons. It is apparent from Figure 8.2b that the momentum of the $Z \to \mu^+\mu^-$ and $Z \to e^+e^-$ events is not carried by hadrons and therefore nearly all of these events are collected in the first bin of the distribution. Nearly 35% of the τ leptons undergo pure leptonic decays, jets containing τ leptons that decay in this fashion are also clustered in the first bin.

An event is selected if both jets of the event pass the threshold at every successive criterion. The full set of these criteria is summarised below:

- jet momentum magnitude ($|p_{\text{jet}}| > 20\,\text{GeV}$)
- jet axis angle ($\cos\theta_{\text{jet}} < 0.97$)
- invariant mass of the two-jet system ($81.2\,\text{GeV} < M_{\text{inv}} < 101.2\,\text{GeV}$)
- number of track in the event ($N_{\text{tr}} > 2$)
- jet ID with muons (< 0.9)
- jet ID with hadrons (> 0.01)

The selection efficiency of each of these successive cuts is presented in Table 8.1. A high percentage of the $Z \to q\bar{q}$ events pass these cuts, except for a slightly lower efficiency of the $Z \to b\bar{b}$ and $Z \to c\bar{c}$ events to pass the invariant mass threshold due to the hadronic decays of the b and c hadrons. The electron and muon channel background is almost completely removed by applying a threshold on the number of tracks in an event and by requiring the hadrons of the jets to carry the majority of the momentum. The tau channel background, which is relatively harder to remove, is reduced significantly with the application of the invariant mass threshold. But it is mostly unaffected by the other selection criteria and is therefore the dominant background after this selection.

The distribution of the reconstructed invariant mass of the Z boson before and after these selections is presented in Figure 8.3. The Z resonance, as shown in Figure 8.3a, is narrower compared to the samples used in Chapters 6 and 7. This is because the samples used for the two studies are slightly different, and the treatment of the neutral particles in the two samples

	Efficiency [%]							
	$Zb\bar{b}$	$Zc\bar{c}$	$Zs\bar{s}$	$Zu\bar{u}$	$Zd\bar{d}$	Ze^+e^-	$Z\mu^+\mu^-$	$Z\tau^+\tau^-$
Jet $\lvert p\rvert$	99.99	>99.99	>99.99	>99.99	99.99	100	100	99.98
Jet axis $\cos\theta$	96.65	96.51	96.49	96.44	96.45	96.34	97.39	97.05
M_{inv}	72.98	88.10	95.62	98.57	98.35	99.83	99.81	4.89
N_{tr}	100	>99.99	>99.99	>99.99	>99.99	0.05	0.06	55.07
Muon Jet ID	>99.99	>99.99	>99.99	>99.99	>99.99	99.64	1.51	96.95
Hadron Jet ID	99.98	99.93	99.97	99.91	99.95	0.40	0	95.77
Total	**70.43**	**84.73**	**91.86**	**94.72**	**94.61**	**<0.01**	**0**	**1.34**

Table 8.1: The efficiencies to select the visible $Z \to f\bar{f}$ events (denoted by $Zf\bar{f}$) for six selection variables. The first two selection criteria impose the fiducial limits, while the rest are imposed to reduce or remove the leptonic background.

is different. The visible mass resolution of neutral particles in these samples is close to the ideal visible mass resolution, where the ideal resolution comes from the combined tracking, ECAL, and HCAL resolutions for the photon, charged, and neutral hadron components.

8.2 Flavour Tagging

Particle Transformer [129], tuned for the FCC-ee, is used for jet flavour tagging, which is applied sequentially to identify b-, c-, and s-flavour jets. The working points used are chosen to have 0.1%, 0.1%, and 1% mistag rates, respectively. The flavour mistagging background is of the order of 0.01% for all three flavours, as can be seen in Table 8.3. The procedure to choose the

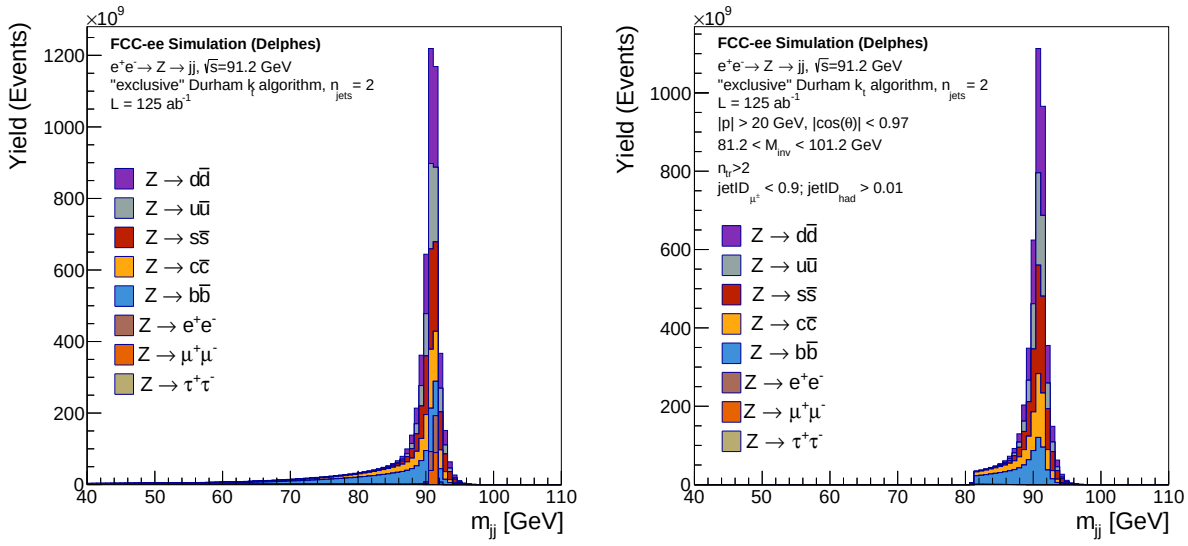

(a) **(b)**

Figure 8.3: The distribution of the reconstructed invariant mass of the dijet system (a) before and (b) after applying any event or jet selection criteria, with contributions from events of all five quark flavours and three lepton flavours indicated.

working points is detailed below.

8.2.1 Particle Transformer for FCC-ee

Events are successively selected to be $Z \to b\bar{b}$, $Z \to c\bar{c}$, or $Z \to s\bar{s}$ by tagging the two jets of every event using Particle Transformer. Tagging performance is evaluated for jets which are within the fiducial boundaries of the detector. A discriminant is defined, using Eq. 6.1 to identify the b-jets and extract the $Z \to b\bar{b}$ events:

$$S_{b \text{ vs } csq} = \frac{S_b}{S_b + S_c + S_s + S_q}, \tag{8.3}$$

where q denotes the combination of jets containing either the up or the down quark. The ROC curve corresponding to this discriminant is presented in Figure 8.4a. An excellent b-tagging performance is achieved with over 90% signal efficiency for mistag rates as low as 0.2%. An event is selected as a $Z \to b\bar{b}$ event if both jets from the event pass the threshold required at any certain working point.

A second discriminant is defined for jets from events that do not satisfy the b-tagging threshold to isolate the $Z \to c\bar{c}$ events:

$$S_{c \text{ vs } bsq} = \frac{S_c}{S_b + S_c + S_s + S_q}. \tag{8.4}$$

The ROC curve corresponding to this discriminant for a 0.1% mistag rate b-tagging working point is shown in Figure 8.4b. A signal efficiency of over 80% can be achieved for a mistag rate of 1%, allowing for a very pure $Z \to c\bar{c}$ sample to be selected. Similar to the $Z \to b\bar{b}$ selection, an event is selected as a $Z \to c\bar{c}$ event if both jets from the event pass the threshold required at any certain working point.

After the $Z \to b\bar{b}$ and $Z \to c\bar{c}$ events have been isolated from the sample, a final discriminant is defined to identify the $Z \to s\bar{s}$ events from the remaining sample:

$$S_{s \text{ vs } bcq} = \frac{S_s}{S_b + S_c + S_s + S_q}. \tag{8.5}$$

The ROC curve corresponding to this discriminant for a 0.1% mistag rate b-tagging working point and a 0.1% mistag rate c-tagging working point is shown in Figure 8.4c. As discussed in Chapters 6 and 7, tagging strange jets is the most challenging task, and it can be seen that the s-tagging performance is not comparable to the b/c-tagging performances. However, a signal efficiency of about 30% can still be achieved for a mistag rate of 1%. Given the ultra-high statistics available at the Z resonance at the FCC-ee, this allows for the selection of a very pure $Z \to s\bar{s}$ sample. An event is selected as a $Z \to s\bar{s}$ event if both jets from the event pass the threshold required at any certain working point, as done for b/c tagging.

	***b*-tagging**	***c*-tagging**	***s*-tagging**
efficiency [%]	87.23	53.04	30.89
mistag rate [%]	0.10	0.10	0.99

Table 8.2: The signal efficiencies and mistag rates corresponding to the chosen working points (WPs) for b-, c-, and s-tagging.

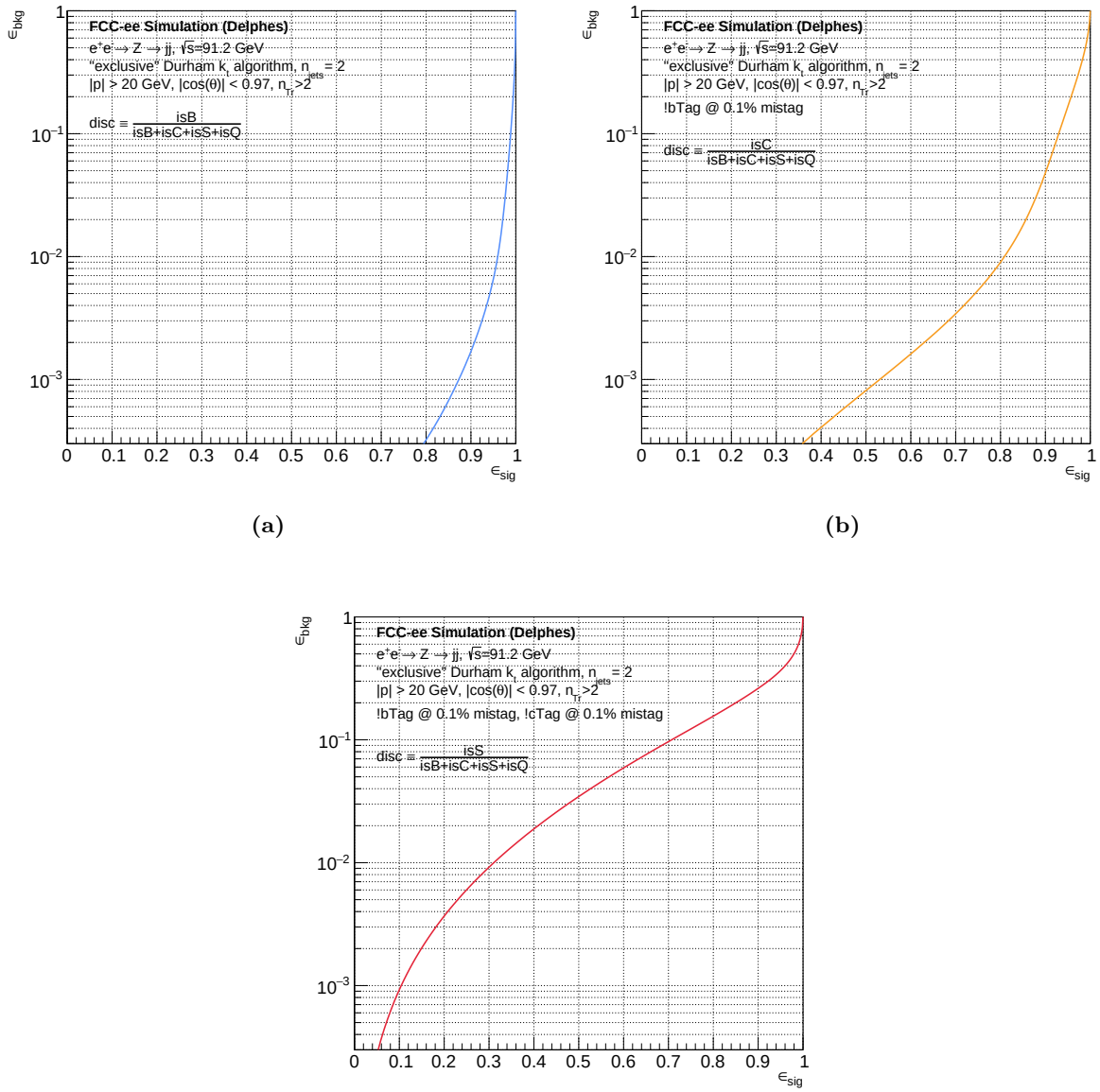

(a) **(b)**

(c)

Figure 8.4: The ROC curve showing the performance of (a) b-tagging (b) c-tagging, and (c) s-tagging with `ParticleTransformer`. It must be noted that the tagging steps are performed consecutively, therefore c-tagging is performed on jets that are not identified as b-jets and s-tagging is applied on jets that are not identified as either b- or c-jets.

8.2.2 Selection of $Z \to b\bar{b}$, $Z \to c\bar{c}$, and $Z \to s\bar{s}$ Events

The working points for b- and c-tagging are chosen at a 0.1% mistag rate and for s-tagging at a 1% mistag rate. The tagging efficiencies at these working points are summarised in Table 8.2.

Table 8.3 presents the efficiency of events with jets of a particular flavour to be correctly identified. The mistag rate denotes the rate with which events with jets of a different flavour are incorrectly identified as a specific flavour.

	$Z \to b\bar{b}$ (0.1% WP)	$Z \to c\bar{c}$ (0.1% WP)	$Z \to s\bar{s}$ (1% WP)
efficiency [%]	76.04	27.04	9.52
mistag rate [%]	0.05	<0.01	0.03

Table 8.3: The efficiencies to select $Z \to b\bar{b}$, $Z \to c\bar{c}$, and $Z \to s\bar{s}$ events and the mistag rates to select $Z \to q\bar{q}$ events with other flavours at the corresponding working points.

8.3 Jet Charge Tagging

Jet charge tagging is performed to identify and discriminate the jets originating from quarks and antiquarks. The jet charge can be defined in several ways, and it has been defined differently in various experiments.[171–173]. A few such definitions have been described below, and their performance is assessed against each other.

8.3.1 Few Different Definitions

Momentum-weighted jet charge can be defined with different momentum weightings or normalisations. These variables were defined with the charge and momentum of the jet constituents, q and p, respectively, and the momentum of the jet, p_{jet}.

Weighted by Transverse Momentum

The first of these definitions uses the transverse momentum of the jet and its constituents for the weighting and normalisation. This definition is more suited for hadron colliders, where precisely measuring the z component of the momentum can be challenging. This definition has been denoted as JC1 in the following.

$$\text{JC1} = \frac{\sum\limits_{i \in \text{jet}} q_i \cdot |p_i^{\text{T}}|}{|p_{\text{jet}}^{\text{T}}|}. \tag{8.6}$$

The distribution of JC1 for every jet flavour, separated for quark and antiquarks, is presented in Figure 8.5a.

Weighted by Momentum

The next definition uses the magnitude of the 3-momentum of the jet and its constituents for the weighting and normalisation instead of the transverse momentum. This definition is expected to perform slightly better than JC1, as the full momentum information is being exploited. This definition is denoted as JC2 in the following.

$$\text{JC2} = \frac{\sum\limits_{i \in \text{jet}} q_i \cdot |p_i|}{|p_{\text{jet}}|}. \tag{8.7}$$

The distribution of JC2 for every jet flavour, separated for quark and antiquarks, is presented in Figure 8.5b.

Weighted by Fractional Power of Momentum

It was seen at the LEP experiments that weighting with a fractional power of the momentum optimises the quark-antiquark separation with jet charge [173]. Therefore, the jet constituent charge is weighted in this definition by a power of 0.3 of the momentum. This definition is

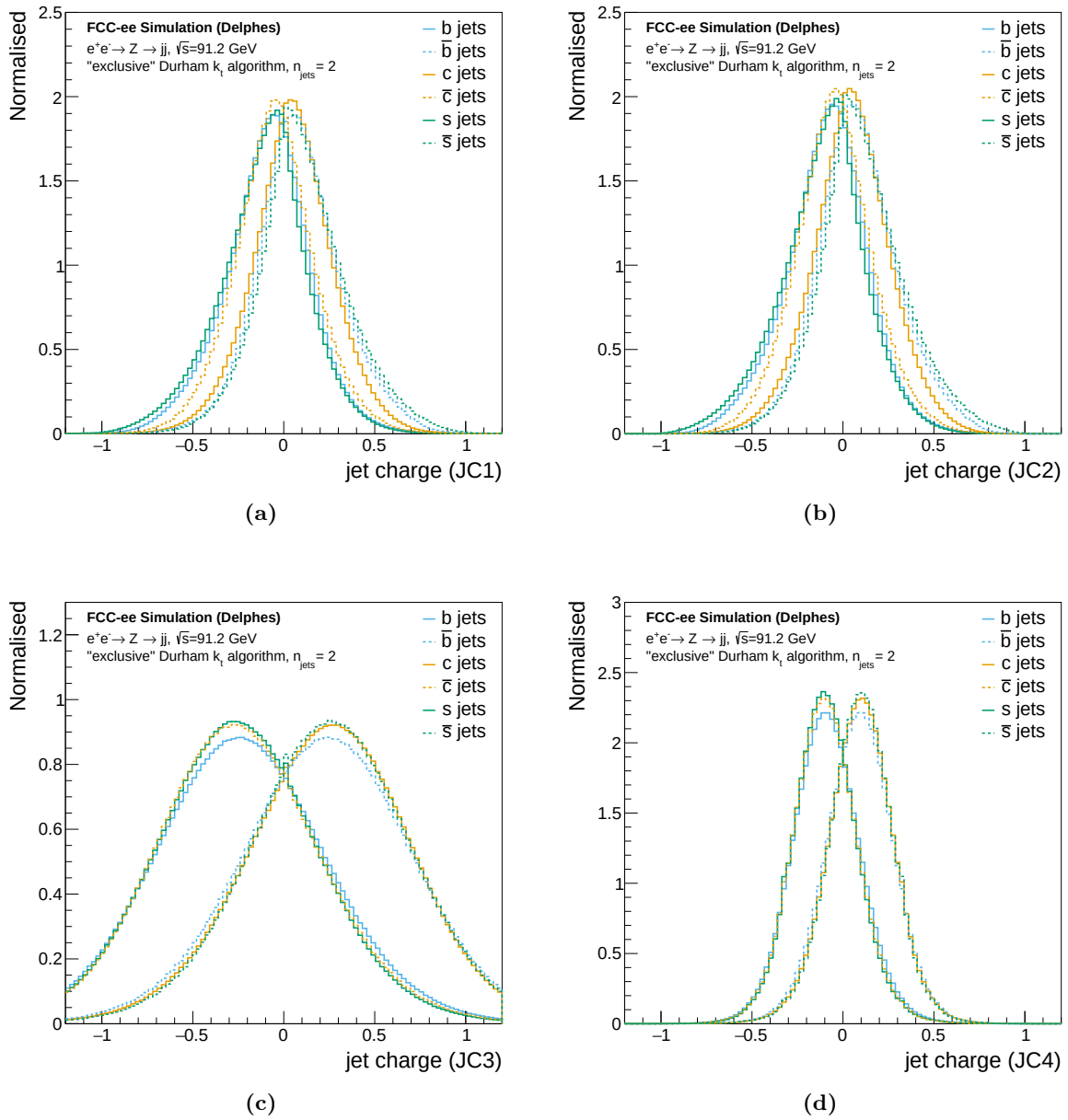

Figure 8.5: The distribution of jet charge with different momentum-weightings for quark jets and antiquark jets of b, c, and s flavours.

denoted as JC3 in the following.

$$\mathrm{JC3} = \frac{\sum\limits_{i \in \mathrm{jet}} q_i \cdot |p_i|^{0.3}}{|p_{\mathrm{jet}}|^{0.3}}. \tag{8.8}$$

The distribution of JC3 for every jet flavour, separated for quark and antiquarks, is presented in Figure 8.5c.

Weighted by Fractional Power of Momentum and Normalised by Sum of Track Momenta

This definition uses the same weighting as JC3 but uses a different normalisation factor. Since only tracks contribute to the charge of the jet, the charge weighted by the fractional power of momentum is normalised by the fractional power of the sum of track momenta instead of the

jet momentum. This definition is denoted as JC4 in the following.

$$\mathrm{JC4} = \frac{\sum\limits_{i \in \mathrm{jet}} q_i \cdot |p_i|^{0.3}}{\left| \sum\limits_{i \in \mathrm{jet}} p_i \right|^{0.3}}. \tag{8.9}$$

The distribution of JC4 for every jet flavour, separated for quark and antiquarks, is presented in Figure 8.5d.

		b-jets	$\bar{b}$-jets	c-jets	$\bar{c}$-jets	s-jets	$\bar{s}$-jets
JC1	**efficiency [%]**	64.75	64.77	59.74	59.68	67.93	68.02
	mistag rate [%]	35.23	35.25	40.32	40.26	31.98	32.07
JC2	**efficiency [%]**	64.95	64.98	59.87	59.83	68.16	68.27
	mistag rate [%]	35.02	35.05	40.17	40.13	31.73	31.84
JC3	**efficiency [%]**	69.58	69.62	71.61	71.55	71.96	72.05
	mistag rate [%]	30.38	30.42	28.45	28.39	27.95	28.04
JC4	**efficiency [%]**	69.58	69.62	71.61	71.55	71.96	72.05
	mistag rate [%]	30.38	30.42	28.45	28.39	27.95	28.04

Table 8.4: The efficiencies to select the quark (antiquark) jets of b, c, and s flavour and the mistag rates to select the antiquark (quark) jets of the same flavour. The evaluation was performed by looking at the sign of the jet charge.

Figure 8.5 shows that the distributions of JC1 and JC2 are very similar. It can be seen from Table 8.4 that the performance of these two variables is also very similar. The distributions of JC3 and JC4 in Figures 8.5c and 8.5d show that a comparatively better separation of the quark-antiquark jets can be achieved using a fractional power of the momentum for the weighting. The difference between JC3 and JC4 is only the normalisation factor; hence, the sign of the jet charge for a jet is the same for the two definitions. Therefore, the performance of these two variables to separate the quark-antiquark jets by evaluating the sign of the jet charge is identical, as presented in Table 8.4.

8.3.2 Quark-antiquark Separation

Due to its superior performance, JC3 was chosen as the definition for the momentum-weighted jet charge used in this study. An event is selected when the two jets have opposite jet charge. A loose working point is selected, where the jet charge misidentification leads to the dominant background being of the order of 10%. This is a conservative approach; in realistic analyses, the charge misidentification can be optimised much more stringently with simultaneous fits of the same-charge contribution or the use of charge-sensitive event variables. Table 8.5 summarises the performance of this method to correctly or incorrectly identify the charge of both jets for every event in the sample. It can be seen that the performance of quark-antiquark separation is worse for $Z \to b\bar{b}$ events than $Z \to c\bar{c}$ and $Z \to s\bar{s}$ events. This is because b-jets have a higher particle multiplicity and can be more spread out than c- and s-jets, which can lead to tracks being lost, the momentum being shared among a larger number of constituents, and being affected by detector effects.

	$Z \to b\bar{b}$	$Z \to c\bar{c}$	$Z \to s\bar{s}$
efficiency [%]	52.41	55.44	55.93
mistag rate [%]	13.22	12.28	11.95

Table 8.5: The efficiencies to select $Z \to b\bar{b}$, $Z \to c\bar{c}$, and $Z \to s\bar{s}$ events with the correct selection of quark and antiquark jet pairs and the mistag rates to select events with incorrect selection of quark and antiquark jet pairs, by evaluating the sign of the jet charge.

8.4 Asymmetry Measurement

After the event selection has been performed to reduce/remove the background from the $Z \to l^+l^-$ events, $Z \to b\bar{b}$, $Z \to c\bar{c}$, and $Z \to s\bar{s}$ events have been identified using the jet flavour tagger, and the quark-antiquark jets have been separated with momentum-weighted jet charge tagging, the measurement of the forward-backward asymmetry can be initiated. The forward-backward asymmetry can either be measured by counting the number of events with the quark jets in the forward or backward hemispheres or by fitting the asymmetry of the angular distribution of the quark and antiquark jets. The expected precisions on the forward-backward asymmetry measurement will be different for the two methods and will be assessed in this section.

The polar angle is typically defined as the angle between the incoming electron and the outgoing fermion, the outgoing quark in this particular case. This is the definition used in the asymmetry formalism presented in Section 1.5. The variable θ' is used for this traditional definition of the polar angle. However, the coordinate system used at the FCC-ee detector concepts, described in Section 3.2.1, define the polar angle, denoted by the variable θ, as the angle between the incoming positron and the outgoing fermion.

Since, $\theta = \pi - \theta'$, this leads to,

$$\cos\theta = -\cos\theta'. \tag{8.10}$$

The change in the sign of $\cos\theta$ due to the change in the coordinate system results in the flip of the sign of the asymmetry parameter. This can be countered by either flipping the sign of $\cos\theta$ in the mathematical formalism or by simply redefining the forward and the backward regions.

Therefore, in the following, the forward and the backward hemispheres are defined in reference to the polar angle described in the coordinate system used for the FCC-ee detector concepts.

8.4.1 Counting Measurement

This method counts the number of events with the quark jet in the forward or the backward hemisphere. The events with the quark jet in the forward direction ($\cos\theta > 0$) are counted as forward events, denoted N_F and the events with the antiquark jet in the forward direction are counted as backward jets, denoted N_B. The forward-backward asymmetry can then be calculated by performing the following operation:

$$A_\mathrm{FB} = \frac{N_\mathrm{F} - N_\mathrm{B}}{N_\mathrm{F} + N_\mathrm{B}}. \tag{8.11}$$

The resulting values of the forward-backward asymmetries for the b, c, s quarks are:

$$A^b_\mathrm{FB} = 0.0952175 \pm 0.0000018 \text{ (stat.)}$$
$$A^c_\mathrm{FB} = 0.0604802 \pm 0.0000028 \text{ (stat.)}$$
$$A^s_\mathrm{FB} = 0.0963924 \pm 0.0000037 \text{ (stat.)},$$

The achievable statistical precision on A_{FB}^{s} is much less than 1% when the measurement is performed with this method. This is a significant improvement over the past measurements performed at the LEP collider [174], but the measurement with the total number of forward and backward events is only valid for experiments with a full 4π acceptance. Therefore, a more sophisticated analysis, where the angular distribution of the forward-backward asymmetry is fitted, is typically performed to measure the forward-backward asymmetry.

8.4.2 Quark-antiquark Angular Distributions

Once the quark and antiquark jets from every event have been identified, the cosine of the polar angle of the jet axes can be used to construct an angular distribution. Figures 8.6, 8.7, and 8.8 show these angular distributions while individually considering the quark and antiquark jets of each of the three flavours as signal. The contribution from the background from each of the other processes is also noted. The background from the momentum-weighted jet charge mistagging is shown only for the signal flavour, as it was comparatively minute for the background flavours. The jet charge mistagging background is the dominant background for all cases, as was expected. The signal-to-background ratio is the worst in the distributions of jets from the $Z \to s\bar{s}$ events, since the working point was chosen to be not as pure as for the jets from $Z \to b\bar{b}$ and $Z \to c\bar{c}$ events.

The jet flavour mistagging background has a uniform distribution over the entire range of polar angles because it contains both the quark and the antiquark jets from each flavour. However, the jet charge mistagging background is expected to affect the asymmetry measurement, specifically by reducing it, since the angular distribution for quark and antiquark jets exhibits the dominant peak at the opposite signs of the $\cos\theta$ values, for ex. the quark jets are more prominent at negative values of $\cos\theta$, while the antiquark jets at the positive values of $\cos\theta$. Therefore, extracting the signal from these distributions is essential to accurately measure the

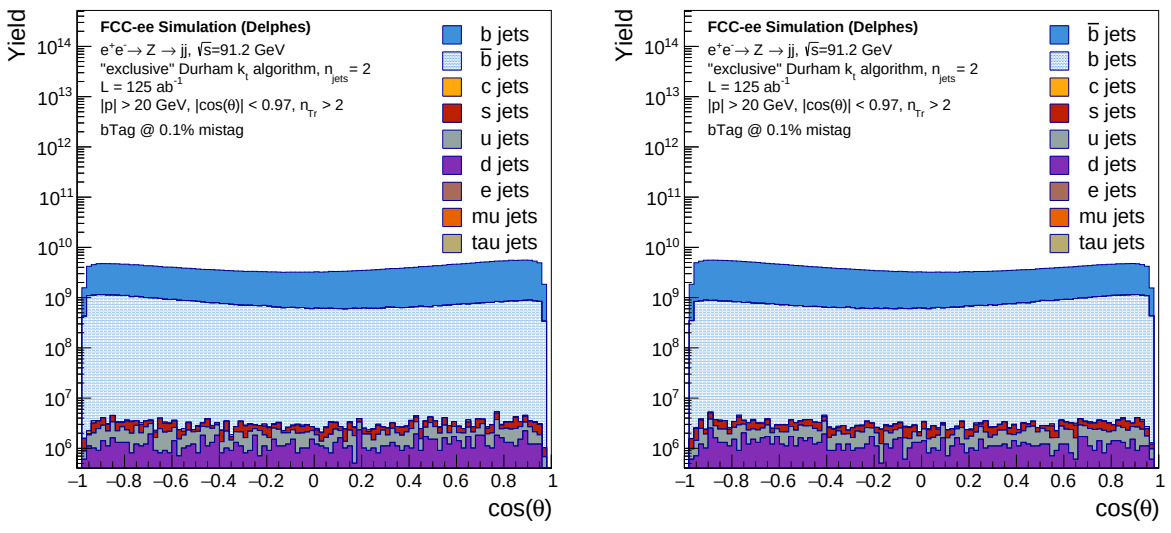

Figure 8.6: The distributions of the polar angle for (a) b-jets and (b) $\bar{b}$-jets, denoting the signal and the background. Background from the (anti)quark jets of the same flavour, i.e. the jet charge tagging background, are separately indicated, while backgrounds from quark and antiquark jets of other flavours, i.e. the jet flavour tagging background, are merged and only indicated by flavour.

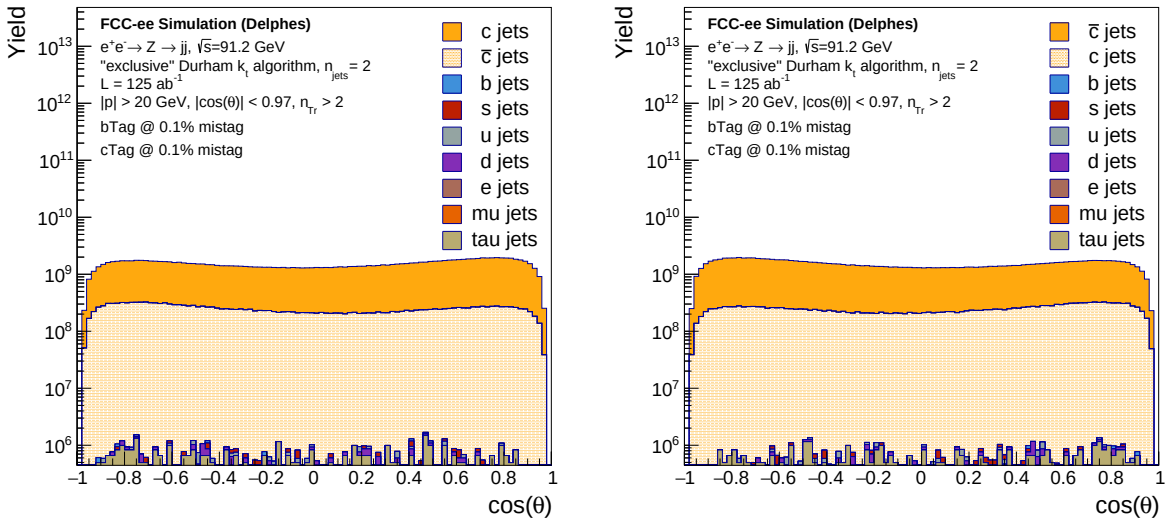

Figure 8.7: The distributions of the polar angle for (a) c-jets and (b) $\bar{c}$-jets, denoting the signal and the background. Background from the (anti)quark jets of the same flavour, i.e. the jet charge tagging background, are separately indicated, while backgrounds from quark and antiquark jets of other flavours, i.e. the jet flavour tagging background, are merged and only indicated by flavour.

asymmetry.

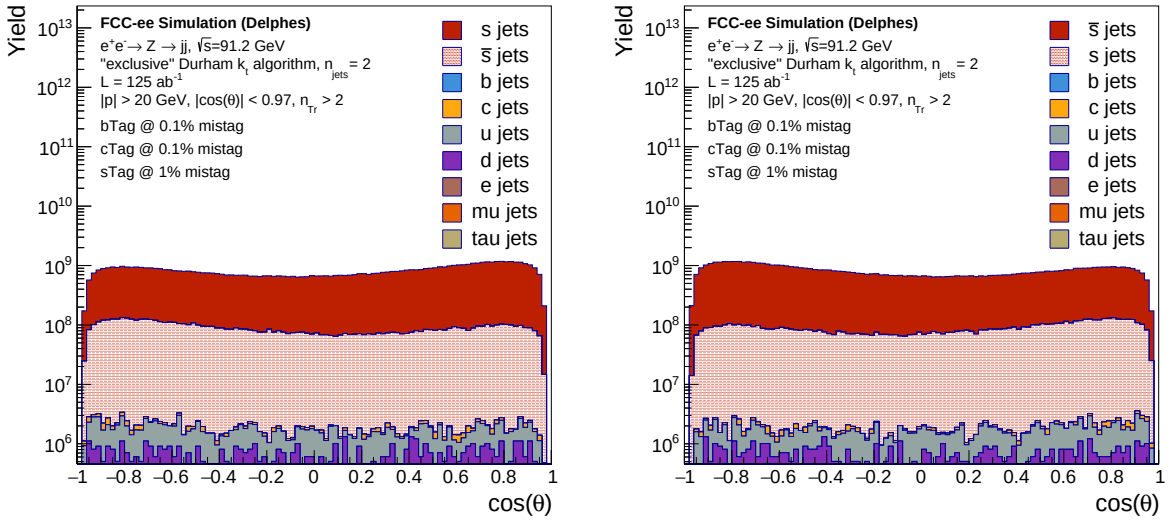

Figure 8.8: The distributions of the polar angle for (a) s-jets and (b) $\bar{s}$-jets, denoting the signal and the background. Background from the (anti)quark jets of the same flavour, i.e. the jet charge tagging background, are separately indicated, while backgrounds from quark and antiquark jets of other flavours, i.e. the jet flavour tagging background, are merged and only indicated by flavour.

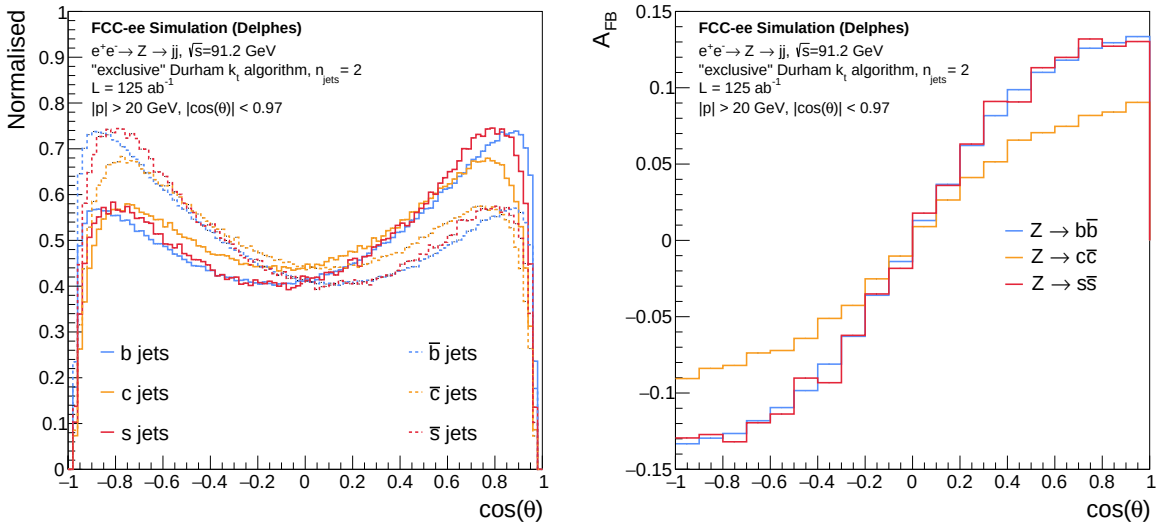

(a) **(b)**

Figure 8.9: (a) The distributions of the polar angle for b-, $\bar{b}$-, c-, $\bar{c}$-, s-, and $\bar{s}$-jets. (b) The forward-backward asymmetry calculated per bin for all three flavours.

8.4.3 Signal Extraction

In the simplest case of a realistic analysis, the leptonic background can be easily modelled from a Monte Carlo simulation. The background from jet flavour mistagging can be measured with an uncertainty derived from the calibration in the control regions, but it will be known. Therefore, this background can be rejected. The background from momentum-weighted jet charge mistagging can probably be easily modelled in simultaneous fits of both the quark and antiquark distributions shown in Figures 8.6, 8.7, and 8.8, but is not done in this study. The background from the jet charge mistagging is treated as if it can be rejected with a known uncertainty.

Hence, it was assumed that all backgrounds can be modelled and removed. The uncertainty assumed for the mistag rate measurement of the jet flavour tagger is assumed to be 2.5%, which is very conservative compared to expected uncertainties at the FCC-ee, but is the current standard at the LHC experiments. The same uncertainty was assumed for the measurement of the momentum-weighted jet charge mistag rate.

8.4.4 Fitting the Angular Distribution

To perform the A_{FB} measurement, the signal events are selected after passing the previously listed jet quality criteria and flavour and jet charge tagging. The leptonic and mistagging backgrounds are assumed to be modelled reasonably well, with associated uncertainties, and consequently removed. The $\cos\theta$ distribution of the signal quark and antiquark jets for each flavour is shown in the 8.9a. The forward-backward asymmetry, $A_{\mathrm{FB}}^{q,i}$, for a quark q is measured for each bin i as:

$$A_{\mathrm{FB}}^{q,i} = \frac{N^{q}(i) - N^{\bar{q}}(i)}{N^{q}(i) + N^{\bar{q}}(i)}, \tag{8.12}$$

where $N^{q}(i)$ is the number of entries in bin i of the $\cos\theta$ distribution of the jets containing the quark q and $N^{\bar{q}}(i)$ is the same for jets containing the antiquark $\bar{q}$. The distribution of A_{FB}^{q} is re-binned by merging every five consecutive bins, and the resulting distribution is shown in Figure 8.9b.

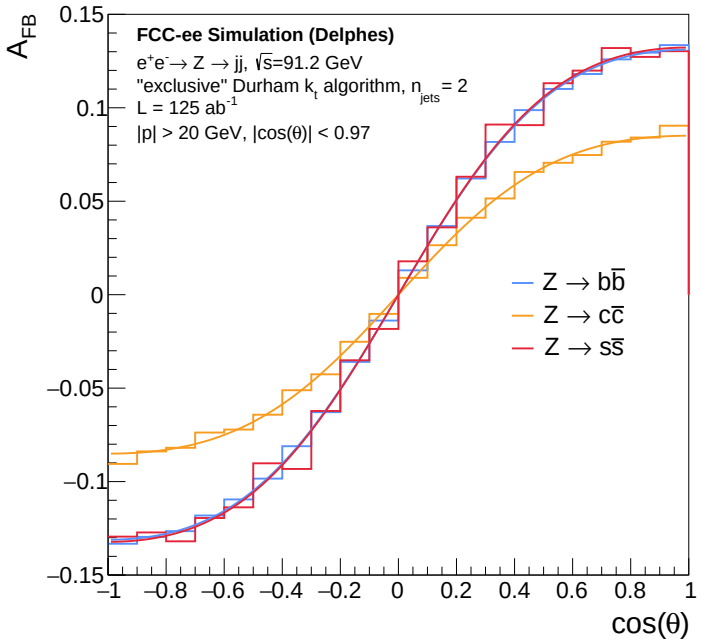

Figure 8.10: The forward-backward asymmetry calculated per bin for all three flavours along with their individual fits.

This re-binned distribution of A^q_{FB} is fitted over the entire range of $\cos\theta$ with the function:

$$A^q_{\mathrm{FB}}(\cos\theta) = 4\left(\frac{1-4|Q_e|\sin^2\theta^{\mathrm{eff}}}{1+8Q_e^2(\sin^2\theta^{\mathrm{eff}})^2-4|Q_e|\sin^2\theta^{\mathrm{eff}}}\right) \left(\frac{1-4|Q_q|\sin^2\theta^{\mathrm{eff}}}{1+8Q_q^2(\sin^2\theta^{\mathrm{eff}})^2-4|Q_q|\sin^2\theta^{\mathrm{eff}}}\right)\frac{\cos\theta}{1+\cos^2\theta} \tag{8.13}$$

and $\sin^2\theta^{\mathrm{eff}}$ as the fit parameter [175]. This expression is extracted from the following set of equations:

$$A^q_{\mathrm{FB}}(\cos\theta) = \frac{8}{3}\cdot A^q_{\mathrm{FB}}\cdot\frac{\cos\theta}{1+\cos^2\theta}, \tag{8.14}$$

$$A^q_{\mathrm{FB}} = \frac{3}{4}\cdot\mathcal{A}_e\cdot\mathcal{A}_q, \tag{8.15}$$

where Eq. 8.15 follows directly from Eq. 1.34 with $\mathcal{A}_f$ being the chiral coupling asymmetry for a fermion f. $\mathcal{A}_f$ is related to the ratio of the vector and axial-vector couplings of the Z boson to the fermion f, g^f_{V} and g^f_{A}, as shown in Eq. 1.31 which in turn has a one-to-one relation with $\sin^2\theta^{\mathrm{eff}}$ through Eq. 1.19.

The asymmetry distributions are individually fitted for the three flavours. These distributions, along with the fit, are presented in 8.10. The values of A^q_{FB} are calculated from the fit parameters $\sin^2\theta^q_{\mathrm{eff}}$ using Eq. 8.15, 1.31, and 1.19. The resulting forward-backward asymmetry

values for the three flavours are:

$$A_{\mathrm{FB}}^{b} = 0.0983222 \pm 0.0000012 \text{ (stat.)}$$
$$A_{\mathrm{FB}}^{c} = 0.0637820 \pm 0.0000020 \text{ (stat.)}$$
$$A_{\mathrm{FB}}^{s} = 0.0991786 \pm 0.0000026 \text{ (stat.)},$$

where the A_{FB}^{b} and A_{FB}^{c} values were used to test the robustness of the A_{FB}^{s} measurement method but not used in the measurement itself. The measurement by fitting the angular distribution results in a statistical precision on the forward-backward asymmetry of the same order as that by the counting method. The asymmetry for the strange quark, A_{FB}^{s}, can be measured with a statistical precision of much less than 1%. For comparison, the measurement of strange quark forward-backward asymmetry performed by the DELPHI experiment at the LEP collider had a statistical precision of over 10% [174].

8.5 Conclusion

This investigation shows that the forward-backward asymmetry in the bottom and charm decay channel of the Z boson can be measured with an absolute statistical precision of $1.2 \cdot 10^{-6}$ and $2.0 \cdot 10^{-6}$, respectively. Assuming systematic uncertainties below 10^{-5}, an improvement by almost three orders of magnitude compared to the combined measurements by the experiments at the LEP collider and SLD [176].

This study also presents that the forward-backward asymmetry measurement in the strange decay channel of the Z boson is possible with an absolute statistical precision of $2.6 \cdot 10^{-6}$ at the FCC-ee, considering a luminosity of $125\,\mathrm{ab}^{-1}$ at the Z resonance and the current developments in jet flavour tagging. Using an alternative approach, the systematic uncertainty on A_{FB}^{s} was shown to be possible to be constrained to below 10^{-5} [177].

8.6 Discussion

The assessment of systematic uncertainties was not performed for these studies. However, an alternative recent assessment of the systematic and statistical uncertainty on A_{FB}^{s} gives values of the order of 10^{-5} [177]. This estimate was obtained by extrapolating the ALEPH measurements of A_{FB} in inclusive hadronic decays [172, 173], and the b-asymmetry measurement [178]. That analysis is based on hemisphere charge asymmetries and their first and second moments, and is robust against QCD gluon radiation, a dominant systematic effect. Statistical uncertainties were dominant at the LEP collider, with systematic uncertainties at the 10^{-3} level at that time, primarily driven by the experimental statistics on jet charge determination. The uncertainty from the charge separation is expected to decrease by a factor of 300 at the FCC-ee, while the modern flavour taggers [2, 158] and planned detector improvements are assumed to improve the systematic uncertainties originating from flavour purities by more than a factor of 15. With the anticipated improvements in the measurement and modelling of strange particle and baryon production, and of secondary interactions, together with the extensive internal controls offered by modern analysis methods, the total statistical and systematic uncertainties for this method were optimized to be of similar size by applying a substantially tighter flavour tag requirement, and projected to be around 10^{-5}. This confirms that systematic uncertainties will likely be dominant over the statistical uncertainty determined earlier in this study.

Part IV

Vertex Detector Technology

9 Silicon Detectors

The first multi-layered sub-detector system of most collider experiments is the tracking detector. The goal of tracking detectors is to measure the path, or the trajectory, of charged particles as they traverse the detector. The innermost layers of the tracking detector, which are positioned the closest to the beam pipe, and thus the interaction point, are generally referred to as the vertex detectors and are designed to precisely measure the passage of charged particles through each layer in a high particle flux and radiation environment. These precise measurements are necessary for an accurate reconstruction of the particle tracks and consequently the interaction and decay vertices, known as the primary and secondary vertices, respectively.

The pointing resolution of a detector, describing the precision with which a track can be extrapolated back to its point of origin, is mainly affected by two aspects: multiple Coulomb scattering and the geometrical contribution to the error on the impact parameter, i.e. the distance of closest approach of a track to the interaction point from geometrical extrapolation.

Multiple Coulomb scattering, or simply multiple scattering, occurs in the beam pipe as well as in the layers of the detector system. Multiple scattering of a charged particle depends on the material of the layers through which it passes. The angular deflection, θ, due to multiple scattering roughly follows a Gaussian distribution, the RMS of which is given by [20],

$$\theta_{\mathrm{RMS}} = \frac{13.6[\mathrm{MeV}]}{\beta cp} \cdot z \cdot \sqrt{\frac{x}{X_0}} \left[1 + 0.038 \ln\left(\frac{x}{X_0}\right)\right] , \tag{9.1}$$

where z, p, and βc are the charge, the momentum, and the velocity of the charged particle, respectively, and x/X_0 is the thickness of the material in units of the radiation length. The radiation length, X_0, is the mean distance over which an electron loses all but $1/e$ of its energy through bremsstrahlung. It signifies how far highly energetic electrons can travel within a material before undergoing a significant interaction.

The impact parameter resolution is dependent on the intrinsic resolution and the positions of the detector layers. A simplified two-layer detector, shown in Figure 9.1, demonstrates which parameters are crucial for the performance of a vertex detector. For simplification, the layers are assumed to be arranged in perfect concentric cylinders around the beam pipe at a distance of r_1 and r_2. Only straight tracks are considered, passing the detector layers perpendicularly, and the intrinsic resolutions of the two detector layers in the plane perpendicular to the beam pipe are σ_1 and σ_2.

In the first scenario, the second detector layer is assumed to be perfect with $\sigma_2 = 0$, while the first detector layer has a resolution $\sigma_1 > 0$. The error on the impact parameter, σ_b, is defined as the scaled image of the position error due to the intrinsic resolution of the first detector layer.

$$\frac{\sigma_b}{\sigma_1} = \frac{r_2}{r_2 - r_1}. \tag{9.2}$$

Similarly, when the first detector layer is assumed to be perfect, while the second detector layer has an intrinsic resolution $\sigma_2 > 0$, the error on the impact parameter is,

$$\frac{\sigma_b}{\sigma_1} = \frac{r_1}{r_2 - r_1}. \tag{9.3}$$

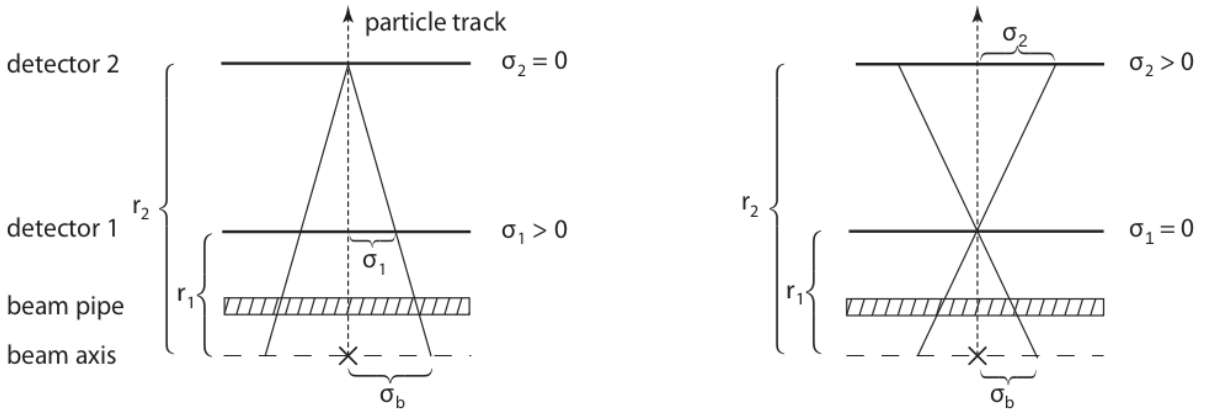

(a) Detector 2 assumed to be perfect. (b) Detector 1 assumed to be perfect.

Figure 9.1: A simplified two-layer detector in planar geometry. The × symbol denotes the interaction point, r_1 and r_2 are the distances of the two layers from the plane of the interaction point, parallel to the detector layers. [179]

The total impact parameter resolution can be achieved by summing these two resolutions in quadrature and adding the term σ_{ms}, originating from multiple scattering in the beam pipe and the first detector layer,

$$\sigma_b^2 = \left(\frac{r_2}{r_2 - r_1} \cdot \sigma_1\right)^2 + \left(\frac{r_1}{r_2 - r_1} \cdot \sigma_2\right)^2 + \sigma_{\text{ms}}^2 \ . \tag{9.4}$$

It must be noted that the impact parameter resolution directly depends on multiple scattering. In first approximation, the measurement error from multiple scattering by a layer is $\sigma_{\text{ms}} = r \cdot \theta_{\text{RMS}}$, where r is the radial distance of the layer. The impact parameter resolution of a detector is typically parametrised as,

$$\sigma_b = a \oplus \frac{b}{p \sin^{3/2} \theta}, \tag{9.5}$$

where a is the intrinsic resolution of the detector, b is the coefficient for multiple scattering, p is the momentum and θ is the polar angle of incidence of a charged particle.

Certain detector characteristics, concluded based on Equation 9.4, are summarised below:

- Since $r_2 > r_1$, the coefficient of σ_1 will always be greater than that of σ_2. Therefore, the resolution of the innermost detector layer should be as good as possible. Thus, the use of high-resolution silicon pixel detectors is crucial for the innermost section of a particle detector.
- The 'lever arm', i.e. the distance between the inner and outer layers, should be large to minimise the scaling factor $r_2 - r_1$, but should be optimised to minimise the coefficient of σ_1.
- To minimise the coefficient of σ_2 as well as the impact of the multiple scattering term, r_1 should be small; therefore, the inner layer should be positioned as close to the beam pipe as possible.
- To reduce the impact of multiple scattering from the beam pipe and the inner detector layer, these should constitute as low a material budget as possible. Therefore, for a high-resolution silicon-based inner detector, the inner detector layer should be as thin as possible.

A thin silicon-based vertex detector, with its innermost layer positioned very close to the

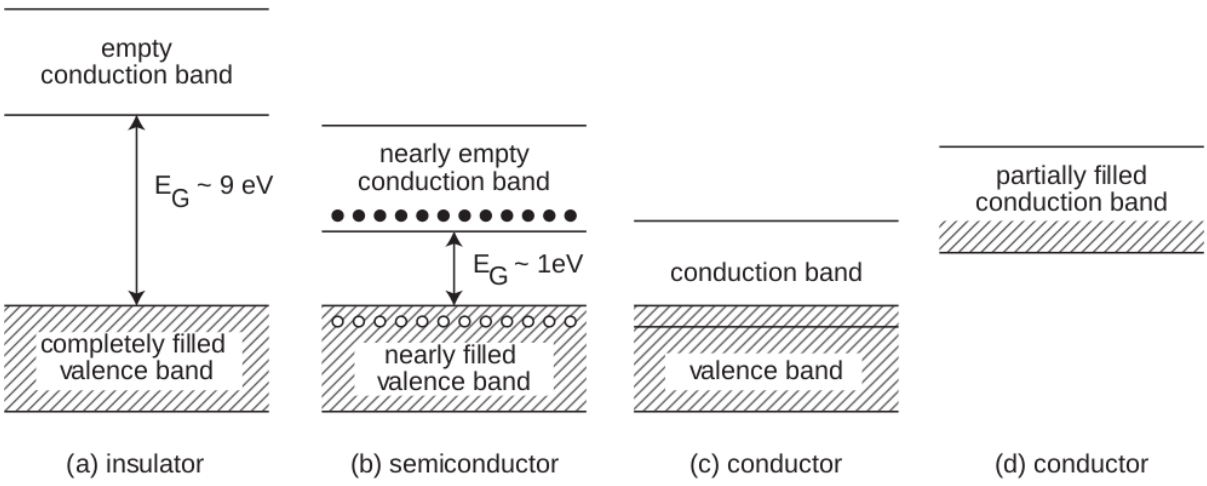

Figure 9.2: The schematic of the energy-band structure of different categories of solids: (a) insulators, (b) semiconductors, (c,d) conductors. The shaded region denotes a filled band. E_G is the energy difference between the two bands, also called the band gap. [179]

beam pipe, satisfies all these criteria. The working principle, basic design elements, types, and performance of silicon-based detectors will be detailed in the following.

9.1 Semiconductor Devices

All solids can be divided into three broad groups based on their electrical conductivity: conductors, semiconductors, and insulators, as shown in Figure 9.2. Silicon (Si), germanium (Ge), gallium arsenide (GaAs), cadmium telluride (CdTe), and silicon carbide (SiC) are the most important semiconductors used for particle or radiation (X-rays or Gamma rays) detection, with silicon being the most widely used material in semiconductor detectors. The bonds between neighbouring atoms in semiconductors are less strong than in insulators, leading to a small energy-band gap between the valence and conduction bands. This low energy-band gap can be overcome by either thermal excitation or an external electric field, resulting in free electrons in the conduction band and the absence of electrons, also referred to as holes, in the valence band. Electrons and holes can move freely within their respective bands.

Semiconductors without external impurities are known as 'intrinsic' semiconductors. The four valence electrons in a silicon atom form bonds with one neighbouring silicon atom each to form the silicon lattice, in the same structure as that of the diamond lattice. In thermal equilibrium, the generation and recombination of electrons in the conduction band and the holes in the valence band are in balance, leading to $n = p = n_i$, where n is the density of electrons, p is the density of holes, and n_i is the intrinsic carrier charge density. Through the law of mass-action, this results in,

$$n \cdot p = n_i^2 = \text{constant}. \tag{9.6}$$

The resistivity, ρ, of a semiconductor is defined as,

$$\rho = \frac{1}{e(n\mu_e + p\mu_p)}, \tag{9.7}$$

where μ_e and μ_p are the mobilities of electrons and holes, respectively, and e is the elementary

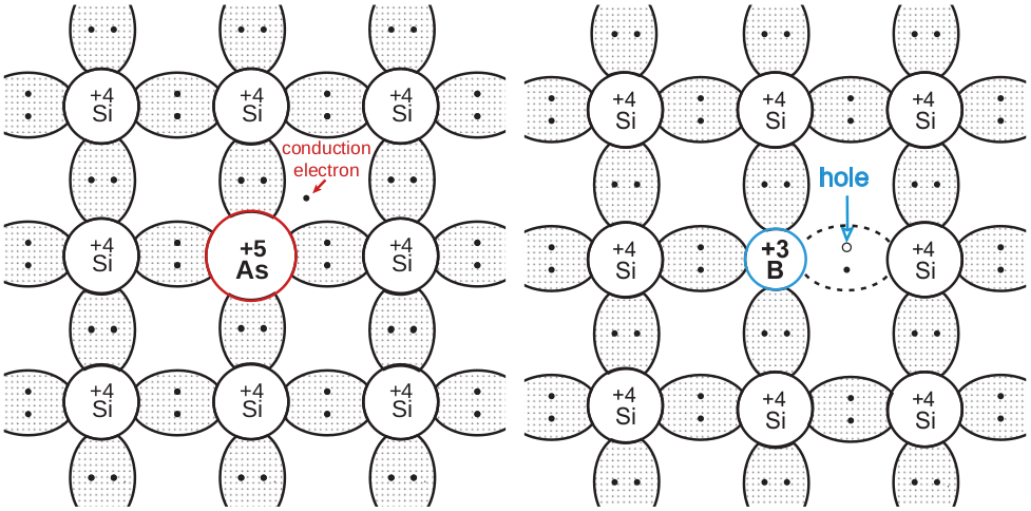

(a) n doped (b) p doped

Figure 9.3: The schematic of the bond structures within (a) an n-doped and (b) a p-doped silicon lattice. [179]

charge. In the condition of thermal equilibrium, Eq. 9.7 reduces to,

$$\rho = \frac{1}{en_i(\mu_e + \mu_p)}. \tag{9.8}$$

The electron and hole mobilities in silicon at the room temperature of 300 K are known to be 1450 and 500 $\mathrm{cm^2\,V^{-1}\,s^{-1}}$, respectively, while the intrinsic charge carrier density, n_i, is approximately $1 \times 10^{10}\,\mathrm{cm^{-3}}$ [179]. Therefore, the resistivity, ρ, of silicon at room temperature is $\approx$360 kΩ cm.

9.1.1 Doping

The conduction properties of a semiconductor can be selectively changed by introducing impurities. These semiconductors are referred to as 'extrinsic' semiconductors. When an atom with five valence electrons, like phosphorus (P) or Arsenic (As), is placed in the silicon lattice, it leads to an excess of conduction electrons compared to the holes. This is called n-type doping, and the impurity element is called a donor. Conversely, when an atom with three valence electrons, like boron (B) or Aluminium (Al), is placed in the silicon lattice, it results in an excess of holes. This is called p-type doping, and the impurity element is called an acceptor. The two doping schemes are presented in Figure 9.3. Since the added impurity atoms are electrically neutral, the extrinsic semiconductor is also electrically neutral. The majority carriers in an n-type semiconductor are electrons, and holes are the minority carriers, and vice versa for p-type semiconductors.

Stronger n-type doping relative to the standard doping concentration is typically denoted by n^+ or n^{++}, while weaker doping is denoted by n^- or n^{--}. p^+, p^{++}, p^-, and p^{--} are similarly defined for varying strengths of p-type doping.

The positive charge carrier concentration, p, in a p-type semiconductor is approximately the same as the concentration of the acceptor impurity, N_A, because $N_A \gg n_i$. Following Eq. 9.6, $n \approx n_i^2/N_A$, while $p \approx N_A \gg n$. Updating Eq. 9.7 for a p-type semiconductor, the resistivity is given by,

$$\rho_p \approx \frac{1}{eN_A\mu_p}. \tag{9.9}$$

Similarly, the resistivity of an n-type semiconductor is $\rho_n \approx 1/eN_D\mu_e$.

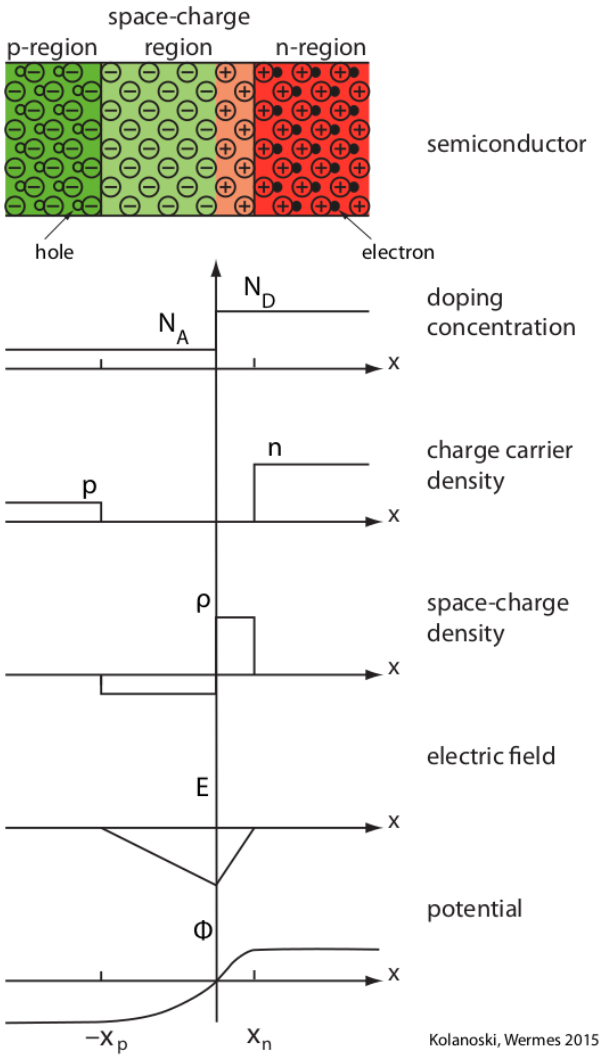

Figure 9.4: The doping and space-charge concentrations, strength of the electric field, and the electrostatic potential at a p-n junction. [179]

9.1.2 Junctions

A semiconductor sensor to detect radiation constitutes a specialised case of a diode, which is a fundamental electronic circuit element. When a p-type and an n-type semiconductor are brought in contact, a p-n boundary, also called a p-n junction, is formed. The dominant charge carriers or the majority carriers in p-type semiconductors are holes, while in n-type semiconductors, these are electrons. The concentration gradient at the boundary results in a diffusion current, where the electrons diffuse from the n-doped part to the p-doped part and the holes diffuse in the opposite direction. These charge carriers recombine at the junction, forming a zone free of mobile charge carriers, called the depletion zone or the depletion region.

Although the depletion zone is devoid of charge carriers, the atoms in the lattice remain ionised. Therefore, the depletion zone is no longer neutral but features the so-called space charge, as shown in Figure 9.4. With its holes having recombined, the p-doped part has a negative charge density. Inversely, the n-doped part has a positive charge density. Therefore, the depletion zone is also called the space-charge region. These opposite space charges in the p- and n-doped regions create an intrinsic electric field. A drift current is induced due to this intrinsic electric field in the opposite direction of the diffusion current. In the absence of an external voltage, the diffusion current and the drift current are balanced. It must be noted that despite the space-charge region, the whole semiconductor is still electrically neutral. The

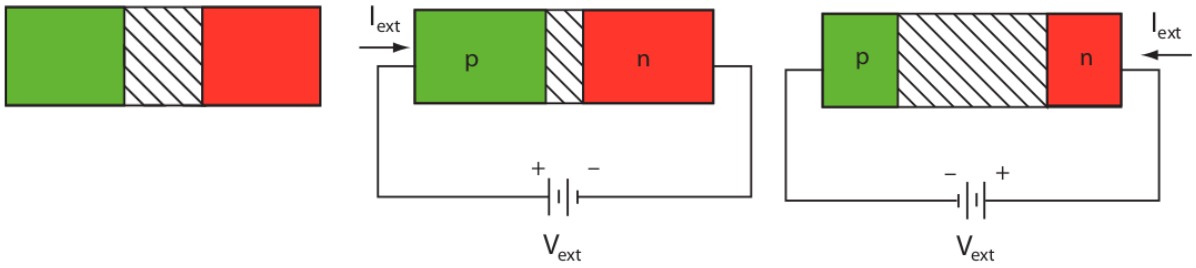

(a) (b) (c)

Figure 9.5: A p-n junction under three different biasing conditions: (a) without external voltage, (b) with external voltage applied in forward biasing, (c) with external voltage applied in reverse biasing. [179]

depletion region reaches deeper in the part which is more weakly doped, and the rise of the electric field is slower compared to the strongly doped part. The magnitude of the electric field is at a maximum at the junction.

In the energy-band model, at room temperature and in the absence of externally applied voltage, this is represented by the bending of the valence and conduction energy-bands, with the Fermi level being closer to the valence band of the p-type semiconductor due to holes being the majority charge carrier, while being closer to the conduction band of the n-type semiconductor due to the electrons being the majority charge carriers.

Depletion under External Voltage

The width of the depletion region can be manipulated by applying an external voltage difference between the n-doped and the p-doped sides of the junction, and the electrostatic potential between the two sides can either be enhanced or reduced depending on the polarity of the external voltage. As the system is no longer in thermal equilibrium, the law of mass action no longer holds, i.e. $n \cdot p > n_i^2$ or $n \cdot p < n_i^2$.

If the external voltage applied to the p-doped side is positive relative to the n-doped side, it is referred to as forward biasing the junction. The drift current is reduced compared to the diffusion current. Under the influence of the external potential difference, more holes diffuse from the p-doped side to the n-doped side and more electrons diffuse from the n-doped side to the p-doped side compared to the diffusion rate at thermal equilibrium. The depletion region in turn becomes narrower, as shown in Figure 9.5.

On the other hand, reverse biasing is when the external voltage applied is more positive on the n-doped side or more negative on the p-doped side, relative to the opposite side. The bending of the energy-bands becomes stronger, effectively reducing the diffusion current. The depletion region becomes wider, as shown in Figure 9.5.

Diode Capacitance

As the depletion region at the junction of a p-n diode is free of mobile charge carriers, a planar diode can be considered as a plate capacitor filled with a dielectric. Hence, the capacitance per unit area can be defined as,

$$\frac{C}{A} = \frac{\epsilon\epsilon_0}{d}. \tag{9.10}$$

Here A is the area and d is the width of the depletion region. The relative permittivity, ϵ, of silicon is 11.9. Therefore, for a planar diode of thickness 25 µm, that is fully depleted along its

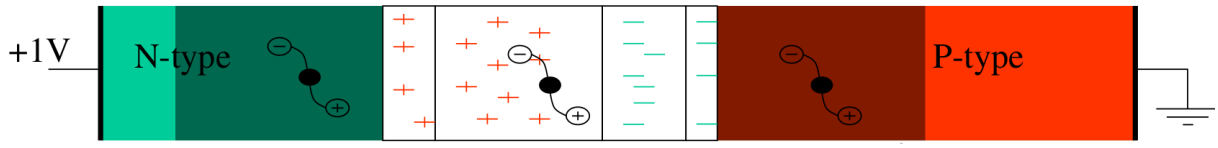

Figure 9.6: A p-n junction as a semiconductor detector.

width, the capacitance per unit area is,

$$\frac{C}{A} \simeq 420 \frac{\text{pF}}{\text{cm}^2}.$$

As the thickness of the depletion region is directly dependent on the externally applied bias voltage, the voltage required to fully deplete a sensor, referred to as the full depletion voltage, can be determined by measuring the sensor capacitance. Increasing the reverse bias voltage increases the thickness of the depletion region, thus decreasing the capacitance. However, the thickness of the depletion region cannot exceed the thickness of the sensor. Hence, the voltage at which the sensor capacitance converges to the minimum, reaching a plateau, represents the depletion voltage. The capacitance does not reduce further upon increasing the reverse bias voltage over the depletion voltage.

A p-n Diode as a Particle Detector

Figure 9.6 shows the cross-section of a reverse-biased planar diode, with the depletion region highlighted by the marked region. A charged particle passing through the diode loses energy due to ionisation, as will be detailed in Section 9.2, and generates electron-hole pairs. Photons from radiation similarly transfer energy via the photoelectric effect and Compton scattering to generate electron-hole pairs. The charges can be generated in three different regions based on where the charged particle passes. A single electron-hole pair is considered in the following for simplification. If the pair is generated in the p-doped region, the electron and hole diffuse and when the electron, if it avoids recombination, reaches the boundary of the depletion region, it experiences the electric field and drifts towards the positive electrode to get collected. Similarly, a hole generated in the n-doped region will diffuse to the depletion region boundary and be collected by the negative electrode.

When an electron-hole pair is generated within the depletion region, the electron and hole experience the force due to the electric field in opposite directions and induce a current in the respective electrode. The current generated by the collection of these charges can be measured, possibly amplified, and read out. Thus, a hit can be detected. A fully depleted diode is desirable for particle detection, as the lack of free mobile carriers in the depletion region reduces the probability of recombination of the generated charge. The strong electric field in the depletion region also makes the charge collection fast, as drift is the main mode of transport within the depletion region. The lack of free mobile charges also results in lower noise within the depletion region compared to the undepleted region, where the concentration of the thermally generated charge carriers may significantly exceed that of charge generated by an ionising particle.

Leakage Current

A small undesirable current is observed in semiconductor detectors and reverse-biased semiconductor junctions. Even in ideal diodes, the current is observed due to the movement of the minority charge carriers. This is called the leakage current. In semiconductor detectors, the main cause for leakage current is the thermal generation of electron-hole pairs in the depletion

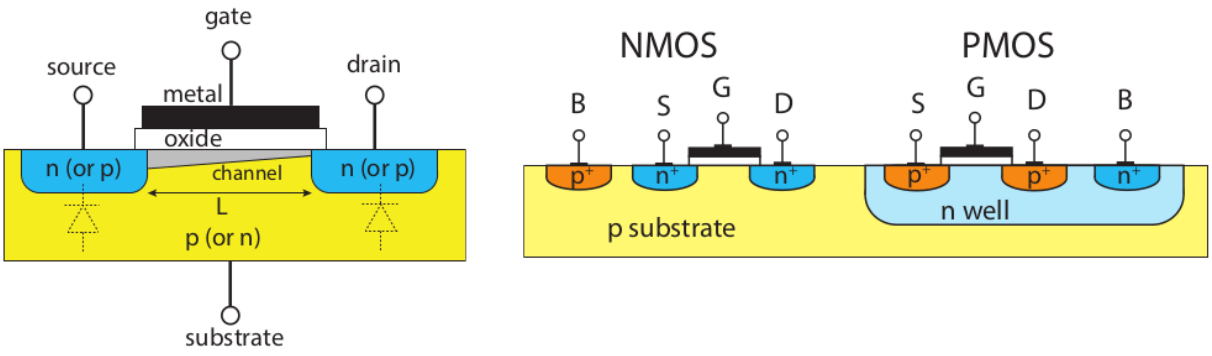

(a) MOSFET. (b) CMOS.

Figure 9.7: The cross-section of (a) a basic MOSFET structure and (b) the realisation of an NMOS and PMOS transistors on the same substrate, also called CMOS. [179]

region. This current manifests as one of the sources of noise in silicon-based radiation detectors.

9.1.3 Transistors

The metal-oxide-semiconductor (MOS) structure is a double interface made of the three media. It is the most widely used structure in field-effect transistors (FET). Chip electronics nowadays, including detector readout, consists of MOSFETs. The MOSFETs are used in combination of the so-called NMOS and PMOS, fabricated on the same substrate, into the complementary MOS (CMOS) electronics. A cross-section of the MOSFET and a CMOS structure is shown in Figure 9.7. An NMOS transistor uses high-dose n-wells within a lightly p-doped substrate to form the source and the drain nodes of the transistor. However, as the substrates are generally p-doped, a deep n-well is formed within the substrate that houses the PMOS transistor and high-dose p-wells within this deep n-well are used to form the source and the drain nodes of the transistor. The channel is an inversion region to which minority charge carriers are attracted at high enough reverse bias voltages at the metal gate contact. The current then flows between the source and drain and is steered by the gate voltage.

The current through a MOSFET is exponentially dependent on the gate voltage and the voltage difference between the source and the drain nodes when it's being operated in the so-called triode or linear regime. The current I_{ds} is defined as,

$$I_{\mathrm{ds}} = I_0 e^{(\kappa V_{\mathrm{g}} - V_{\mathrm{s}})/U_{\mathrm{T}}} \left(1 - e^{-(V_{\mathrm{d}} - V_{\mathrm{s}})/U_{\mathrm{T}}}\right), \tag{9.11}$$

where V_{g}, V_{s}, and V_{d} are the voltages of the gate, the source, and the drain, respectively, and U_{T} is the thermal voltage. κ is the sub-threshold slope factor, signifying the influence of the gate voltage on the channel potential. This current, however, saturates after the drain-source voltage gradient crosses a threshold and becomes independent of further increase. The current after saturation is,

$$I_{\mathrm{ds}} = I_0 e^{(\kappa V_{\mathrm{g}} - V_{\mathrm{s}})/U_{\mathrm{T}}}. \tag{9.12}$$

9.1.4 Basic CMOS Circuits

The CMOS technology is used extensively to design electronic circuits of varying complexity. A few basic circuits, such as the source-follower and the multiplexer, are fundamental components of the in-pixel or on-chip circuitry of the test systems studied and detailed in this thesis. These are briefly described below.

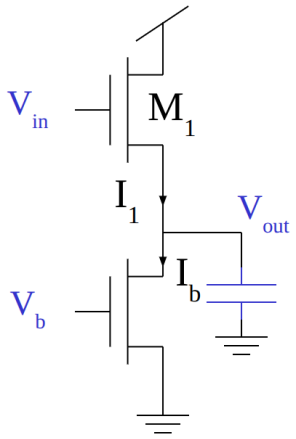

Figure 9.8: The schematic circuit diagram of a source-follower.

Source-follower

Figure 9.8 shows the schematic of a source-follower. It consists of an input transistor, whose source is connected to the drain of a biasing transistor that acts as a current source. An NMOS source-follower, as shown in Figure 9.8, consists of two NMOS transistors, while a PMOS source-follower consists of two PMOS transistors.

The gate voltage of the bottom transistor, with its source kept at ground, is biased to make it act as a constant current source. The drain of the upper transistor is set to the upper ceiling. The gate of the upper transistor is the input node of the source-follower. The output node is the shared node between the two transistors. Once the input voltage turns the upper transistors on, the current through it starts charging the node capacitance of the output node. The output voltage settles once the capacitor is fully charged, making I_1 equal to the bias current I_b. The two currents, following Eq. 9.12 and assuming the two transistors to be identical, are,

$$I_1 = I_0 e^{(\kappa V_\mathrm{in} - V_\mathrm{out})/U_\mathrm{T}},$$
$$I_\mathrm{b} = I_0 e^{(\kappa V_\mathrm{b})/U_\mathrm{T}}.$$

Since, $I_1 = I_\mathrm{b}$, this results in,

$$\kappa V_\mathrm{in} - V_\mathrm{out} = \kappa V_\mathrm{b} \tag{9.13}$$
$$\Rightarrow V_\mathrm{out} = \kappa(V_\mathrm{in} - V_\mathrm{b}). \tag{9.14}$$

Thus, the output voltage follows the input voltage with an amplification factor less than one.

4-to-1 multiplexer

Transistors can be used to build circuit elements that perform dedicated logic operations, like `AND`, `OR`, and `NOT`, called logic gates. The logic gates take several inputs, perform the predefined logic operation, and produce an output. These logic gates can be combined to perform more complex operations in the so-called combinatorial logic circuits. One such circuit is the multiplexer, which takes several inputs and passes one of them to the output. The selection of the input that will be passed to the output is done by the selection bits.

Figure 9.9 shows a 4-to-1 multiplexer, which takes four inputs and has two selection bits to select which input to pass through to the output node. Table 9.1 shows the output values of the circuit for every possible combination of the selection bits. Here, I_i is the ith input, Y is the output, and S_0 and S_1 are the selection bits. The truth table can directly be translated into a

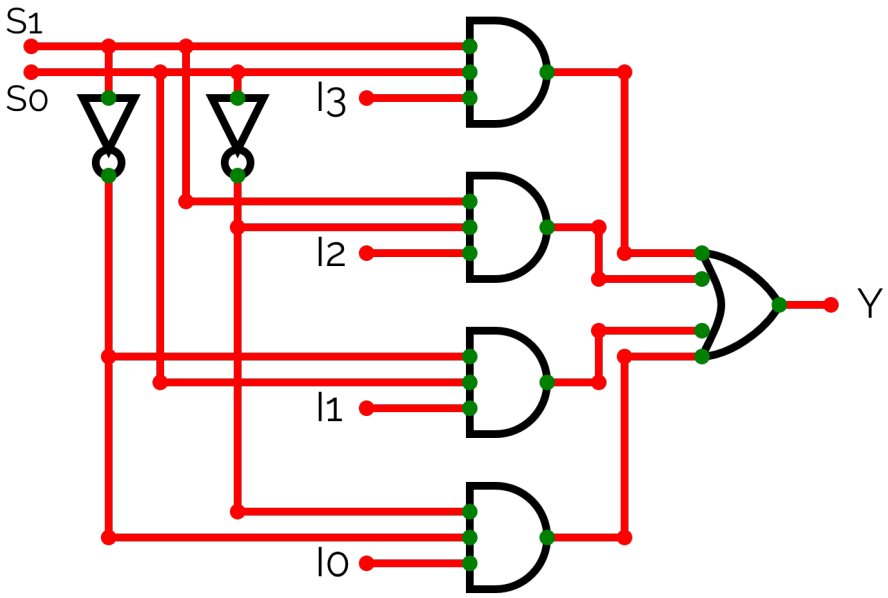

Figure 9.9: The schematic diagram of a 4-to-1 multiplexer. The shown circuit elements are different logic gates.

S_0	S_1	Output
0	0	I_0
1	0	I_1
0	1	I_2
1	1	I_3

Table 9.1: Truth table for a 4-to-1 multiplexer.

Boolean logic as,

$$Y = \bar{S}_0\bar{S}_1I_0 + S_0\bar{S}_1I_1 + \bar{S}_0S_1I_2 + S_0S_1I_3, \tag{9.15}$$

where a bar represents a `NOT` operation, a multiplication represents an `AND` operation, and an addition represents an `OR` operation. This Boolean logic is represented by the circuit shown in Figure 9.9 that can be used to select one out of four possible input options.

9.1.5 Radiation Damage

Semiconductor detectors are affected by damage when operated in environments with highly energetic radiation. The mechanism for radiation damage is classified into two main types: non-ionising radiation damage and ionising radiation damage.

Ionising Radiation Damage

The sensor volume of the silicon bulk in a semiconductor detector is unaffected by the ionising radiation damage. The charge generated in the sensitive layer of the silicon bulk by an ionising particle drifts or diffuses towards the corresponding electrode and is collected. However, highly energetic ionising radiation can also generate charge in the insulating layers, like the SiO_2 layer in a MOS structure, which can drift or diffuse towards the Si-SiO_2 interface and get trapped there. Therefore, this type of damage is also known as surface damage. Accumulation of these charges at the interface can result in parasitic electric fields and alter the gate voltage of the MOSFETs in the readout circuitry of silicon detectors.

The total ionising dose (TID) effects are independent of the particle type and are quantised by the radiation dose, representing the ionisation energy absorbed by the detector. The radiation dose is specified in two related units: Gray (Gy), which is equivalent to $1\,\mathrm{J\,kg^{-1}}$, and rad, which is equivalent to 0.01 Gy.

The importance of the TID effect tends to diminish with decreasing technology feature size, primarily due to the reduced thickness of the insulating SiO_2 layers. In the 65 nm CMOS technology, which constitutes the test structure presented in this thesis, the TID effect is minimal at the radiation levels expected at the FCC-ee; therefore, it is not discussed further.

Non-ionising Radiation Damage

The non-ionising radiation damage is associated with the non-ionising energy loss (NIEL) mechanism, which is dependent on the type and the energy of the particle. The NIEL damage manifests in bulk damage of the silicon lattice, as the non-ionising radiation displaces silicon atoms from their position in the lattice. This damage results in changes in the electrical characteristics of the silicon bulk and is seen in effects like increased leakage current and trapping of generated charges. NIEL is represented in the equivalent fluence of neutrons with the energy of 1 MeV per square centimetre, thus with a unit of $1\,\mathrm{MeV\ n_{eq}\ cm^{-2}}$.

The lifetime of the mobile carriers is impacted by the NIEL damage. The doping characteristic of the p-doped bulk or n-doped wells can also be affected due to the displacement of the donor or acceptor atoms, or the formation of localised positively- or negatively-charged regions within the space-charge region, thus affecting the depletion.

The leakage current, introduced in Section 9.1, also increases with NIEL damage, resulting in higher noise post irradiation. The change in leakage current in a p-n junction is directly proportional to the fluence Φ,

$$\Delta I = \alpha A z \Phi, \tag{9.16}$$

where, α is the current damage factor, A is the area of the p-n junction, and z is the thickness of the depletion region [180].

Annealing

The radiation-induced damages mentioned above, as well as their evolution over time, are temperature dependent [179]. The process of treating an irradiated sample with heat to induce physical changes in the solid is called annealing. Short-term annealing can repair certain effects of radiation damage, like reducing the leakage current. However, a prolonged thermal exposure can have a detrimental impact on the detector, resulting in an increased depletion voltage and worsened charge trapping. To minimise the impact of annealing on irradiated test structures while they were not being studied, they were kept at a temperature of $-18\,^{\circ}\mathrm{C}$.

9.2 Particle Interaction with Matter

Particles interact with matter via several different processes, thus depositing energy in the material, and these interaction processes are fundamental in the detection of particles. These interactions can be categorised based on the type of particles. Interactions of three types of particles are discussed here: heavy charged particles, electrons, and photons.

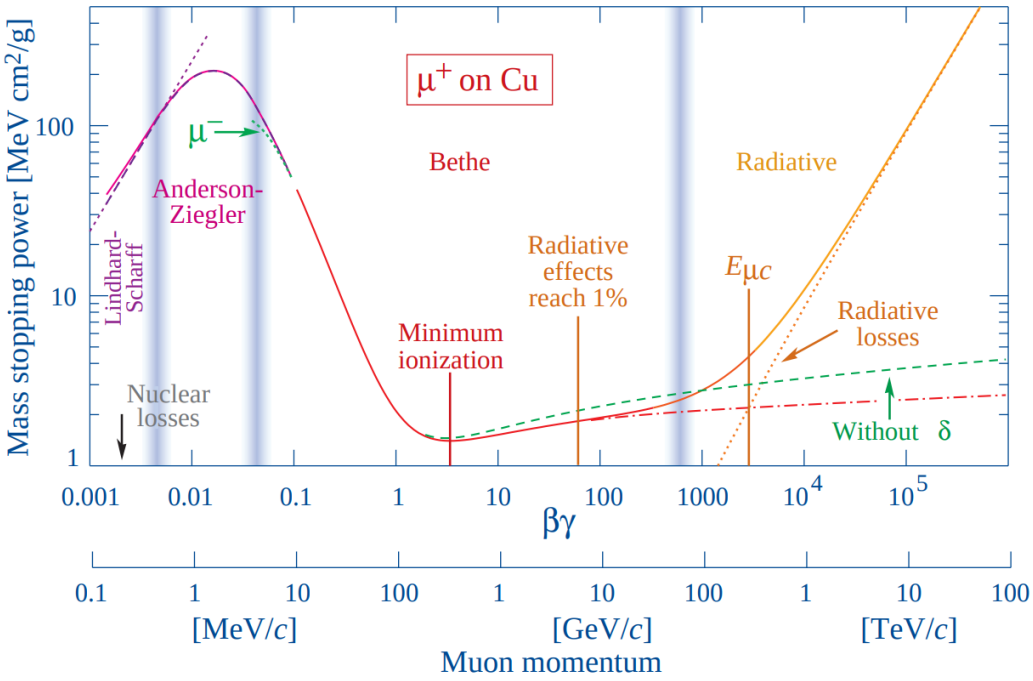

Figure 9.10: The mass stopping power for positive muons μ^+ in copper as a function of $\beta\gamma$ over nine order of momentum magnitudes. The solid curves show the total stopping power and the vertical bands represent the boundaries between different approximations. [20]

9.2.1 Interaction of Heavy Charged Particles with Matter

Heavy charged particles primarily interact with matter via ionisation and atomic excitation, i.e. the charged particle interacts with the orbital electrons, exciting them or forming electron-ion pairs. Ionisation of the material is the basis of several particle detectors, including silicon detectors. The mean energy loss of a charged particle, dE, over a path length, dx, or the stopping power, is described by the Bethe-Bloch equation [20]:

$$-\left\langle \frac{dE}{dx} \right\rangle = 4\pi N_{\mathrm{A}} r_e^2 m_e c^2 \frac{z^2}{\beta^2} \frac{Z}{A} \left[\frac{1}{2} \ln \left(\frac{2 m_e c^2 \beta^2 \gamma^2 T_{\max}}{I^2} \right) - \beta^2 - \frac{\delta}{2} \right], \tag{9.17}$$

where z is the charge of the incoming charged particle, and $\beta = v/c$ and $\gamma = 1/\sqrt{1-\beta^2}$ are its relativistic parameters with v being the particle's velocity, Z and A are the atomic number and atomic mass of the material, while I is the mean excitation potential, $T_{\max}$ is the maximum transferable kinetic energy to an electron in a single collision, and δ is the density effect correction, dependent on $\beta\gamma$.

The energy loss or the stopping power for a positively-charged muon as a function of its momentum is shown in Figure 9.10. The Bethe-Bloch equation approximates the behaviour in the central region of the plot for the range $0.1 \lesssim \beta\gamma \lesssim 1000$. The mean energy loss reaches a minimum for $\beta\gamma \approx 3$, and the particles with the corresponding energy are referred to as minimum ionising particles (MIPs). Given that all charged particles deposit energies equivalent to or higher than MIPs, detection of MIPs forms the limiting case in particle detection through ionisation. Further quantum effects, like atomic binding of the electrons, have to be considered at lower energies and radiative losses, like bremsstrahlung, become relevant at very high energies [20].

The probability density function (PDF) of the fluctuations in energy loss, called the energy straggling function, is dependent on the thickness of the absorber material. For thick absorbers, the PDF can be approximated by a Gaussian function. However, for thin silicon absorbers, as

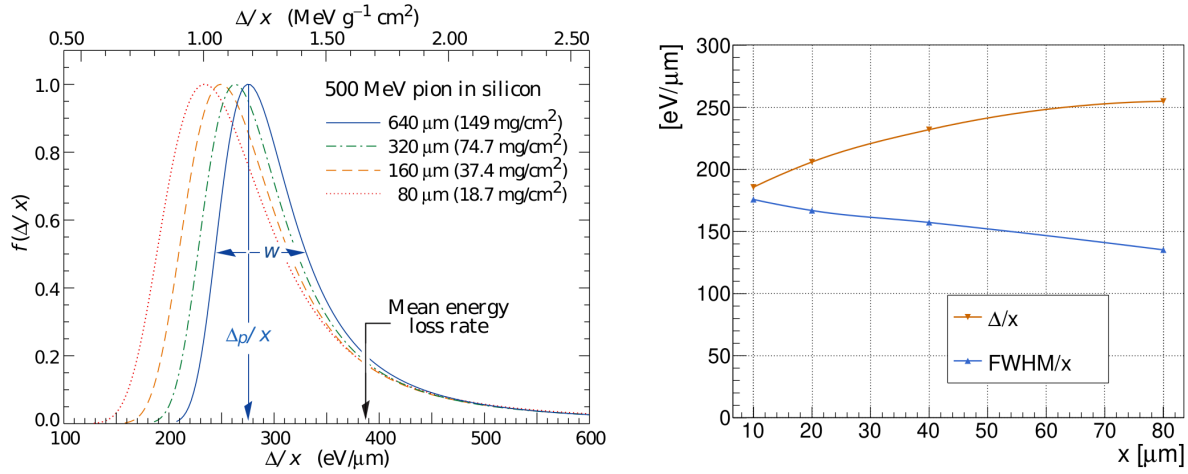

(a) **(b)**

Figure 9.11: Energy loss in thin silicon absorbers. (a) Energy straggling function of a 500 MeV pion in silicon layers with varying thickness. The function has been normalised to unity at the most probable energy loss value (Δ/x). w is the full-width-at-half-maximum (FWHM). [20] (b) The most probable energy loss values for very thin silicon as a function of the layer thickness, following the Bichsel function, for all particles with $\beta\gamma > 100$. [181]

in silicon detectors, the PDF is better described by a Landau function [20], with the ionisation by the secondary δ-electrons resulting in the tail of the function, as shown in Figure 9.11a. For ultra-thin absorbers with $x < 160\,\mu\text{m}$, even the Landau model becomes inadequate, and a better description of energy loss PDF is given by the 'Bichsel functions' [181], as the Landau model underestimates the most probable energy loss. The dependence of the most probable energy loss and the full-width-at-half-maximum as a function of the thickness, x, following the Bichsel model, is shown in Figure 9.11b. It must be noted that the most probable energy loss in a silicon layer with a thickness 20–30 µm, similar to detectors presented in this thesis, generates around 60 electron-hole (e-h) pairs per micron of path length, unlike the generally quoted value of 80 e-h pairs per micron, which is valid for thicker layers [182].

9.2.2 Interaction of Electrons with Matter

Due to their low mass, the interactions of electrons must be considered separately. Electrons interact with the orbital electrons of the material they are passing through, resulting in scattering and the loss of a large fraction of their energy. Additionally, the electrons can also lose their energy through interactions with the atomic nuclei and radiative processes like bremsstrahlung. Unlike heavier charged particles, where radiative losses only become relevant at the highest energies, electrons with moderately high energies of a few tens of MeV lose their energies mainly through radiative processes.

The material budget of detectors is generally conveyed in the units of radiation length, X_0. However, the energy loss through ionisation is still the most important effect in detection techniques.

9.2.3 Interaction of Photons with Matter

The three processes that dominate the interaction of photons with matter are: photoelectric effect, incoherent or Compton scattering, and pair production [183]. The photoelectric effect refers to the absorption of a photon by an orbital electron, which is consequently ejected from

the atom. The energy of the ejected electron, E, is given by,

$$E = h\nu - E_0, \tag{9.18}$$

where ν is the frequency of the incident photon and E_0 is the binding energy of the electron. The photoelectric effect is the dominant interaction process for low-energy photons. Compton scattering refers to the inelastic scattering of photons with free electrons. If the energy of the incident photon is high enough compared to the binding energy, the electrons can, in principle, be considered free. High-energy photons undergo pair production, which is the conversion of a photon into an electron-positron pair. It occurs in the presence of an electric field and a third body, typically atomic nuclei, in order to conserve momentum. The minimum energy required for pair production is $2m_e c^2$. The mean free path for pair production, λ_γ, is related to the radiation length [20],

$$\lambda_\gamma = \frac{9}{7} X_0. \tag{9.19}$$

9.3 Methods for Charged Particle Detection

Particle detectors are generally designed to detect particular types of particles and are specialised to measure certain properties of these particles. Experiments mentioned in Chapter 3 host sub-detectors that are each sensitive to different types of particles and each measure specific properties of the particles that pass through them. Detectors designed to measure the trajectories, charge, and/or momentum of charged particles are classified as tracking detectors.

Table 9.2 summarises the typical spatial resolution of several charged particle detectors. The physical principle used by all these detectors is essentially the same. An incoming charged particle ionises the sensitive medium within the detector, and the charge generated this way is either directly collected by or indirectly induces charge on an electrode, which is then read out. The readout is typically done electronically.

Detector Technology	**Typical spatial resolution**
Bubble chamber	10–150 µm
Drift chamber	50–100 µm
Micro-pattern gas detectors	30–40 µm
Silicon strip	pitch/$\sqrt{12}$
Silicon pixel	$\lesssim$10 µm

Table 9.2: Typical spatial resolution of different charged particle detectors. [20].

9.4 Particle Detection with Semiconductor Detectors

Detection of charged particles with semiconductor devices follows the same fundamental principle as the one described in Section 9.1 for a reverse-biased p-n junction. A charged particle passing through the sensor generates charge within the p-bulk, which can be implemented by silicon grown by the float-zone (FZ) or Czochralski (Cz) processes or epitaxial silicon, depending on the type of sensor. In the reverse-biased configuration, the electron carriers move towards the positive n^+-implants, while the holes move in the opposite direction towards the p^{++}-substrate or backplane. The charge is either directly collected by the input pad of the readout electronics or induces a signal by moving in the electric field.

When the charge collection implant and the readout metal pad are separated by a capacitor, they are said to be capacitively-coupled or AC-coupled, as opposed to when they are directly connected, which is referred to as DC-coupled. DC-coupling generally results in a shift in the baseline as well as its variations, due to the leakage current reaching the readout stage, whereas only the AC signal is propagated to the readout channel by the capacitor in the AC-coupled configuration. Hence, better noise performance is seen in AC-coupled detectors, and this configuration allows for the application of higher voltages for the depletion of the sensitive area of the detector.

Silicon is the most widely used element in semiconductor detectors, also referred to as solid-state detectors or SSDs. Several reasons make silicon a suitable medium for designing detectors [184]. The small band gap in silicon means that very low energy of 3.6 eV is required to generate an electron-hole pair. In comparison, the energy required to generate an electron-ion pair in a gas is about 30 eV. This fact, combined with the increased mass density of silicon, makes it possible to design compact detector modules. Silicon detectors also do not typically employ charge multiplication techniques, unlike most gaseous detectors. The charge deposition by minimum ionising particles in a silicon detector with the thickness of the sensitive region of 300 µm produces a charge of about 3.5 fC or 22000 electrons [20].

Most of the commercial electronics are silicon-based, making the large-scale production of highly granular detectors streamlined. Silicon detectors can also be designed to withstand high irradiation levels, making them an appropriate detection technology to be placed very close to the interaction point.

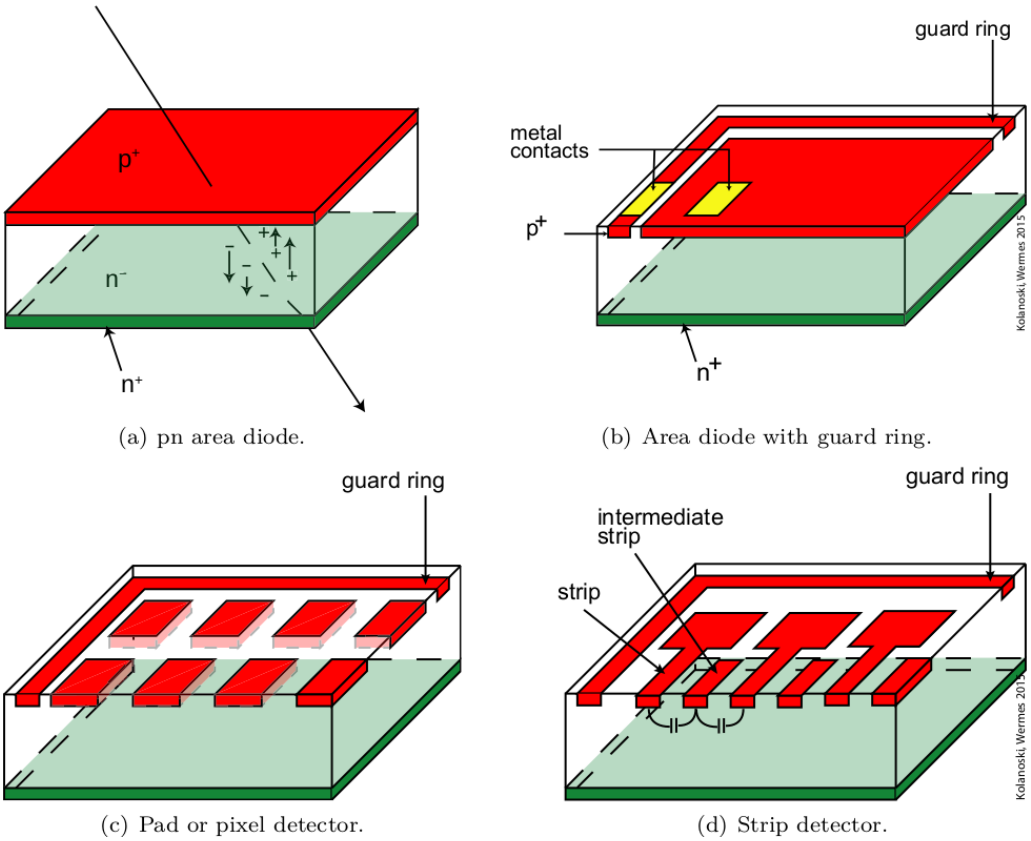

(a) pn area diode.

(b) Area diode with guard ring.

(c) Pad or pixel detector.

(d) Strip detector.

Figure 9.12: The conceptual design of single-sided silicon detectors with different geometries. n^+ and n^- refer to stronger or weaker doping relative to the standard n-type doping, similar representations are used for p-type doping. [179]

9.4.1 Silicon Detector Geometries

Semiconductor detectors can be designed single-sided or double-sided, depending on whether the silicon wafer undergoes fabrication processing on only one side or both sides. Double-sided detectors can incorporate more variable and complex designs and can be used for two-dimensional measurements with the same material. However, this requires excessive precautions to protect the already processed side of the wafer. On the other hand, single-sided detectors are simpler and more cost-effective to fabricate. Therefore, most large area detectors for high-energy physics experiments, including the test structure presented in this thesis, are designed as single-sided detectors. Hence, only single-sided detectors will be discussed in the following.

Some of the important geometrical configurations of silicon particle detectors can be p-n junction or area diodes, strip detectors, and pad or pixel detectors, as shown in Figure 9.12. An area diode is the simplest detector geometry of the size of a few cm^2, doped to create a p-n junction, which is depleted by operating the diode in reverse bias configuration. The area diode can be surrounded by a guard ring to sink the leakage current coming from the edges of the sensitive volume, thus reducing the noise.

If the top implant of the diode is subdivided into strips, the device is known as a strip detector. Strip detectors can be used to precisely measure only one spatial coordinate, but do not host a very complex readout system. The pitch of the detector is defined as the distance between the centers of two adjacent strips. The chip electronics can be placed at the edges of the strips, and the detector with N strips requires only N readout channels. The ATLAS and CMS experiments at the LHC employ silicon microstrip detectors as their large area tracking detectors.

The detector can be subdivided into smaller implant areas at the surface instead of strips. If the size of these implants or pads is small enough, they are referred to as pixel detectors. Pixel detectors in high-energy physics experiments generally have rectangular or square shapes; however, other geometrical structures, like a hexagon, can also be used. Unlike strip detectors,

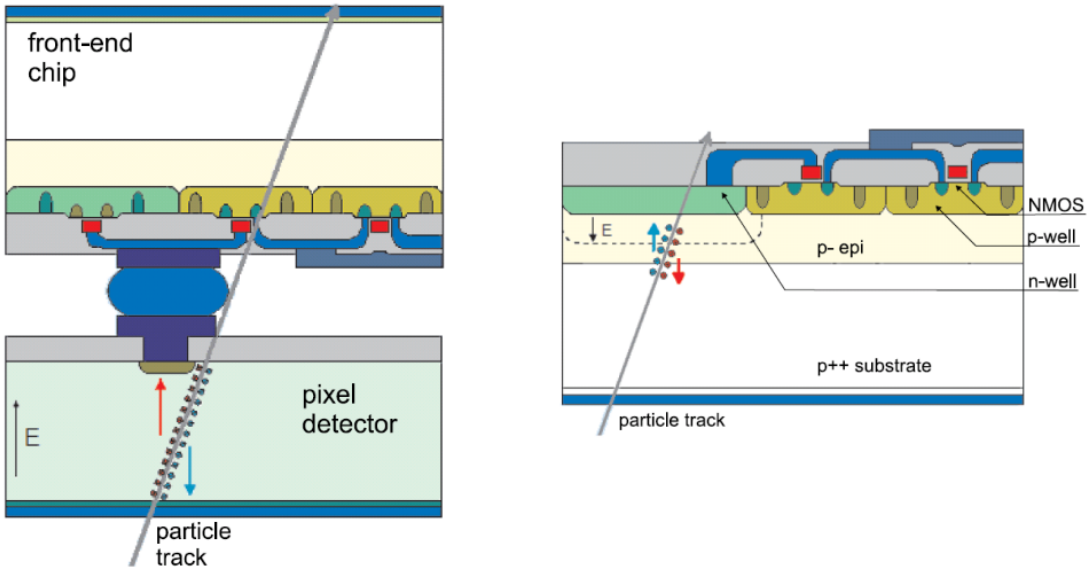

(a) Hybrid pixel **(b)** MAPS pixel

Figure 9.13: The cross-section of (a) a typical hybrid pixel detector and (b) a typical MAPS-based pixel detector. The hybrid pixel detector features a sensor that is bump-bonded with the readout electronics, while the MAPS-based pixel detector combines the two into a single silicon volume. [182]

pixel detectors have more complex readout architectures and require significantly more readout channels: N^2 readout channels for a detector with $N \times N$ pixel grid. The innermost layers of the tracking detectors in the ATLAS and CMS experiments use hybrid pixel detectors.

Pixel detectors enable a precise three-dimensional space-point measurement, even in environments with high particle fluxes. The occupation density or occupancy, signifying the fraction of readout channels registering a hit by a traversing particle, in vertex or tracking detectors, is very high due to their proximity to the interaction point. Pixel detectors are therefore ideal for the detector subsystem placed closest to the interaction point. Two broad categories of pixel detectors, based on the fabrication of the sensor and readout electronics, namely, hybrid and monolithic, will be discussed below.

9.4.1.1 Hybrid Pixel Detectors

Hybrid pixel detectors, shown in Figure 9.13, are composed of two parts, the sensing volume and the section containing the readout circuitry. The pixel sensor is a silicon diode subdivided into pixel cells, and the readout chip with CMOS architecture is designed with exactly the same cell pattern. The sensor and the readout chip are connected via a microscopic connection that is electrically and thermally conductive, referred to as a bump bond, for every pixel. The pixel sensor is operated in a reverse bias configuration at a high voltage to fully deplete the sensing volume. The full depletion of the sensor and the high electric fields experienced by the mobile charge carriers generated by a passing particle make hybrid pixel sensors the detector of choice in high radiation environments. The fine granularity of the pixel detectors also makes them very efficient in applications with a high rate of particle incidence. Therefore, the majority of the HEP experiments use hybrid pixel detectors as the detector technology for layers closest to the interaction point.

The sensor and the readout chip of a hybrid pixel sensor can be optimised individually, and the same readout chip can be used for different types of sensors. However, the fabrication and the assembly of the pixel sensor and the readout chip can be cost-intensive, and the readout chip adds to the material budget, affecting the track reconstruction and the momentum resolution of the detector due to multiple scattering and secondary interactions in the readout part of the detector. Additionally, the bump bonding can be a limit to the pixel pitch size.

9.4.1.2 Monolithic Pixel Detectors

Since the pixel sensor and the readout chip are both fabricated on silicon, it is possible to integrate the two on the same silicon wafer, resulting in a monolithic pixel detector, as shown in Figure 9.13. Thus, monolithic pixel detectors significantly reduce the material thickness of the detector. There are several technologies that can be used to achieve monolithic detectors, like DEPFET, silicon-on-insulator (SoI), and monolithic active pixel sensors (MAPS).

Monolithic pixel detectors have a few major challenges. Designing monolithic detectors with commercial CMOS technologies is important to reduce costs. Achieving a sufficiently large depletion region while keeping the pixel capacitance low to attain a good signal-to-noise ratio and reduce the power consumption is difficult and requires advanced optimisation. For application in HEP experiments, tolerance to a high radiation environment is critical, which can be hard due to the lower depletion depths in monolithic detectors because of the limits on the applied depletion voltages.

Most of the commercial CMOS technologies only offer low-resistivity substrates, which are not suitable for designing monolithic sensors, as the depletion depth d is dependent on the

substrate resistivity (ρ) and bias voltage (V),

$$d \propto \sqrt{\rho V}. \tag{9.20}$$

However, CMOS imaging technologies feature an epitaxially grown high-resistivity layer with a thickness of the order of 10 µm. Unlike DEPFET pixel detectors, MAPS use commercial CMOS technology. Deep n-type and p-type implants, called wells, are introduced within the epitaxial p-type bulk. The n-type implants form the collection diodes to collect electrons, while the readout electronics of the MAPS are implemented within deep p-wells. The high resistivity of the epitaxial layer, compared to the substrate, allows it to be used as the sensing volume of the MAPS-based pixel detector. The n-well that houses the PMOS transistors of the readout CMOS circuitry can also collect the charge generated by a traversing charged particle. The deep p-well shields the PMOS transistors of the readout circuitry from collecting the generated charge.

The small pixel size in MAPS-based pixel detectors results in an excellent spatial resolution. However, the energy resolution of MAPS tends to be lower than hybrid pixel detectors, as about 1500 electron-hole pairs are generated in a 25 µm thick epitaxial layer by a traversing minimum ionising particle. This is lower by an order compared to the typical 300 µm thick silicon detectors. The lower energy resolution consequently limits the particle identification capabilities of MAPS.

With considerably shallower depletion depths compared to hybrid pixel detectors, MAPS are not as tolerant to extremely high radiation levels. However, they are still efficient at low to moderate levels of irradiation ($\mathcal{O}(10^{13}$-10^{15} NIEL)). Their performance can be further enhanced by improving the depletion of the sensitive volume. With some design optimisations, even full depletion of the sensing volume of the MAPS-based pixel detectors can be achieved. Such monolithic sensors are called depleted MAPS or DMAPS, which are the subject of this thesis.

9.5 MAPS Detector Properties

A few properties of pixel detectors, the measurements of which are critical to characterise a developing detector technology, are described below. These properties will be repeatedly referenced while studying the performance of the test structures presented in this thesis.

9.5.1 Charge Collection

During laboratory tests of MAPS-based test structures, a radioactive source with monochromatic X-rays is used. The main process of interaction of soft X-rays is the photoelectric conversion. The emitted photo-electron has a range of $\lesssim$1 µm, hence, it will generate almost all of the electron-hole pairs inside the region where the photoelectric conversion has taken place. Three such regions can be identified: depleted region, undepleted region, and substrate.

If the photoelectric conversion takes place within the depleted region in the epitaxial layer, all of the charge tends to be collected by the same pixel by drift. However, if it takes place outside the depleted region but still within the epitaxial region, the electrons are trapped within the epitaxial layer and thermally diffuse within it until they either recombine or encounter the boundary of the depletion region of the pixel or one of the neighbouring pixels and get collected. In this case, the charge may be shared among neighbouring pixels. If the photo-electron generates charge in the substrate, the electrons diffuse within the substrate, and the ones that reach the epitaxial layer get trapped there and either recombine or get collected.

The entire charge generated in the first two cases is expected to be collected, but in the third

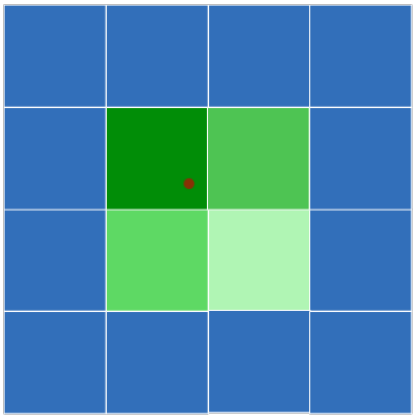

Figure 9.14: Section of a pixel matrix showing charge generated by a passing charged particle being shared among neighbouring pixels. The red dot represents the incidence of a charged particle. The region with the green shade shows the pixels that collected the charge generated by the incident particle, with the darker shade representing a larger fraction of charge collected.

case, the collected charge tends to be less than the generated charge.

9.5.2 Charge Sharing

When a charged particle passes through the matrix of a silicon pixel detector, it generates charge in the form of electron-hole pairs by ionising the sensitive region of the pixel. In the reverse-biased configuration, the electrons drift towards the n-doped collection electrode. However, when the incident charged particle passes near the edge or the corner of a pixel, the generated charge can diffuse across the pixel boundary and get collected by the neighbouring pixel. This phenomenon is generally referred to as charge sharing among pixels. The group of pixels that collect charge generated by a passing charged particle are referred to as a cluster.

Charge sharing has a direct impact on the detector performance. If a large fraction of the generated charge is shared with the neighbouring pixels, the charge collected by the seed pixel, which is the pixel that collects the most charge, may not exceed the threshold set to reduce noise. Therefore, detectors with high charge sharing tend to have low efficiencies at higher thresholds. Since the charge is mainly shared between the pixels by diffusion, especially in the case of very thin detectors, partial depletion of the sensitive region tends to increase charge sharing, while there is minimal charge sharing in fully-depleted detectors.

However, if the charge is only collected by the pixel on which the charged particle was incident, the position of the particle hit can be best assigned as the center of the pixel. Whereas, in the case of charge sharing, the cluster position can be defined by the center of gravity of the pixels that collect charge over the threshold, improving the spatial resolution of the detector. If the information on the charge collected by the pixels is available, a charge-weighted center of gravity can be calculated, which may further improve the spatial resolution of the detector.

9.5.3 Spatial Resolution

The position of a passing particle is defined either by the seed pixel position or the cluster position within the matrix of the silicon pixel detector. A residual is defined as the distance between the cluster position and the true point of incidence of the charged particle on the detector. The residuals are generally defined separately in the x- and y-axis. The standard deviations of the Gaussian distributions of these residuals are referred to as the resolutions in the respective axes. The arithmetic or geometric mean of these resolutions, depending on the

geometry and correlation of the residuals in the two axes, is referred to as the spatial resolution of the detector.

The limit of the spatial resolution along a particular axis is the spatial resolution of a detector with no charge sharing. For such a detector with a pitch of p along the dimension x, assuming a uniform distribution of points of incidence of charged particles, the variance of the spatial residuals will be,

$$\langle \Delta x^2 \rangle = \frac{1}{p} \int_{-p/2}^{p/2} x^2 dx = \frac{p^2}{12} \ . \tag{9.21}$$

Therefore, the limit of the spatial resolution along an axis is $p/\sqrt{12}$, where p is the pitch of the detector along that dimension.

9.6 FCC-ee Vertex Detector

MAPS, with a potential to achieve excellent spatial resolution, low material budget, and minimal power consumption, are ideally suited to satisfy the stringent requirements of the FCC-ee vertex detector. It has, therefore, been chosen as the technology for the vertex detectors of all four detector concepts being developed for the FCC-ee, as mentioned in Chapter 3. Continued R&D efforts in collaboration with experiments that have synergistic detector requirements are essential to optimise the MAPS technology, making it the most promising candidate for the FCC-ee vertex detector. The upgrade of the ALICE inner tracking system offers such a possibility, and the developments towards the same will be detailed in the following chapters.

10 The ALICE Tracking System Evolution and the Analogue Pixel Test Structure

A Large Ion Collider Experiment (ALICE) [185] is one of the four experiments at the Large Hadron Collider. It was designed as a specialised experiment to study nuclear collisions. It primarily investigates the nature of the Quark-Gluon Plasma (QGP) through the heavy ion Pb-Pb collisions. The heavy ion studies are complemented by the precision measurements from p-Pb and p-p collisions. The innermost parts of the ALICE apparatus encounter a high flux of charged particles. The ALICE apparatus features tracking detectors with excellent position resolutions, which are required to measure the trajectory of these charged particles and detectors to aid in the particle identification (PID) of these charged particles.

Figure 10.1 shows that the ALICE experiment consists of a barrel and a forward muon arm. The barrel consists of the inner silicon tracking detectors called the Inner Tracking System (ITS), a Time Projection Chamber (TPC), two subdetectors to aid in particle identification: the Transition Radiation Detector (TRD) and the Time-of-Flight (ToF) detector, two electromagnetic calorimeters: EMCAL and PHOS. These detector systems are enveloped by a solenoid magnet. The forward muon arm comprises a complex arrangement of muon tracking detectors, muon walls, and muon triggers.

FCC-ee, being an ultra-precision machine, imposes extreme requirements on its vertex detectors, similar to the ALICE inner tracking system. Excellent vertex reconstruction and resolving secondary vertices is essential to precision studies of the Higgs boson and flavour physics at the Z resonance. Heavy flavour tagging performance can be improved with vertex reconstruction, and the reconstruction of the τ lepton decay vertices is essential for precision τ physics.

The requirements from the innermost sub-detectors of the FCC-ee and the ALICE apparatus to meet their respective physics goal are equivalent, as presented in Table 10.1. An excellent spatial resolution, resulting in a good vertex resolution, is critical for heavy-flavour tagging. A low material budget is crucial to measure the low momentum tracks in heavy ion collisions

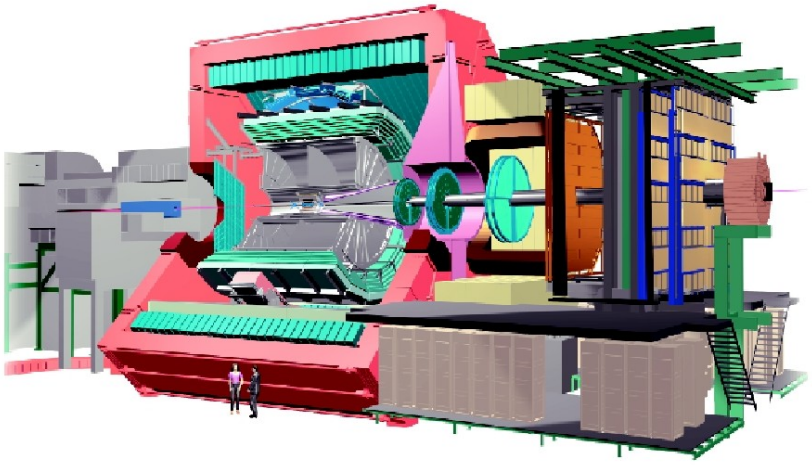

Figure 10.1: The detector layout of the ALICE apparatus. [185]

	ALICE ITS3	FCC-ee
Spatial resolution	5 µm	3 µm
Material budget (x/X_0 per layer)	0.07 %	0.3 %
Radiation tolerance (NIEL)	10^{13} 1 MeV $n_{eq}cm^{-2}$	$\sim 10^{13}$ 1 MeV $n_{eq}cm^{-2}$
Radiation tolerance (TID)	10 kGy	~10 kGy
First layer radius	19 mm	13.7 mm
Power density	<40 mW cm^{-2}	~50 mW cm^{-2}

Table 10.1: The requirements from ALICE Inner Tracking System upgrade (ITS3) and the vertex detector of the FCC-ee that must be satisfied to meet the main physics goals [91, 186, 187].

in ALICE, and the excellent track resolution needed by the FCC-ee. The radiation tolerance required by the sensors is moderate in the case of ALICE and moderate to high for the FCC-ee. Low power density is needed in both experiments to allow air-cooling of the sub-detectors. This alignment in the requirements makes ITS3 a stepping stone for the R&D on the FCC-ee vertex detector.

10.1 The ALICE Inner Tracking System

The ALICE ITS serves as an ideal example to demonstrate the evolution of tracking and vertex detector technology. The first version of the ITS [189] consisted of two innermost layers of Silicon Pixel Detectors (SPD), two middle layers of Silicon Drift Detectors (SDD), and two outer layers of double-sided Silicon Strip Detectors (SSD). These layers were located between the radii of 39 mm and 430 mm. The inner layers were designed for a high particle density of up to 100 particles per cm^2 per readout frame, while strip detectors were deemed sufficient for the outer layers with track densities falling to the level of one particle per cm^2 per readout frame. All detector components were optimised to achieve a radiation length of 1.14% X_0 per layer, the lowest among all LHC experiments at the time [190]. The impact parameter resolution of the ITS was 75 µm at transverse momentum above 1 GeV. A major limitation of the ITS was its maximum readout rate of 1 kHz irrespective of the detector occupancy, with a dead time close

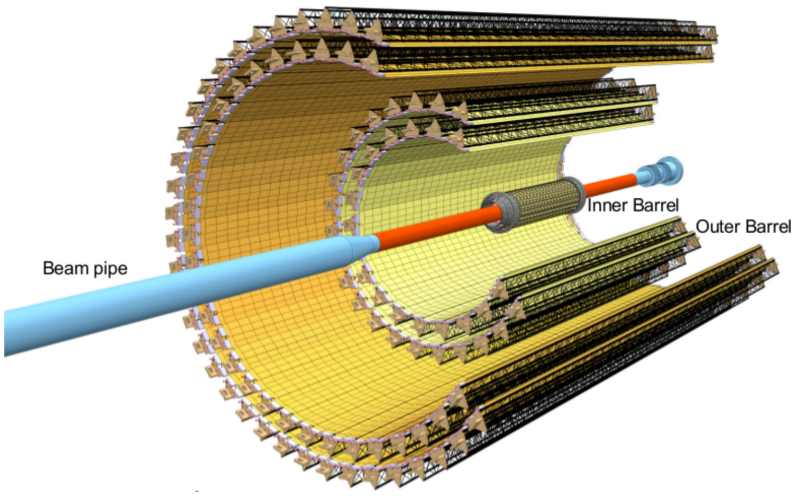

Figure 10.2: The conceptual layout of the ITS2. The inner barrel consists of the three innermost layers while the outer barrel consists of the two middle and the two outer layers. [188]

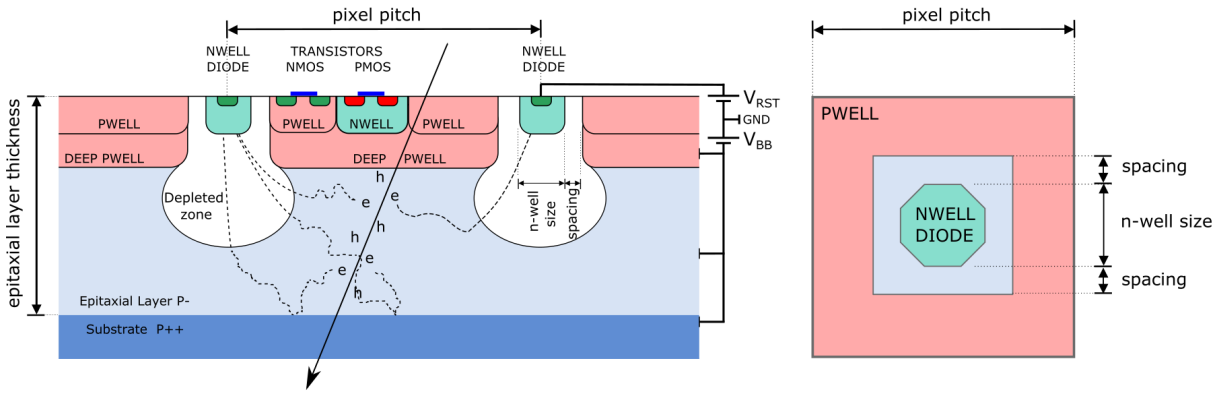

Figure 10.3: The cross section and the top view of a pixel of a MAPS used in the ALPIDE chip. The arrow represents a charged particle passing through the pixel sensor and the wobbling lines represent the excited electrons. [194]

to 100% [182].

The upgraded version of the ITS [188], referred to as the ITS2, replaced the entire detector with a seven-layer pixel detector. The Inner Barrel (IB) consists of the three innermost layers, while the Outer Barrel (OB) consists of the two middle and the two outer layers. Figure 10.2 shows the detector layout. The detector upgrade consists of several improvements: reduction of the radius of the innermost layer from 39 mm to 23 mm; reduction of the material budget from 1.14% of a radiation length per layer to 0.36% of a radiation length per layer; reduction in the pixel size from 50 µm × 425 µm to 27 µm × 29 µm, which are thinned down to 50 µm and 100 µm for the IB layers and the OB layers, respectively. The barrel layers are segmented in the azimuth into mechanically independent elements called staves. The structure of these staves consists of a carbon fibre-based truss-like lightweight support structure, referred to as the Space Frame, a cold plate that embeds the cooling pipes, and the Hybrid Integrated Circuit (HIC), consisting of a flexible printed circuit which interconnects several pixel chips and contains other passive components. The ITS2 consists of 12.5 Gigapixels, comprising a total active silicon area of 10 m^2.

10.1.1 The ALPIDE Chip

The ITS2 upgrade requirements led to the development and design of the ALICE Pixel Detector (ALPIDE) chip [191]. It is based on MAPS, enabling the fabrication of remarkably thin sensors through the integration of the sensor and readout chip, which can be designed cost-effectively using commercial CMOS technologies. MAPS were already being used in high-energy physics experiments, like the STAR PXL detector [192], but further R&D was necessary owing to the stringent requirements of the ITS2 upgrade. The ALPIDE chip was designed in the 180 nm CMOS technology and was fabricated with a deep p-well imaging process provided by TowerJazz [193]. Figure 10.3 shows the cross-section of a pixel in the ALPIDE chip. The pixel consists of a very small n-well collection electrode of a 2 µm diameter leading to a minute capacitance (∼ fF). The p-type epitaxial layer has a thickness of 25 µm. The deep p-well shields the in-pixel circuitry from collecting the generated charge. A reverse bias is applied via the collection electrode to expand the depletion region for better charge collection.

The chip satisfied the key objectives of low power consumption of about 40 mW cm^{-2} and achieving higher radiation tolerance. With the pixel size of 27 µm × 29 µm, the ALPIDE chip can reach resolution lower than the required 5 µm for the inner barrel layers and 10 µm for the outer barrel layers. Since its installation, the ITS2 has continuously operated over 24000 chips with over 99% of the chips being functional and the fake hit rate for every layer remaining about

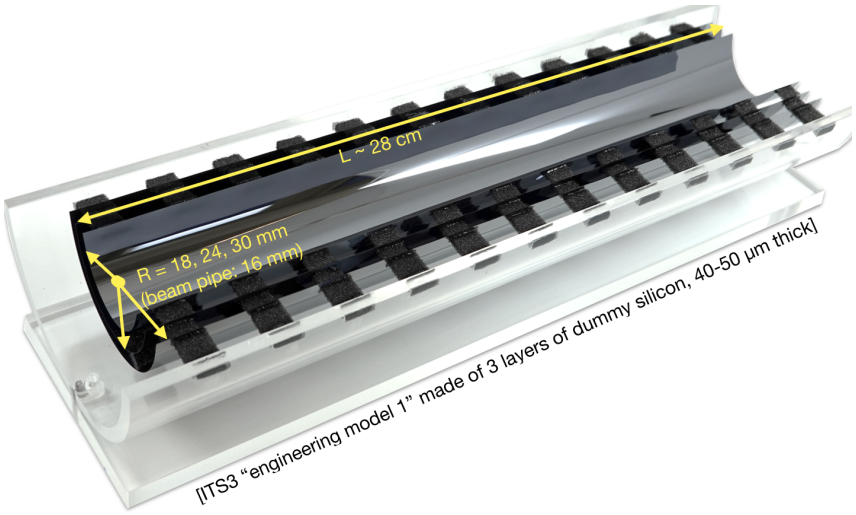

Figure 10.4: Engineering model of the layout of the ITS3 design. Three wafer-size dummy silicon pieces with thickness 40 µm and length 280 mm, simulating the three half-layers, are kept bent by carbon foam spacers only at the edges of the half-layers. [186]

a factor below the requirement of 10^{-6} per event per pixel.

It must be noted that even after these advancements, the silicon constitutes less than 15% of the material budget of the ITS2, with the rest composed of the liquid cooling system, circuit boards for power and data transmission, and mechanical support. Further improvement can be achieved by eliminating these components. This inspired the next planned upgrade of the innermost three layers of the ITS2 to a nearly perfect cylindrical detector design.

10.2 The Inner Tracking System Upgrade

The next planned upgrade of the Inner Tracking System (ITS3) [186] aims to replace the innermost three layers of the detector by wafer-scale sensors thinned down to 50 µm and bent into half-cylinders forming a half-barrel. Thus, each half-layer will be formed by a single piece of silicon. The innermost layer will be moved even closer to the interaction point at a radius of 19 mm. The non-ionising radiation load is expected to increase to 10^{13} 1 MeV n_{eq} cm^{-2} and the ionising radiation load is expected to increase to 10 kGy.

The wafer-scale sensors are enabled using a technique called stitching [195, 196] to eliminate the need for circuit boards to transmit power and data signals. The stitching technique allows manufacturing devices significantly larger than the size of the design reticle. The circuits to transmit power and data will be at the smaller edge of the sensor. The support structure can be removed by benefitting from the increased stiffness from rolling silicon, which becomes flexible at very low thicknesses ($\sim$ 50 µm). The wafer-scale sensor units can be supported using carbon foam half-rings at the shorter edges, which also work as radiators and help to dissipate heat from the power circuits and carbon foam longerons at the longer edges. The power consumption of the sensor matrix is targeted to be reduced below 20 mW cm^{-2} so that the detector does not require liquid cooling and can be air-cooled. This is achieved by moving from the 180 nm CMOS technology to the 65 nm technology node. These developments are expected to reduce the material budget to 0.07% of radiation length per layer. Figure 10.4 shows the engineering model depicting the mechanical feasibility of the design.

An improvement in the pointing resolution by a factor of 2 is expected over the complete range of transverse momentum of interest. Additionally, substantial gains are also foreseen in the tracking efficiency at low momenta. This would have a significant impact on physics studies,

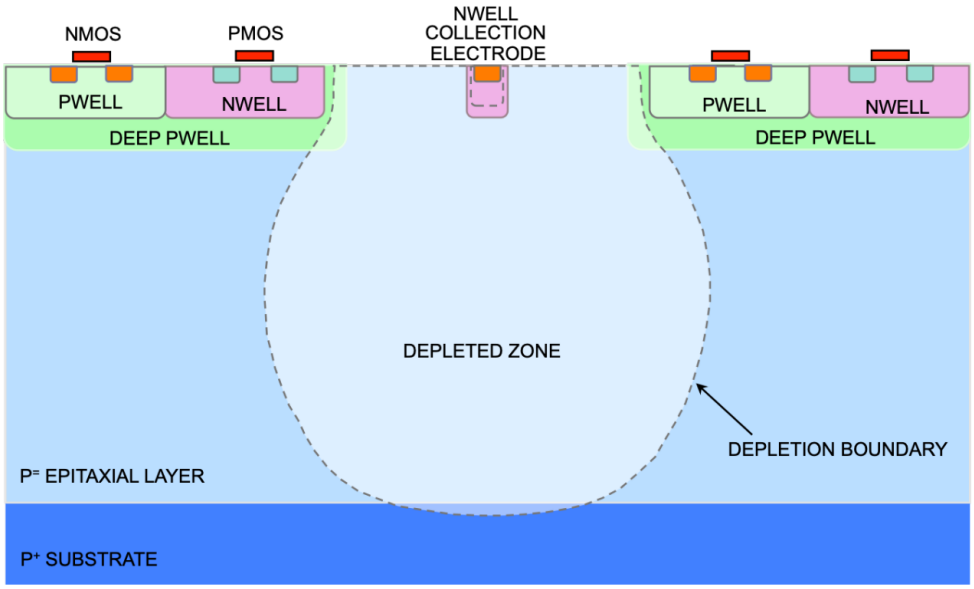

Figure 10.5: Cross-section of the pixel design labelled 'Standard' process. The dashed lines show the boundaries of the depletion region. [197]

particularly in heavy flavour decays, as it will result in an improved precision to distinguish secondary decay vertices.

10.2.1 Process Modification

The pixels in the ALPIDE chip host a very small collection electrode, as shown in Figure 10.5, in order to reduce the pixel input capacitance. The depletion region begins at the junction of the collection electrode and the epitaxial layer and expands with increasing reverse bias voltage. However, the depletion region does not extend far laterally into the epitaxial layer between the deep p-well shielding the in-pixel circuitry and the low resistivity substrate due to the lack of a potential gradient. This results in a balloon-shaped depletion region close to the collection electrode, and diffusion is the dominant mode of transport for the generated charge as it moves towards the collection electrode. This process variant is labelled as the 'Standard' process. The charge transport in this manner leads to a slow charge collection and a significant charge sharing among the neighbouring pixels, as described in Section 9.4. Charge sharing can contribute to the improvement of the position resolution, but can lead to the degradation of efficiency, especially after radiation damage. The depletion region can be extended to the full width of the pixel by increasing the size of the collection electrode and, in effect, the junction, but that would significantly increase the pixel input capacitance. Reducing the area of the deep p-well would also improve the depletion, although it would reduce the available area for the in-pixel circuitry. Alternatively, a planar junction can be introduced by inserting a layer with the same type of doping as the collection electrode. The depletion will begin from the junction and extend to the full area of the pixel. The depletion region can then further be extended towards the collection electrode by increasing the reverse bias voltage, thus reducing the effective pixel input capacitance.

A low-dose deep n-type implant is introduced to implement such a planar junction in the process modification for the ITS3 upgrade [197]. This implant is placed in the pixel matrix below the deep p-well holding the in-pixel circuitry. It has a low enough dose to be fully depleted up to the n-well collection electrode with small reverse bias voltages. Such a design ensures the depletion over the full area of the pixel while keeping the pixel input capacitance of the order of a few fF. This process variant is labelled the 'Modified' process and is shown in Figure

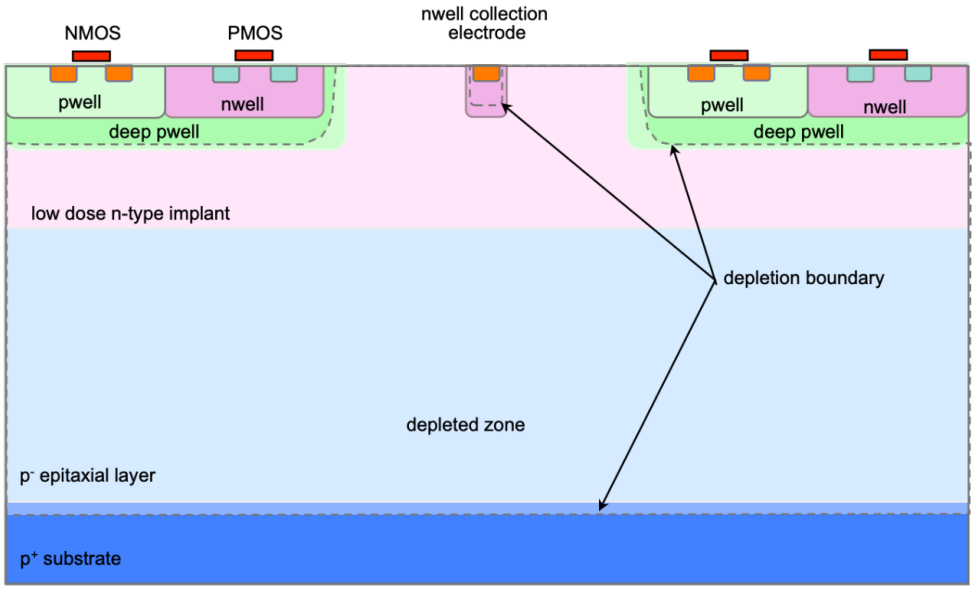

(a)

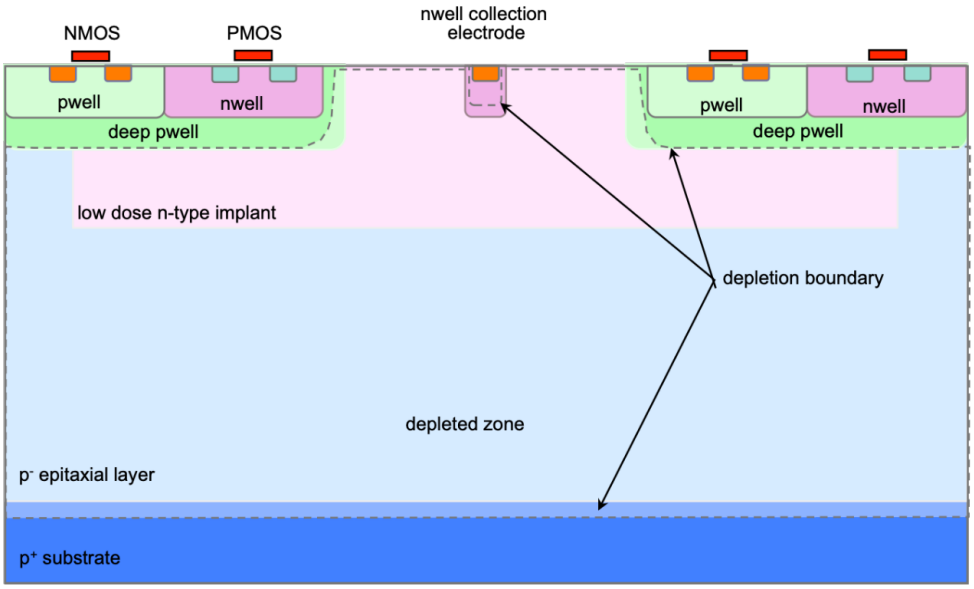

(b)

Figure 10.6: Cross-section of the pixel design labelled (a)'Modified' process: with deep blanket low-dose n-type implant and (b) 'Modified with Gap' process: with gap in the deep low-dose n-type implant. The dashed lines show the boundaries of the depletion region. [197, 198]

10.6a. With the depletion region extending over the full area of the pixel, the dominant mode of transport for the generated charge would be drift, and charge collection would be faster than in the 'Standard' process. This modification is also expected to significantly reduce charge sharing, thereby slightly impacting the position resolution.

An additional modification has been introduced to optimise the electric fields at the pixel boundaries. The lateral electric field at the pixel boundaries can be increased by introducing gaps in the low-dose n-type implant at the pixel boundaries [198]. This further speeds up the charge collection. This process variant is labelled 'Modified with Gap' process and is presented in Figure 10.6b.

10.3 Small Scale Sensors

Moving from the 180 nm CMOS technology to the 65 nm CMOS technology aids in reducing the power consumption per transistor and allows for a higher granularity of transistors, leading to the accommodation of more complex in-pixel circuits. The characterisation and validation of this process is the first step towards realising a wafer-scale detector. This led to the design and fabrication of small-scale sensor prototypes to study the analogue charge collection and charge sharing properties and the digital detection efficiency. Three such prototypes were designed in the Multi-Layer Reticle-1 (MLR1) campaign to study different aspects of the sensor performance: the Analogue Pixel Test Structure (APTS) [4] hosting a small matrix with fast direct analogue readout; the Charge Exploratoire 65 (CE-65) [199] hosting a large matrix with a slow rolling shutter analogue readout; and the Digital Pixel Test Structure (DPTS) [200] hosting a large matrix with an asynchronous digital readout with time-over-threshold.

The simplified layout of the in-pixel circuitry and the on-chip circuit components of the analogue test device facilitates a more straightforward chip design than a digital implementation. Additionally, the analogue chip works with reduced power consumption. Direct access to the raw analogue sensor signal enables detailed observation of the complete signal evolution and provides a better insight into device physics. Beyond characterising the charge collection properties, the full analogue signal allows the investigation of the ultimate achievable analogue resolution, as well as the loss incurred by moving from the analogue to the digital resolution. The analogue test structures are also more suitable for studying the input capacitance and the energy resolution of the sensor. The analogue test structure designed as a part of the MLR1 campaign, the APTS, is the focus of this thesis.

10.3.1 The Analogue Pixel Test Structure

The APTS, as shown in Figure 10.7, was fabricated in the TPSCo CMOS 65 nm ISC technology. It is a prototype test chip of size 1.5 mm × 1.5 mm and hosts a 6 × 6 pixel matrix of which the pixels in the inner 4 × 4 matrix have a direct analogue readout individually buffered and connected to an output pad, allowing full access of the signal. The outermost pixels are used to reduce the edge effects originating from the distortion of the electric field. Several variations of the APTS were designed by varying properties like pitch size, in-pixel readout buffer, sensor coupling with the readout, the doping levels of various implants, and the process. Table 10.2 summarises all the different properties of the available APTS chips. All variants of the APTS

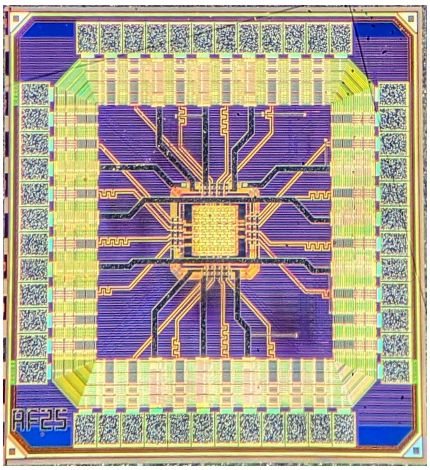

Figure 10.7: The layout of the analogue pixel test structure (APTS) measuring 1.5 mm×1.5 mm under a microscope. [4]

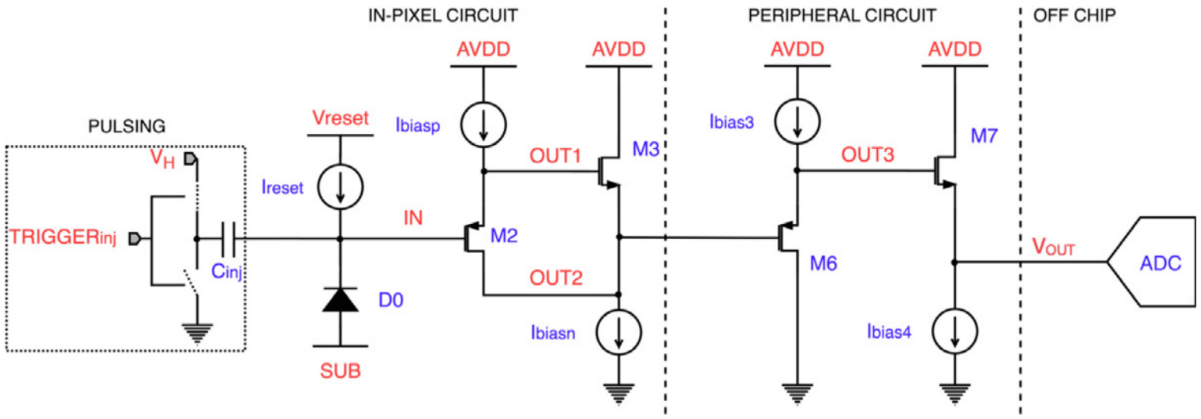

Figure 10.8: The schematic of the in-pixel source-follower readout buffer of the APTS. [4]

chips were also irradiated to varying levels of irradiation up to 3 MGy and 10^{16} 1 MeV n_{eq} cm^{-2}. A reverse bias voltage can be applied to the n-well collection electrode of the APTS in the range of 0 V to −5 V.

Process	Pitch Size [µm]	Readout Buffer	Coupling
Standard, Modified, Modified with Gap	10, 15, 20, 25	source-follower, in-pixel amplifier + source-follower	DC, AC

Table 10.2: The properties of the available APTS chips.

In-pixel Source-follower Buffer

The in-pixel readout of the APTS chip described in this thesis, the APTS-SF, consists of a source-follower (SF) buffer, as shown in Figure 10.8. One PMOS stage and one NMOS stage SF buffers are implemented within the pixel circuitry, and a similar two-stage buffer is implemented outside the pixel. As the input signal from the sensor diode comes, which is negative of the baseline, as will be explained in Chapter 11.2.1, the PMOS M2 will turn on. Therefore, the gate voltage of the NMOS M3, which is initially high to stop the current from flowing through the PMOS current source, will drop to allow the current to flow freely through the first SF stage. As the gate voltage of M3 drops, it will turn off, and to stop the current through this second SF stage, the gate voltage of M6 will go down, turning it on. The third and fourth SF stage buffer and pass the signal similar to the first two stages. The biasing parameters, IBIASP, IBIASN, IBIAS3, and IBIAS4, are used to control the limits of the voltage drops and to shape the signal.

The DC voltage at the collection electrode is kept close to V_{reset}, whereas the current I_{reset} is used to reset the voltage at the collection electrode back to the baseline. In the absence of a signal, I_{reset} compensates the leakage current of the sensor. However, when a signal is recorded, a constant I_{reset}, larger than the leakage current, is provided by the current source and the difference between it and the leakage current is used to reset the voltage at the collection electrode. The magnitude of I_{reset} controls how quickly the voltage returns to the baseline.

Pulsing Circuit

The injection capacitor C_{inj}, with a nominal value of 242 aF, within the pixel pulsing circuit can be used to inject charge into the collection electrode. The voltage setting V_H is used to tune the injected charge, and the injection is controlled with $TRIGGER_{inj}$.

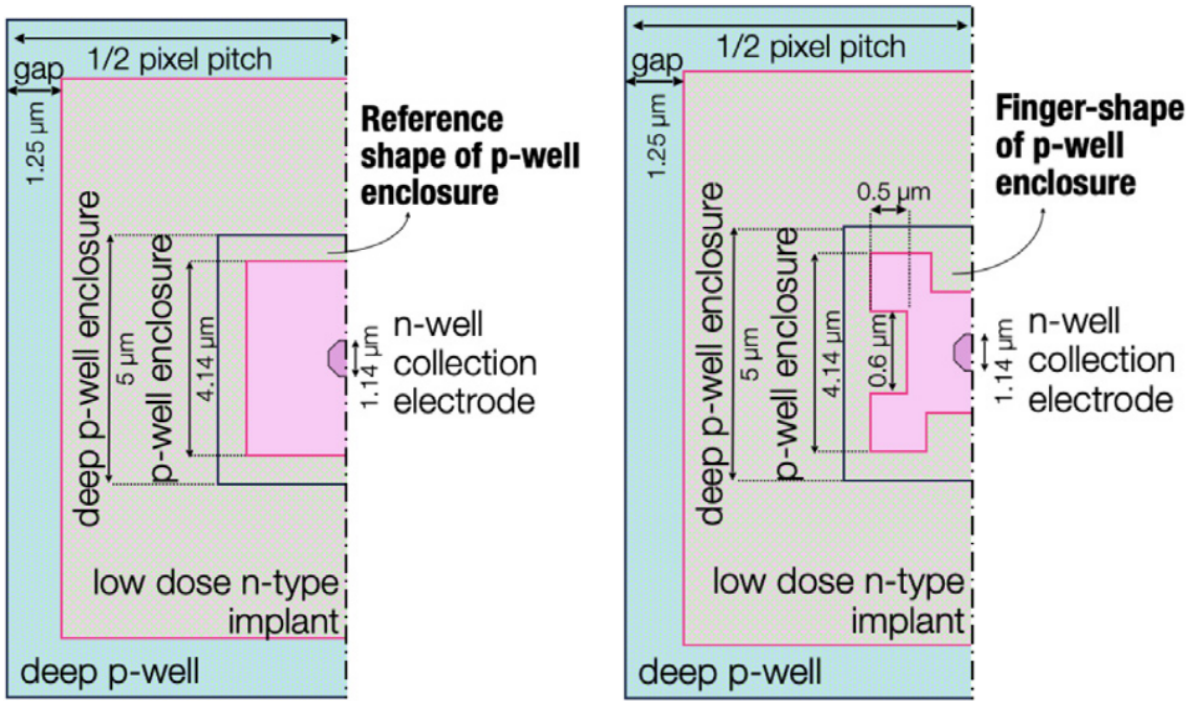

Figure 10.9: The top view of the pixel geometry variants with (a) reference and (b) finger-shaped p-well enclosure on the APTS multiplexer. [4]

10.3.2 The APTS Multiplexer

The tests with varying parameters of the pixel geometry in the sensors produced in the 180 nm CMOS technology by TowerJazz had shown the influence of the size of the collection electrode and the addition and size of the spacing between the collection electrode and the deep p-well, also referred to as the p-well enclosure, on the performance of these sensors [194]. Critical properties like the charge collection efficiency, input capacitance, and charge sharing were seen to be directly impacted by the variations in the geometry parameters. Studying the effect of these properties with sensors fabricated in the 65 nm CMOS technology chosen for the ITS3 upgrade is essential.

The n-well collection electrode and the p-well enclosure were implemented in four separate variants to explore the impact on capacitance and charge collection. These pixel geometry variants were implemented in the 'Modified with Gap' process with two pixel pitch sizes of 10 µm and 20 µm. Four matrices with different pixel geometries were implemented on one chip, labelled the APTS-multiplexer (APTS-MUX), where any of the four matrices could be read out with the help of a multiplexer. The APTS-MUX chips were also irradiated to varying levels of irradiation up to 10^{15} 1 MeV n_{eq} cm^{-2}. The four geometry variants are described below.

Reference

Each APTS-MUX chip hosts one matrix with an identical pixel geometry to the APTS chips that host a single matrix. This variant is referred to as 'Reference' and contains an n-well collection electrode of the size of 1.14 µm and a square p-well enclosure with the width of 4.14 µm. Figure 10.9a shows a top view of this variant.

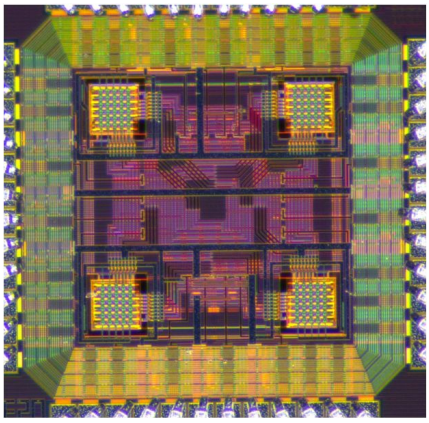

Figure 10.10: The layout of the APTS-multiplexer chip measuring 1.5 mm × 1.5 mm under a microscope. The four matrices hosted on the chip can be seen in the four corners.

Smaller p-well enclosure

This variant has a similar geometry to the 'Reference' variant, but the width of the p-well enclosure is reduced to 3.14 µm. The size of the n-well collection electrode is kept the same.

Large n-well collection electrode

This variant is designed by increasing the size of the n-well collection electrode to 2.28 µm, while keeping the dimensions of the other components the same as the 'Reference' variant.

Finger-shaped p-well enclosure

The dimensions of the n-well collection electrode and the p-well enclosure are kept the same as the 'Reference' variant, but the shape of the p-well enclosure is changed as shown in Figure 10.9b. This results in p-well fingers that further approach the collection electrode.

On-chip Multiplexer

A multiplexer is an electronic circuit configuration with multiple inputs and a single output, as described in Section 9.1.4. The output can be selected by setting the values of the selection bits, which can be either 0 or 1. A 4-to-1 multiplexer is implemented on the APTS-MUX chip, which allows the selection of one of the four matrices for each of the four possible combinations of the two selection bits, denoted as '`mux<0>`' and '`mux<1>`'. The position of these variants on the APTS-MUX chip is noted in Table 10.3.

`mux<0>`	`mux<1>`	**Position**	**Variant**
`0`	`0`	top-left	larger n-well collection electrode
`1`	`0`	bottom-left	reference
`0`	`1`	top-right	finger-shaped p-well enclosure
`1`	`1`	bottom-right	smaller p-well enclosure

Table 10.3: The pixel geometry variants of the APTS and their position on the APTS-MUX chip.

The APTS-MUX hosts four pixel matrices. All four matrices are turned on even though only one is being read out. Therefore, the amount of current passing through it is higher than that

of an APTS chip with a single matrix. Hence, the APTS-MUX chip gets hotter than a regular APTS chip and has higher noise. This also made it difficult to test these variants using the APTS-MUX chip at very high irradiation levels.

10.3.3 Chip Labelling

Several APTS chips were designed to study the effects of changing individual parameters. These chips were annotated using two labels connected with an underscore. The first label describes the properties of the chip, while the second label locates the chip on a particular wafer.

First label

The first letter of the first label is always '`A`' to denote that it is an analogue chip. The second letter represents the readout buffer used in the chip: '`F`' is used for chips with the basic source-follower version; '`A`' is used for chips with a source-follower buffer with an in-pixel amplifier; '`O`' is used for chips with an operational amplifier (OpAmp). These first two letters are followed by two numbers denoting the pitch size of the pixels in the unit of µm. Following this, the letter '`A`' is added for chips where the sensor diode is AC-coupled. No letter is used if the sensor diode is DC-coupled. A letter is added after this to denote any process modifications: no letter is added for the 'Standard' process; '`B`' is used for the 'Modified' process to indicate the blanket deep implant; '`P`' is used for the 'Modified with Gap' process to indicate the patterned deep implant. Finally, an '`M`' is added for the APTS-MUX chips, while no additional letter is used for APTS chips with a single matrix.

Second label

The first three characters of the second label are always the letter '`W`' followed by two numbers to denote the wafer number on which the chip was fabricated. These are followed by the letter '`B`' and a number to signify the index of the chip on the wafer.

Example - change title

The description of a chip labelled `AF20PM_W22B6` is that it is an analogue chip with a source-follower buffer. The pixels have a pitch size of 20 µm and are fabricated in the 'Modified with Gap' process. It is an APTS-multiplexer chip and the sixth chip from the 22nd wafer.

The analogue test device, the APTS, is crucial to characterise the MAPS-based pixel detectors fabricated in the 65 nm CMOS technology. The APTS were tested in the controlled lab environment with a radioactive source and with hadronic particle beams to enable comprehensive studies of the device physics and performance. The following chapters present the results of these test campaigns, focusing on performance metrics such as noise, charge collection efficiency, spatial resolution, and radiation tolerance. These investigations are vital to studying the device physics and optimising the sensor designs.

11 Energy Calibration with a Radioactive Source

A comprehensive measurement campaign was conducted with an ^{55}Fe radioactive source to assess the performance of the APTS-MUX chips, studying their charge collection and energy resolution. Additionally, a comparison of the performance across all available versions was conducted. The principal aim of this work was to evaluate the impact of pixel geometry variation on the signal-to-noise ratio, charge collection and sharing, and energy resolution.

The linearity of the energy calibration and the calibration of the pixel response were also accomplished with the measurements done with the ^{55}Fe radioactive source, which is essential for the conversion of the digitised output from the analogue-to-digital converters (ADCs) to electrons.

This work is partly presented in two NIM-A publications [4, 5].

11.1 Measurement Setup

The test setup consists of three separate boards: the DAQ board, the proximity board, and the carrier board, as shown in Figure 11.1, each with a dedicated function. This system, along with the power supply, the mini-chiller, and the radioactive source, composed the full measurement setup.

Carrier Board

The carrier board hosts the device-under-test (DUT), which in this case is the APTS-MUX chip. Every carrier board hosted an individual APTS-MUX chip. Seven chips were tested using the

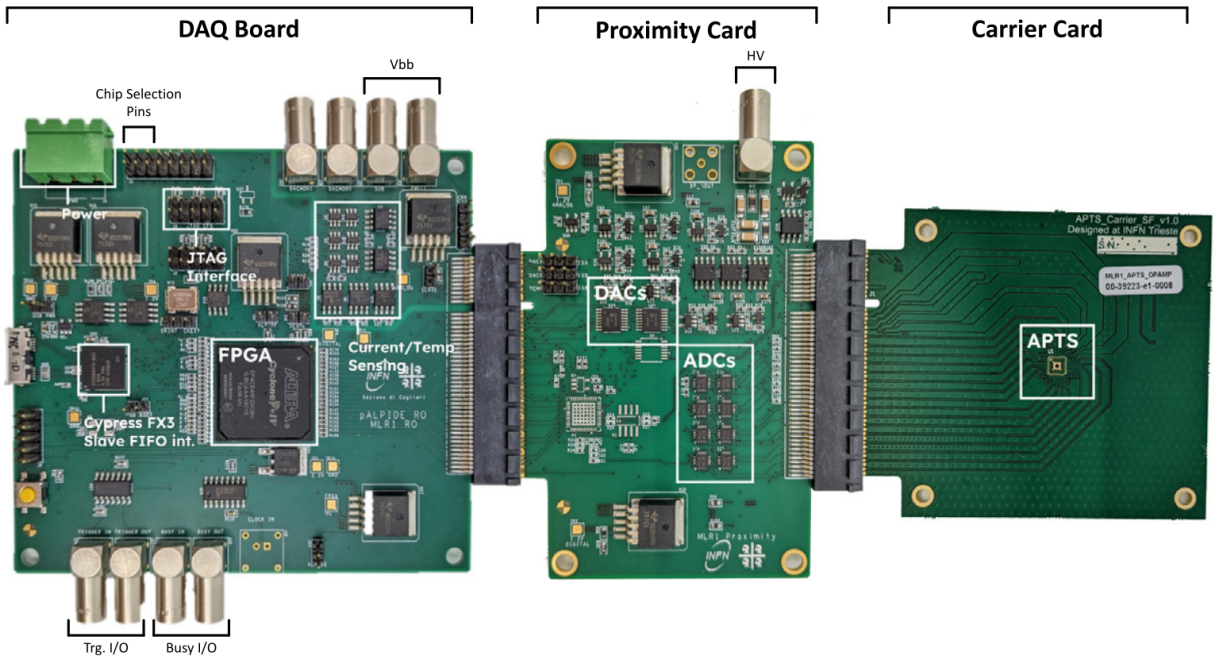

Figure 11.1: The test system including the FPGA-based DAQ board, the chip-specific proximity board, and the carrier board hosting the APTS chip. [4]

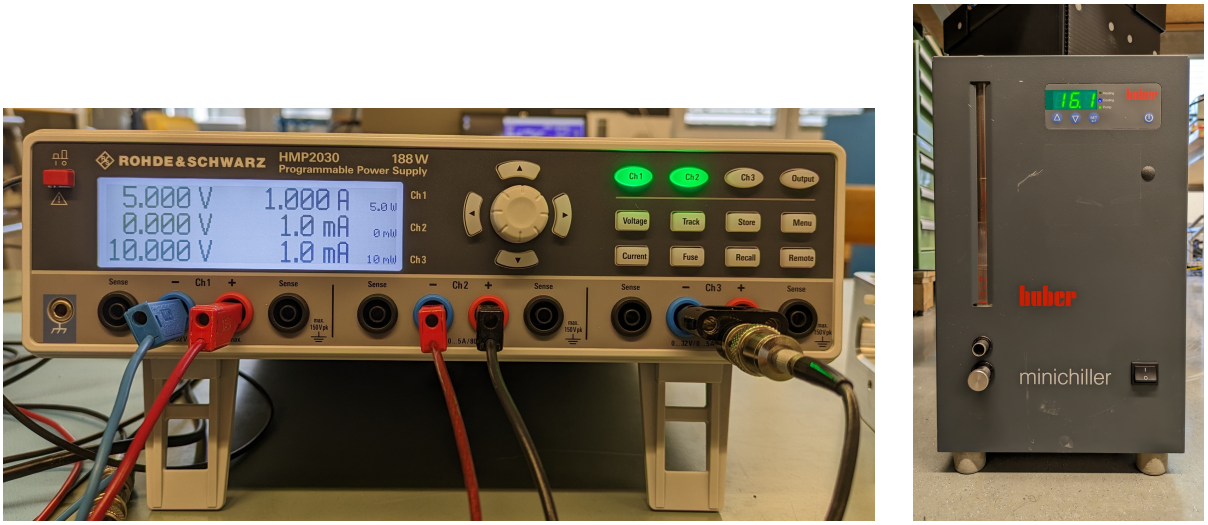

(a) **(b)**

Figure 11.2: Additional components of the laboratory test setup: (a) the Rohde and Schwarz power supply featuring three channels and (b) the Huber minichiller.

setup described in this section: one APTS chip with a single pixel matrix and six APTS-MUX chips, including two irradiated chips. The NIEL irradiation was performed with neutrons at JSI Ljubljana. These chips were labelled:

- `AF10P_W22B28` (pitch = 10 µm, not irradiated)
- `AF10PM_W22B3` and `AF10PM_W22B4` (pitch = 10 µm, multiplexer, not irradiated)
- `AF20PM_W22B6` and `AF20PM_W22B7` (pitch = 20 µm, multiplexer, not irradiated)
- `AF20PM_W22B9` and `AF20PM_W22B11` (pitch = 20 µm, multiplexer, irradiated to 10^{14} and 10^{15} 1 MeV n_{eq} cm^{-2} respectively)

Proximity Board

The proximity board is chip-specific and hosts components specifically tuned for the DUT. It features two 8-channel 16-bit digital-to-analogue converters (DACs) that supply voltages to the chip and supply and monitor the bias voltages and currents. It also hosts the ADCs to digitise the analogue outputs from the 16 pixels with a resolution of 16 bits.

DAQ Board

The central component of the data acquisition (DAQ) board is the field-programmable gate array (FPGA). It utilises a USB3 interface for control and readout with a computer system and uses a digital `I/O` interface for the proximity board. The power is supplied to the test system through the DAQ board. It also contains voltage regulators, including circuitry to monitor and supply current to the on-board circuits, as well as the proximity board. It includes a temperature measurement circuit, and the on-board LEMO connectors can be used to apply voltages to the substrate and the p-wells of the chip.

Table Setup

The model HMP2030, by Rohde and Schwarz, featuring three channels, was used to power the test system and to apply the substrate and p-well voltages. A filter board was placed between

the power supply and the LEMO connector on the DAQ board, which takes in the bias voltage and passes it via the proximity board to the chip on the carrier board. The filter board features an RC π filter, a passive RC low-pass filter comprising two capacitors and a resistor arranged in a π-shaped configuration. This design aids in filtering noise and blocking high-frequency interference or irregularities from the power supply, ensuring a clean bias voltage, which is critical for depletion.

A Huber minichiller was utilised to standardise and regulate the temperature during the tests. The temperatures quoted with the results presented in this chapter refer to the water cooling temperature set on the minichiller. The actual temperature on the chip can be higher by $1 - 3°C$, depending on the testing environment. A mechanical setup mount was designed to host the test system. It was fitted with inlets and pipes for easy and direct application of cooling to the chip on the carrier board from below, as well as to hold the radioactive source in position above the chip.

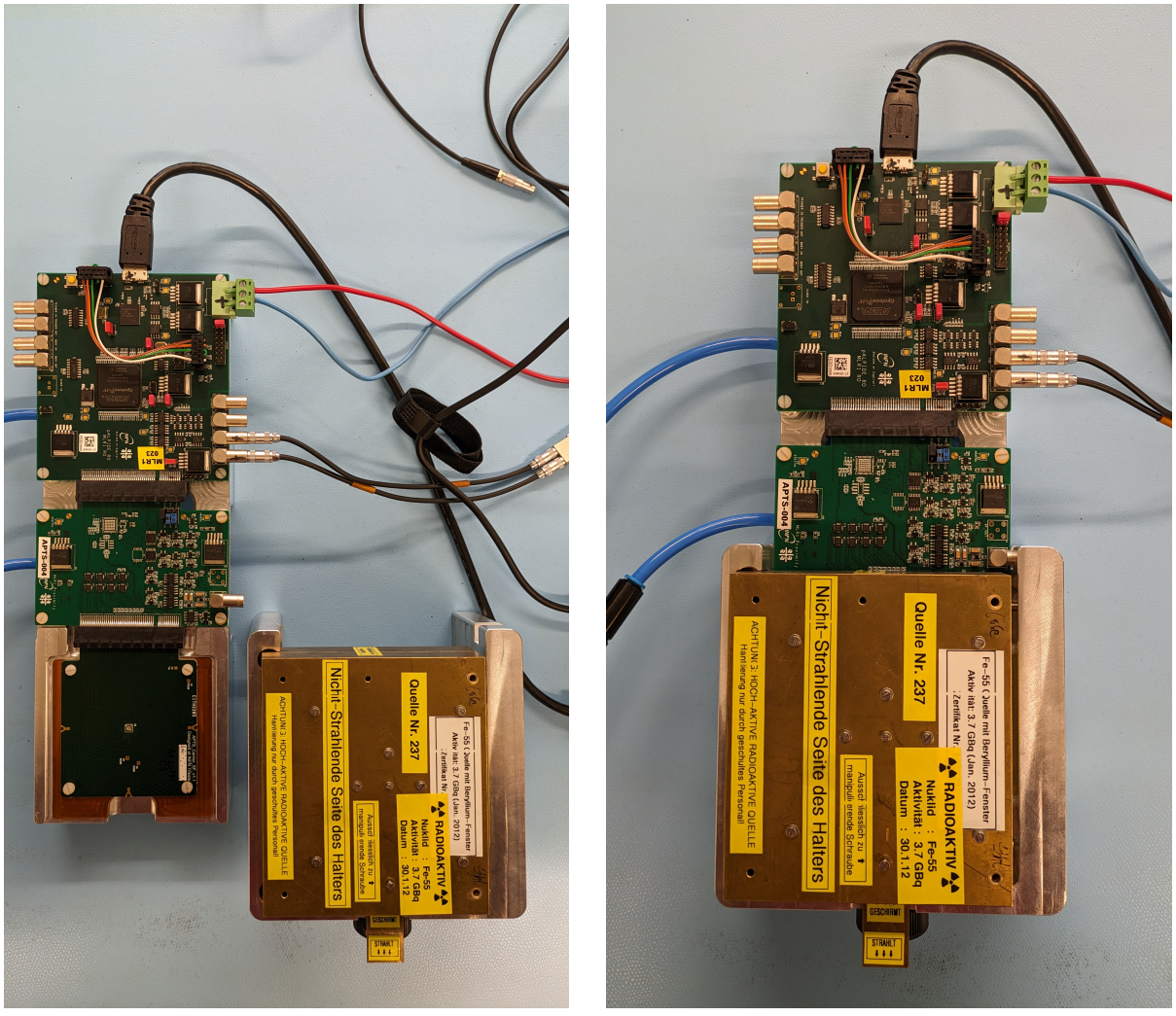

(a) **(b)**

Figure 11.3: The test system with the ^{55}Fe radioactive source (a) off and (b) on the carrier board, centered on the APTS-MUX chip.

^{55}Fe Radioactive Source

The ^{55}Fe radioactive source is used in the characterisation of silicon detectors as the emitted X-rays are monochromatic, i.e. they produce photons of the same energy, thus providing an ideal reference to calibrate the pixel response, study detector properties, such as charge collection and energy resolution, and compare the performance of the available variants. The $^{55}_{26}$Fe isotope decays by electron capture with a half-life of 2.747 years, and the particles produced in the decay, along with their energies and rates normalised to 100 decays, are presented in Table 11.1.

The emission probability of the high-energy γ-rays is negligible compared to the X-rays and therefore is not considered. The Auger electrons with the energy of ∼5–6 keV have a very short range in air and do not reach the test structure, which is kept at a distance of a few centimetres. Similarly, the X-rays with the energy of <1 keV are attenuated to a negligible flux. Hence, only the rest of the soft X-rays are incident on the detector.

	Energy [keV]	**Emissions per 100 decays**
Auger electrons	0.47 – 0.67	140.2 (8)
	4.95 – 6.53	60.1 (5)
X-rays	0.56 – 0.72	0.524 (21)
	5.888	8.45 (14)
	5.899	16.57 (27)
	6.490	3.40 (7)
	6.535	
γ-rays	125.959	$1.3\,(1) \times 10^{-7}$

Table 11.1: The emitted particles in ^{55}Fe radioactive decays. The numbers in parenthesis indicate the uncertainties on the last digit(s) of the preceding value [201].

The soft X-rays interact with matter via the photoelectric effect, and the emitted photoelectron ionises the silicon to generate electron-hole (e-h) pairs. With an energy of 3.6 eV required to generate an e-h pair, the photo-electrons with the energy of 5.9 keV and 6.5 keV generate approximately 1640 and 1800 e-h pairs, respectively. With an intrinsic resolution of 2%, equivalent to 120 eV, for photo-electron energies between 5.9–6.5 keV, the X-rays with energies 5.888 keV and 5.899 keV (and similarly 6.490 keV and 6.535 keV) cannot be resolved [182]. Therefore, only two peaks are expected to be observed while measuring the ^{55}Fe radioactive spectrum with a silicon detector.

An ^{55}Fe radioactive source was used to perform the lab characterisation and the calibration of the pixel response in this study. The emitted X-rays at the energies of 5.9 keV are referred to as the Mn-K$_\alpha$ or simply K$_\alpha$ emission, and at 6.5 keV are referred to as the Mn-K$_\beta$ or simply K$_\beta$ emission. The activity of the ^{55}Fe source at the start of the testing campaign was 210 MBq.

11.1.1 Software Framework

An automated data acquisition framework was used to configure the analogue and digital settings of the chip and the readout buffer chain, and to collect the digitised data for multiple triggers, each consisting of several frames before and after the signal trigger. Noise-triggered events were suppressed by setting a trigger threshold, which is evaluated by measuring the readout rate in the absence of the radioactive source. The digitised data is stored in a binary format optimised for speed and file size.

The analysis software decodes this raw binary data into a structured array format for further

processing. The decoded data is used for event building and signal extraction. Individual modules perform clustering, the fitting of the measured spectra, and measurements of physical parameters. Calibration maps, once calculated, are used for conversion from ADC counts to physical units, such as voltage or charge.

11.2 Laboratory Measurements

The laboratory test setup described above was used to perform measurements using the ^{55}Fe radioactive source. A baseline was defined individually for the signal from every pixel, and the gain of the readout buffer chain was measured to assert the linearity of the gain. The noise of the pixel response was evaluated to select appropriate thresholds while taking measurements. The analogue response of the pixels from the passing X-ray photons from the radioactive source was finally observed to characterise and calibrate the pixel response.

11.2.1 Signal Shape and Extraction

A typical uncalibrated output signal at the `OUT` node after injecting a charge equivalent to 1800 electrons using the in-pixel pulsing circuit at a reverse substrate voltage (V_{sub}) of 1.2 V is shown in Figure 11.4. The signal amplitude is defined as the difference between the baseline and the signal minimum. The baseline is defined as the fourth sample before the minimum, which is far enough from the signal edge but is close enough to reduce the low-frequency variations of the output signal. The baseline for each pixel is evaluated independently.

The front-end settings were optimised for the signal-to-noise (S/N) ratio, the gain, and the linearity of the response. The settings used for all displayed results in this chapter, unless stated

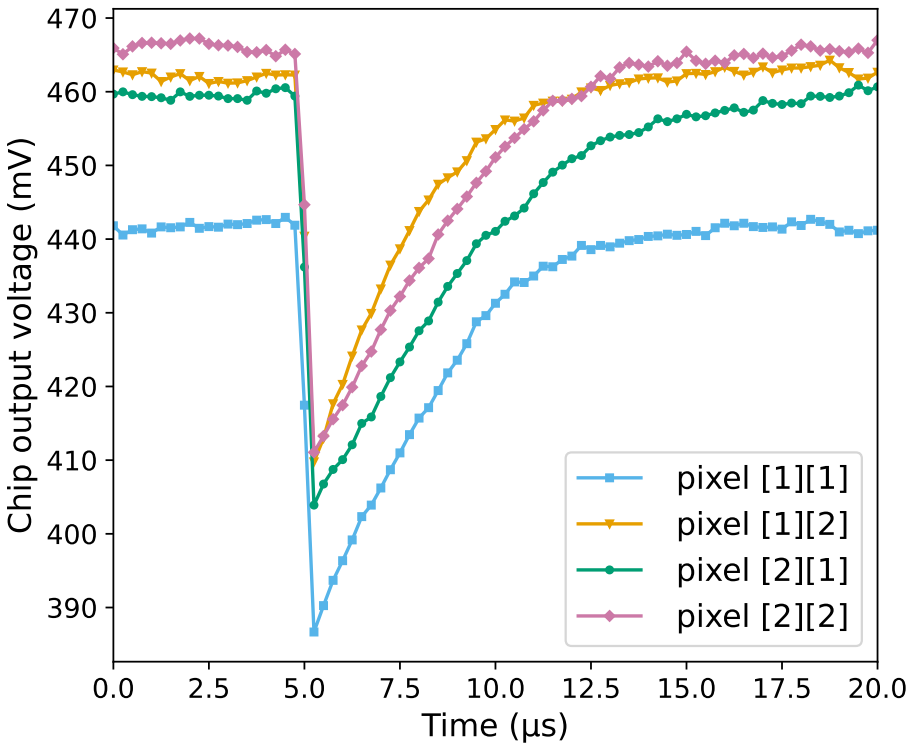

Figure 11.4: A typical uncalibrated output signal for the four innermost pixels of an APTS chip pulsed with $V_{\text{H}} = 1.2\,\text{V}$. The pixel pitch size of the APTS chip was 15 µm and the reverse substrate voltage of 1.2 V was applied.

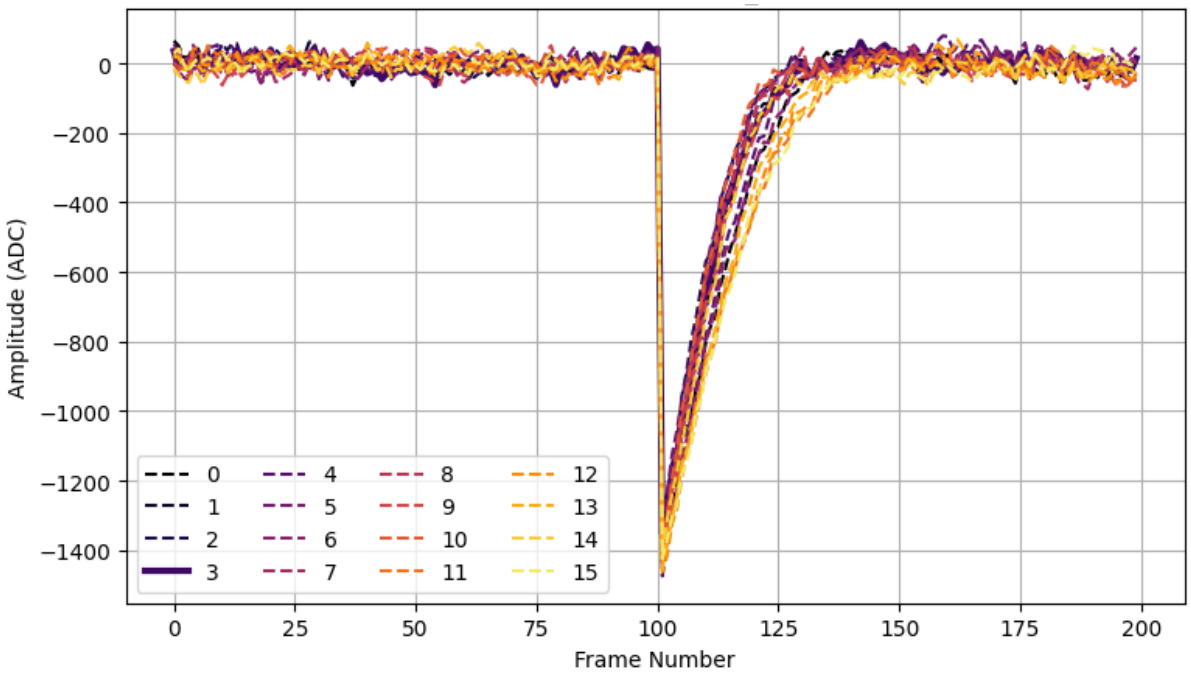

Figure 11.5: The output signal of the 16 pixels of the reference variant of the APTS MUX chips pulsed with $V_{\mathrm{H}} = 1.2\,\mathrm{V}$ after shifting the baseline to zero. The pixel pitch size of the APTS chip was 20 µm and the reverse substrate voltage of 1.2 V was applied.

otherwise, are the following: $I_{\mathrm{biasn}} = 5\,\mu\mathrm{A}$, $I_{\mathrm{biasp}} = 0.5\,\mu\mathrm{A}$, $I_{\mathrm{bias3}} = 200\,\mu\mathrm{A}$, $I_{\mathrm{bias4}} = 150\,\mu\mathrm{A}$, $I_{\mathrm{reset}} = 100\,\mathrm{pA}$, $V_{\mathrm{reset}} = 500\,\mathrm{mV}$.

The output signal's return to baseline is dictated by I_{reset} and takes around 10 µs at the standard operating point with the above settings. The return to baseline of the output signal is affected by leakage current, which can increase due to several factors. Some of these are the increase in the reverse substrate voltage, irradiation, and temperature. An increased leakage current causes the fraction of the I_{reset} available as the reset current to reduce. To counteract this effect, the I_{reset} must be increased, which can also increase the noise. Approximately 15% higher noise is seen for an I_{reset} value of 250 pA compared to the standard setting.

Figure 11.5 shows the output signal after injecting the pixels of the matrix with the reference geometry variant on the APTS-MUX chip of pixel pitch size of 20 µm with a charge equivalent to 1800 electrons at a reverse substrate voltage of 1.2 V. The baseline has been subtracted from the pixel responses.

11.2.2 Noise Estimation

The baseline fluctuations of the pixels were studied to evaluate the noise of the matrices. As mentioned in Section 10.3.2, the noise of the APTS-MUX chip tends to be higher than the APTS chip with a single matrix, as it hosts four matrices, which are all powered at the same time. The average of the noise RMS for all four geometries ranged between 30 and 36 electrons, while the variation among the pixels of the matrix was about 3 to 4 electrons. The conversion to electrons, performed on values shown in Figure 11.6, is detailed in the following subsections.

11.2.3 Gain

The gain of the readout circuit, combining both the in-pixel and the peripheral source-follower buffers, was studied before performing the measurements with the radioactive source. V_{reset} was varied as a proxy for V_{in}, as there is no direct external control for V_{in}. As the chip is turned on,

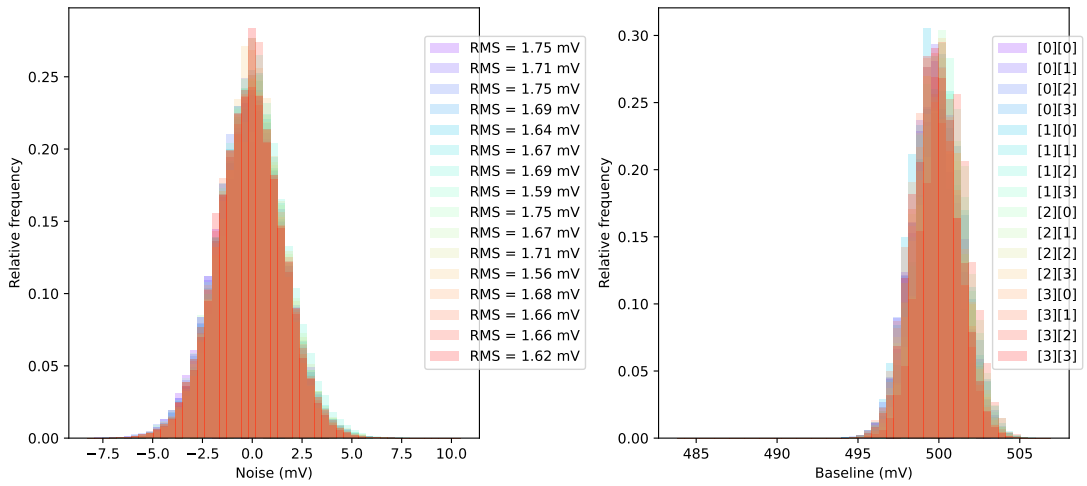

Figure 11.6: The fluctuations of the baseline and the evaluated noise of the reference variant of the APTS-MUX chip with the pixel pitch size of 20 µm at a reverse substrate voltage of 1.2 V.

the current source, I_{reset}, formed by a PMOS transistor in saturation, charges the sensing node capacitance. As V_{in} approached V_{reset}, the PMOS transistor comes out of saturation into the triode region, and the current passing through it is no longer constant but starts to decrease. Thus V_{in} is capped at a value slightly smaller than V_{reset}. Since the PMOS transistor is no longer in saturation but in the triode region, essentially acting as a resistor, a small change in V_{reset} is linearly reflected in V_{in}. Thus, an input-output characteristic, also known as the gain curve, measured by varying V_{reset} would have the same slope as that measured by varying V_{in}, but it would have a small translational shift on the x-axis. The gain, as measured by taking the ratio of V_{out} and V_{in} and graphically represented by the slope of the input-output characteristic, would be the same in both cases.

Figure 11.7 shows the input-output characteristic and its derivative, showing the gain. The value of V_{reset} is chosen so that the output response of the readout is linear and the gain is

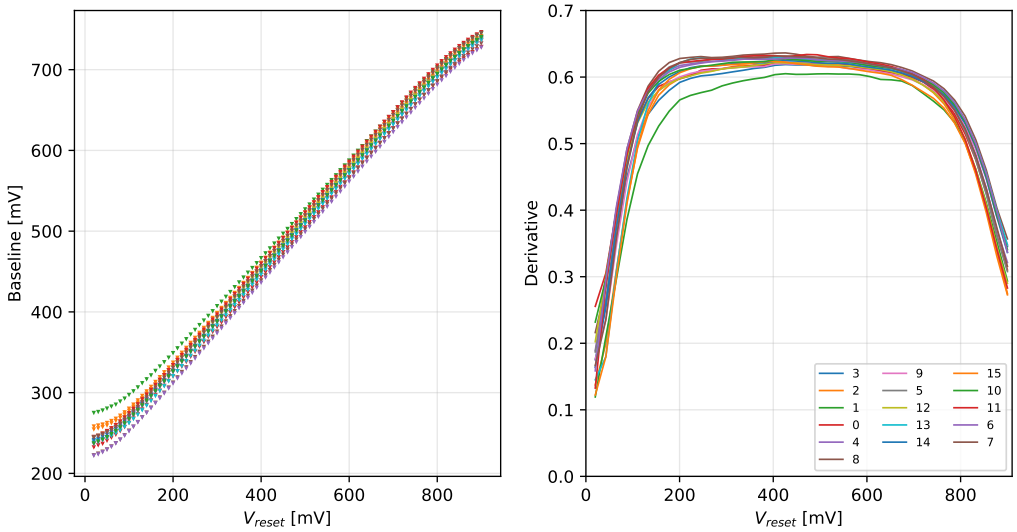

Figure 11.7: Gain curve and its derivative for the reference variant of the APTS-MUX chip with the pixel pitch size of 20 µm at a reverse substrate voltage of 1.2 V. V_{reset} is changed from near 0 mV to 900 mV. During the measurements with the ^{55}Fe radioactive source, the chip is operated at a setting of V_{reset}, where the readout response is linear and the gain is stable.

stable. Hence, V_{reset} was kept at a value of 500 mV. The gain between the OUT and IN nodes in Figure 10.8 is approximately 0.6 for an input signal ranging from 200 mV to 600 mV. The same gain was seen for all four pixel-geometry variants.

Some reduction in the range of linearity was observed for some pixels in the matrix at high bias voltages, but the response was linear with a stable gain of ~ 0.6 around the V_{reset} value of 500 mV. A non-uniform output response was seen among the pixels from the same matrix after irradiation. A higher value of I_{reset} had to be applied to achieve uniformity of pixel responses for chips with irradiation of 10^{15} 1 MeV n_{eq} cm^{-2}, which is the highest available irradiation level for the APTS-MUX chips.

11.2.4 Clustering

When the pixel matrix is hit by a charged particle or a photon, the pixel that collects the most charge over a certain threshold is referred to as the 'seed' pixel. Pixels adjacent to the seed pixel that collect charge over a certain threshold are termed 'neighbouring' pixels. The collection of the seed and the neighbouring pixels is denoted as a 'matrix cluster' or simply 'cluster'. A cluster is formed when the charge generated by a passing charged particle or a photon is not entirely collected by the seed pixel but is shared among neighbouring pixels. This phenomenon is known as charge sharing, as detailed in Section 9.4. Events for which the entire generated charge is collected within the seed pixel or the charge collected by the neighbouring pixels does not pass the threshold are labelled as single-pixel clusters.

11.2.4.1 Clustering Methods

Different algorithms can be used to form these matrix clusters with a direct impact on performance parameters like the charge collection efficiency and the spatial resolution. Two such algorithms are described below.

Window Method

In this clustering method, the seed pixel is identified first. Then, the pixels within a predefined window around the seed pixel are grouped into the cluster. The window size can be arbitrary, but the most common window sizes are 3×3 and 5×5 pixels. This is a simple and computationally efficient clustering method. However, it may lead to loss of charge for pixel detectors with significant charge sharing, e.g. the ALPIDE sensor with the 'Standard' process, where the charge may be spread beyond the predefined window size. For cases with less to no charge sharing, e.g. sensors designed in the 'Modified with Gap' process, the window method can lead to the addition of noise from pixels which do not collect any charge, resulting in a considerable impact on performance, especially after radiation damage. The position of a cluster formed with the window method is generally defined as the charge-weighted center-of-gravity of the pixels in the cluster.

The results reported in this chapter utilise this clustering method with a window size of 3×3 unless specified otherwise. In the following, the term 'matrix' refers to the group of pixels within a 3×3 window centered around the seed pixel.

Cluster Method

In the cluster method, neighbouring pixels passing a threshold are grouped into the cluster. It is possible to limit the cluster size to a predefined window for sensors known to share minimal

charge outside the seed pixel, like the ones designed in the 'Modified with Gap' process. In such a case, the seed pixel is identified first, and then, the pixels adjacent to the seed pixel passing a certain threshold are grouped, along with the seed pixel, into the cluster. This clustering method is more adaptive and better for long-term operation in an irradiated environment, as the threshold can be tuned to counteract the noise effects by raising the signal-to-noise (S/N) threshold. The cluster position can either be defined by calculating the center-of-gravity without charge weighting, as done for binary (or hit/no-hit) sensors or by calculating the charge-weighted center-of-gravity to exploit the full analogue information of the pixels. The difference between these two is expected to be minute for sensors with low to no charge sharing.

In the following, the term 'cluster' refers to a set of adjacent pixels inside a 3×3 matrix centred around the seed pixel, which collected a charge higher than a predefined threshold.

11.2.5 ^{55}Fe Measurement

Figure 11.8a shows the ^{55}Fe spectrum for the reference variant of the APTS-MUX chip of pitch size 20 µm at a reverse substrate voltage of 1.2 V. The distribution corresponds to single-pixel cluster events, i.e. events with a cluster size of 1. Events are considered only if one of the four inner pixels is the seed pixel to avoid edge effects and to have access to all clusters within a 3×3 matrix centered around the seed pixel. The K_α and K_β peaks of the spectrum are fitted with Gaussian functions. The values of the mean of the two fits are used to assert the linearity of the energy calibration, as shown in Figure 11.8b. The correlation between the seed pixel signal amplitude and the corresponding photon energy is fitted with a linear function with the intercept set to 0. The linearity of the matrix response is critical to the application of a conversion factor for energy calibration. Since the signal response is linear, the value of the mean of the prominent K_α peak fit is used to convert the mV or the ADC units into electrons (e^-).

Seed Pixel Signal

Figure 11.9a shows an example of the seed pixel signal at four increasing reverse substrate voltages. It can be seen that the amplitude of the peak increases with the reverse substrate

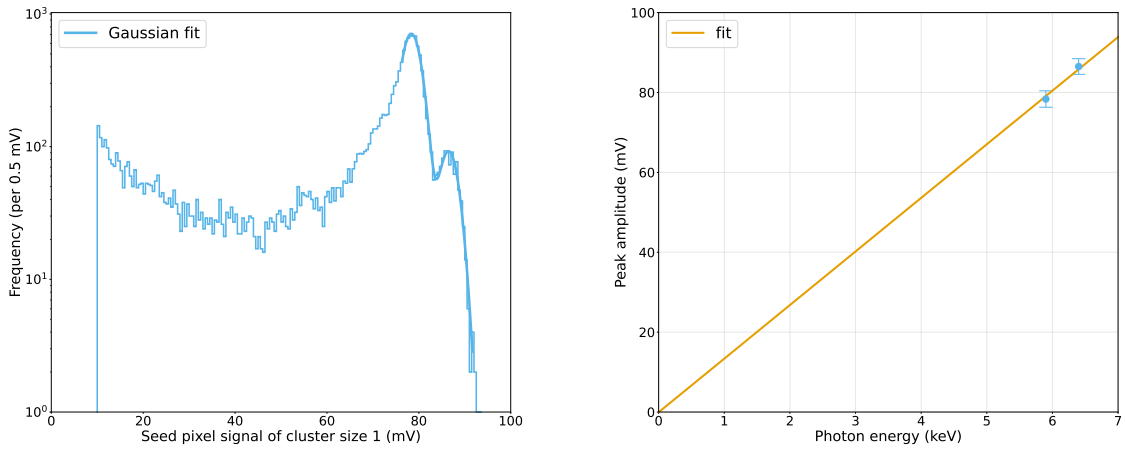

(a) **(b)**

Figure 11.8: The ^{55}Fe spectrum with the cluster size of 1, measured with the reference variant of the APTS-MUX chip with the pitch size of 20 µm. Only the four innermost pixels are allowed to be the seed pixels.

voltage. This is because, with increasing reverse substrate voltage, the depletion region reaches deeper into the epitaxial layer. At the same time, the depletion region boundary in the low-dose implant reaches the n-well collection electrode, thus decreasing the capacitance. When the same distribution is re-plotted after converting the mV units to electrons (e^-) using the conversion factor, as shown in Figure 11.9b, no deviation is seen among the distributions at different reverse substrate voltages. This displays that the full generated charge is being collected by the pixels, and near-full depletion is achieved at small reverse substrate voltages.

Figure 11.10a shows the seed pixel signal for the four pixel geometry variants on the APTS-MUX chip. The pitch size of the pixels is 20 µm and the reverse substrate voltage of 1.2 V. It can be seen that the variant with the larger n-well collection electrode has a lower amplitude compared to the other three variants. Re-plotting this distribution in e^-s, as presented in Figure 11.10b, shows that all four variants collect the full generated charge. The difference in the signal distributions plotted in the mV units is because the variant with the larger n-well collection electrode has a higher input capacitance, as was expected.

All of the above distributions were normalised by the total number of events. Similar trends

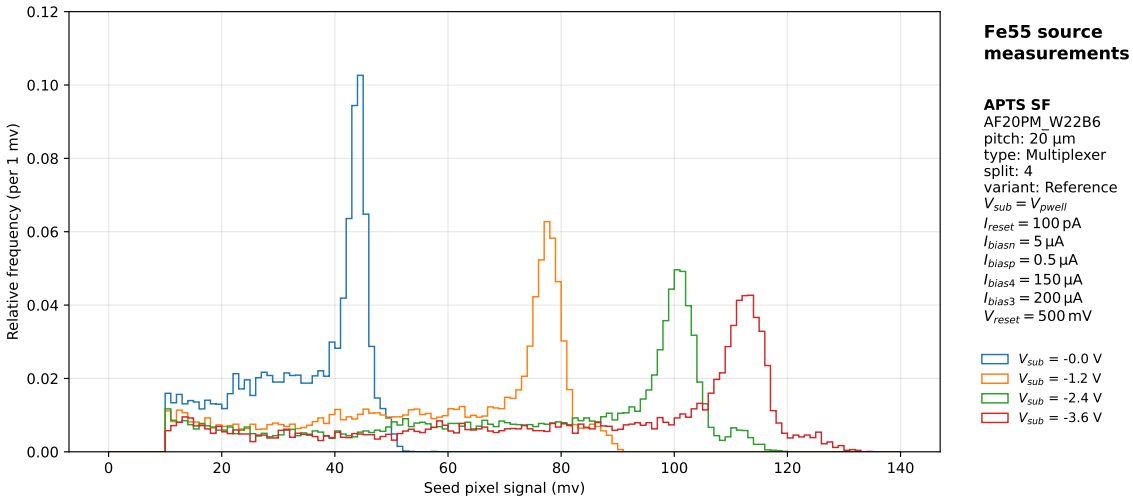

(a)

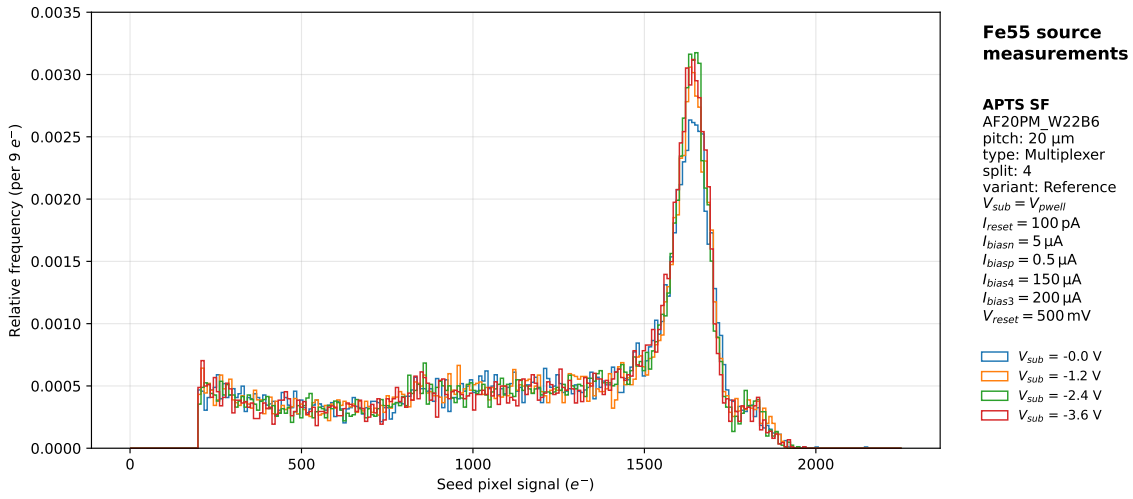

(b)

Figure 11.9: ^{55}Fe seed signal distribution comparing the four different reverse substrate voltages. The reference variant of the APTS-MUX chip with pixel pitch size of 20 µm.

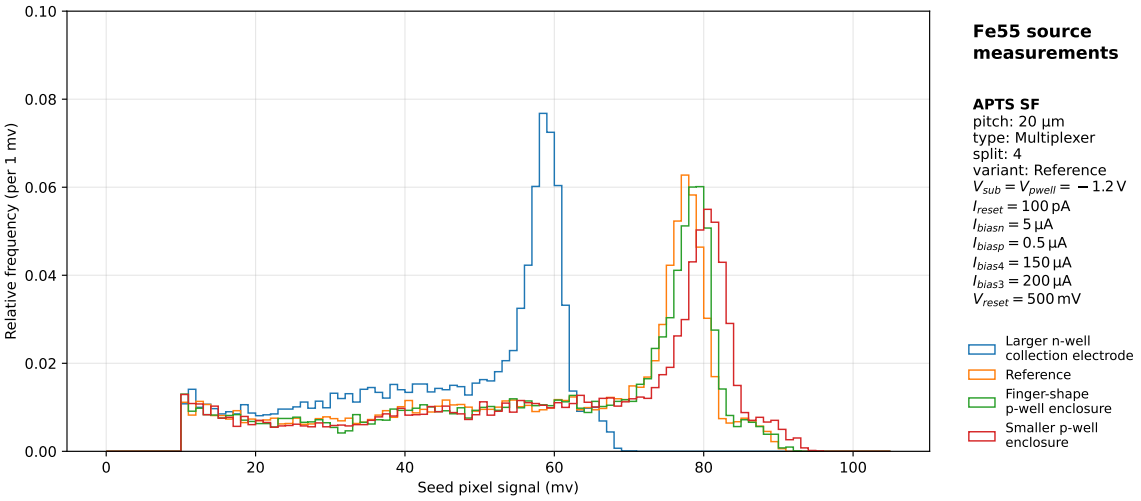

(a)

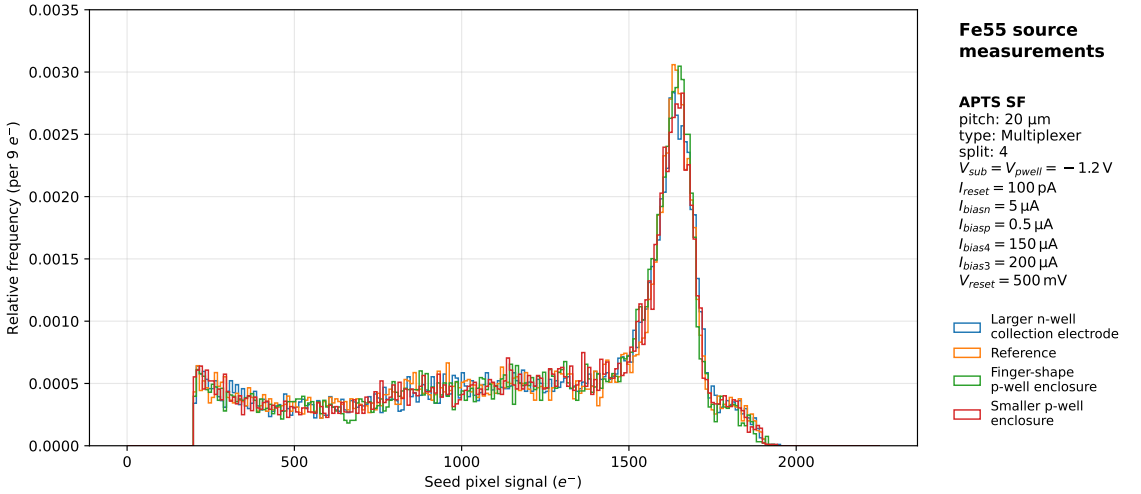

(b)

Figure 11.10: ^{55}Fe seed signal distribution comparing the four pixel geometry variants. The APTS-MUX chip with pixel pitch size of 20 µm and reverse substrate voltage of 1.2 V.

are seen in the seed pixel signal distributions of matrices on the APTS-MUX chip with the pitch size of 10 µm.

Matrix Signal

The matrix signal distributions follow a similar trend to the seed signal distributions. Figure 11.11a, corresponding to the same settings as Figure 11.10a, shows that the variant with the larger n-well collection electrode has a smaller amplitude compared to the other three variants, similar to the seed pixel signal distribution. Re-plotting the distributions after conversion from mV to e^-, as shown in Figure 11.11b, shows no distinction among the four variants. It can be seen that the Gaussian peaks of the matrix signal distributions are wider than the seed pixel signal distributions due to the cumulative noise of a higher number of pixels in the case of the matrix signal.

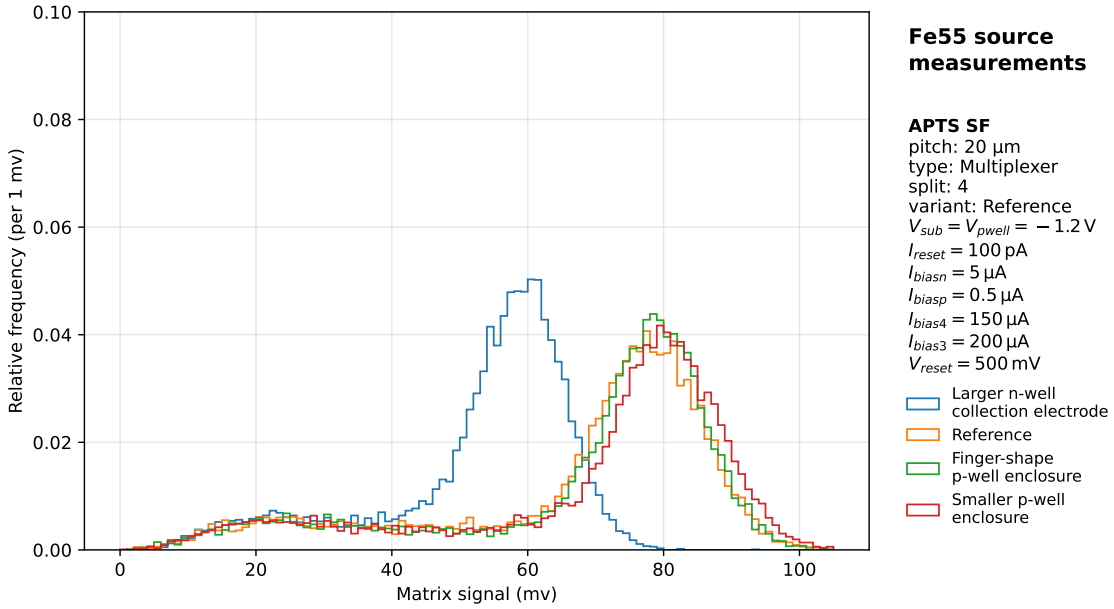

(a)

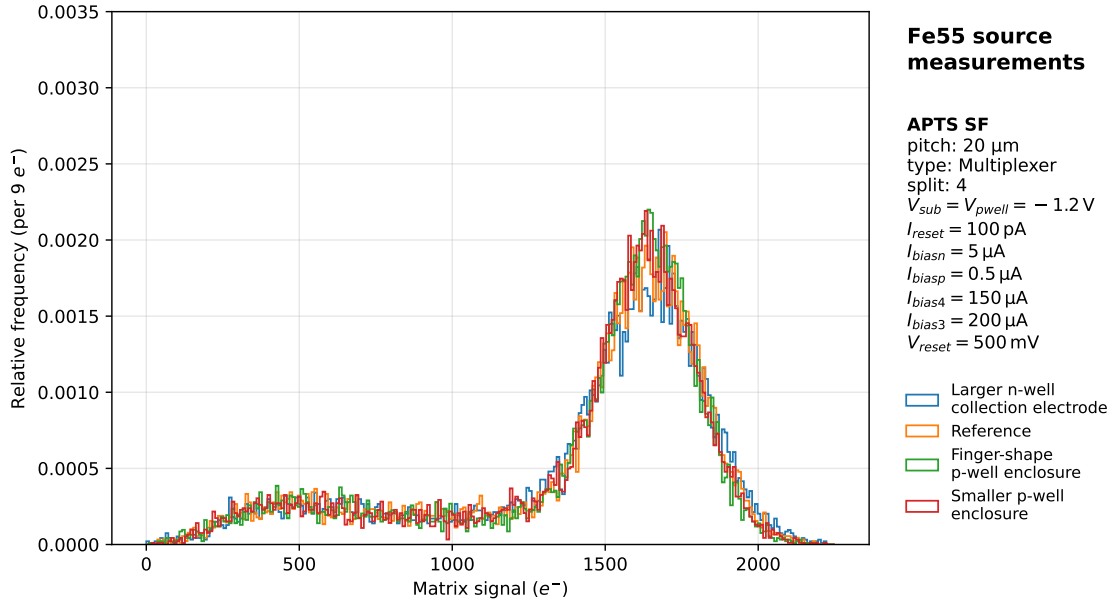

(b)

Figure 11.11: ^{55}Fe matrix signal distribution comparing the four pixel geometry variants. The APTS-MUX chip with pixel pitch size of 20 µm and reverse substrate voltage of 1.2 V.

Charge Sharing

Figure 11.12 shows the correlation between the seed pixel signal and the clustered matrix signal, removing the contribution from the seed signal. The latter is referred to as the 'sum of neighbours' signal. The pitch size of the pixels in the two matrices is 20 µm, and the applied reverse substrate voltage is 1.2 V. Figure 11.12a corresponds to the reference variant, while Figure 11.12b corresponds to the variant with the larger n-well collection electrode. It can be seen that a majority of the events are single-pixel cluster events in both cases, and the events where the charge is shared with neighbouring pixels are represented by the faint yellow-green lines. The signal amplitudes are lower for the variant with the larger n-well collection electrode,

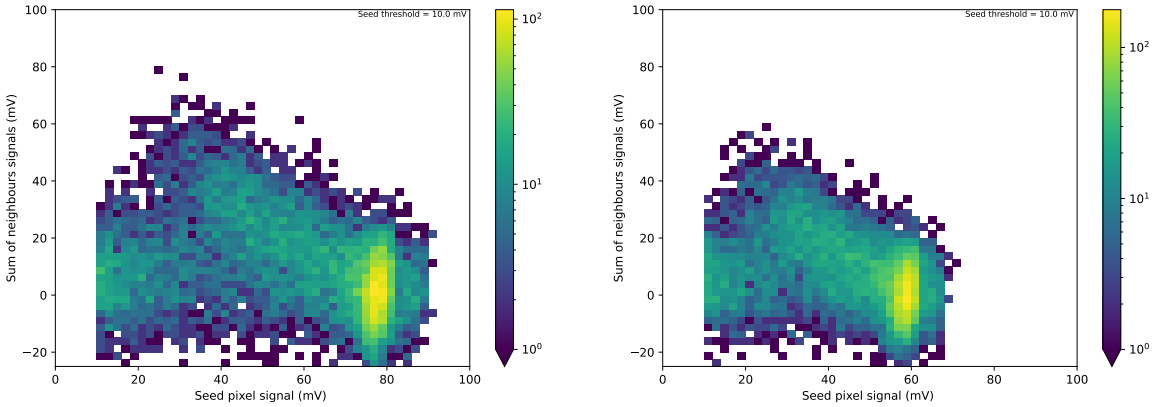

(a) **(b)**

Figure 11.12: Distribution showing the correlation of the seed pixel signal and the sum of the neighbours signal for the (a) reference variant and (b) the variant with the larger n-well collection electrode. The APTS-MUX chip with pixel pitch size of 20 µm and reverse substrate voltage of 1.2 V.

as expected, due to the higher input capacitance of its pixels.

Cluster Size

Figure 11.13 shows the cluster size distribution for matrices of the reference variant with pixel pitch size of 20 µm. The impact of the reverse substrate voltage on charge sharing among neighbouring pixels can be seen in Figure 11.13a. The increasing reverse substrate bias leads to the increasing depth of the depletion region in the epitaxial layer, which results in less charge sharing and therefore a larger fraction of single-pixel clusters. The variant with the larger n-well collection electrode has a higher fraction of single-pixel cluster events in comparison to the other three variants, as shown in Figure 11.13b. This demonstrates that the variant with the larger n-well collection electrode shows less charge sharing among the neighbouring pixels than the other three geometries.

The distributions shown above were normalised by the total number of events. Similar results and trends are seen in the distributions of matrices on the APTS-MUX chip with the pitch size of 10 µm.

Effect of Irradiation

The fraction of single pixel cluster events increases at higher irradiation levels, as shown in Figure 11.14 for the reference variant with the pixel pitch size of 20 µm at a reverse substrate voltage of 1.2 V. As the charge shared with the neighbouring pixels is minuscule compared to the charge collected by the seed pixel, there's a higher probability after irradiation that this charge gets trapped before it is collected. Since a threshold is applied to the pixels adjacent to the seed pixels before they are added to the cluster, this results in a higher fraction of single-pixel cluster events.

It should be noted that the APTS-MUX chip irradiated to 10^{15} 1 MeV n_{eq} cm^{-2}, `AF20PM_W22B11`, is run at an I_{reset} value of 250 pA. This increase results in an increased noise, but is necessary because the return to baseline of the signal from pixels of the irradiated matrices is non-uniform at the reference value of I_{reset}. Figure 11.15 shows the output signals after injecting the pixels of the reference variant of the irradiated chip with pixel pitch size of 20 µm with a charge equivalent to 1800 electrons at a reverse substrate voltage of 1.2 V at the two values

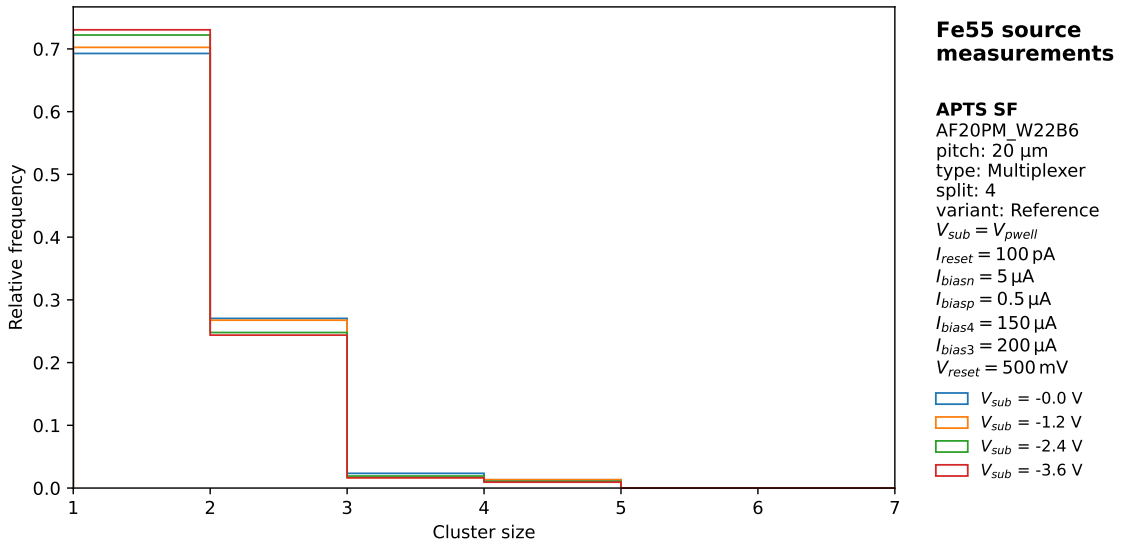

(a)

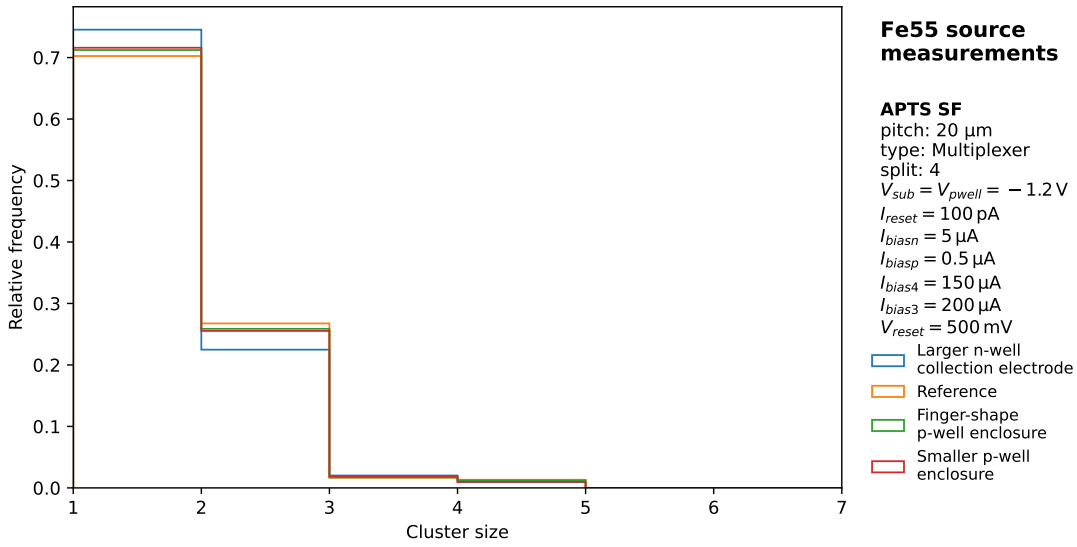

(b)

Figure 11.13: Distribution of the cluster size comparing (a) different reverse substrate voltages for the reference variant and (b) the four pixel geometry variants at the reverse substrate voltage of 1.2 V. The APTS-MUX chip with pixel pitch size of 20 µm.

of I_{reset}. The return to baseline is non-uniform for the pixels at an I_{reset} value of 100 pA and is longer than for a unirradiated pixel matrix due to higher leakage current. Increasing the I_{reset} value to 250 pA results in a uniform response from the pixel matrix as the increased I_{reset} compensates for the higher leakage current caused by the irradiation.

11.2.6 Measured Quantities

Several quantities have been extracted from the seed pixel signal distributions and are presented in Figure 11.16. These quantities are defined below.

Input Capacitance

The input capacitance, C_{input} is related to the measured capacitance, C_{measured}, as

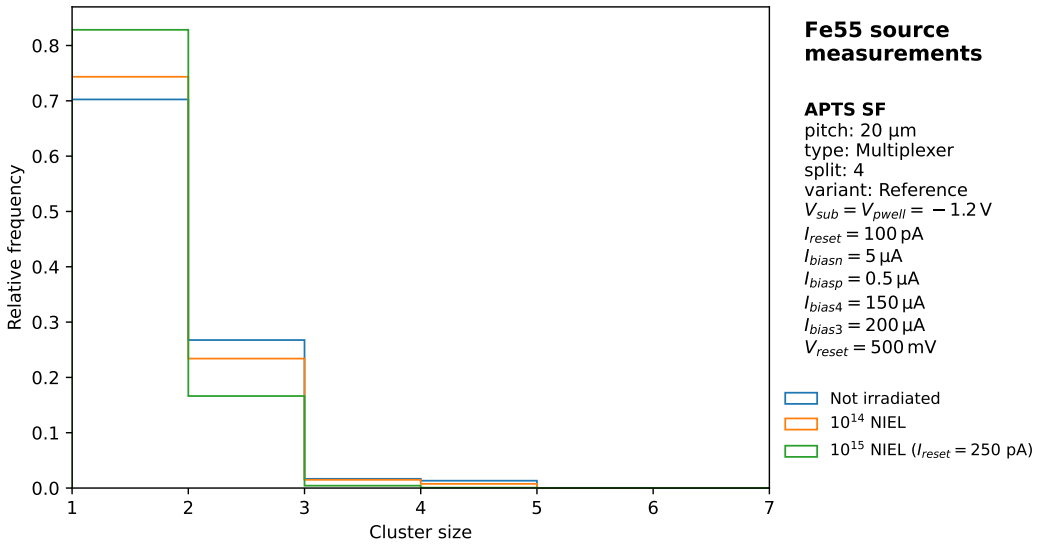

Figure 11.14: Cluster size distribution of the reference variant at different irradiation levels. The APTS-MUX chip with pixel pitch size of 20 µm and reverse substrate voltage of 1.2 V.

$$C_{\text{input}} = C_{\text{measured}} - C_{\text{injection}} = \frac{n_{\text{el}} \cdot q_{\text{el}}}{V_{\text{Mn-K}_\alpha}} - C_{\text{injection}}, \tag{11.1}$$

where $V_{\text{Mn-}K_\alpha}$ is the mean of the Gaussian function fitted over the K_α peak of the seed pixel signal distribution, n_{el} is the number of electrons generated by an X-ray photon from the K_α emission of the ^{55}Fe radioactive source, thus set to 1640, q_{el} is the elementary charge, and $C_{\text{injection}}$ is the injection capacitance in the in-pixel pulsing circuit with a value ranging from 242 aF to 259 aF. A lower input capacitance leads to an improved voltage signal at the input of the front-end readout for the same charge, resulting in an enhanced signal-to-noise ratio (S/N) and analogue performance at the same power consumption. It alternatively allows for reducing the power of the readout circuit for the same performance.

The first row in Figure 11.16 shows the effect of several variables on the sensor input capacitance, starting from the reverse substrate voltage. All APTS-MUX chips are fabricated in the 'Modified with Gap' process. Hence, the depletion begins at the junction created by the low-dose n-type implant and does not reach the n-well collection electrode at zero reverse bias voltage. As the reverse substrate bias voltage is increased, the depletion region boundary ex-

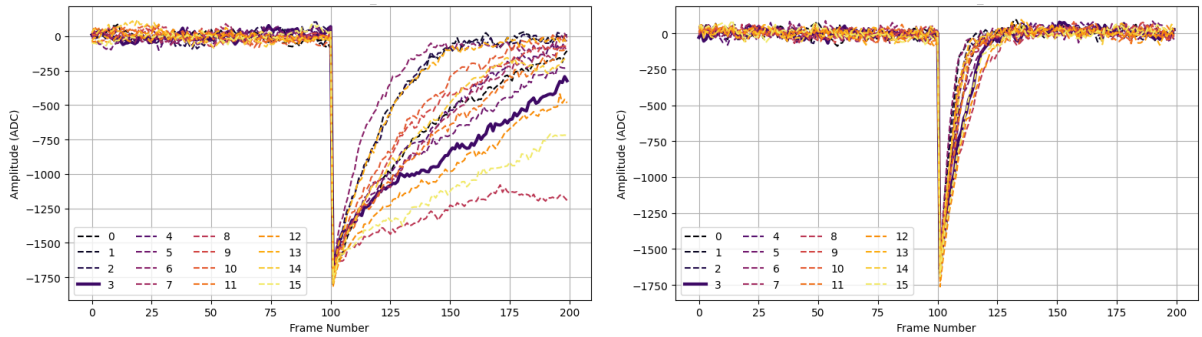

(a) **(b)**

Figure 11.15: The output signal of the 16 pixels of the reference variant of the APTS MUX chip exposed to NIEL irradiation of 10^{15} 1 MeV n_{eq} cm^{-2}, pulsed with $V_H = 1.2$ V at (a) $I_{reset} = 100$ pA and (b) $I_{reset} = 250$ pA. The pixel pitch size was 20 µm and the reverse substrate voltage of 1.2 V was applied.

tends towards the n-well collection electrode, significantly reducing the size of the undepleted region around the n-well collection electrode. It is the dominant factor in the calculation of the sensor input capacitance. Thus, the capacitance converges to a value of about 2 fF, similar to a sensor designed in the 'Standard' process, as the depletion region reaches the boundary of the n-well collection electrode and is more than two orders smaller than the capacitance of a typical high voltage (HV) DMAPS. The input capacitance is found to be unaffected by the pixel pitch size. The pixel geometry variant with the larger n-well collection electrode had a higher capacitance value, as was expected due to the limit imposed on the depletion region boundary by the size of the n-well collection electrode.

Energy Resolution

The energy resolution of the sensor is defined as the full width at half maximum (FWHM) of the Gaussian function fitted over the K_α peak of the seed pixel signal distribution divided by

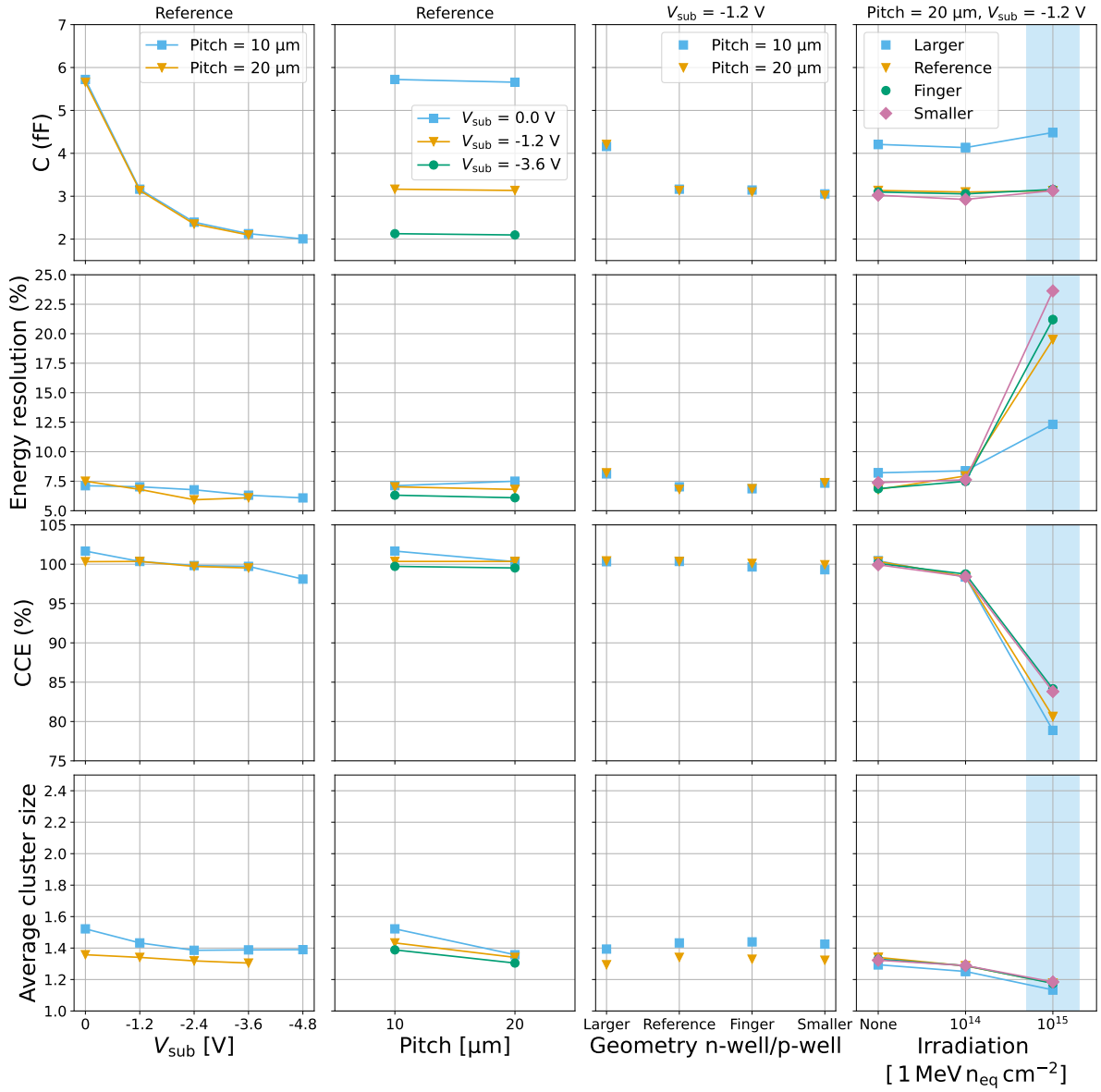

Figure 11.16: Comparison of the major quantities extracted from the measured ^{55}Fe spectra of various APTS-MUX chips. The light blue band in the last column corresponds to data points measured with an I_{reset} value of 250 pA.

its mean, denoted by $V_{\text{Mn-}K_\alpha}$.

The energy resolution decreases after the application of the reverse substrate voltage but is mostly unaffected by a further increase of this voltage, as shown in Figure 11.16. The energy resolution is similar for different pitch sizes and worsens with irradiation. The pixel geometry variant with the larger n-well collection electrode has a slightly worse energy resolution compared to the other three pixel geometries, which show similar resolutions. The energy resolution worsens with increasing irradiation level due to higher leakage and charge losses. However, the pixel geometry variant with the larger n-well collection electrode shows a lesser impact from irradiation, as a larger fraction of the pixel area is covered by the collection electrode, resulting in slightly shorter collection paths.

Charge Collection Efficiency

The charge collection efficiency (CCE) is the ratio of the most probable value of the matrix signal distribution to the most probable value of the seed pixel signal distribution of events with a cluster size of one, also referred to as single-pixel clusters.

As seen in Figure 11.16, a CCE of 100% can be achieved even without a reverse substrate voltage due to the lateral spread of the depletion region to the full pixel area. The same trend is seen for the different pixel pitch sizes and pixel geometry variants. Fluctuations to values above 100% can be seen due to the cumulative noise from the pixels in the matrix signal distribution. A reduction in CCE is seen with increasing irradiation levels due to charge loss.

Average Cluster Size

The average cluster size corresponds to the weighted average of the cluster size distribution at a threshold of 200 e^-.

Figure 11.16 shows that the average cluster size goes down with increasing reverse substrate voltage. Due to the increasing depth of the depletion region with increasing reverse substrate voltage, the charge shared with the pixels neighbouring the seed pixel decreases, resulting in a larger fraction of events with single-pixel clusters. Pixels with a smaller pitch size share more charge among the neighbouring pixels due to the smaller distance between the collection electrodes, leading to larger average cluster sizes. It can also be seen that the pixel geometry variant with the larger n-well collection electrode shares less charge; therefore, it has a lower average cluster size than the other three variants. The charge losses due to longer collection paths result in lower average cluster sizes with increasing irradiation.

11.3 Conclusion

The performance of several versions of the first production of analogue MAPS implemented in the TPSCo 65 nm technology and tested with the laboratory setup using an ^{55}Fe radioactive source has been presented. Pixel geometry variants with two pixel pitch sizes have been studied at different reverse substrate bias and NIEL irradiation levels.

All variants demonstrate high CCE and low charge sharing, having been implemented in the 'Modified with Gap' process. It leads to a higher signal-to-noise ratio and lower average cluster size than would be achievable with the 'Standard' process. An energy resolution of less than 7% can be achieved for the Mn-K_α peak of the ^{55}Fe spectrum at the I_{reset} value of 100 µA. The charge collection was seen to deteriorate with increasing NIEL irradiation. However, the signal peak can still be extracted up to the irradiation level of 10^{15} 1 MeV n_{eq} cm^{-2}, which is

significantly above the requirements of both the ALICE ITS3 and the FCC-ee vertex detector.

The calibration of the pixel response performed with the ^{55}Fe radioactive source is used to study the performance of the APTS-MUX chips with particle beams of positively charged hadrons.

12 Characterisation with a Test Beam

Test beam campaigns are crucial for characterising particle detectors under controlled, high-energy particle beams, enabling precise studies of sensor performance such as spatial resolution, detection efficiency, and charge collection. This is facilitated by the setup, referred to as a tracking telescope, which provides an external, high-precision reference for particle trajectories, allowing accurate determination of the intrinsic properties of the sensor being studied. By correlating the extrapolated particle impact positions with the sensor response, effects such as charge sharing and position-dependent efficiency maps can be thoroughly investigated.

Tests of the APTS chips were carried out with a positive hadron particle beam with the energy of 120 GeV/c at the H6 line of the CERN–SPS facility [202].

This work is partly presented in two NIM-A publications [4, 5].

12.1 Measurement Setup

The telescope was made of six reference planes, three on either side, with the device-under-test (DUT) and the trigger plane in the middle. Figure 12.1 shows the schematic of the telescope, detailing the distances between the planes, the direction of the beam, as well as the coordinate system. The telescope was kept within a light-tight box, and the DUT was cooled using a mini-chiller set to a temperature of 14 °C. This temperature was chosen in order to operate the DUT at the same temperature as the ^{55}Fe radioactive source measurements, as shown in Chapter 11, as a difference of 2 °C was seen between the set temperature and the temperature measured next to the DUT using a RTD-23 temperature sensor. Figure 12.2 shows two images of the telescope and of the full setup in the beam-line.

Reference Planes

Six ALPIDE sensors were used as reference planes, which provided tracking resolution, σ_{track}, of 2.1 µm [203]. The reference planes were operated at a reverse bias voltage of 3 V and were labelled in the ascending order from 'ALPIDE 0' to 'ALPIDE 5' in the direction of travel of the

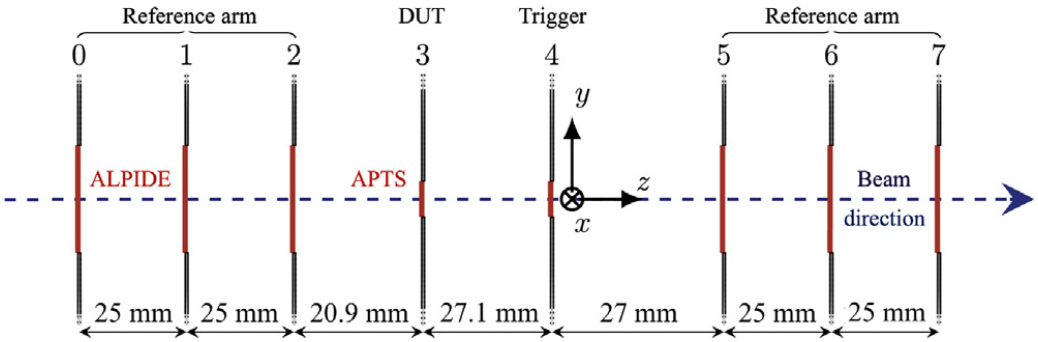

Figure 12.1: Schematic of the tracking telescope setup used at the CERN-SPS facility. The DUT and the trigger planes were formed by APTS chips, while the planes in the reference arms consisted of ALPIDE chips. The direction of the beam, the direction of the axes of the coordinate system, and the distance between the planes are shown. [4]

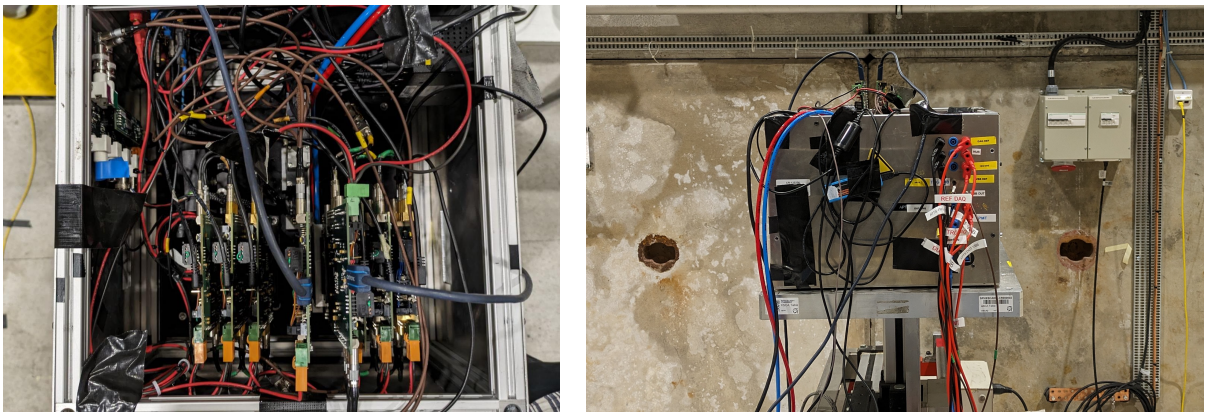

(a) (b)

Figure 12.2: Image of the tracking telescope within the metal box. (a) The setup of the ALPIDE reference planes, the APTS trigger, and the APTS DUT inside the metal box are shown. The trigger is mounted on a movable stage. (b) The tracking telescope box in the beam line on a movable table.

particle beam.

Trigger Plane

An APTS chip with a single matrix designed in the 'Modified with Gap' process and the pixel pitch size of 25 µm was used as the trigger device. The larger pitch size was used to make sure that every available DUT can fit within the shadow of the APTS trigger plane. A shadow of a plane is the cross-sectional area it covers in the path of the beam. The APTS chip was operated at a reverse substrate voltage of 1.2 V and is triggered internally by setting a threshold to suppress noise-triggered events.

Device-under-test

The DUTs tested at the testbeam are the four matrices on the APTS-MUX chip with different pixel geometry variations. All the matrices tested at different chip settings and irradiation levels are listed in Table 12.1.

pitch [µm]	**geometry variant**	$V_{\mathbf{sub}}$ [V]	**NIEL** [1 MeV n_{eq} cm^{-2}]
10	reference	0 and −1.2	none
	larger n-well collection electrode	0 and −1.2	none
	finger-shaped p-well enclosure	0 and −1.2	none
	smaller p-well enclosure	0 and −1.2	none
20	reference	0 and −1.2	none, 10^{14}, 10^{15}
	larger n-well collection electrode	0 and −1.2	none, 10^{14}, 10^{15}
	finger-shaped p-well enclosure	0 and −1.2	none, 10^{14}, 10^{15}
	smaller p-well enclosure	0 and −1.2	none, 10^{14}, 10^{15}

Table 12.1: List of the APTS variants that were tested at the CERN-SPS facility with different biasing setting settings and irradiation levels.

It was chosen to test the APTS-MUX chips at the reverse substrate voltage of 0 V and 1.2 V to study its impact on the performance of pixel geometry variants. The APTS chips with the reference pixel geometry variant were tested up to the reverse substrate voltage of 4.8 V [4].

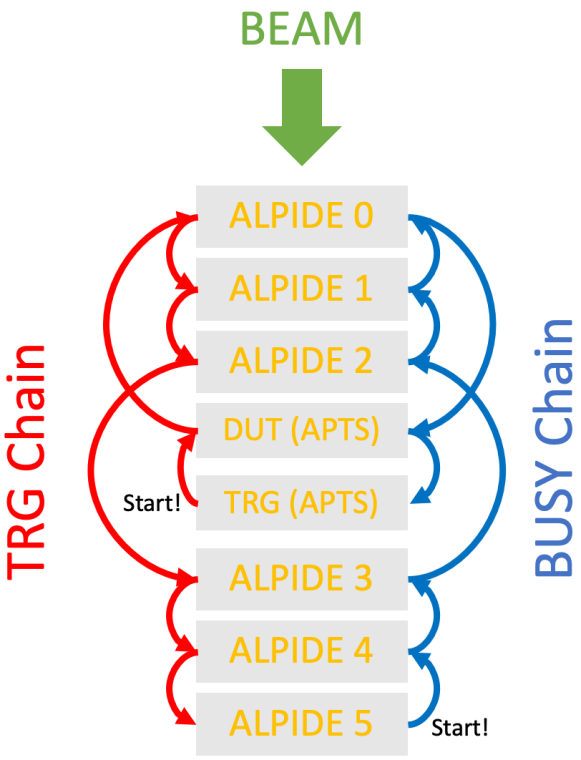

Figure 12.3: The logic chain for the trigger and the busy signals conveyed among the planes of the telescope during data acquisition.

Trigger and Busy Logic Chain

An external trigger signal is required by the DUT and the reference planes of the telescope to commence data acquisition. Once the trigger signal is received, 100 frames from before receiving the trigger signal and 100 frames from after receiving it are read out. While the readout systems of all of the planes are capturing data, a busy signal is asserted on the planes to block them from receiving new triggers in order to prevent the overflow of the readout buffer or data corruption.

The trigger and busy logic chain is shown in Figure 12.3. When the APTS-chip on the trigger plane collects a track hit that passes the pre-set threshold, it sends a trigger signal to the DUT. The DUT, in turn, sends a trigger signal to the first reference plane in the direction of travel of the beam, ALPIDE 0, which sends a trigger signal to the next reference plane and so on until the last reference plane in the direction of travel of the beam, ALPIDE 5, receives a trigger signal. Once the final plane in the telescope receives a trigger signal to begin data acquisition, a busy signal is sent up the chain, starting from the last reference plane to receive the trigger signal, ALPIDE 5, all the way to ALPIDE 0. ALPIDE 0 sends a busy signal to DUT, which finally sends a busy signal to the trigger. The duration of the busy signal tends to be of the order of milliseconds and blocks all the planes of the telescope from receiving new triggers.

The trigger signal begins, and the busy signal ends, at the scintillator plane when the telescope is being aligned in the beam path.

12.1.1 Global Coordinate System and Telescope Arrangement

The direction of travel of the beam is annotated as the positive z-axis. The plane of reference planes and the trigger and the DUT APTS chips is defined as the x-y plane, with the x-axis (y-axis) along the longer (shorter) edges of the ALPIDE chip on the reference planes. The origin of this global coordinate system is defined as the center of the first reference plane in the path of the beam, ALPIDE 0.

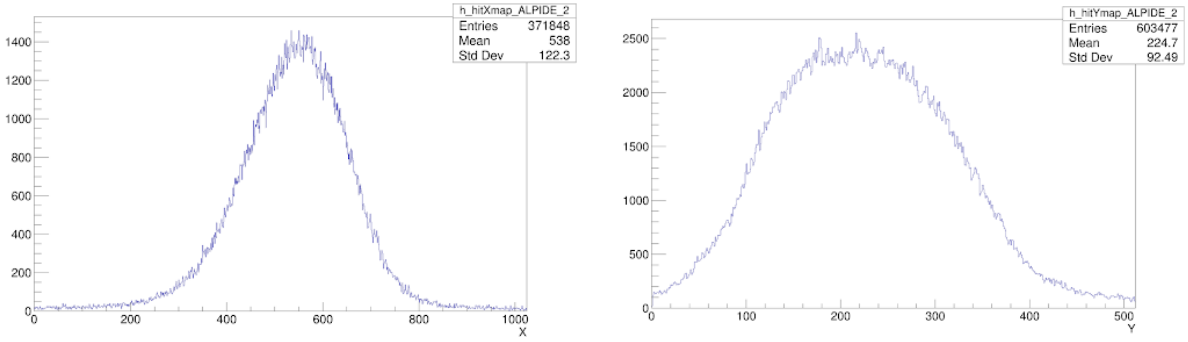

(a) **(b)**

Figure 12.4: The x-axis and y-axis projections of the shadow of the beam on the ALPIDE plane closest to the DUT, ALPIDE 2, while using the scintillator plane as the trigger device.

Three reference planes were positioned on each side of the telescope, with the trigger and the DUT planes sandwiched between them. The order of these planes in the positive z-axis direction was ALPIDE 0, ALPIDE 1, ALPIDE 2, DUT, trigger APTS, ALPIDE 3, ALPIDE 4, ALPIDE 5. The three ALPIDE planes on each side of the telescope were equidistant from each other at a distance of 25 mm. The DUT was positioned at a distance of 21 mm from ALPIDE 2. The trigger APTS plane was placed on a movable stage at a distance of 25.5 mm. ALPIDE 3 was positioned at a distance of 28.5 mm from the trigger APTS plane.

12.1.2 Telescope and Trigger Plane Alignment

A scintillator plane connected to a photomultiplier was used to align the telescope to the beam trajectory. The area of this scintillator plane was sufficiently larger than the area of the matrix of the ALPIDE chip. The telescope is moved in the x-y plane to align the telescope with the beam. The events triggered by the scintillators, after the telescope was aligned with the beam, as recorded by the ALPIDE plane closest to the DUT, are shown in Figure 12.4.

After the telescope is aligned to the beam, the location of the DUT with respect to the ALPIDE plane is found by using the DUT as the trigger device. The location of the APTS on the trigger plane is similarly measured with respect to the ALPIDE plane. Then, the trigger plane is moved in the x-y plane to coincide with the DUT. The shadow of the trigger plane on the reference plane closest to the DUT, after its alignment with the DUT, is shown in Figure

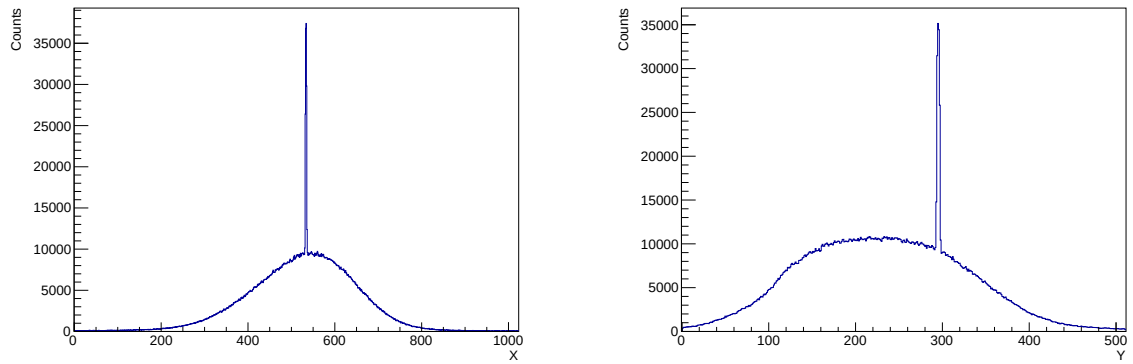

(a) **(b)**

Figure 12.5: The x-axis and y-axis projections of the shadow of the beam on the ALPIDE plane closest to the DUT, ALPIDE 2, while using the APTS trigger plane as the trigger device after its alignment with the DUT. The spikes denote the position of the APTS trigger plane.

12.5. The positions of the four variants on the APTS-MUX chips are predefined and the same for all of the APTS-MUX chips. Therefore, the APTS chip on the trigger plane is first aligned to one of the four variants, and then the alignment of the trigger APTS to the other variants on the same chip is done by moving the trigger relative to the first alignment position.

12.1.3 Data Acquisition

A modular cross-platform framework, EUDAQ2 [204], is used for data acquisition during the test beam measurements. It allows for the integration of and a synchronised data collection from heterogeneous devices as required by a test beam telescope comprising various sensors and trigger systems. Modules called `Producers` are used as an interface between the DAQ framework and the specific hardware components. These producers are defined for each individual detector, and they facilitate the configuration, control, and data acquisition of the corresponding detector. The readout mechanism and software, controlled by EUDAQ2, used for the DUT are the same as those used for the measurements in the laboratory.

12.2 Analysis Methodology

The Corryvreckan framework [205] is used to analyse the data acquired with the test beam. It is a high-performance modular framework that is flexible and versatile, and can be configured for a wide range of experimental setups. It is consistently used for nearly all silicon sensor characterisation studies, therefore making the comparison of the results easier.

The reconstruction chain is built via a central configuration file, where individual processing steps are implemented as dedicated modules. The roles of the telescope planes, along with their geometrical details and performance parameters, are defined in a separate geometry configuration file. This configuration file is essential for the alignment procedure and track reconstruction.

The key processes carried out at each stage of the analysis chain are described below.

12.2.1 Event Building

The `Metronome` module of the Corryvreckan framework segments the data stream into individual triggers, assigning a unique trigger ID to each event. Data from the ALPIDE reference planes corresponding to each trigger is incorporated into the event via the `EventLoaderEUDAQ2` module. A separate instance of this module is configured for the DUT, wherein 200 stored frames are associated with each trigger. A predefined frame establishes the baseline, and a search window

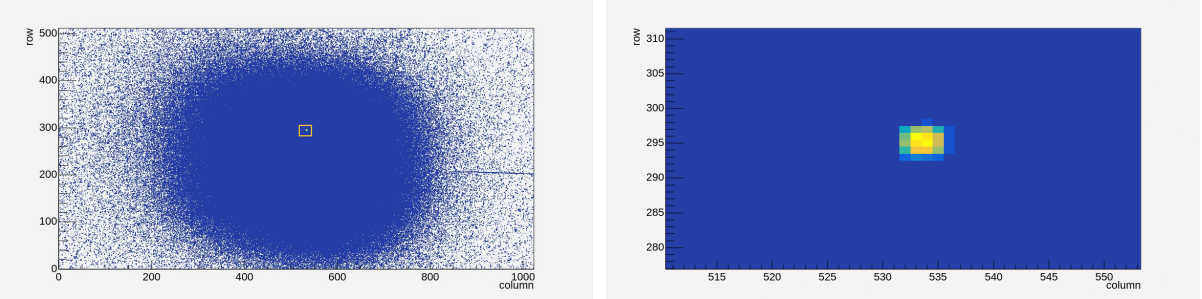

(a) **(b)**

Figure 12.6: (a) The hitmap of the ALPIDE plane closest to the DUT, ALPIDE 2. The blue region shows the position of the beam, while the yellow box highlights the position of the APTS trigger plane. (b) The hitmap of ALPIDE 2, zoomed-in to the APTS trigger plane position.

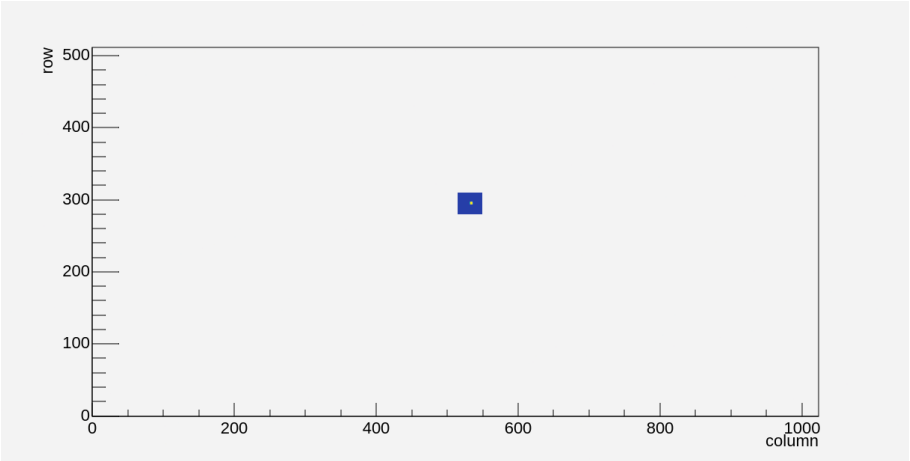

Figure 12.7: (a) The hitmap of the ALPIDE plane closest to the DUT, ALPIDE 2, after selecting a region-of-interest (ROI) for reconstruction.

is defined to identify the signal minimum. Signal extraction is performed using only the frame containing the minimum, which is evaluated relative to the baseline.

Figure 12.6a shows the hitmap on the reference plane closest to the DUT. The position of the trigger APTS can be clearly seen by zooming in on the appropriate section of the hitmap, as shown in Figure 12.6b. A region of interest (ROI) can be defined in such a manner to limit the reconstruction of clusters and tracks in the selected region and speed up the analysis by rejecting clusters and tracks outside the ROI, as shown in Figure 12.7.

12.2.2 Clustering for the Digital Reference Planes

The clustering module `ClusteringSpatial` is used for sensors where no timing information is available. This clustering algorithm only uses the positional information of the sensors collecting charge. In the case of the digital ALPIDE sensors used in the reference planes, the pixels collecting charge above a pre-defined threshold are clustered. The pixels in the clusters are required to be adjacent to each other. The cluster position can either be charge-weighted center-of-gravity, if the charge collected by each pixel is measured, or the arithmetic mean if the pixel information is binary.

12.2.3 Clustering for the Analogue DUT

The clustering module in the Corryvreckan framework, dedicated to analogue sensors, called `ClusteringAnalogue`, provides several clustering methods. Two such methods used in the laboratory measurements with the ^{55}Fe radioactive source were detailed in Section 11.2.4. The cluster positioning performed by these methods is as follows:

- **Seed:** The position of the seed pixel is assigned as the position of the cluster. This method leads to a resolution of pitch/$\sqrt{12}$, which is the upper limit of resolution for square pixel sensors.
- **Binary:** The position of the cluster is defined as the mean position of the pixels in the cluster, similar to a digital sensor. Separate thresholds can be set for the seed pixel and the neighbouring pixels, but are set to the same value in this study. The resolution obtained from this method is referred to as 'hit/no-hit' resolution in the following.
- **Cluster:** The position of the cluster is defined as the charge-weighted mean position of the pixels in the cluster. Thresholds for the seed pixel and the neighbouring pixels can be

set to different values, but are set to the same value in this study.

- **Window:** The position of the cluster is given by the charge-weighted mean position of the pixels in the cluster. No threshold is used to select the neighbour pixels in the cluster, and all pixels within a 3×3 window around the seed pixel are added to the cluster, leading to a constant cluster size of 9. In APTS, only the four innermost pixels are allowed to be the seed to have access to pixels within the 3×3 window around the seed pixel. Therefore, this method cannot be used for detection efficiency measurement.

The resolutions measured by using the window method for clustering are the lowest of all the available methods for clustering for sensors which have not been irradiated. As no threshold is used to add the neighbouring pixels to the cluster, no small fractions of charges shared with the neighbouring pixels are rejected, resulting in an excellent resolution. However, when the sensors are irradiated, the noise in the pixels due to leakage also increases, leading to worse resolutions. This effect is exaggerated with increasing irradiation level. The window method, with no threshold enforced on the neighbouring pixels, can also not be standardised for pixels with different levels of irradiation.

Varying charge sharing in different processes, as well as the assignment of the cluster position by the clustering algorithm, heavily influences the spatial resolution, which is dependent on the distribution of the residuals. Residuals are defined as the distance between the center of the cluster, assigned by the clustering method, and the interpolated position of the track intercept along the x- and y-axis.

The pixels designed in the 'Modified with Gap' process exhibit non-linear charge sharing due to the enhanced lateral electric field at the edges of the sensor caused by the gaps in the deep low-dose n-type implant. This non-linear charge sharing results in a lower weight being assigned to the neighbouring pixels in the cluster, while using the cluster method. As a consequence, most clusters are assigned positions near the center of the seed pixel, leading to large residuals for tracks passing away from the center of the seed pixel. This effect from the non-linear charge sharing can be corrected for through a process called 'η correction', where the correlation between the cluster position and the track position, both with respect to the seed pixel position, separately for the x- and y-axis, is measured and used to correct the cluster position. This process, however, can only be applied to clusters with a width of two pixels in the respective axis and must be repeated for every threshold, based on which the cluster size might change.

It must be noted that the binary method for clustering, which leads to the 'hit/no-hit' resolution, is equivalent to a rough η correction as it assigns more weight to the neighbouring pixels in the cluster. It was also seen in previous studies with the APTS chip that the binary method results in a resolution similar to the resolution achieved by the cluster method in conjunction with η correction.

In this study, the same threshold is used for the seed pixel and the neighbouring pixels during clustering. The cluster position used in the measurement of the spatial resolution is calculated using the binary method for clustering, and all the reported spatial resolutions are 'hit/no-hit' resolution.

12.2.4 Track Reconstruction

All combinations of clusters in the first and the last reference planes, i.e. ALPIDE 0 and ALPIDE 5, are connected to form straight lines. Clusters in the intermediate detectors are consecutively added if they are within the region defined by the spatial cuts. The DUT and the trigger device are excluded from the track reconstruction process. The General-Broken-Lines (GBL) model

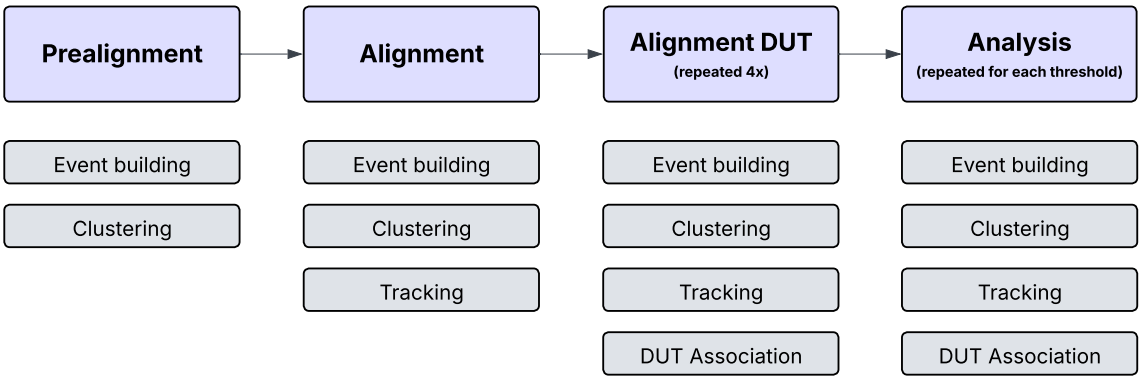

Figure 12.8: A flow chart of the tasks undertaken during the reconstruction and analysis of the testbeam data.

[206] is used for track reconstruction, which accounts for multiple scattering.

A track is only accepted if it has associated clusters in all six reference planes. Only tracks with a χ^2/n_{dof} value of less than 5 are accepted. When a cluster can potentially be assigned to multiple tracks, the track with the lowest χ^2/n_{dof} is kept. One track is selected per event, and only the tracks passing through the four innermost pixels of the DUT are considered in order to avoid edge effects.

Track reconstruction is used interchangeably with tracking in the following.

12.2.5 DUT Association

The clusters in the DUT must be associated with tracks reconstructed from the six reference planes to perform measurements of detection efficiency and spatial resolution. A search radius of 75 µm is defined around the intercept of the track on the DUT plane. A cluster with its center within the region defined by the search radius is associated with the track. A maximum of one cluster is allowed to be associated with each track. In case of multiple clusters being within the search radius, the cluster closest to the track is associated with the track.

12.3 Analysis Chain

Figure 12.8 summarises the steps executed during the analysis of the data acquired with the telescope during the testbeam campaign.

Prealignment and alignment are performed to correct for small inaccuracies in the predefined geometry of the planes of the telescope, including both the reference planes and the DUT plane. This process is necessary as the telescope geometry cannot be manually measured with the required precision. The precise position of the plane, as well as its orientation, highly influences the track reconstruction and the association of reconstructed tracks with the clusters on the DUT. The performance of the DUT is analysed after aligning the planes of the telescope, reconstructing the tracks with the clusters on the reference planes, and associating the clusters on the DUT with the tracks passing through the DUT.

12.3.1 Prealignment

Translational shifts of the reference and DUT planes are performed in the prealignment stage along the x- and y-axis. Correlations of the cluster position are measured with respect to the

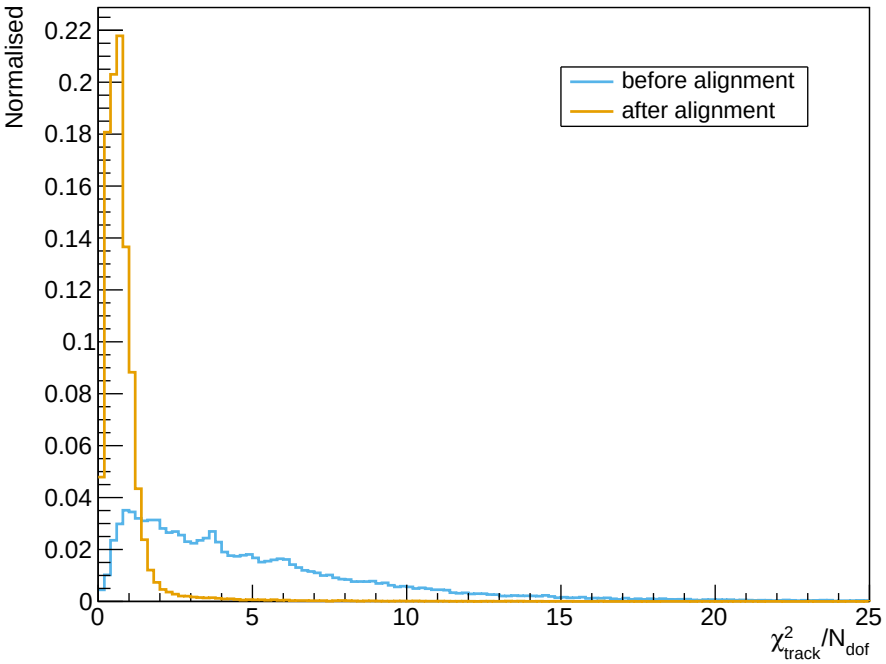

Figure 12.9: The χ^2/N_{Dof} of reconstructed tracks before and after the alignment of the reference planes of the telescope, showing the quality of the track reconstruction fits.

plane used as the geometrical reference plane, ALPIDE 0, and the planes are shifted along the x- and y-axis to bring the correlation parameters to zero. The correlations of the ALPIDE planes are fitted with a Gaussian function, and the mean of the Gaussian fit function is used as the parameter. If a Gaussian function cannot be fitted, the mean of the correlation histogram is used. The bin with the maximum amplitude is used as the parameter in the case of the APTS plane.

The prealignment is performed without employing track reconstruction, and therefore must be done before performing telescope alignment.

12.3.2 Telescope Alignment

During the telescope alignment, the planes are aligned by performing translational shifts along the x- and y-axis and rotational shifts around the z-axis. The DUT plane is excluded from this process. The tracks are reconstructed and simultaneous fits are performed for the track χ^2 and the alignment parameters, aiming to minimise the global residuals of all tracks across the six reference planes. The χ^2 of the reconstructed track and the global residuals of the reference planes are minimised instead of simply moving the planes by measuring the correlation compared to the geometrical reference plane, as the shifts in correlation may correspond to a physical misalignment of the telescope planes.

Figure 12.9 shows the χ^2/n_{dof} of the reconstructed tracks before and after performing telescope alignment. The residuals along the x- and y-axis on the reference plane closest to the DUT, ALPIDE 2, after aligning the telescope planes, are shown in Figure 12.10.

12.3.3 DUT Alignment

Once the reference planes have been aligned, the alignment of the DUT plane is performed in a similar fashion. The tracks are reconstructed, and the clusters on the DUT plane are associated

with the tracks passing through the DUT area. Track reconstruction is only done within the selected ROI on the reference planes. Translational alignment is performed along the x- and y-axis relative to the geometrical reference plane, and rotational alignment is performed around all three axes. The alignment aims to minimise the residuals calculated from the track intercepts on the DUT plane and center them around zero. This procedure is iterated four times.

Figure 12.11 shows the residuals along the x- and y-axis of the DUT[1] plane after the four iterations of the DUT alignment.

Temperature Impact on Alignment

The alignment procedure is the most time-intensive step in the analysis chain; therefore, it was a standard practice to perform alignment once and use it to analyse all data-taking runs until the DUT was disturbed or replaced. However, a shift in the mean of the residuals was observed during the analysis. This shift followed the trend of the difference between the ambient temperature of the telescope and the temperature of the DUT.

It was concluded that the temperature variation directly impacted the shift in the residuals [207]. The DUT is cooled using a minichiller, which results in the DUT and its holder being at a relatively constant temperature of 15 °C. The temperature inside the telescope, on the other hand, rises by approximately 10 °C over time due to the electronics in the box. Hence, the reference planes and their holders undergo thermal expansion while the DUT plane and its holder do not, resulting in shifted residuals over time. Thus, it was decided to perform the alignment steps for each data-taking run individually.

12.3.4 Detector Performance Analysis

Once the reconstructed tracks from the reference planes have been associated with clusters on the DUT, spatial resolution and detection efficiency measurements are performed.

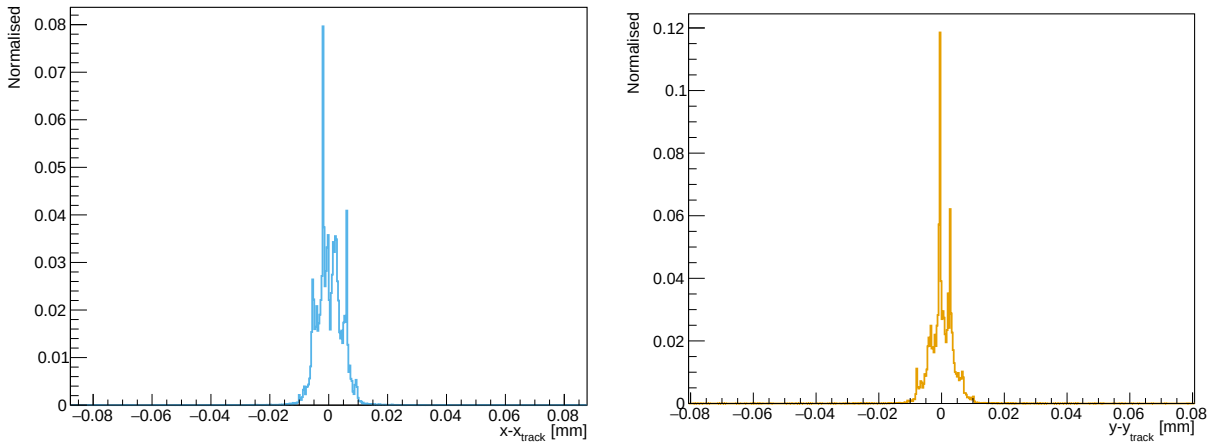

(a) **(b)**

Figure 12.10: The residuals along the x- and y-axis for the ALPIDE closest to the DUT, ALPIDE 2, centered around zero after the alignment of the reference planes of the telescope.

[1]The residuals correspond to an APTS with a pixel pitch size of 20 µm in the 'Modified with Gap' process, operated at the reverse substrate voltage of 1.2 V.

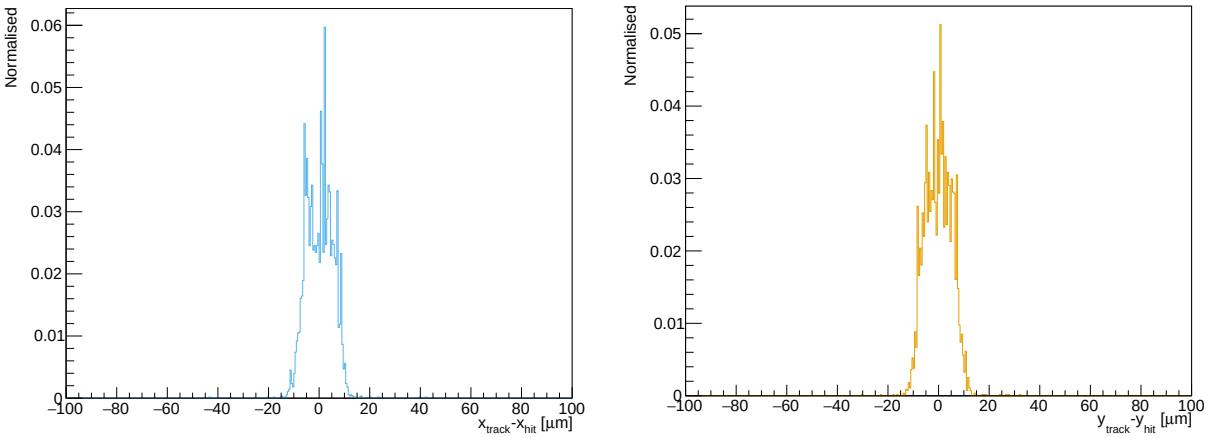

(a) **(b)**

Figure 12.11: The residuals along the x- and y-axis for the DUT, centered around zero after four iterations of DUT alignment using the reconstructed track and the associated clusters on the DUT.

Spatial Resolution

The standard deviation of both the x- and y-residuals is calculated and the track uncertainty, σ_{track}, is quadratically subtracted to obtain σ_{x} and σ_{y}. The spatial resolution is defined as the arithmetic mean of σ_{x} and σ_{y}.

Detection Efficiency

The detection efficiency is defined as the fraction of tracks with associated clusters on the DUT, referred to as efficient tracks, out of all tracks intercepting the DUT. Thus, the detection efficiency, ε, is

$$\varepsilon = \frac{k}{n}, \tag{12.1}$$

where k is the number of efficient tracks and n is the number of total tracks. The uncertainty is calculated by the default method used by ROOT's `TEfficiency` class [208].

12.4 Performance

The detection efficiency, spatial resolution, and cluster size were calculated from the analogue data acquired for all of the DUTs. These three performance parameters are presented with increasing threshold, which is used by the clustering algorithm to form pixel clusters. The noise of the DUTs was analysed to set the lowest threshold at which the performance of the DUTs is presented, which was chosen to be three times the RMS of the noise distribution.

The performance was studied for several varying properties of the APTS chips: pixel geometry, reverse substrate voltage, pixel pitch size, and NIEL irradiation level.

12.4.1 Seed Pixel Signal

Figure 12.12 shows the charge distribution of the seed pixel for different pixel geometry variations, pixel pitch sizes, and irradiation levels. The top-left figure shows that the most probable value (MPV) of the seed signal distribution follows the opposite trend of the average cluster size shown in Figure 11.16. The lower charge sharing in the variant with the larger n-well collection electrode results in a slightly larger MPV for the seed pixel signal.

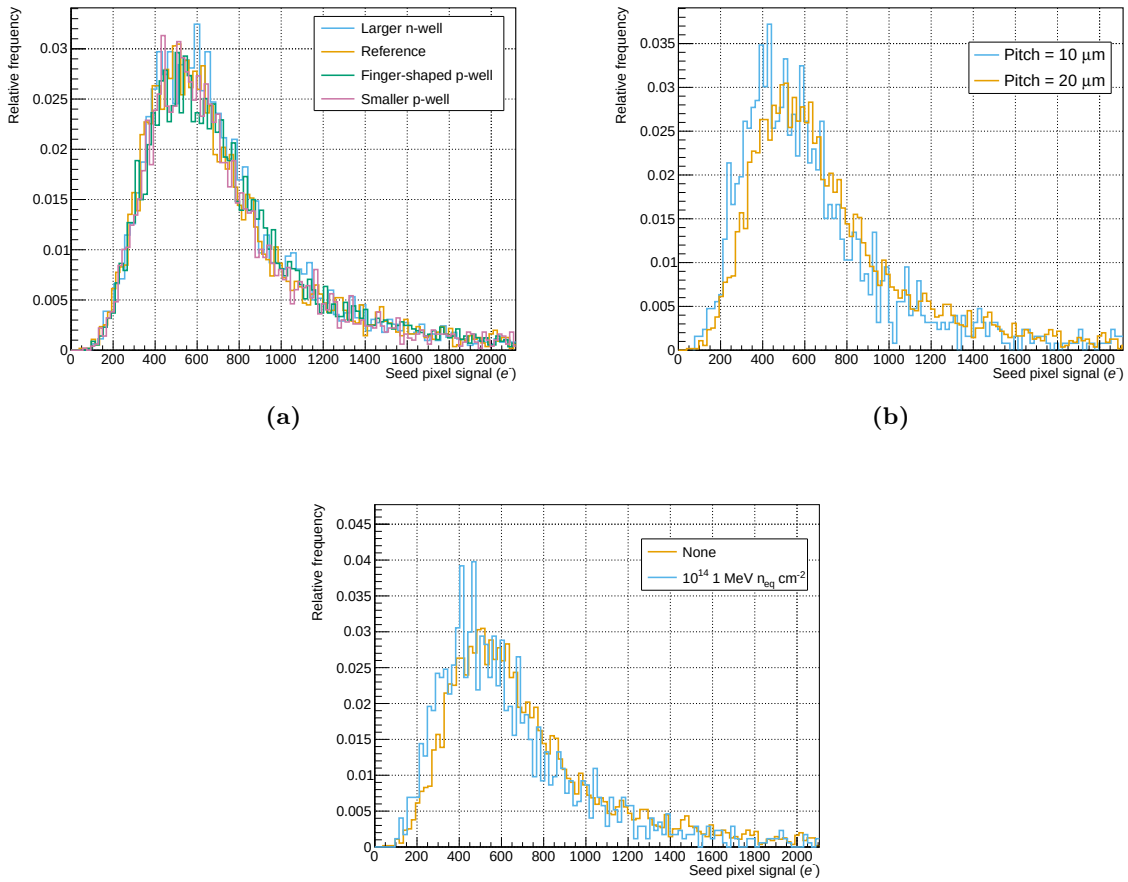

Figure 12.12: The distributions of the seed pixel signal charge showing comparisons among (a) the four pixel geometry variants, (b) the two pixel pitch sizes, and (c) NIEL irradiation levels. All measurements correspond to APTS chips produced in the 'Modified with Gap' process at the reverse substrate voltage of 1.2 V. All measurements correspond to the pixel pitch size of 20 µm, with the exception of one distribution in the top-right figure.

The top right figure shows the impact of different pixel pitch sizes on the charge distribution. It can be seen that the MPV of the seed pixel signal increases with increasing pixel pitch size. This is also in agreement with the fact that less charge sharing in larger pixel pitch sizes results in a smaller average cluster size.

The bottom figure shows the seed pixel charge distribution at various irradiation levels. The MPV of the charge shifts lower with increasing irradiation levels. This is due to the worse charge collection by irradiated sensors, as was also seen with the ^{55}Fe measurements.

12.4.2 Detection Efficiency

Figure 12.13 presents the detection efficiency of the four different pixel geometry variants on the APTS-MUX chip with a pixel pitch size of 20 µm at the reverse substrate voltage of 1.2 V. The detection efficiency of an APTS chip with a single matrix, labelled 'P-type', is added for reference. It is presented as a function of threshold in electron units (e^-). The measurement point with the lowest value of the threshold corresponds to 3 times the RMS of the noise; all other values of the threshold are larger than 3×RMS. It can be seen that the detection efficiency is independent of the pixel geometry. Increasing the threshold results in the loss of clusters in which a large fraction of the generated charge is shared among neighbouring pixels, leading to

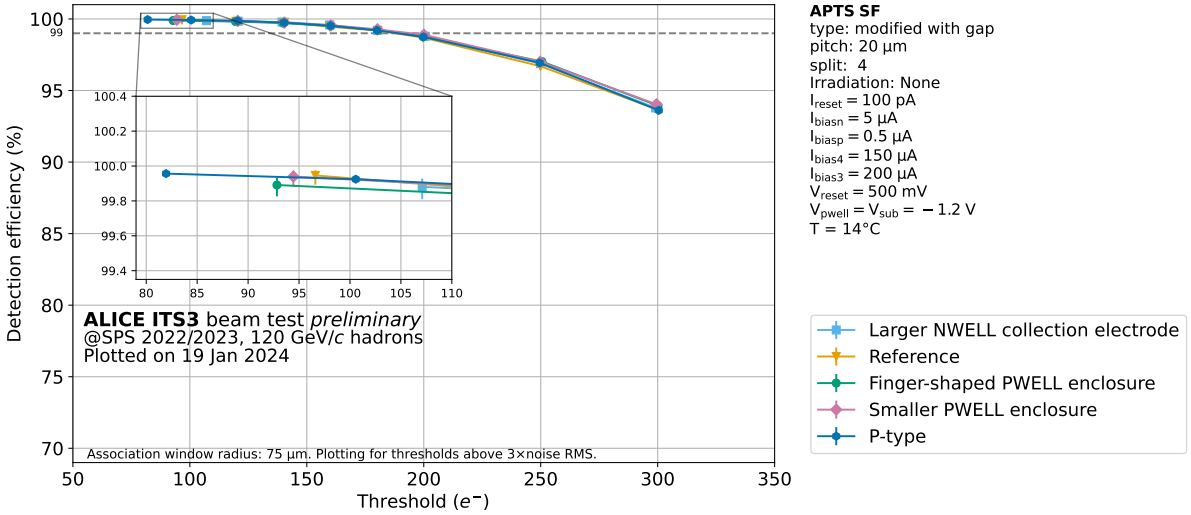

Figure 12.13: Efficiency as a function of the applied seed threshold, comparing different pixel geometry variants. The first points of measurement, as clearly visible in the zoomed inset, correspond to the threshold equivalent to 3 times the noise RMS value. The measurements shown are for the APTS with a pixel pitch size of 20 µm in the 'Modified with Gap' process, at the reverse substrate voltage of 1.2 V.

a lower efficiency.

The pixel geometry variant with the larger n-well collection electrode has a higher input capacitance than the other three variants; therefore, the noise is the highest for this variant, whereas the noise is the lowest for the variant with the smaller p-well enclosure, as can be seen in the zoomed-in inset of Figure 12.13. The best operational margin can be achieved with the variant with the smaller p-well enclosure, while the worst operational margin is achieved by the variant with the larger collection electrode. The noise of the APTS chip with a single matrix is lower than the reference matrix on the APTS-MUX chip due to the higher noise of the APTS-MUX chip resulting from the higher currents in the chip. Similar trends were observed at the

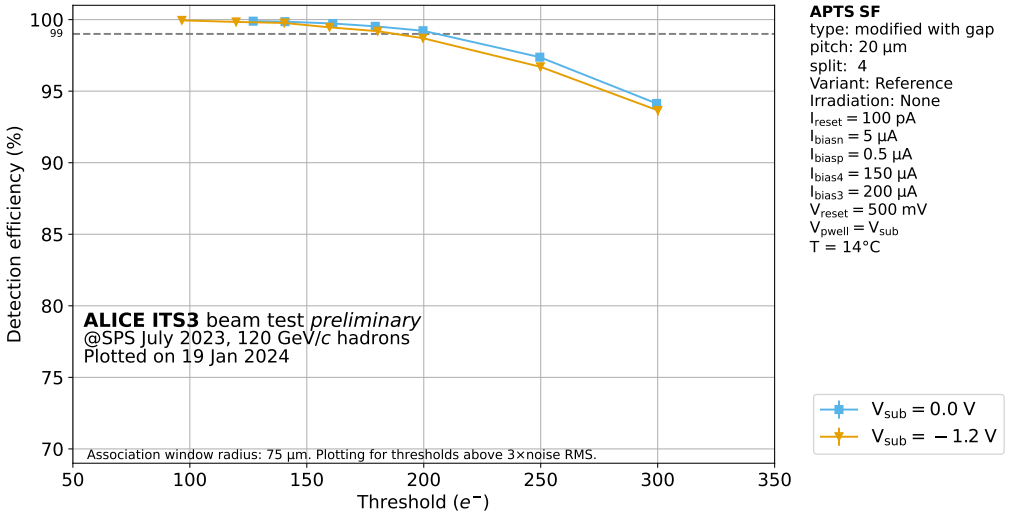

Figure 12.14: Efficiency as a function of the applied seed threshold, comparing different reverse substrate voltages. The first points of measurement correspond to the threshold equivalent to 3 times the noise RMS value. The measurements shown are for the reference pixel geometry variant of the APTS with a pixel pitch size of 20 µm in the 'Modified with Gap' process.

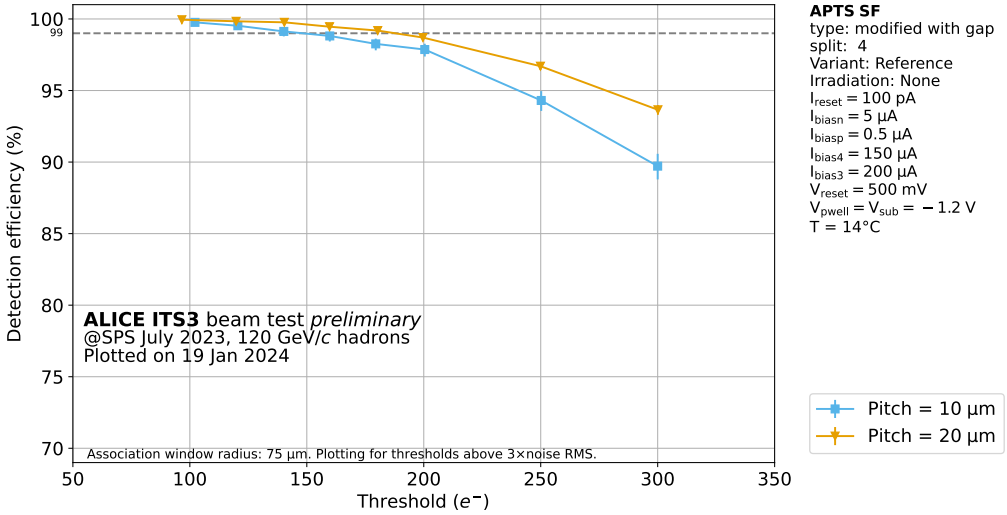

Figure 12.15: Efficiency as a function of the applied seed threshold, comparing different pixel pitch sizes. The first points of measurement correspond to the threshold equivalent to 3 times the noise RMS value. The measurements shown are for the reference pixel geometry variant of the APTS in the 'Modified with Gap' process, at the reverse substrate voltage of 1.2 V.

reverse substrate voltage of 0 V and for the APTS-MUX chip with the pixel pitch size of 10 µm.

Figure 12.14 shows the effect of reverse substrate voltage on the detection efficiency of the reference pixel geometry variant of the APTS-MUX chip with a pixel pitch size of 20 µm. The detection efficiency is presented as a function of the charge threshold for threshold values larger than 3 times the RMS of the noise. The detection efficiency is seen to be mostly independent of the reverse substrate voltage and goes down with increasing threshold. The measurement point with the smallest threshold value corresponds to 3 times the RMS of the noise. As the input capacitance decreases with increasing reverse substrate voltage, lower noise can be achieved with higher reverse substrate voltages. This allows access to lower threshold values while still maintaining a good signal-to-noise ratio, as can be seen in Figure 12.14, thus granting a larger operational margin. Similar performance was seen for the APTS-MUX chip with the pixel pitch size of 10 µm.

The detection efficiency of the reference pixel geometry variant of the APTS-MUX chips with different pixel pitch sizes is shown in Figure 12.15. The reverse substrate voltage is 1.2 V. In the 'Modified with Gap' process modification, sensors with higher pixel pitch size have less charge sharing among the neighbouring pixels, therefore a higher efficiency is seen for the sensor with pixel pitch size of 20 µm compared to the sensor with pixel pitch size of 10 µm. This difference in performance is exaggerated at higher values of the threshold. This effect leads to a larger operational margin above a 99% detection efficiency for sensors with larger pixel pitch sizes. Similar trends were seen for the other three pixel geometry variants on the APTS-MUX chip.

Summary

All pixel geometry variants show similar detection efficiencies. However, the higher noise in the variant with the larger collection electrode results in a smaller range of operation.

The efficiency is approximately the same at the two reverse substrate voltages. The threshold value at 99% efficiency slightly reduces with increasing reverse substrate voltage, but the noise also reduces, so the range of operation is slightly improved.

Both pixel pitch sizes show over 99% detection efficiency. The larger pixel pitch size shows

a larger range of operation than the smaller pixel pitch size. This behaviour was expected based on the trend seen in the average cluster size, which represents charge sharing, in the ^{55}Fe radioactive source measurements.

12.4.3 In-Pixel Detection Efficiency

The in-pixel studies were performed with high-statistics data by merging several runs to test the pattern of loss of detection efficiency at high thresholds [207]. The hits from the innermost four pixels are superimposed.

The in-pixel detection efficiency of the reference pixel geometry variant of the APTS-MUX chip with the pixel pitch size of 10 µm at a reverse substrate voltage of 1.2 V is presented in Figure 12.16. It corresponds to the threshold value of 250 e^- and a total efficiency of about 93.75%. The pixel is binned in a grid of 10×10, where the size of each bin is 1 µm × 1 µm. The detection efficiency of each bin refers to the efficiency of detecting a track hit when the track passes through the area of the bin. The point 'A' refers to the center of the pixel. The path from point 'A' to point 'B', marked by the blue arrows, moves from the center of the pixel to the center of the top edge of the pixel. The path marked by the orange arrows moves along the edge from the center of the edge to the corner of the pixel, noted by point 'C'. The path marked by the green arrows moves from the corner of the pixel to the pixel center. The figure on the right shows the efficiency average as the point is moved from 'A' to 'B' to 'C' for all possible path sections within the pixel.

The efficiency at the center of the pixel, where the collection electrode is located, is close to 99%, even at the high threshold of 250 e^-. When a track passes near the center of the pixel, the majority of the charge is collected by the seed pixel, and the transport paths of the generated charge are shorter; thus, the efficiency in this region is mostly unaffected by the threshold. A continuous decrease in efficiency is seen moving from 'A' to 'B'. When a track passes near the center of an edge of the pixel, the point is almost equidistant from the collection electrodes of

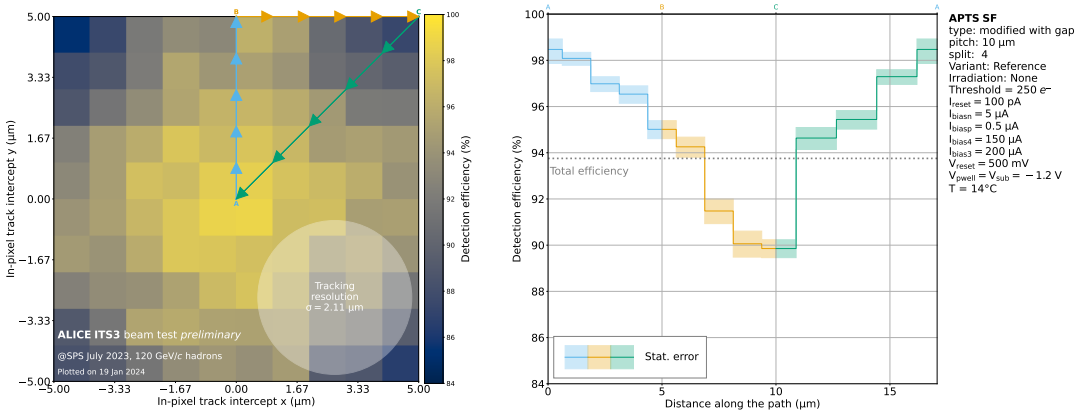

Figure 12.16: The in-pixel detection efficiency at the seed threshold value of 250 e^-. The left figure shows a single pixel divided into a grid of 10×10 bins, each representing the local detection efficiency. The right figure shows the efficiency along the path within the pixel, as marked in the left figure. The blue histogram indicates the efficiency while moving from the center of the pixel, Point A, to the edge, Point B. the orange histogram illustrates the efficiency while moving along the edge to the corner of the pixel, Point C. And the green path indicates the efficiency while moving from the corner, Point C, back to the center, Point A. The measurements shown correspond to the reference pixel geometry variant APTS with a pixel pitch size of 10 µm in the 'Modified with Gap' process, at the reverse substrate voltage of 1.2 V.

two pixels. The generated charge is typically shared with the neighbouring pixel that shares the particular pixel edge. The seed pixel tends to be the pixel through which the track passed due to the lateral electric field induced by the gap in the low-dose n-type implant. But at high threshold values, the efficiency goes down. Further reduction in efficiency is seen moving from 'B' to 'C'. The minimum of the detection efficiency is about 90% at the corner of the pixel. Tracks passing near the corners of the pixel generate a charge which is nearly equidistant from the collection electrodes of four pixels. The generated charge is likely to be collected by all four pixels, leading to lower detection efficiency compared to the rest of the pixel area at high threshold values. The efficiency starts to increase moving from 'C' back to 'A', reaching close to 99%.

12.4.4 Spatial Resolution and Average Cluster Size

The spatial resolution of the four different pixel geometry variants on the APTS-MUX chip with a pixel pitch size of 20 µm at the reverse substrate voltage of 1.2 V are presented in Figure 12.17 as a function of the charge threshold. The average cluster size is also shown in the same figure, represented by dashed lines. The spatial resolution and the average cluster size of a particular pixel geometry variant are represented by the same colour. It can be seen that the spatial resolution is lower than the binary resolution without any charge sharing ($\equiv$ pitch/$\sqrt{12}$). This is due to the charge being shared among the neighbouring pixels, as evident from the average cluster size of greater than one for all values of threshold shown in the figure. With the increase in threshold, the average cluster size decreases as the fraction of events with cluster size greater than one decreases. It also reflects in the worsening spatial resolution. The spatial resolution of the pixel geometry variant with the larger n-well collection electrode is worse than the other three variants, as the larger size of the collection electrode leads to less charge sharing and therefore a larger fraction of single-pixel cluster events. This can also be seen in the average cluster size, which is lower for the pixel geometry variant with the larger n-well collection electrode at any given threshold. Similar trends, albeit with lower values of spatial resolution, are seen for the APTS-MUX chip with the pixel pitch size of 10 µm.

Figure 12.18 shows the spatial resolution of the reference pixel geometry variant on the APTS-MUX chip with a pixel pitch size of 20 µm at different reverse substrate voltages. The depletion

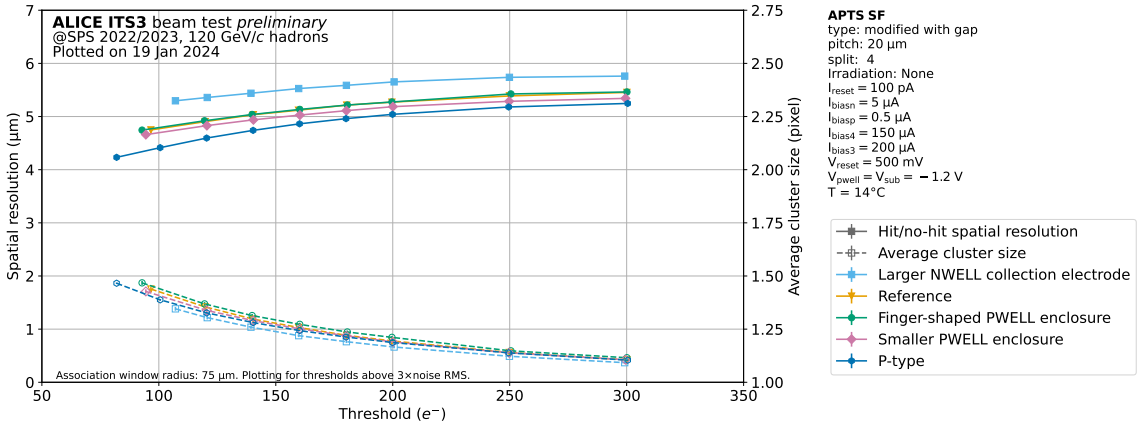

Figure 12.17: The hit/no-hit spatial resolution and the average cluster size as a function of the applied seed threshold, comparing different pixel geometry variants. The first points of measurement correspond to the threshold equivalent to 3 times the noise RMS value. The measurements shown are for the APTS with a pixel pitch size of 20 µm in the 'Modified with Gap' process, at the reverse substrate voltage of 1.2 V.

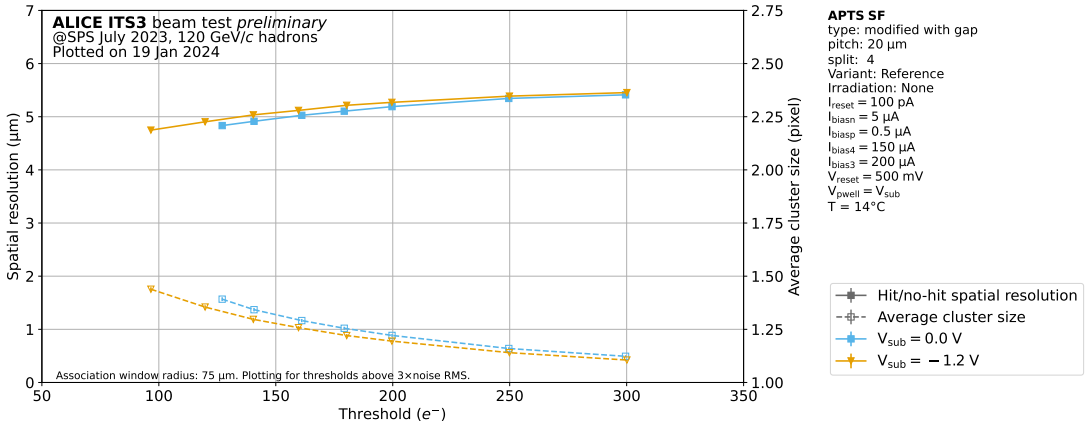

Figure 12.18: The hit/no-hit spatial resolution and the average cluster size as a function of the applied seed threshold, comparing different reverse substrate voltages. The first points of measurement correspond to the threshold equivalent to 3 times the noise RMS value. The measurements shown are for the reference pixel geometry variant of the APTS with a pixel pitch size of 20 µm in the 'Modified with Gap' process.

region extends further into the epitaxial layer with the application of the reverse substrate bias, which reduces the charge sharing among the neighbouring pixels as most of the generated charge is collected by the seed pixel. It can be seen that the average cluster size decreases with the application of reverse substrate voltage. This effect is reflected in the slightly worse resolution at the reverse substrate voltage of 1.2 V. Similar trends are seen for the other three pixel geometry variants on the APTS-MUX chip, as well as for the APTS-MUX chip with the pixel pitch size of 10 µm.

The spatial resolution of the reference pixel geometry variant on the APTS-MUX chip with different pixel pitch sizes at the reverse substrate voltage of 1.2 V is presented in Figure 12.19. It can be seen that the average cluster size is higher for the pixel pitch size of 10 µm compared to the pixel pitch size of 20 µm, as more charge is shared among the neighbouring pixels for a lower pixel pitch size due to the reduced distance between the collection electrodes. The lower pixel pitch size also corresponds to a lower binary resolution, and an improved resolution than binary resolution is achieved due to some charge sharing. It should be noted that an impressive

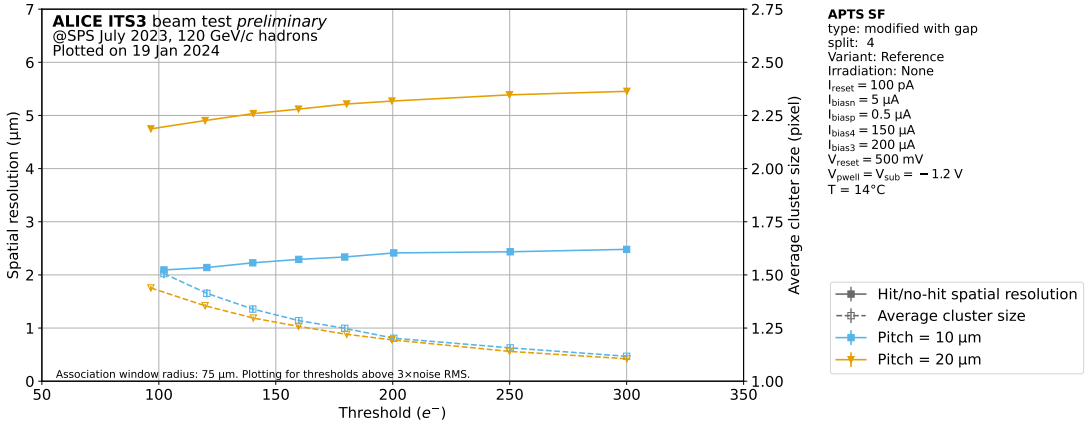

Figure 12.19: The hit/no-hit spatial resolution and the average cluster size as a function of the applied seed threshold, comparing different pixel pitch sizes. The first points of measurement correspond to the threshold equivalent to 3 times the noise RMS value. The measurements shown are for the reference pixel geometry variant of the APTS in the 'Modified with Gap' process, at the reverse substrate voltage of 1.2 V.

sub-3 µm resolution can be achieved with the pixel pitch size of 10 µm. Similar trends are seen at different reverse substrate voltages and for the other three pixel geometry variants on the APTS-MUX chip.

Summary

The resolution was measured to be better than the binary resolution for all pixel geometries and pitch sizes, and it was observed to slightly degrade with increasing threshold.

The average cluster size was seen to be lower for the larger pixel pitch size, as was also seen in the ^{55}Fe radioactive source measurements.

The average cluster size was lower for the variant with the larger n-well collection electrode. Consequently, the lesser charge sharing results in a worse resolution for this variant.

12.4.5 Radiation Tolerance

The detection efficiency is expected to reduce with increasing NIEL irradiation level, owing to effects like charge trapping. Less charge loss is expected for the pixel geometry variant with the larger collection electrode due to slightly shorter collection paths. Thus, fewer clusters with a size larger than 1 are expected to be lost. As a result, it is expected to be more radiation-tolerant than the other three pixel geometry variants.

The charge loss due to trapping defects arising from the NIEL irradiation results in a loss in detection efficiency as shown in Figure 12.20. This effect is exaggerated with increasing threshold, with more clusters being lost at higher thresholds. This leads to a smaller operational margin with efficiencies higher than 99%. The higher noise due to more leakage after irradiation is reflected in the higher noise RMS.

Figure 12.21 shows that the spatial resolution is mostly unaffected by irradiation, even though the average cluster size is consistently lower after irradiation. The cluster size is lower after irradiation because the pixels designed in the 'Modified with Gap' process share minimal charge outside the seed pixel. However, the charge collected by the neighbouring pixels will not cross the threshold in some cases, as the charge may get trapped due to the longer collection paths to

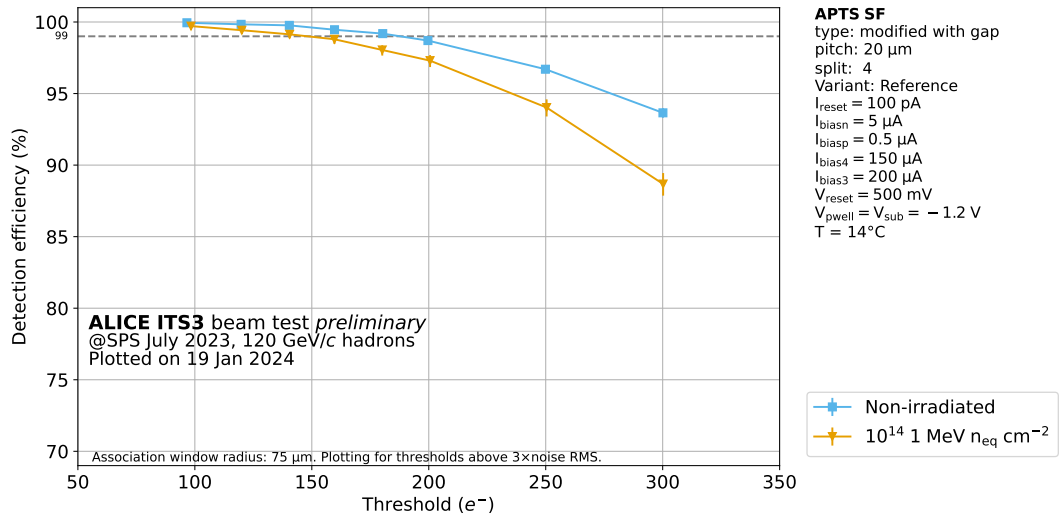

Figure 12.20: Efficiency as a function of the applied seed threshold, comparing different NIEL irradiation levels. The first points of measurement correspond to the threshold equivalent to 3 times the noise RMS value. The measurements shown are for the APTS with a pixel pitch size of 20 µm in the 'Modified with Gap' process, at the reverse substrate voltage of 1.2 V.

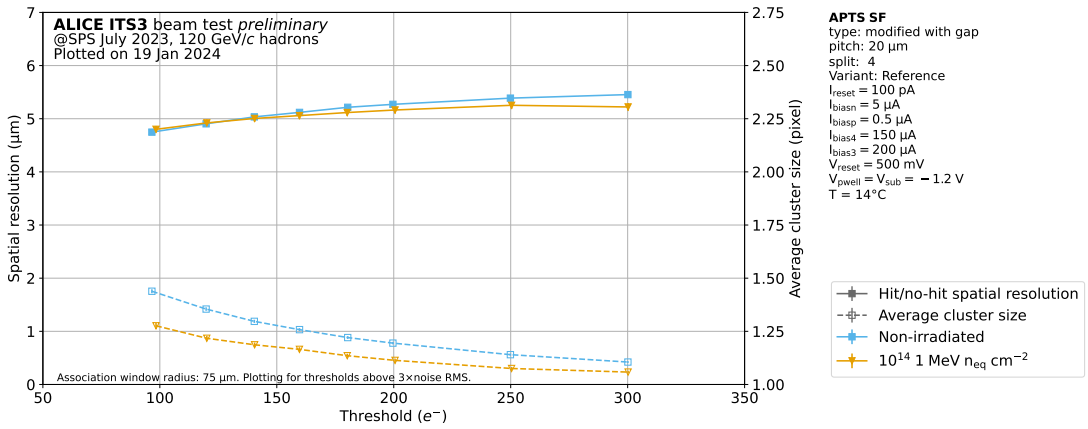

Figure 12.21: The hit/no-hit spatial resolution and the average cluster size as a function of the applied seed threshold, comparing different NIEL irradiation levels. The first points of measurement correspond to the threshold equivalent to 3 times the noise RMS value. The measurements shown are for the APTS with a pixel pitch size of 20 µm in the 'Modified with Gap' process, at the reverse substrate voltage of 1.2 V.

the collection electrodes of the neighbouring pixels. Similarly, some events with tracks passing close to the edges and corners of the pixel may get lost due to the trapping defects. This will leave a larger fraction of events where the tracks pass close to the center of the pixel, contributing to a lower spatial resolution.

The detection efficiency of the four pixel geometry variants is roughly similar after being irradiated, as shown in Figure 12.22. However, the variant with the larger collection electrode achieves slightly better efficiency compared to the other variants, as highlighted in the zoomed-in inset.

It can be seen in Figure 12.23 that after being irradiated to a high enough level, the differences between the four pixel geometry variants converge, and all four show similar average cluster size and spatial resolution.

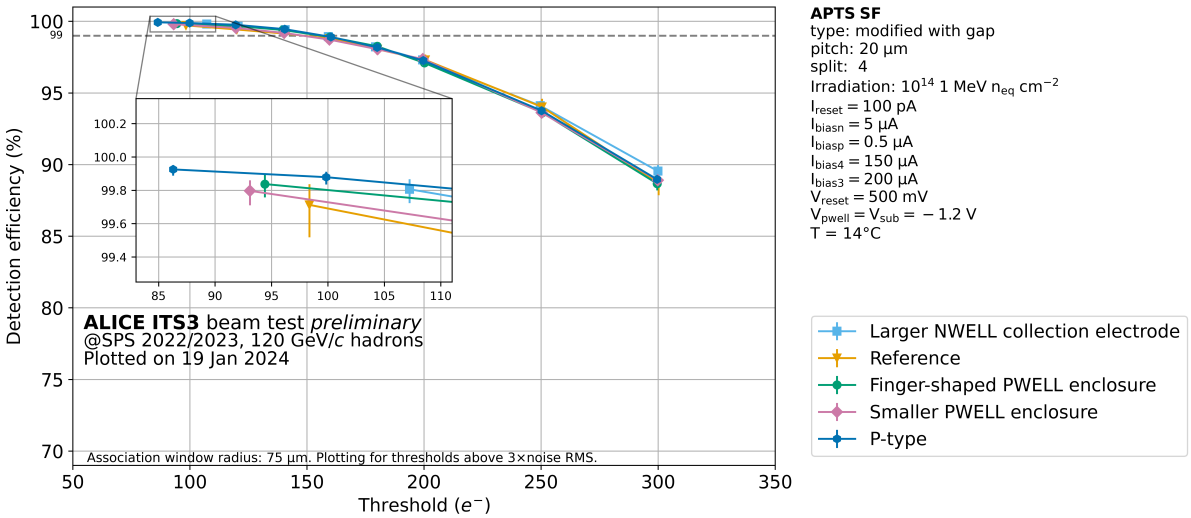

Figure 12.22: Efficiency as a function of the applied seed threshold, comparing different pixel geometry variants, irradiated to 10^{14} 1 MeV n_{eq} cm^{-2}. The first points of measurement correspond to the threshold equivalent to 3 times the noise RMS value. The measurements shown are for the APTS with a pixel pitch size of 20 µm in the 'Modified with Gap' process, at the reverse substrate voltage of 1.2 V.

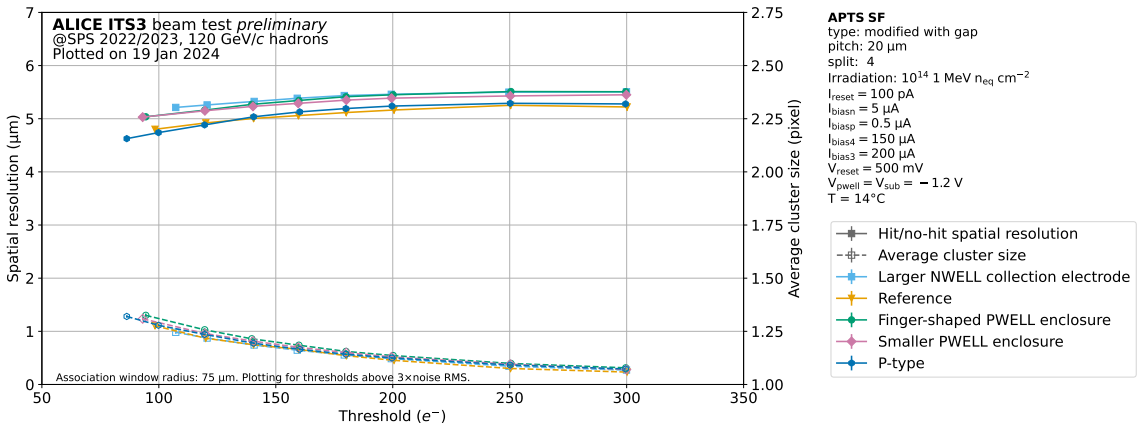

Figure 12.23: The hit/no-hit spatial resolution and the average cluster size as a function of the applied seed threshold, comparing different pixel geometry variants, irradiated to 10^{14} 1 MeV n_{eq} cm^{-2}. The first points of measurement correspond to the threshold equivalent to 3 times the noise RMS value. The measurements shown are for the APTS with a pixel pitch size of 20 µm in the 'Modified with Gap' process, at the reverse substrate voltage of 1.2 V.

The APTS-MUX chip was also tested at the irradiation level of 10^{15} 1 MeV n_{eq} cm^{-2}. However, due to the higher noise of the APTS-MUX chips as reported in Chapter 11, the ADC unit to e^- conversion factor could not be measured precisely, thus the results cannot be presented reliably.

Summary

The efficiency is comparable at low seed threshold for the two NIEL irradiation levels; however, it diverges at high seed thresholds, with worse efficiency for higher irradiation levels. It is also observed that the noise increases with increasing irradiation level.

Little impact is seen on the spatial resolution, but the average cluster size reduces significantly with increasing irradiation levels.

12.5 Conclusion

The characterisation of multiple analogue MAPS prototypes, fabricated in the TPSCo 65 nm CMOS technology, has been carried out in a test beam campaign. Analogue test structures with two different pixel pitch sizes (10 µm and 20 µm) and four pixel geometry variations were studied in the presence and absence of a reverse bias voltage, as well as at different irradiation levels.

The 'Modified with Gap' process leads to a high signal-to-noise ratio and less charge sharing. A spatial resolution of sub-3 µm can still be reached with a small pixel pitch size. All pixel geometry variants reach a detection efficiency over 99%, irrespective of the reverse bias voltage or the pitch size, and the pixel matrix with the larger pitch size demonstrated a larger operational margin.

A deterioration in the collected pixel charge and the detection efficiency was seen with increasing NIEL irradiation levels. The detection efficiency over 99% could still be reached at moderate NIEL irradiation levels of 10^{14} 1 MeV n_{eq} cm^{-2}, which is above the ALICE ITS3 requirements, as well as the current specifications of the FCC-ee vertex detectors.

The excellent detection efficiency in moderate radiation environments and small spatial resolution make MAPS developed in the 65 nm process a viable candidate for the vertex detectors at future lepton colliders, including FCC-ee.

Part V

Final Words

13 Conclusion and Perspective

The advancement of scientific knowledge requires a collaborative and interdisciplinary effort, and the same is the case for high-energy physics. Particle colliders and detector experiments are designed, built, and operated on the timescale of decades. The analysis techniques and the detector technologies are constantly evolving; future projects learn from the successes and failures of the past and improve upon the existing frameworks. This thesis presents synergistic efforts to develop new and improved data analysis techniques, jet flavour identification with a transformer-based neural network, and state-of-the-art detector technology, Monolithic Active Pixel Sensors (MAPS) produced in the 65 nm CMOS imaging technology.

`DeepJetTransformer`, a jet flavour tagging model based on a transformer neural network architecture, was employed to evaluate the influence of different reconstruction techniques, including particle identification (PID) and V^0 reconstruction, on jet flavour tagging performance.

Building on the success of deep learning techniques in jet structure analysis, `DeepJetTransformer` achieves excellent jet flavour identification performance while offering short training times, making it a strong candidate for studying the impact of detector designs on jet flavour tagging performance. Alongside its remarkable bottom and charm jet tagging performance, `DeepJetTransformer` exhibits an impressive discrimination of strange jets, highlighting the crucial contribution of PID and vertex reconstruction, in the form of secondary vertices and V^0s, to achieve optimal jet flavour tagging performance. These results are broadly applicable beyond the FCC-ee environment and the IDEA detector concept, provided adjustments are made for energy regimes, detector configurations, jet clustering, and PID strategies.

The efficient jet flavour tagging performance of `DeepJetTransformer`, combined with the high-statistics event samples at the Z resonance at the FCC-ee, enables the isolation of pure $Z \to b\bar{b}$, $Z \to c\bar{c}$, and $Z \to s\bar{s}$ samples, which allows for precise measurements of quark-specific asymmetries at the FCC-ee. This thesis presents results that show that an improvement by almost three orders of magnitude on the precision of the bottom and charm quark forward-backward asymmetry measurements at the Z pole can be achieved at the FCC-ee, compared to the combined measurements by the LEP/SLD electroweak collaboration.

The access to the hitherto scarcely studied strange decay channel of the Z boson allows for precise measurements of the strange quark forward-backward asymmetry at the Z pole, achieving an absolute statistical precision of $2.6 \cdot 10^{-6}$ at the FCC-ee, considering a luminosity of $125\,\mathrm{ab}^{-1}$ at the Z resonance.

These measurement improvements vitally depend on the ability of the detector technologies to achieve the performance targets anticipated at future collider facilities, including sub-3 µm spatial resolution, robustness under moderate irradiation levels, and a low material budget. The results presented in this thesis indicate that MAPS are well-positioned to meet these stringent requirements.

MAPS integrate the sensitive detector volume and the readout circuitry within a single device. Design modifications have been implemented through the addition of a low-dose n-type implant, which extends the depletion region across the full sensor area, thereby enhancing charge collection while maintaining low sensor capacitance. In the 'Modified-with-Gap' process, gaps are introduced in this additional implant layer at the pixel borders to increase the lateral electric

field within the sensor. The Analogue Pixel Test Structure (APTS) was specifically developed to evaluate the analogue performance of MAPS fabricated in the 65 nm CMOS imaging technology, incorporating multiple pixel geometry variations and pitch sizes, operated under different reverse substrate voltages, and tested across a range of NIEL irradiation levels.

Under laboratory conditions, the APTS demonstrated excellent energy resolution and a clear reduction in capacitance with increasing reverse substrate voltage, reaching a minimum at low bias. The measurements with an ^{55}Fe radioactive source also confirmed the linearity of the detector response.

The improved signal-to-noise ratio and reduced charge sharing achieved with the 'Modified-with-Gap' process enabled detection efficiencies exceeding 99%, irrespective of bias voltage or pixel pitch. The larger pitch matrix exhibited a broader operational margin and lower noise, while the smaller pitch provided sub-3 µm spatial resolution. Although both collected charge and detection efficiency degraded with increasing NIEL irradiation, efficiencies above 99% were sustained up to moderate irradiation levels.

The 65 nm CMOS process has now been validated, and the analogue properties of MAPS have been characterised by consistent results from the small and large matrix prototypes. The performance satisfies the specifications set forth by the ALICE ITS3 project and the FCC-ee.

The work presented in this thesis establishes a solid foundation for the integrated advancement of experimental methodologies for future colliders such as the FCC-ee.

Outlook

The experimental framework continues to evolve, and with time remaining before the construction and operation of the FCC-ee, it offers significant opportunities for further improvement and optimisation of both analysis methodologies and detector technologies.

The performance of the jet flavour tagger can be further enhanced by optimising the input feature set, particularly by adopting more realistic PID assumptions tailored to specific detector scenarios. Additional improvements may be achieved through optimisation of the network parameters and architecture, as well as by significantly enlarging the training dataset. Introducing flavour subdivisions to better handle processes such as gluon splitting could strengthen discrimination capabilities. Furthermore, event-level tagging may offer additional potential for performance gains by leveraging correlated features between jets, such as oppositely-charged high-momentum kaons in the outgoing jets in $Z \to s\bar{s}$ events.

Improvements in detector design, such as moving the innermost layer of the vertex detector closer to the beam pipe and reducing the thickness of the vertex layers, can significantly enhance heavy-flavour jet tagging by improving the impact parameter resolution and, consequently, the reconstruction of displaced vertices. Additionally, incorporating a dedicated PID detector could support strange-quark tagging.

A natural extension of isolating $Z \to s\bar{s}$ events and measuring quark-specific asymmetries would be to measure the branching fraction and coupling of the Z boson to the s quark and investigate further flavour-dependent properties at the Z pole that are particularly sensitive to extensions of the standard model. Extrapolating the excellent performance of `DeepJetTransformer` in discriminating strange jets and the continuing improvement of jet flavour taggers along with more sophisticated input features, there exists a promising opportunity for the precise study of the light u and d quarks at the Z resonance at the FCC-ee. The much larger Z boson cross-section will also provide opportunities for calibration and performance validation on data before the Higgs boson decay to s quarks is examined, which is likely to reduce experimental

uncertainties.

Detector technology is rapidly evolving and continues to offer substantial opportunities for refinement and innovation. Wafer-scale sensors can be realised using the stitching technique, while silicon thinned to 50 µm becomes sufficiently flexible to be bent into a cylindrical shape. This approach enables the construction of truly cylindrical vertex detectors with minimal supporting structures, as aimed by the ALICE ITS3 design. Prototypes of stitched sensors are currently being tested. Adopting a similar concept for the FCC-ee will necessitate further mechanical design developments. Additionally, there remains scope for improving the radiation tolerance of MAPS, as well as enhancing in-pixel circuit density and optimising the power budget through the transition to finer technology nodes.

The continued development of advanced analysis techniques, including jet flavour tagging, along with sustained innovation in detector technologies, such as MAPS, as presented in this thesis, will be crucial to maximise the physics potential of future collider experiments. The synergy between these efforts will enable unprecedented precision in measurements and expand the discovery capabilities of the next generation of facilities.

So long,

and thanks for all the fish!

References

[1] T. Suehara and T. Tanabe, "LCFIPlus: A framework for jet analysis in linear collider studies", *Nuclear Instruments and Methods in Physics Research Section A: Accelerators, Spectrometers, Detectors and Associated Equipment* **808** (feb, 2016) 109–116, doi:10.1016/j.nima.2015.11.054, arXiv:1506.08371.

[2] F. Blekman et al., "Tagging more quark jet flavours at FCC-ee at 91 GeV with a transformer-based neural network", *The European Physical Journal C* **85** (February, 2025) doi:10.1140/epjc/s10052-025-13785-y, arXiv:2406.08590.

[3] J. Altmann et al., "ECFA Higgs, electroweak, and top Factory Study", volume 5/2025 of *CERN Yellow Reports: Monographs*. 6, 2025. doi:10.23731/CYRM-2025-005, ISBN 978-92-9083-700-8, 978-92-9083-701-5.

[4] G. Aglieri Rinella et al., "Characterization of analogue Monolithic Active Pixel Sensor test structures implemented in a 65 nm CMOS imaging process", *Nuclear Instruments and Methods in Physics Research Section A: Accelerators, Spectrometers, Detectors and Associated Equipment* **1069** (2024) 169896, doi:https://doi.org/10.1016/j.nima.2024.169896.

[5] K. Gautam and A. Kumar, "Characterisation of analogue MAPS fabricated in 65 nm technology for the ALICE ITS3", *Nucl. Instrum. Meth. A* **1068** (2024) 169787, doi:10.1016/j.nima.2024.169787, arXiv:2409.07543.

[6] P. A. M. Dirac, "The quantum theory of the electron", *Proc. Roy. Soc. Lond. A* **117** (1928) 610–624, doi:10.1098/rspa.1928.0023.

[7] C.-N. Yang and R. L. Mills, "Conservation of Isotopic Spin and Isotopic Gauge Invariance", *Phys. Rev.* **96** (1954) 191–195, doi:10.1103/PhysRev.96.191.

[8] S. Weinberg, "The Making of the standard model", *Eur. Phys. J. C* **34** (2004) 5–13, doi:10.1140/epjc/s2004-01761-1, arXiv:hep-ph/0401010.

[9] S. L. Glashow, "Partial Symmetries of Weak Interactions", *Nucl. Phys.* **22** (1961) 579–588, doi:10.1016/0029-5582(61)90469-2.

[10] J. Goldstone, A. Salam, and S. Weinberg, "Broken Symmetries", *Phys. Rev.* **127** (1962) 965–970, doi:10.1103/PhysRev.127.965.

[11] P. W. Higgs, "Broken Symmetries and the Masses of Gauge Bosons", *Phys. Rev. Lett.* **13** (1964) 508–509, doi:10.1103/PhysRevLett.13.508.

[12] F. Englert and R. Brout, "Broken Symmetry and the Mass of Gauge Vector Mesons", *Phys. Rev. Lett.* **13** (1964) 321–323, doi:10.1103/PhysRevLett.13.321.

[13] P. W. Higgs, "Spontaneous Symmetry Breakdown without Massless Bosons", *Phys. Rev.* **145** (1966) 1156–1163, doi:10.1103/PhysRev.145.1156.

[14] S. Weinberg, "A Model of Leptons", *Phys.Rev.Lett,* **19** (November, 1967) 1264–1266,

doi:10.1103/physrevlett.19.1264.

[15] P. A. M. Dirac, "Quantum theory of emission and absorption of radiation", *Proc. Roy. Soc. Lond. A* **114** (1927) 243, doi:10.1098/rspa.1927.0039.

[16] R. P. Feynman, "QED: The Strange Theory of Light and Matter". Princeton University Press, 10, 2014. ISBN 978-0-691-16409-0, 978-0-691-02417-2.

[17] R. P. Feynman, "Space - time approach to quantum electrodynamics", *Phys. Rev.* **76** (1949) 769–789, doi:10.1103/PhysRev.76.769.

[18] M. Gell-Mann, "Symmetries of baryons and mesons", *Phys. Rev.* **125** (1962) 1067–1084, doi:10.1103/PhysRev.125.1067.

[19] K. G. Wilson, "Confinement of Quarks", *Phys. Rev. D* **10** (1974) 2445–2459, doi:10.1103/PhysRevD.10.2445.

[20] **Particle Data** Group, "Review of Particle Physics", *Phys. Rev. D* **98** (Aug, 2018) 030001, doi:10.1103/PhysRevD.98.030001.

[21] P. F. de Salas et al., "2020 global reassessment of the neutrino oscillation picture", *JHEP* **02** (2021) 071, doi:10.1007/JHEP02(2021)071, arXiv:2006.11237.

[22] N. Cabibbo, "Unitary Symmetry and Leptonic Decays", *Phys. Rev. Lett.* **10** (1963) 531–533, doi:10.1103/PhysRevLett.10.531.

[23] M. Kobayashi and T. Maskawa, "CP Violation in the Renormalizable Theory of Weak Interaction", *Prog. Theor. Phys.* **49** (1973) 652–657, doi:10.1143/PTP.49.652.

[24] M. Thomson, "Modern Particle Physics", 2013.

[25] ALEPH, DELPHI, L3, OPAL, SLD Collaborations, "Precision Electroweak Measurements on the Z Resonance", *Physics Reports* **427** (2006), no. 5, 257–454, doi:https://doi.org/10.1016/j.physrep.2005.12.006, arXiv:hep-ex/0509008.

[26] D. Bardin and G. Passarino, "The Standard Model in the Making: Precision Study of the Electroweak Interactions". Oxford University Press, 08, 1999. doi:10.1093/oso/9780198502807.001.0001, ISBN 9780198502807.

[27] J. H. Kühn et al., "Heavy Flavours at LEP", doi:10.5170/CERN-1989-008-V-1.267. Some results publ. in CERN 92-06.

[28] M. Dam, "Tests of the Electroweak Theory with the DELPHI detector at LEP", *CDS* (Apr, 1995).

[29] O. S. Brüning et al., "LHC Design Report". CERN Yellow Reports: Monographs. CERN, Geneva, 2004. doi:10.5170/CERN-2004-003-V-1.

[30] "HERA - A Proposal for a Large Electron Proton Colliding Beam Facility at DESY", technical report, 1981.

[31] S. Bethke, "Precision Physics at LEP", doi:10.1142/9789813238053_0005, arXiv:1712.03035. 20 pages, 17 figures, to appear in the book "From my vast repertoire - the legacy of Guido Altarelli". V2: typos removed and improved potentially misleading phrases in sections 3 and 5.

[32] "LEP design report". Report. CERN, Geneva, 1984. Copies shelved as reports in LEP,

PS and SPS libraries.

[33] R. Erickson, "SLC Design Handbook", technical report, SLAC National Accelerator Lab., Menlo Park, CA (United States), 04, 2004. doi:10.2172/826885.

[34] V. Shiltsev and F. Zimmermann, "Modern and Future Colliders", *Rev. Mod. Phys.* **93** (2021) 015006, doi:10.1103/RevModPhys.93.015006, arXiv:2003.09084. Submitted to Rev.Mod.Phys.

[35] K. Hübner, "The CERN intersecting storage rings (ISR)", *The European Physical Journal H* **36** (2012), no. 4, 509–522, doi:10.1140/epjh/e2011-20058-8.

[36] D. E.-S. (DESY), "PETRA: A model for the extension of the DESY storage rings to high energy", technical report, Deutsches Elektronen-Synchrotron (DESY), Hamburg (F.R. Germany); Zentralstelle fuer Atomkernenergie-Dokumentation, Leopoldshafen (F.R. Germany), 11, 1974.

[37] D. P. Barber et al., "Discovery of Three-Jet Events and a Test of Quantum Chromodynamics at PETRA", *Phys. Rev. Lett.* **43** (September, 1979) 830–833, doi:10.1103/PhysRevLett.43.830.

[38] R. B. et al., "Evidence for a spin-1 gluon in three-jet events", *Physics Letters B* **97** (1980) 453–458, doi:10.1016/0370-2693(80)90639-5.

[39] "Report on the design study of a 300 GeV proton synchrotron". Report. CERN, Geneva, 1964. French version available.

[40] F. N. A. L. (FNAL), "Design Report Tevatron 1 project", technical report, Fermi National Accelerator Lab. (FNAL), Batavia, IL (United States), 1984.

[41] **CDF** Collaboration, "Observation of top quark production in $\bar{p}p$ collisions", *Phys. Rev. Lett.* **74** (1995) 2626–2631, doi:10.1103/PhysRevLett.74.2626, arXiv:hep-ex/9503002.

[42] **D0** Collaboration, "Observation of the top quark", *Phys. Rev. Lett.* **74** (1995) 2632–2637, doi:10.1103/PhysRevLett.74.2632, arXiv:hep-ex/9503003.

[43] N. Toge, "KEK B-factory Design Report", technical report, KEK, Tsukuba, 1995.

[44] **SuperKEKB** Collaboration, "SuperKEKB Collider", *Nucl. Instrum. Meth. A* **907** (2018) 188–199, doi:10.1016/j.nima.2018.08.017, arXiv:1809.01958.

[45] **UA1** Collaboration, "Experimental Observation of Lepton Pairs of Invariant Mass Around 95 GeV/c^2 at the CERN SPS Collider", *Phys. Lett. B* **126** (1983) 398–410, doi:10.1016/0370-2693(83)90188-0.

[46] **UA2** Collaboration, "Evidence for $Z^0 \to e^+e^-$ at the CERN $\bar{p}p$ Collider", *Phys. Lett. B* **129** (1983) 130–140, doi:10.1016/0370-2693(83)90744-X.

[47] **ALEPH** Collaboration, "Measurement of the Z Resonance Parameters at LEP", *Eur. Phys. J. C* **14** (2000), no. 1, 1–50, doi:10.1007/s100520000319.

[48] **DELPHI** Collaboration, "Measurement of the Mass and Width of the Z^0 Particle from Multi - Hadronic Final States Produced in e^+e^- Annihilations", *Phys. Lett. B* **231** (1989) 539–547, doi:10.1016/0370-2693(89)90706-5.

[49] **OPAL** Collaboration, "Measurement of the Z^0 Mass and Width with the OPAL Detector

at LEP", *Phys. Lett. B* **231** (1989) 530–538, doi:10.1016/0370-2693(89)90705-3.

[50] **MarkII** Collaboration, "Initial Measurements of Z-boson Resonance Parameters in e^+e^- Annihilation", *Phys.Rev.Lett.* **63** (Aug, 1989) 724–727, doi:10.1103/PhysRevLett.63.724.

[51] C. Wyss, "LEP design report, v.3". CERN, Geneva, 1996. Vol. 1-2 publ. in 1983-84.

[52] A. Lopez-Fernandez, J. Ramão, F. de Campos, and J. Valle, "Model-independent Higgs boson mass limits at LEP", *Physics Letters B* **312** (Aug, 1993) 240–246, doi:10.1016/0370-2693(93)90518-m.

[53] A. Collaboration", "Observation of a new particle in the search for the Standard Model Higgs boson with the ATLAS detector at the LHC", *Physics Letters B* **716** (Sept, 2012) 1–29, doi:10.1016/j.physletb.2012.08.020.

[54] C. Collaboration, "Observation of a new boson at a mass of 125 GeV with the CMS experiment at the LHC", *Physics Letters B* **716** (Sept, 2012) 30–61, doi:10.1016/j.physletb.2012.08.021.

[55] **International Muon** Collaboration, "Interim report for the International Muon Collider Collaboration (IMCC)", *CERN Yellow Rep. Monogr.* **2/2024** (2024) 176, doi:10.23731/CYRM-2024-002, arXiv:2407.12450.

[56] **Linear** Collaboration, "The Linear Collider Facility (LCF) at CERN", arXiv:2503.24049.

[57] "The International Linear Collider Technical Design Report - Volume 3.II: Accelerator Baseline Design", arXiv:1306.6328.

[58] L. Linssen, A. Miyamoto, M. Stanitzki, and H. Weerts, "Physics and Detectors at CLIC: CLIC Conceptual Design Report", 2012.

[59] M. Bai et al., "C^3: A "Cool" Route to the Higgs Boson and Beyond", in *Snowmass 2021*. 10, 2021. arXiv:2110.15800.

[60] **HALHF** Collaboration, "HALHF: a hybrid, asymmetric, linear Higgs factory using plasma- and RF-based acceleration", arXiv:2503.19880.

[61] The CEPC Study Group, "CEPC Conceptual Design Report: Volume 2 - Physics & Detector", arXiv:1811.10545.

[62] **CEPC Study** Group, "CEPC Technical Design Report: Accelerator", *Radiat. Detect. Technol. Methods* **8** (2024), no. 1, 1–1105, doi:10.1007/s41605-024-00463-y, arXiv:2312.14363. [Erratum: Radiat.Detect.Technol.Methods 9, 184–192 (2025)].

[63] **FCC** Collaboration, "FCC Physics Opportunities: Future Circular Collider Conceptual Design Report Volume 1", *Eur. Phys. J. C* **79** (2019), no. 6, 474, doi:10.1140/epjc/s10052-019-6904-3.

[64] B. Auchmann et al., "FCC Midterm Report", *CDS* (2024) doi:10.17181/ZH1GZ-52T41.

[65] **FCC** Collaboration, "Future Circular Collider Feasibility Study Report: Volume 2, Accelerators, Technical Infrastructure and Safety", doi:10.17181/CERN.EBAY.7W4X, arXiv:2505.00274.

[66] Future Colliders Comparative Evaluation Working Group, "Input to the European

Strategy for Particle Physics update", technical report, CERN, Geneva, Switzerland, September 1, 2024. Submitted as input to the European Strategy for Particle Physics update.

[67] FCC Collaboration et al., "FCC-ee: The Lepton Collider: Future Circular Collider Conceptual Design Report Volume 2", *European Physical Journal: Special Topics* **228** (Jun, 2019) 261–623, doi:10.1140/epjst/e2019-900045-4.

[68] T. C. S. Group, "CEPC Conceptual Design Report: Volume 1 - Accelerator", 2018.

[69] K. Fujii et al., "Physics Case for the 250 GeV Stage of the International Linear Collider", 2017.

[70] M. B. e. a. CLIC Collaboration, "Updated baseline for a staged Compact Linear Collider", 2016. doi:10.5170/CERN-2016-004.

[71] M. Bicer et al., "First look at the physics case of TLEP", *Journal of High Energy Physics* **2014** (Jan, 2014) doi:10.1007/jhep01(2014)164.

[72] M. Benedikt et al., "FCC-ee: The Lepton Collider : Future Circular Collider Conceptual Design Report Volume 2", *Eur.Phys.J. Spec. Top* (Dec, 2018) doi:10.1140/epjst/e2019-900045-4.

[73] **FCC** Collaboration, "Future Circular Collider Feasibility Study Report: Volume 1, Physics, Experiments, Detectors", doi:10.17181/CERN.9DKX.TDH9, arXiv:2505.00272.

[74] **DELPHI** Collaboration, "Measurement of the strange quark forward-backward asymmetry around the Z^0 peak", *Eur.Phys.J. C - Particles and Fields* **14** (06, 2000) 613–631, doi:https://doi.org/10.1007/s100520000378.

[75] F. Bedeschi, "A detector concept proposal for a circular e+e- collider", *PoS* **ICHEP2020** (2021) 819, doi:10.22323/1.390.0819.

[76] **IDEA Study** Group, "The IDEA detector concept for FCC-ee", arXiv:2502.21223.

[77] N. Bacchetta et al., "CLD – A Detector Concept for the FCC-ee", doi:10.48550/ARXIV.1911.12230, arXiv:1911.12230.

[78] B. Francois, "Noble liquid calorimetry for a future FCC-ee experiment", *Nuclear Instruments and Methods in Physics Research Section A: Accelerators, Spectrometers, Detectors and Associated Equipment* **1040** (10, 2022) 167035, doi:10.1016/j.nima.2022.167035.

[79] **ILD Concept** Group, "International Large Detector: Interim Design Report", arXiv:2003.01116.

[80] ALEPH Collaboration, "Letter of Intent: ALEPH detector - Apparatus for LEP PHysics", Geneva, 1981.

[81] DELPHI Collaboration, "Letter of Intent: DELPHI detector (DEtector with Lepton Photon + Hadron Identification)", Geneva, 1982.

[82] G. F. von Dardel, A. H. Walenta, E. Lorenz, and P. Duinker, "L3: Letter of intent; 1982 ed.", Geneva, 1982.

[83] OPAL Collaboration, "Letter of Intent: OPAL Detector", Geneva, 1982.

[84] **The ATLAS** Collaboration, "The ATLAS Experiment at the CERN Large Hadron Collider", *Journal of Instrumentation* **3** (aug, 2008) S08003, doi:10.1088/1748-0221/3/08/S08003.

[85] **CMS** Collaboration, "The CMS experiment at the CERN LHC", *JINST* **3** (2008) S08004, doi:10.1088/1748-0221/3/08/S08004.

[86] C. Lippmann, "Particle identification", *Nuclear Instruments and Methods in Physics Research Section A: Accelerators, Spectrometers, Detectors and Associated Equipment* **666** (February, 2012) 148–172, doi:10.1016/j.nima.2011.03.009, arXiv:1101.3276.

[87] G. Cataldi, F. Grancagnolo, and S. Spagnolo, "Cluster counting in helium based gas mixtures", *Nucl. Instrum. Meth. A* **386** (1997) 458–469, doi:10.1016/S0168-9002(96)01164-3.

[88] S. Lee, M. Livan, and R. Wigmans, "Dual-Readout Calorimetry", *Rev. Mod. Phys.* **90** (2018), no. 2, 025002, doi:10.1103/RevModPhys.90.025002, arXiv:1712.05494.

[89] W. Klempt, "Review of particle identification by time-of-flight techniques", *Nucl. Instrum. Meth. A* **433** (1999) 542–553, doi:10.1016/S0168-9002(99)00323-X.

[90] **CLICdp** Collaboration, "A detector for CLIC: main parameters and performance", arXiv:1812.07337.

[91] E. D. R. R. P. Group, "The 2021 ECFA detector research and development roadmap", technical report, Geneva, 2020. doi:10.17181/CERN.XDPL.W2EX.

[92] M. Selvaggi, F. Bedeschi, and M. Ghilardi, "FCC-ee IDEA detector Delphes card",.

[93] J. de Favereau et al., "DELPHES 3: a modular framework for fast simulation of a generic collider experiment", *JHEP* **2014** (feb, 2014) doi:10.1007/jhep02(2014)057, arXiv:1307.6346.

[94] C. Bierlich et al., "A comprehensive guide to the physics and usage of PYTHIA 8.3", doi:10.48550/ARXIV.2203.11601, arXiv:2203.11601.

[95] **GEANT4** Collaboration, "GEANT4 — a simulation toolkit", *Nucl. Instrum. Meth. A* **506** (2003) 250, doi:10.1016/S0168-9002(03)01368-8.

[96] HEP-FCC, "card_IDEA.tcl: Delphes configuration card for IDEA (spring2021)". https://github.com/HEP-FCC/FCC-config/blob/spring2021/FCCee/Delphes/card_IDEA.tcl, 2021. Accessed: 2025-08-27 (spring2021 branch).

[97] HEP-FCC, "card_IDEA.tcl: Delphes configuration card for IDEA (winter2023)". https://github.com/HEP-FCC/FCC-config/blob/winter2023/FCCee/Delphes/card_IDEA.tcl, 2023. Accessed: 2025-08-27 (winter2023 branch).

[98] K. Gautam, "Flavour Identification Techniques", Master's thesis, University of Copenhagen, 2020. Presented 18 Sep 2020.

[99] P. Avery, "Applied Fitting Theory IV: Formulas for Track Fitting", https://www.phys.ufl.edu/~avery/fitting/fitting4.pdf, 1992.

[100] **CMS** Collaboration, "Particle-flow reconstruction and global event description with the CMS detector", *JINST* **12** (2017), no. 10, P10003, doi:10.1088/1748-0221/12/10/P10003, arXiv:1706.04965.

[101] C. Caputo et al., "Particle identification with the cluster counting technique for the IDEA drift chamber", *Nuclear Instruments and Methods in Physics Research Section A: Accelerators, Spectrometers, Detectors and Associated Equipment* **1048** (2023) 167969, doi:https://doi.org/10.1016/j.nima.2022.167969, arXiv:2211.04220.

[102] G. Wilkinson, "Particle identification at FCC-ee", *Eur.Phys.J. Plus* **136** (August, 2021) doi:10.1140/epjp/s13360-021-01810-4.

[103] E. Nakano, "Belle PID", *Nuclear Instruments and Methods in Physics Research Section A: Accelerators, Spectrometers, Detectors and Associated Equipment* **494** (2002), no. 1, 402–408, doi:https://doi.org/10.1016/S0168-9002(02)01510-3. Proceedings of the 8th International Conference on Instrumentation for Colliding Beam Physics.

[104] B. Andersson, G. Gustafson, G. Ingelman, and T. Sjöstrand, "Parton fragmentation and string dynamics", *Physics Reports* **97** (1983), no. 2, 31–145, doi:https://doi.org/10.1016/0370-1573(83)90080-7.

[105] M. Cacciari, G. P. Salam, and G. Soyez, "FastJet user manual", *Eur.Phys.J. C* **72** (mar, 2012) doi:10.1140/epjc/s10052-012-1896-2, arXiv:1111.6097.

[106] M. Cacciari, G. P. Salam, and G. Soyez, "The anti-kt jet clustering algorithm", *JHEP* **2008** (April, 2008) 063–063, doi:10.1088/1126-6708/2008/04/063, arXiv:0802.1189.

[107] S. Catani et al., "New clustering algorithm for multi - jet cross-sections in e+ e- annihilation", *Phys. Lett. B* **269** (1991) 432–438, doi:10.1016/0370-2693(91)90196-W.

[108] A. Albert et al., "Strange quark as a probe for new physics in the Higgs sector", doi:10.48550/ARXIV.2203.07535, arXiv:2203.07535.

[109] C. Helsens et al., "HEP-FCC/FCCAnalyses: v0.9.0", *Zenodo* (February, 2024) doi:10.5281/zenodo.10693709.

[110] F. Bedeschi, "A vertex fitting package", *CDS* (2024) doi:10.17181/HVCPV-BK752, arXiv:2409.19326.

[111] V. Nair and G. E. Hinton, "Rectified linear units improve restricted boltzmann machines", in *Proceedings of the 27th International Conference on International Conference on Machine Learning*, ICML'10, p. 807–814. Omnipress, Madison, WI, USA, 2010.

[112] N. Srivastava et al., "Dropout: A Simple Way to Prevent Neural Networks from Overfitting", *Journal of Machine Learning Research* **15** (2014), no. 56, 1929–1958.

[113] **ATLAS** Collaboration, "ATLAS flavour-tagging algorithms for the LHC Run 2 pp collision dataset", *Eur. Phys. J. C* **83** (2023), no. 7, 681, doi:10.1140/epjc/s10052-023-11699-1, arXiv:2211.16345.

[114] **CMS** Collaboration, "Identification of heavy-flavour jets with the CMS detector in pp collisions at 13 TeV", *JINST* **13** (2018), no. 05, P05011, doi:10.1088/1748-0221/13/05/P05011, arXiv:1712.07158.

[115] H. Qu and L. Gouskos, "ParticleNet: Jet Tagging via Particle Clouds", *Phys.Rev.D* **101** (2020), no. 5, 056019, doi:10.1103/PhysRevD.101.056019, arXiv:1902.08570.

[116] A. De Moor, "Deep learning for jet algorithms". PhD thesis, Vrije Universiteit Brussel, Belgium, 2024.

[117] **ATLAS** Collaboration, "Performance of b-Jet Identification in the ATLAS Experiment", *JINST* **11** (2016), no. 04, P04008, doi:10.1088/1748-0221/11/04/P04008, arXiv:1512.01094.

[118] **ATLAS** Collaboration, "ATLAS b-jet identification performance and efficiency measurement with $t\bar{t}$ events in pp collisions at $\sqrt{s} = 13$ TeV", *Eur. Phys. J. C* **79** (2019), no. 11, 970, doi:10.1140/epjc/s10052-019-7450-8, arXiv:1907.05120.

[119] S. Mondal and L. Mastrolorenzo, "Machine learning in high energy physics: a review of heavy-flavor jet tagging at the LHC", *Eur.Phys.J. Special Topics* (July, 2024) doi:10.1140/epjs/s11734-024-01234-y, arXiv:2404.01071.

[120] H. Luo et al., "Quark jet versus gluon jet: fully-connected neural networks with high-level features", *Sci. China Phys. Mech. Astron.* **62** (2019), no. 9, 991011, doi:10.1007/s11433-019-9390-8, arXiv:1712.03634.

[121] D. Guest et al., "Jet Flavor Classification in High-Energy Physics with Deep Neural Networks", *Phys.Rev.D* **94** (2016), no. 11, 112002, doi:10.1103/PhysRevD.94.112002, arXiv:1607.08633.

[122] P. T. Komiske, E. M. Metodiev, and M. D. Schwartz, "Deep learning in color: towards automated quark/gluon jet discrimination", *JHEP* **01** (2017) 110, doi:10.1007/JHEP01(2017)110, arXiv:1612.01551.

[123] **ATLAS** Collaboration, "Quark versus Gluon Jet Tagging Using Jet Images with the ATLAS Detector", 2017. All figures including auxiliary figures are available at https://atlas.web.cern.ch/Atlas/GROUPS/PHYSICS/PUBNOTES/ATL-PHYS-PUB-2017-017.

[124] V. Mikuni and F. Canelli, "ABCNet: An attention-based method for particle tagging", *Eur. Phys. J. Plus* **135** (2020), no. 6, 463, doi:10.1140/epjp/s13360-020-00497-3, arXiv:2001.05311.

[125] **ATLAS** Collaboration, "Graph Neural Network Jet Flavour Tagging with the ATLAS Detector", Geneva, 2022. All figures including auxiliary figures are available at https://atlas.web.cern.ch/Atlas/GROUPS/PHYSICS/PUBNOTES/ATL-PHYS-PUB-2022-027.

[126] A. Vaswani et al., "Attention Is All You Need", *Advances in Neural Information Processing Systems 30 (NIPS 2017)* (2017) doi:10.48550/ARXIV.1706.03762, arXiv:1706.03762.

[127] A. Duperrin, "Flavour tagging with graph neural networks with the ATLAS detector", arXiv:2306.04415.

[128] **ATLAS** Collaboration, "Transformer Neural Networks for Identifying Boosted Higgs Bosons decaying into $b\bar{b}$ and $c\bar{c}$ in ATLAS", Geneva, 8, 2023. All figures including auxiliary figures are available at https://atlas.web.cern.ch/Atlas/GROUPS/PHYSICS/PUBNOTES/ATL-PHYS-PUB-2023-021.

[129] H. Qu, C. Li, and S. Qian, "Particle Transformer for Jet Tagging", arXiv:2202.03772.

[130] J. Devlin, M.-W. Chang, K. Lee, and K. Toutanova, "BERT: Pre-training of Deep

Bidirectional Transformers for Language Understanding", arXiv:1810.04805.

[131] A. Dosovitskiy et al., "An Image is Worth 16×16 Words: Transformers for Image Recognition at Scale", arXiv:2010.11929.

[132] D. Parikh et al., "Performance of Graph Neural Networks for Point Cloud Applications", in *2023 IEEE High Performance Extreme Computing Conference (HPEC)*, pp. 1–7. 2023. arXiv:2304.07735. doi:10.1109/HPEC58863.2023.10363595.

[133] H. Xu et al., "Permutation Equivariance of Transformers and Its Applications", arXiv:2304.07735.

[134] A. Paszke et al., "PyTorch: An Imperative Style, High-Performance Deep Learning Library", arXiv:1912.01703.

[135] M. R. Zhang, J. Lucas, G. Hinton, and J. Ba, "Lookahead Optimizer: k steps forward, 1 step back", arXiv:1907.08610.

[136] L. Liu et al., "On the Variance of the Adaptive Learning Rate and Beyond", arXiv:1908.03265.

[137] C. Adolphsen et al., "The International Linear Collider Technical Design Report". CERN, Geneva, Jun, 2013. Comments: See also http://www.linearcollider.org/ILC/TDR . The full list of signatories is inside the Report.

[138] L. Linssen, A. Miyamoto, M. Stanitzki, and H. Weerts, eds., "Physics and Detectors at CLIC: CLIC Conceptual Design Report". CERN, 2, 2012. doi:10.5170/CERN-2012-003.

[139] The European Strategy Group, "Deliberation document on the 2020 Update of the European Strategy for Particle Physics", Geneva, 2020. doi:10.17181/ESU2020Deliberation.

[140] J. de Blas et al., "Higgs Boson studies at future particle colliders", *JHEP* **2020** (jan, 2020) doi:10.1007/jhep01(2020)139, arXiv:1905.03764.

[141] D. d'Enterria, "Higgs physics at the Future Circular Collider", *PoS* **ICHEP2016** (2017) 434, doi:10.22323/1.282.0434, arXiv:1701.02663.

[142] P. Azzi, L. Gouskos, M. Selvaggi, and F. Simon, "Higgs and top physics reconstruction challenges and opportunities at FCC-ee", *Eur.Phys.J. Plus* **137** (December, 2021) doi:10.1140/epjp/s13360-021-02223-z, arXiv:2107.05003.

[143] F. An et al., "Precision Higgs physics at the CEPC", *Chinese Physics C* **43** (April, 2019) 043002, doi:10.1088/1674-1137/43/4/043002, arXiv:1810.09037.

[144] D. M. Asner et al., "ILC Higgs White Paper", in *Snowmass 2013: Snowmass on the Mississippi*. 10, 2013. arXiv:1310.0763.

[145] H. Abramowicz et al., "Higgs physics at the CLIC electron–positron linear collider", *Eur.Phys.J. C* **77** (jul, 2017) doi:10.1140/epjc/s10052-017-4968-5, arXiv:1608.07538.

[146] Y. Nakai, D. Shih, and S. Thomas, "Strange Jet Tagging", arXiv:2003.09517.

[147] J. Erdmann, "A tagger for strange jets based on tracking information using long short-term memory", *Journal of Instrumentation* **15** (jan, 2020) P01021, doi:10.1088/1748-0221/15/01/P01021, arXiv:1907.07505.

[148] J. Erdmann, O. Nackenhorst, and S. V. Zeißner, "Maximum performance of strange-jet tagging at hadron colliders", *JINST* **16** (2021), no. 08, P08039, doi:10.1088/1748-0221/16/08/P08039, arXiv:2011.10736.

[149] **SLD** Collaboration, "SLD Design Report", 5, 1984.

[150] **SLD** Collaboration, "First Direct Measurement of the Parity-Violating Coupling of the Z^0 to the s Quark", *Phys.Rev.Lett.* **85** (Dec, 2000) 5059–5063, doi:10.1103/PhysRevLett.85.5059, arXiv:hep-ex/0006019.

[151] DELPHI Collaboration, "b-tagging in DELPHI at LEP", *Eur.Phys.J. C* **32** (jan, 2004) 185–208, doi:10.1140/epjc/s2003-01441-8, arXiv:hep-ex/0311003.

[152] J. Proriol et al., "Tagging B quark events in ALEPH with neural networks: comparison of different methods", *Int. J. Neural Syst.* **3** (Aug, 1991) Supp. 267–270. 26 p.

[153] V. Abazov et al., "b-Jet identification in the D0 experiment", *Nuclear Instruments and Methods in Physics Research Section A: Accelerators, Spectrometers, Detectors and Associated Equipment* **620** (aug, 2010) 490–517, doi:10.1016/j.nima.2010.03.118, arXiv:1002.4224.

[154] J. Freeman et al., "Introduction to HOBIT, a b-jet identification tagger at the CDF experiment optimized for light Higgs boson searches", *Nuclear Instruments and Methods in Physics Research Section A: Accelerators, Spectrometers, Detectors and Associated Equipment* **697** (jan, 2013) 64–76, doi:10.1016/j.nima.2012.09.021, arXiv:1205.1812.

[155] A. J. Larkoski, J. Thaler, and W. J. Waalewijn, "Gaining (Mutual) Information about Quark/Gluon Discrimination", *JHEP* **11** (2014) 129, doi:10.1007/JHEP11(2014)129, arXiv:1408.3122.

[156] D. Buskulic et al., "Performance of the ALEPH detector at LEP", *Nuclear Instruments and Methods in Physics Research Section A: Accelerators, Spectrometers, Detectors and Associated Equipment* **360** (1995), no. 3, 481–506, doi:https://doi.org/10.1016/0168-9002(95)00138-7.

[157] **CMS** Collaboration, "Particle-Flow Event Reconstruction in CMS and Performance for Jets, Taus, and MET", CERN, Geneva, 4, 2009.

[158] F. Bedeschi, L. Gouskos, and M. Selvaggi, "Jet flavour tagging for future colliders with fast simulation", *Eur.Phys.J.C* **82** (jul, 2022) doi:10.1140/epjc/s10052-022-10609-1, arXiv:2202.03285.

[159] K. Gautam, "Jet-Flavour Tagging at FCC-ee", *PoS* **ICHEP2022** (2022) 1147, doi:10.22323/1.414.1147, arXiv:2210.10322.

[160] R. D. Field and R. P. Feynman, "A Parametrization of the Properties of Quark Jets", *Nucl. Phys. B* **136** (1978) 1, doi:10.1016/0550-3213(78)90015-9.

[161] D. Krohn, M. D. Schwartz, T. Lin, and W. J. Waalewijn, "Jet Charge at the LHC", *Phys. Rev. Lett.* **110** (2013), no. 21, 212001, doi:10.1103/PhysRevLett.110.212001, arXiv:1209.2421.

[162] L. Breiman, "Random Forests", *Machine Learning* **45** (Oct, 2001) 5–32, doi:10.1023/A:1010933404324.

[163] A. Fisher, C. Rudin, and F. Dominici, "All models are wrong, but many are useful: Learning a variable's importance by studying an entire class of prediction models simultaneously", *Journal of Machine Learning Research* **20** (2019), no. 177, 1–81, doi:https://doi.org/10.48550/arXiv.1801.01489, arXiv:1801.01489.

[164] M. Cacciari and G. P. Salam, "Pileup subtraction using jet areas", *Phys.Lett.B* **659** (2008), no. 1, 119–126, doi:https://doi.org/10.1016/j.physletb.2007.09.077, arXiv:0707.1378.

[165] J. Duarte-Campderros, G. Perez, M. Schlaffer, and A. Soffer, "Probing the Higgs–strange-quark coupling at e^+e^- colliders using light-jet flavor tagging", *Phys.Rev.D* **101** (June, 2020) 115005, doi:10.1103/physrevd.101.115005, arXiv:1811.09636.

[166] Glen Cowan, Eilam Gross, "Discovery significance with statistical uncertainty in the background estimate", ATLAS Statistics Forum, 2008.

[167] J. Haller et al., "Update of the global electroweak fit and constraints on two-Higgs-doublet models", *Eur. Phys. J. C* **78** (2018), no. 8, 675, doi:10.1140/epjc/s10052-018-6131-3, arXiv:1803.01853.

[168] J. de Blas et al., "Global analysis of electroweak data in the Standard Model", *Phys. Rev. D* **106** (2022), no. 3, 033003, doi:10.1103/PhysRevD.106.033003, arXiv:2112.07274.

[169] F. Cossutti et al., "Measurement of the strange quark forward- backward asymmetry at the Z peak using fast charged kaons",.

[170] **SLD** Collaboration, "First direct measurement of the parity violating coupling of the Z0 to the s quark", *Phys. Rev. Lett.* **85** (2000) 5059–5063, doi:10.1103/PhysRevLett.85.5059, arXiv:hep-ex/0006019.

[171] **TASSO** Collaboration, "Measurement of the Asymmetry of b Quark Production in e^+e^- Annihilation of s= 35-GeV", *Z. Phys. C* **48** (1990) 433–444, doi:10.1007/BF01572023.

[172] D. Decamp et al., "Measurement of charge asymmetry in hadronic Z decays", *Physics Letters B* **259** (1991), no. 3, 377–388, doi:https://doi.org/10.1016/0370-2693(91)90844-G.

[173] **ALEPH** Collaboration, "Determination of sin**2 theta(w)(eff) using jet charge measurements in hadronic Z decays", *Z. Phys. C* **71** (1996) 357–378, doi:10.1007/s002880050183.

[174] **DELPHI** Collaboration, "Measurement of the strange quark forward backward asymmetry around the Z0 peak", *Eur. Phys. J. C* **14** (2000) 613–631, doi:10.1007/s100520000378.

[175] **L3 OPAL SLD LEP Electroweak Working Group SLD Electroweak Group SLD Heavy Flavour Group** Collaboration, "Precision electroweak measurements on the Z resonance", *Phys. Rept.* **427** (2006) 257–454, doi:10.1016/j.physrep.2005.12.006, arXiv:hep-ex/0509008.

[176] **L3 OPAL LEP Electroweak Working Group SLD Heavy Flavor Electroweak Groups** Collaboration, "A Combination of preliminary electroweak measurements and constraints on the standard model", arXiv:hep-ex/0112021.

[177] A. Blondel, "Jet charges and Electroweak Asymmetry measurements". Presentation at FCC-ee Electroweak Precision – Progress Meeting, jan, 2025.

[178] **ALEPH** Collaboration, "Measurement of A**b(FB) using inclusive b hadron decays", *Eur. Phys. J. C* **22** (2001) 201–215, doi:10.1007/s100520100812, arXiv:hep-ex/0107033.

[179] H. Kolanoski and N. Wermes, "Particle Detectors: Fundamentals and Applications". Oxford University Press, Oxford, UK; New York, NY, USA, 2020. Graduate-level text covering detector principles, technologies, and applications. ISBN 9780191890710, 0191890715.

[180] H. Kraner, Z. Li, and K. Posnecker, "Fast neutron damage in silicon detectors", *Nuclear Instruments and Methods in Physics Research Section A: Accelerators, Spectrometers, Detectors and Associated Equipment* **279** (1989), no. 1, 266–271, doi:https://doi.org/10.1016/0168-9002(89)91091-7.

[181] H. Bichsel, "Straggling in thin silicon detectors", *Rev. Mod. Phys.* **60** (Jul, 1988) 663–699, doi:10.1103/RevModPhys.60.663.

[182] M. Suljic, "Study of Monolithic Active Pixel Sensors for the Upgrade of the ALICE Inner Tracking System", February, 2018.

[183] G. Knoll, "Radiation Detection and Measurement". Wiley, 2010. ISBN 9780470131480.

[184] F. Hartmann, "Evolution of Silicon Sensor Technology in Particle Physics", volume 275 of *Springer Tracts in Modern Physics*. Springer, 2017. doi:10.1007/978-3-319-64436-3, ISBN 978-3-319-64434-9, 978-3-319-64436-3.

[185] **ALICE** Collaboration, "The ALICE experiment at the CERN LHC", *Journal of Instrumentation* **3** (aug, 2008) S08002, doi:10.1088/1748-0221/3/08/S08002.

[186] **ALICE** Collaboration, "Technical Design report for the ALICE Inner Tracking System 3 - ITS3 ; A bent wafer-scale monolithic pixel detector", technical report, CERN, Geneva, 2024. Co-project Manager: Magnus Mager, magnus.mager@cern.chds.

[187] A. Abada et al., "FCC-ee: The Lepton Collider", *The European Physical Journal Special Topics* **228** (2019), no. 2, 261–623, doi:10.1140/epjst/e2019-900045-4.

[188] **ALICE** Collaboration, "Technical Design Report for the Upgrade of the ALICE Inner Tracking System", *Journal of Physics G: Nuclear and Particle Physics* **41** (jul, 2014) 087002, doi:10.1088/0954-3899/41/8/087002.

[189] **ALICE** Collaboration, "ALICE Inner Tracking System (ITS): Technical Design Report". Technical design report. ALICE. CERN, Geneva, 1999.

[190] F. Carminati et al., "ALICE: Physics Performance Report, Volume I", *Journal of Physics G: Nuclear and Particle Physics* **30** (oct, 2004) 1517, doi:10.1088/0954-3899/30/11/001.

[191] G. Aglieri et al., "Monolithic active pixel sensor development for the upgrade of the ALICE inner tracking system", *Journal of Instrumentation* **8** (dec, 2013) C12041, doi:10.1088/1748-0221/8/12/C12041.

[192] J. Schambach et al., "A MAPS Based Micro-Vertex Detector for the STAR Experiment",

Physics Procedia **66** (2015) 514–519, doi:https://doi.org/10.1016/j.phpro.2015.05.067. The 23rd International Conference on the Application of Accelerators in Research and Industry - CAARI 2014.

[193] Tower Semiconductor, "Tower Semiconductor Official Website", https://towersemi.com/, 2025. Accessed: June 13, 2025.

[194] G. Aglieri Rinella et al., "Charge collection properties of TowerJazz 180nm CMOS Pixel Sensors in dependence of pixel geometries and bias parameters, studied using a dedicated test-vehicle: The Investigator chip", *Nuclear Instruments and Methods in Physics Research Section A: Accelerators, Spectrometers, Detectors and Associated Equipment* **988** (2021) 164859, doi:https://doi.org/10.1016/j.nima.2020.164859.

[195] D. Cohen, E. Koltin, M. Ilovich, and A. A. Shacham, "Stitching design rules for forming interconnect layers". U.S. Patent US6225013B1, May, 2001. Assigned to Tower Semiconductor Ltd.

[196] G. Aglieri Rinella, "Developments of stitched monolithic pixel sensors towards the ALICE ITS3", *Nuclear Instruments and Methods in Physics Research Section A: Accelerators, Spectrometers, Detectors and Associated Equipment* **1049** (2023) 168018, doi:https://doi.org/10.1016/j.nima.2023.168018.

[197] W. Snoeys et al., "A process modification for CMOS monolithic active pixel sensors for enhanced depletion, timing performance and radiation tolerance", *Nuclear Instruments and Methods in Physics Research Section A: Accelerators, Spectrometers, Detectors and Associated Equipment* **871** (2017) 90–96, doi:https://doi.org/10.1016/j.nima.2017.07.046.

[198] M. Munker et al., "Simulations of CMOS pixel sensors with a small collection electrode, improved for a faster charge collection and increased radiation tolerance", *Journal of Instrumentation* **14** (may, 2019) C05013, doi:10.1088/1748-0221/14/05/C05013.

[199] S. Bugiel et al., "Charge sensing properties of monolithic CMOS pixel sensors fabricated in a 65 nm technology", *Nuclear Instruments and Methods in Physics Research Section A: Accelerators, Spectrometers, Detectors and Associated Equipment* **1040** (2022) 167213, doi:https://doi.org/10.1016/j.nima.2022.167213.

[200] G. Aglieri Rinella et al., "Digital pixel test structures implemented in a 65 nm CMOS process", *Nuclear Instruments and Methods in Physics Research Section A: Accelerators, Spectrometers, Detectors and Associated Equipment* **1056** (2023) 168589, doi:https://doi.org/10.1016/j.nima.2023.168589.

[201] M. Bé et al., eds., "Monographie BIPM-5: Table of Radionuclides, Volume 3 (A=3 to 244)". Bureau International des Poids et Mesures, Sèvres, France, 2006. Evaluated by the Decay Data Evaluation Project (DDEP) under the CCRI. ISBN 92-822-2218-7.

[202] D. Banerjee et al., "The North Experimental Area at the Cern Super Proton Synchrotron", doi:10.17181/CERN.GP3K.0S1Y. Dedicated to Giorgio Brianti on the 50th anniversary of his founding the SPS Experimental Areas Group of CERN-Lab II and hence initiating the present Enterprise.

[203] EUDET Telescope Collaboration, "EUDET-Type Beam Telescope Tracking Software", https://mmager.web.cern.ch/telescope/tracking.html, 2024. Accessed: June 13,

2025.

[204] P. G. Baesso et al., "EUDAQ2 – A Flexible Data Acquisition Software Framework for Common Test Beams", *Journal of Instrumentation* **14** (2019), no. 10, P10033, doi:10.1088/1748-0221/14/10/P10033. Open Access; modular DAQ framework used in test beams :contentReference[oaicite:1]index=1.

[205] D. Dannheim et al., "Corryvreckan: A Modular 4D Track Reconstruction and Analysis Software for Test Beam Data", *Journal of Instrumentation* **16** (2021), no. 03, P03008, doi:10.1088/1748-0221/16/03/P03008, arXiv:2011.12730. Includes EUDAQ2 integration and test-beam use cases.

[206] V. Blobel, "A new fast track-fit algorithm based on broken lines", *Nuclear Instruments and Methods in Physics Research Section A: Accelerators, Spectrometers, Detectors and Associated Equipment* **566** (2006), no. 1, 14–17, doi:https://doi.org/10.1016/j.nima.2006.05.156. TIME 2005.

[207] R. B. Wittwer, "Vertex Detectors for the Future Circular Collider: Characterising Monolithic Active Pixel Sensors", May, 2024.

[208] ROOT Team, "ROOT: TEfficiency Class Reference", 2025, https://root.cern/doc/master/classTEfficiency.html. Accessed: 2025-07-16.